



TECHNISCHE UNIVERSITÄT MÜNCHEN
TUM School of Natural Sciences

Analysis and Application of Dual Curing Photopolymers in 3D Printing

Joel Micha Bachmann

Vollständiger Abdruck der von der TUM School of Natural Sciences zur Erlangung des akademischen Grades eines

Doktors der Ingenieurwissenschaften (Dr.-Ing.)

genehmigten Dissertation.

Vorsitz: Prof. Dr. Klaus Köhler
Prüfer der Dissertation: 1. Prof. Dr.-Ing. Kai-Olaf M. Hinrichsen
2. Prof. Dr.-Ing. Katrin Wudy

Die Dissertation wurde am 13.02.2023 bei der Technischen Universität München eingereicht und durch die TUM School of Natural Sciences am 19.04.2023 angenommen.

Acknowledgments

The greatest honor belongs to God. Without Him in my life, I would not have been able to begin or end this thesis. His love (John 3.16) is the foundation of my life and Jesus Christ is my anchor.

I would like to thank you Prof. Hinrichsen, for accepting me as an external doctoral student in your research group at the TC-I Chair. Thank you for your support, the many feedback loops, comments, suggestions for improvement and encouragement you have given me in our meetings. I would also like to thank my BMW supervisor Gabriele Fruhmann. You have supported me through all stages of the phd program. Your inquisitiveness and demand for accuracy were sometimes challenging but definitely helped me to develop my writing and researching skills.

Further thanks go to my BMW colleagues from the TI-3 lab: On behalf of the many other colleagues, I would like to thank you Birgit and Ingo for your support concerning all thermal analysis related questions. Working with you in the lab has always been a lot of fun and by exchanging with you Ingo I have learned something new about the DSC every week. Speaking of DSC, special thanks also go to you Stefan Schmölder from NETZSCH. Especially the one week in the application laboratory in Selb, in which we carried out all the tests for the second photo-DSC paper will be very much remembered. More thanks go to my EG-5 materials colleagues, especially Kirstin, Florian and Matthias. Thank you for your support especially through helpful coffee breaks and professional support concerning all material questions. The doctoral group has also been a great asset in the last three years. Here I would like to thank you Raimund, for motivating me in the final phase of writing this dissertation. Thank you Philip and Lukas. Without you, CVPP would not have been invented during the legendary brainstorm session in the coffee kitchen of the AMC. I also enjoyed the further cooperation to create the various patents with you. Thanks also to Elisabeth and Veronika. You both did an amazing job with your master thesis and working together with you was a lot of fun.

One of the most important pillars of the last three years was the weekly monday morning prayer with Joni, Bernhard, Chris, Josh and Ben. The friendship with you is worth more than the Dr. title. The same applies to you Lukas, aka GoProBro. The friendship with you is one of the best things that has happened to me and you inspire me never to settle for the average and to do the right thing despite the cost. Thanks also to my family for your years of investment in my education and also for your unconditional love and support. Finally, I would like to thank my wonderful wife Elena. You are the most important person in my life and I love you with all my heart. Thank you for going with me through the good and bad times of life.

Abstract

Additive manufacturing (AM) is making its way into more and more series applications. The material class of photopolymers plays a special role, as photopolymers have particularly good surface properties. The vat photopolymerization (VPP) technology of Digital Light Synthesis (DLS) enables significantly faster printing times than conventional VPP due to continuous polymerization. The material class of photopolymers has also developed rapidly. If photopolymers were too brittle for functional use only a few years ago, today dual curing photopolymers achieve much tougher properties. These are enabled by a dual curing reaction system: First, photopolymerization takes place, which is initiated by ultraviolet (UV) light and produces a dense network of crosslinked methacrylates. This is followed by a thermal curing, in which the initial crosslinking density is reduced, because thermally unstable groups break up and react with chain extenders. Since the use of dual curing photopolymers in VPP technologies is still quite new, the effects of temperature on the reaction mechanism and process are not yet clear. In DLS, heat is used as a post-processing step to initiate thermal curing, but the effects of heat on the photopolymer before UV curing are still unknown. It could initiate thermal crosslinking, which could also affect the viscosity of the resin. To characterize these effects, the thermal analysis method photo-DSC seems to be particularly suitable, since the experimental setup is very close to the DLS process. However, previous photo-DSC studies have not addressed the sample shape and its effects on the measurement. Also, relevant 3D printing parameters or environmental factors such as dwell time, wavelength and relative humidity have not been investigated. Therefore, the aim of this work is to gain a deeper understanding of the chemistry of dual curing, i.e. UV and thermal curing, photopolymers using a suitable and reproducible photo-DSC testing method, in order to improve the processing of the material in DLS and to find new ways to use the dual curing chemistry for AM. To this end, this work presents a reproducible photo-DSC method for photopolymers that takes into account sample shape, dwell time, light intensity conversion, wavelength, and relative humidity. Furthermore, the preheating of a dual curing urethane-methacrylate resulted in premature thermal crosslinking, which increased the viscosity of the material and, at higher temperatures, significantly altered the mechanical properties of the final parts. Thermal crosslinking can go so far as to transform the liquid urethane-methacrylate resin into a fully developed elastomer. This transformation is also accompanied by a change in polymerization behavior, which can be detected by the photo-DSC method. These findings led to the development of a new multimaterial VPP technology called cavity vat photopolymerization (CVPP), which enables the production of hard-shell/soft-core polymers by purposefully creating cavities in the design at places where elastic functions are later needed. CVPP offers many advantages over other multimaterial VPP approaches.

Kurzzusammenfassung

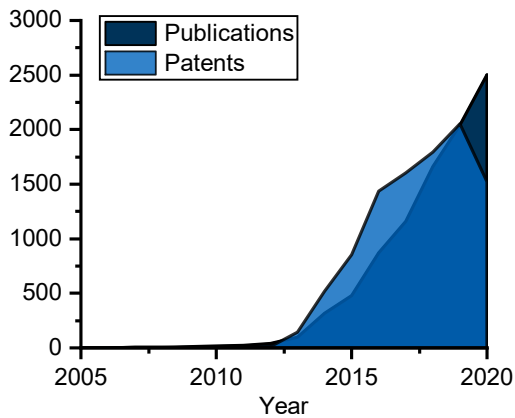
Die additive Fertigung (AM, hier werden die englischen Abkürzungen verwendet) hält in immer mehr Serienanwendungen Einzug. Die Materialklasse der Photopolymere spielt dabei eine besondere Rolle, da Photopolymere besonders gute Oberflächeneigenschaften aufweisen. Darüber hinaus ermöglicht die Digital Light Synthesis (DLS)-Technologie durch kontinuierliche Polymerisation deutlich schnellere Druckzeiten als herkömmliche Harzbad-basierte Photopolymerisationsverfahren (VPP). Bei DLS werden dualhärtende Photopolymere verwendet, die wesentlich zähere Eigenschaften aufweisen als herkömmliche Photopolymere, die aufgrund ihrer hohen Vernetzungsdichte meist sehr spröde sind. Diese werden durch eine duale Aushärtung ermöglicht: Zunächst findet eine Photopolymerisation statt, die durch ultraviolettes (UV) Licht initiiert wird und ein dichtes Netzwerk aus vernetzten Methacrylaten erzeugt. Darauf folgt eine thermische Aushärtung, bei der die anfängliche Vernetzungsdichte reduziert wird. Da die Verwendung von dualhärtenden Photopolymeren in VPP-Technologien noch recht neu ist, sind die Auswirkungen der Temperatur auf den Reaktionsmechanismus und den Prozess noch nicht klar. Bei DLS wird Wärme als Nachbearbeitungsschritt eingesetzt, um die thermische Aushärtung einzuleiten, aber die Auswirkungen von Wärme auf das Photopolymer vor der UV-Härtung sind noch unbekannt. Möglicherweise findet bereits eine thermische Vernetzung statt, die die Viskosität des Harzes verändern könnte. Um diese Effekte zu charakterisieren, scheint die thermische Analysemethode Photo-DSC besonders geeignet, da der Versuchsaufbau dem DLS-Prozess sehr nahe kommt. Bisherige Photo-DSC-Studien haben sich jedoch nicht mit der Probenform und ihren Auswirkungen auf die Messung befasst. Auch relevante 3D-Druckparameter wie Verweilzeit, Wellenlänge und relative Luftfeuchtigkeit wurden nicht untersucht. Ziel dieser Arbeit ist es daher, ein tieferes Verständnis der Chemie von dualhärtenden, d.h. UV- und thermisch härtenden, Photopolymeren mit Hilfe einer geeigneten und reproduzierbaren Photo-DSC-Methodik zu erlangen, um die Verarbeitung des Materials in DLS zu verbessern und neue Wege zur Nutzung von dualhärtenden Harzsystemen für AM zu finden. Zu diesem Zweck wird in dieser Arbeit eine reproduzierbare Photo-DSC-Methode für Photopolymere vorgestellt, die die Probenform, die Verweilzeit, die Umwandlung der Lichtintensität, die Wellenlänge und die relative Luftfeuchtigkeit berücksichtigt. Das Vorheizen eines dualhärtenden Urethanmethacrylats führte zu einer vorzeitigen thermischen Vernetzung, die die Viskosität des Materials erhöhte. Die thermische Vernetzung kann so weit gehen, dass sich das flüssige Urethanmethacrylat-Harz in ein voll entwickeltes Elastomer umwandelt. Diese Umwandlung geht auch mit einer Änderung des Polymerisationsverhaltens einher, die mit der Photo-DSC-Methode nachgewiesen werden kann. Diese Erkenntnisse führten zur Entwicklung einer neuen Multimaterial-VPP Technologie, der so genannten Hohlraum und harzbadbasierte Photopolymerisation (CVPP), die die Herstellung von Polymeren mit harter Schale und weichem Kern ermöglicht.

Contents

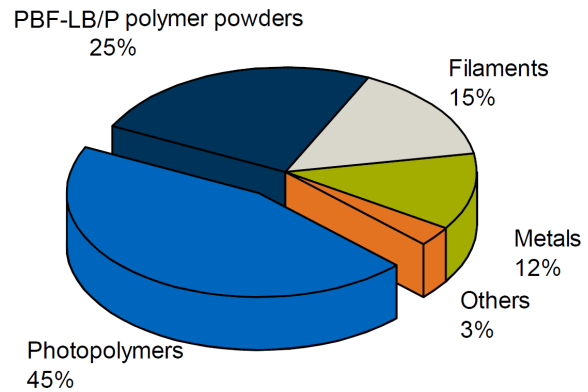
Acknowledgments	i
Abstract	ii
Kurzzusammenfassung	iii
1. Introduction	1
1.1. Vat Photopolymerization (VPP) Technologies	3
1.1.1. Digital Light Synthesis (DLS)	5
1.1.2. DLS Applications	7
1.2. Photopolymers	10
1.2.1. Radical Photopolymerization	13
1.2.2. Dual Curing Systems	13
1.2.3. Characterization Methods for Photopolymers	16
1.3. Multimaterial AM Technologies	17
1.4. Research Gaps and Questions	19
1.5. Objective of this work	19
2. Summary of Publications	21
2.1. Paper 1: Photo-DSC Fundamentals	22
2.2. Paper 2: Photo-DSC Parameter Study	23
2.3. Paper 3: Temperature Influence on a Dual Curing Urethane-Methacrylate	24
2.4. Paper 4: A New Additive Manufacturing Technology	25
3. Discussion	26
4. List of Publications	30
A. Original Peer-Reviewed Publications	32
A.1. Paper 1: Photo-DSC Fundamentals	32
A.2. Paper 2: Photo-DSC Parameter Study	52
A.3. Paper 3: Temperature Influence on a Dual Curing Urethane Methacrylate	66
A.4. Paper 4: A New Additive Manufacturing Technology	84
Acronyms	95
Bibliography	97

1. Introduction

According to the international ISO/ASTM 52900 standard [1], additive manufacturing (AM) or 3D printing is the construction of physical three-dimensional objects from virtual 3D models, also known as computer-aided design (CAD). There are several different AM processes. Most of these AM processes work by adding one layer of material at a time on top of each other without the need for machining or molds. These layers come from either the digital slicing of CAD, 3D scans or tomography data. The search for the term 3D printing and AM in the bibliometric databases scopus and the German Patent and Trademark Office shows an increasing trend of AM over the last 15 years (see Figure 1a). In 2010, only a few papers (17) and patents (10) were published. In contrast, 2505 papers and 1524 patents were published in 2020. This huge increase in general attention on AM can be explained by the wide range



(a) The development of 3D printing.



(b) The AM material market share of photopolymers in 2019 [2]. PBF-LB/P: laser-based powder bed fusion of plastics.

Figure 1.: The development and the material distribution of 3D printing.

of applications of these new technologies in various industries. The top industries currently developing and producing with AM are aerospace, automotive, consumer products, energy, infrastructure, medical & pharmaceutical, food and sports [3].

The largest material group for AM are polymers [2], which include thermoplastics, thermosets, elastomers, functional polymers, hydrogels, polymer blends, biological systems and composites [4, 5]. Metals and ceramics are also printed with AM. In addition, rather unusual materials such as concrete [6–8], glass [9, 10], wood [11, 12], chocolate [13, 14] and

ice [15, 16] can be processed via AM. According to Wohler's 2019 report [2], the total AM market is USD 768.5 million and in Figure 1b this market is segmented by material type. Therein, photopolymers, which are primarily processed via vat photopolymerization (VPP) and material jetting (MTJ), account for the largest AM market share of all materials.

The great advantage of photopolymers is their excellent surface quality and resolution compared to other AM materials [5]. The disadvantage in the past was their limited mechanical properties. However, dual curing photopolymers, which react first by ultraviolet (UV)-light and then with temperature, could solve this problem. The UV-curing is the well-known photopolymerization of reactive monomers, which forms a highly crosslinked polymer network. The chemistry of the thermal curing, on the other hand, describes a reaction of chain extenders (amines or alcohols) with thermally unstable urethane or urea groups, which forms a so-called interpenetrating polymer network (IPN) in the material and thus increases the overall toughness.

Dual cure urethane-methacrylate photopolymers from Carbon, Inc. (Redwood, USA) are processed with digital light synthesis (DLS). The latter is a 3D printing technology formerly called continuous liquid interface production (CLIP) and belongs to the category of VPP [17]. Conventional photopolymers have a good tensile strength due to the high crosslinking density, but their elongation at break is usually $< 10\%$. Dual curing urethane-methacrylates have a tensile strength of 45 MPa and an elongation at break of 100% [18].

With this significant improvement in mechanical properties, the material has also become interesting for use in vehicles. BMW, for example, has set up an individualization series for the MINI blinker, the so-called MINI Side Scuttles, which were manufactured with this urethane-methacrylate. However, the factors influencing process and material are manifold and need to be further investigated.

In this introduction, the various VPP technologies are introduced. This is followed by the detailed explanation of DLS technology and the presentation of various DLS applications. This is preceded by an introduction to photopolymers, explaining both UV-initiated radical photopolymerization and the chemical reactions of dual curing resins. Subsequently, the characterization methods used to study dual curing photopolymers are outlined. Then, the currently researched multi-material approaches are reviewed, which serve as the basis for the discussion following the results section of this work. The introduction concludes by outlining the research gaps and questions and stating the main objective of this work.

1.1. Vat Photopolymerization (VPP) Technologies

Generally, the ISO /ASTM 52900 standard [1] segments the AM technologies into seven different groups, namely:

1. vat photopolymerization (VPP)
2. material extrusion (MEX)
3. material jetting (MTJ)
4. binder jetting (BJT)
5. powder bed fusion (PBF)
6. direct energy deposition (DED)
7. sheet lamination (SHL)

VPP is particularly prominent because historically the first technology for AM comes from the VPP group. Although the first attempt for AM via UV-light can be traced back to Hideo Kodama in 1980 [19], the more prominent name is Charles W. Hull, who filed a patent for a photopolymerization technology called stereolithography (SLA) in 1986 [20]. It describes the selective curing of a viscous photopolymer by means of a movable laser beam. The curing is carried out on the surface of the resin in the vat. Before a new layer can be cured, the build platform is lowered by the height of the layer into the resin bath and the resin flow is ensured by a recoating mechanism. Lowering the platform into the resin bath during the process is often referred to as top-down. However, there are also bottom-up SLA machines like the SLA printers from Formlabs, Inc. (Somerville, USA), in which the build platform is lowered to the transparent window of the vat at the beginning of the process. This is where the curing of the first layer happens. The build platform is moved layer-by-layer out of the resin bath during bottom-up processes. Another closely related VPP process that can also be performed top-down or bottom-up is the digital light processing (DLP) technology. Instead of a UV-laser, the photopolymer is cured by UV-light, which comes from a UV-lamp and is projected into the resin by a digital micromirror device (DMD). In SLA, the horizontal resolution is determined by the spot size of the laser (approximately 25 μm) that writes the layer information into the resin. In DLP, the layer information is transported into the resin via square micro-mirrors of the DMD. These usually have an edge length of 30 μm to 100 μm . The number of micro-mirrors in DLP is equal to the number of pixels and is, for example, 1080 for full-HD. [22–24] Similar to DMD, liquid crystal display (LCD) can be used to enable the curing of entire layers by different grayscale light intensities [25]. The DLS technology uses a set-up similar to a bottom-up DLP, but with a UV and oxygen permeable window. This allows continuous photopolymerization and upward movement of the build platform [26]. Therefore, in addition to SLA and DLP, this technology is part of a new subcategory for VPP, called continuous digital light processing (CDLP). Another technology that enables CDLP is volumetric polymerization inhibition patterning (VPIP), which uses two different

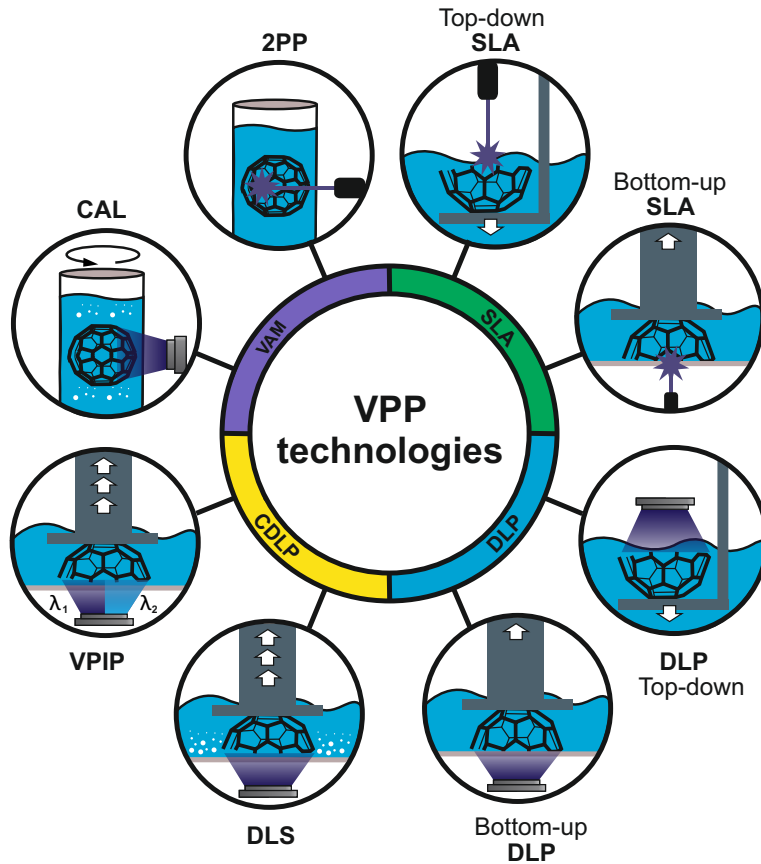


Figure 2.: Vat photopolymerization (VPP) technologies. The white arrow indicates the direction of movement of the build platform. Three arrows represent that it is a continuous and faster movement of the build platform without any recoating mechanism. λ_1 and λ_2 stand for two different wavelengths. The graphical representation is inspired by the review paper from Sampson et al. [21].

wavelengths one for the initiation and one for the inhibition of the photopolymerization [27]. In 2019, a new VPP technology emerged that enables volumetric additive manufacturing (VAM) and is called computed axial lithography (CAL) [28]. Instead of a build platform, CAL uses a rotation stage to pass the volumetric information to the resin via a DLP projector. Another important VPP technology, which is also not limited to a layer-by-layer approach is the two-photon polymerization (2PP) [29]. The photopolymer is transparent to near infrared (NIR) and therefore, the laser can be moved in any direction within the resin. A famous example was demonstrated by the research group from TU Wien, who printed a castle in the range of a few microns on the tip of pencil [30]. A more in depth summary of 2PP can be found in the review paper by Ligon et al. [5]. A visual representation of the various VPP technologies and their corresponding subgroups can be seen in Figure 2.

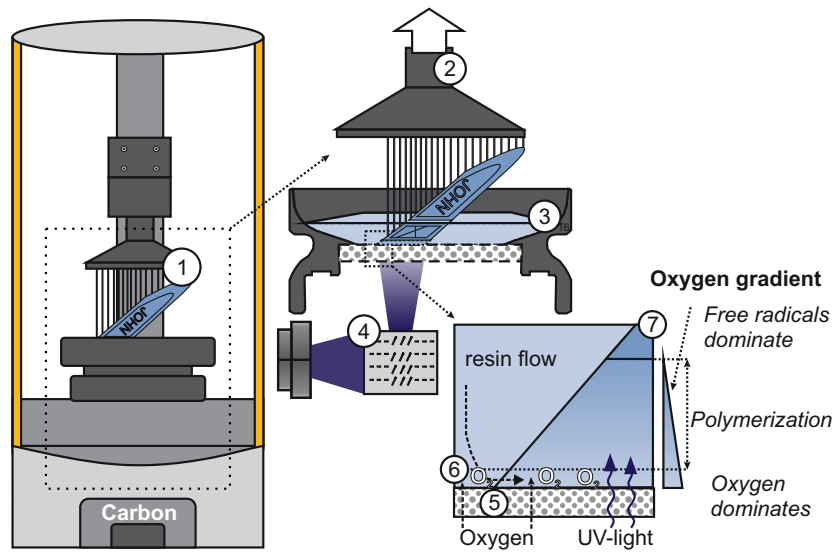


Figure 3.: Graphical illustration of digital light synthesis (DLS). ① 3D object with support structures ② Upward movement of the build platform ③ Vat filled with viscous photopolymer ④ DLP system with DMD ⑤ Oxygen and light permeable window ⑥ Oxygen-dead zone ⑦ Polymerized part [31]

1.1.1. Digital Light Synthesis (DLS)

Continuous liquid interface production (CLIP) was introduced in 2015 [32]. The speed of DLS was previously unmatched in AM and is enabled by a UV and oxygen-transparent window located at the bottom of the vat. A graphical representation of a DLS 3D-printer, the cross-section of the DMD, the vat and the polymerization gradient can be seen in Figure 3. Figure 4 shows the reaction scheme. UV-light that shines through the window at the bottom of the vat with a specific wavelength ($h\nu$) causes a homolytic cleavage of the photoinitiator (I), which produces free radicals ($R\cdot$). The latter react with monomers (M) from the resin. However, since oxygen also flows through the window at the bottom of the vat, the radicals can also react with the oxygen molecules (O_2), which leads to an inhibition of polymerization, as no chain growth takes place. This creates a so-called oxygen-dead zone, which is only a few microns thick [17]. Above the oxygen dead zone, the oxygen concentration decreases, creating a continuous polymerization zone in which free radicals dominate. Therefore, oxygen and reactive monomers compete for free radicals. Oxygen inhibition of (meth-)acrylates is a well-known phenomenon and has been seen as an obstacle in the past with several attempts to avoid it by developing new resin formulations [33]. For CLIP, however, oxygen inhibition serves as the key to unlock a continuous bottom-up process without the conventional recoating mechanism: Since no resin polymerizes in the oxygen dead zone, the build platform can be continuously elevated and a constant resin flow into the polymerization gradient is enabled. This is the main reason why the print speed of DLS is at least ten times faster than the print speed of SLA or DLP. [17, 26]

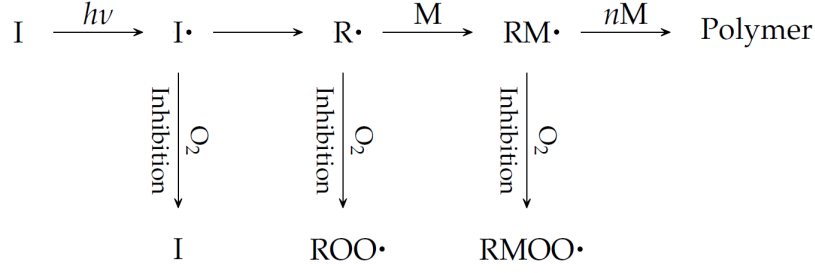


Figure 4.: Reaction scheme of a radical photopolymerization with oxygen inhibition [34].

In the following paragraph, the fundamental equations for DLS by Tumbleston et al. [17] are presented together with the latest studies about DLS.

The dead zone thickness z_{dz} can be controlled by three parameters:

$$z_{dz} = C \left(\frac{\phi_0 \alpha_{PI}}{D_{c0}} \right)^{-0,5} \quad (1.1)$$

The first is ϕ_0 , which is the number of photons per area per time. The second is the absorption coefficient α_{PI} , which is the product of the wavelength-dependent absorptivity and the photoinitiator concentration. The third is the required curing dosage without dye D_{c0} , which decreases as the reactivity of the resin increases. C is a proportionality constant. Based on the Beer-Lambert absorption law, the cured thickness z_{ct} can be calculated by Equation 1.2 as

$$z_{ct} = \frac{1}{\alpha} \ln \left(\frac{\phi_0 \alpha_{PI} t}{D_{c0}} \right). \quad (1.2)$$

In practice, the cured thickness increases with the exposure time t , the photon dosage and the reactivity of the resin (small D_{c0}). In addition to the photoinitiator, the resin usually contains other molecules that can absorb light but do not participate in polymerization, so-called passive absorbers. Therefore, the total resin absorption α is the sum of α_{PI} and the absorption coefficient of the passive absorbers such as dye or pigments α_{dye} :

$$\alpha = \alpha_{PI} + \alpha_{dye}. \quad (1.3)$$

The following correlation applies to print speed:

$$\frac{speed}{h_A} \sim \frac{\phi_0 \alpha_{PI}}{D_{c0}} \quad (1.4)$$

Where h_A is the absorption height defined as

$$h_A = \frac{1}{\alpha} \quad (1.5)$$

and a measure of vertical resolution. Large h_A means that photons can reach far into the resin, which improves the manufacturing speed while reducing vertical resolution. For a given h_A ,

the printing speed can be enhanced by increasing the reactivity of the resin (small D_{c0}), ϕ_0 or α_{PI} . The correlation from Equation 1.4 applies only to a constant resin flow. However, for geometries with a large horizontal cross-section, the time it takes for the resin to flow into the gap τ must be taken into account:

$$\tau \sim \left(\frac{L}{h}\right)^2 \frac{\eta}{p} \quad (1.6)$$

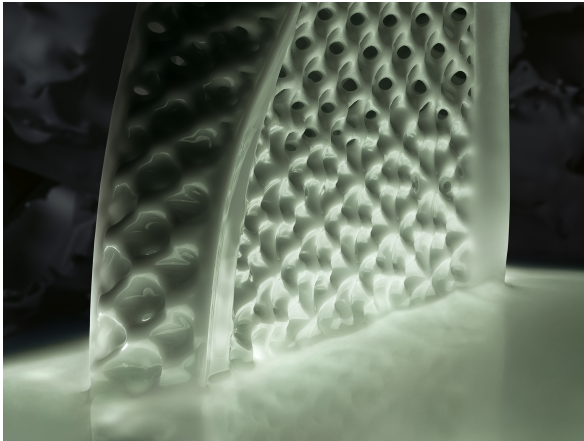
In addition to the cross-sectional line L and the gap height h , τ is also dependent on the atmospheric pressure p and the viscosity of the resin η . Because the micro-gap cannot be filled immediately, a transient vacuum emerges that pulls the part in the direction of the bottom of the vat. Research activities have been performed on modelling the the separation forces depending on process parameters [35–37]. Wang et al. [38] modelled the resin flow behavior in the micro-gap between the bottom of the vat. With CFD modelling, they found that the maximum negative pressure in the micro-gap is at the center of the cross-section. This force is called Stefan adhesion F_{Stefan} (see 1.7). It scales intensively with L , can lead to premature delamination from the platform, and is calculated according to the lubrication theory as follows [39]:

$$F_{Stefan} = \frac{-3\pi L^4 \eta \cdot speed}{32z_{dz}^3} \quad (1.7)$$

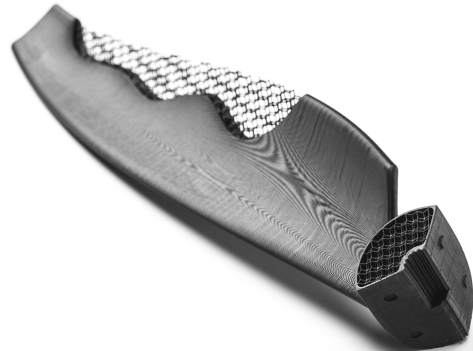
By injecting material through the cured part during DLS, Lipkowitz et al. [39] achieved much lower adhesion forces and faster print speed. With their study, they also highlighted one of the biggest challenges for DLS, which is printing parts with large cross-sections. The application examples from the next subsection make this point even clearer, as they all have relatively small cross-sections.

1.1.2. DLS Applications

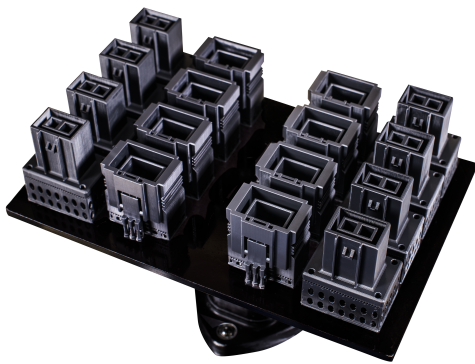
Most AM applications of photopolymers are still used for prototypes, but more and more products are coming to the market for small series production. Figure 5 shows four photopolymer products produced by DLS. Figure 5a displays the DLS production of an Adidas midsole used for sports shoes. The characteristic lattice structure with different mesh sizes allows for changing properties over the entire shoe [40]. Lattice structures are particularly suitable for DLS: in contrast to compact geometries, where large cross-sections are irradiated simultaneously, the UV-exposed areas of lattice structures are relatively small. As described in the section above, smaller cross-sections result in reduced adhesion forces and higher print speed. Additionally, the heat impact can be minimized. Due to the exothermic nature of the photopolymerization, the amount of heat generated in the vat correlates with the UV-exposed area. Consequently, compact geometries with large cross-sections generate a higher local heat input. In addition, heat transfer to the surrounding resin is optimal with the lattice structure, where the ratio of heat transfer area to irradiated area is greater than with bulky objects. Thus, the heat input of the lattice structures can be better transported. A well-known influence of too high temperatures is heat-induced shrinkage [41]. Due to the thermally crosslinking of Carbon, Inc.'s materials further thermal effects are very likely. However, there are no studies



(a) Adidas mid sole printed with an elastomer photopolymer (deviation of EPU 41). [43]. © Carbon, Inc. Used with permission.



(b) Drone blade with lattice structures made of a urethane-methacrylate photopolymer (RPU 70) [43]. © Carbon, Inc. Used with permission.



(c) Connectors made of a rigid epoxy photopolymer (EPX 81) [43]. © Carbon, Inc. Used with permission.



(d) Personalized MINI turn signal housings printed with RPU 70 [44]. © BMW AG.

Figure 5.: Photopolymer products 3D printed with the DLS technology.

yet explaining the effect of temperature on DLS.

The combination of lattice structure with an elastomer material can produce customer-specific mechanical properties and thus offers a great potential for individualization. For this reason, most examples of DLS applications are elastomer lattice structures:

The Adidas midsole has already been further developed and the second generation of the Adidas 4D FWD uses a special lattice design that converts the downward facing force into a forward facing force and thus supports the running movement [42].

Another example are elastomer lattice bicycle saddles from Specialized and Fizik [45]. Ridell's helmet pads for NFL players also consist of an elastomer lattice structure and are produced with DLS [46].

The drone blade printed with a urethane-methacrylate also uses this kind of lattice structure

for lightweight purposes (see Figure 5b). The surface effect visible on the inside of the blade is the so-called moiré pattern, which is very concise on products manufactured with urethane-methacrylates. Depending on the orientation of the part during DLS and the viewing angle, it sometimes appears stronger and sometimes weaker. For example, the moiré pattern in Figure 5d is not quite as strong. It results from the oxygen- and UV-transparent window, which is used in the DLS process at the bottom of the resin vat.

The next example from Figure 5c shows typical connectors used for example in wiring harnesses of cars. The relatively small geometry of these parts makes it possible to print 16 components in one print job. The number of parts per build job is critical to AM. The more parts fit into a build job, the more economical the overall process becomes. The dimensions of the build volume of the M2 carbon printer are 189 mm x 118 mm x 326 mm and of course represent the limiting factor for the maximum part size. The homogeneity of the mechanical parameters over the entire build area is an important requirement for all AM processes. If this cannot be guaranteed, an effective build area must be specified in which the material properties are almost identical. Obst et al. [47] investigated the influence of UV light intensity and exposure time on a urethane-methacrylate material over the entire build plate of the Carbon, Inc. M2. They found that increasing the exposure time and UV light intensity resulted in more brittle material behavior. The data also shows a build area dependence with higher tensile strengths at the periphery and lower tensile strengths in the middle of the build plate. These variations might stem from a non homogeneous UV light distribution of the DMD, but need further investigation.

The last example from Figure 5d shows a personalized MINI turn signal housing, which is also known as the MINI Side Scuttle and is a good example of how AM can improve the individualization of products for customers. In the past, the traditional production of such parts required either new tools or additional processing steps. AM can now produce individualized products within the same production process for small series with comparatively little additional effort.

Unlike most other AM processes, in VPP the material is not just melted, but the photopolymers undergo a complete chemical reaction that also changes the chemical composition of the material. The composition of the feedstock in DLS consists of many different molecules and can be quite complex compared to, for example, PA11 in PBF, which essentially consists of a single type of molecule. To understand the influence of the material on the process and the properties of the final 3D object, it is important to understand the basics of photopolymers in general. This is what this section is about.

1.2. Photopolymers

Photopolymers have a wide range of commercial applications such as electronic and optical materials, adhesives and sealants, coatings and surface modifications, and of course AM technologies such as VPP [48]. Figure 6 shows the structure of the three large polymer classes and indicates to which class photopolymers are assigned. Therefore, the application examples

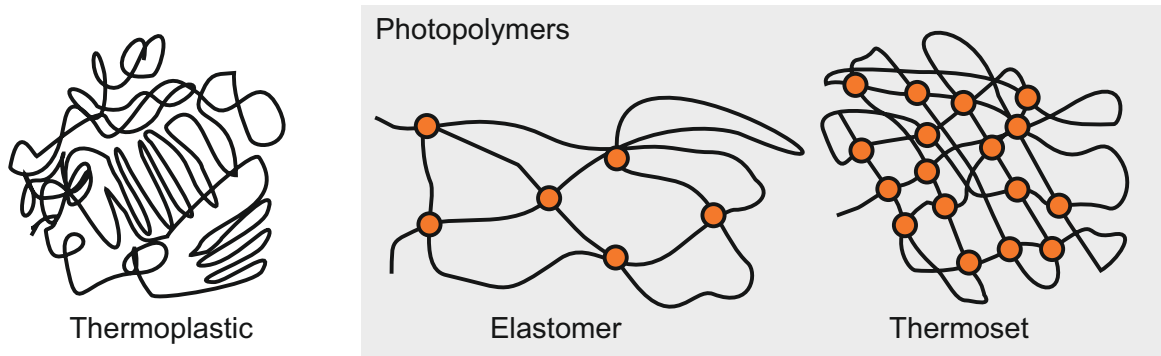


Figure 6.: Polymer classes with and without crosslinks (red circle) [34].

from Figure 5 are either elastomers (shoe sole) or thermosets (all other examples). The difference between these two polymer classes is their crosslinking density, which is lower in elastomers and higher in thermosets. Either way, their cured shape cannot be changed. This is the main difference to the third polymer class of thermoplastics, as they have no crosslinks, which makes their shape reversible with heat. The advantage of thermoplastics used in AM technologies such as MEX and PBF lies in their reusability and recycling potential. Old PBF powder can be melted, for example, into pellets or filaments to be used as the feedstock of MEX.

Table 1.1.: Radical, cationic and hybrid photopolymer systems.

Photopolymer reaction systems	
<i>Radical system</i>	<i>Cationic system</i>
Photoinitiator (PI) + acrylate monomer	Photoacid generator (PAG) + epoxides
PI + methacrylate monomer	PAG + epoxides + vinyl ethers
PI + thiol-en-monomer	PAG + epoxides + oxetanes
<i>Hybrid system</i>	
PI + (meth-)acrylates + (thiol-en) + PAG + epoxides + (vinylethers) + (oxetanes)	

The polymerization mechanism of photopolymers depends on the photopolymer system. The three major photopolymer systems are radical, cationic and hybrid systems (see Table 1.1) [5]. The first requires a photoinitiator (PI) and (meth-)acrylates and reacts in a radical photopolymerization, while the second requires photoacid generators (PAGs) and epoxides that react in a cationic chain growth mechanism. Hybrid systems contain both radical and cationic monomers and initiators and form an IPN.

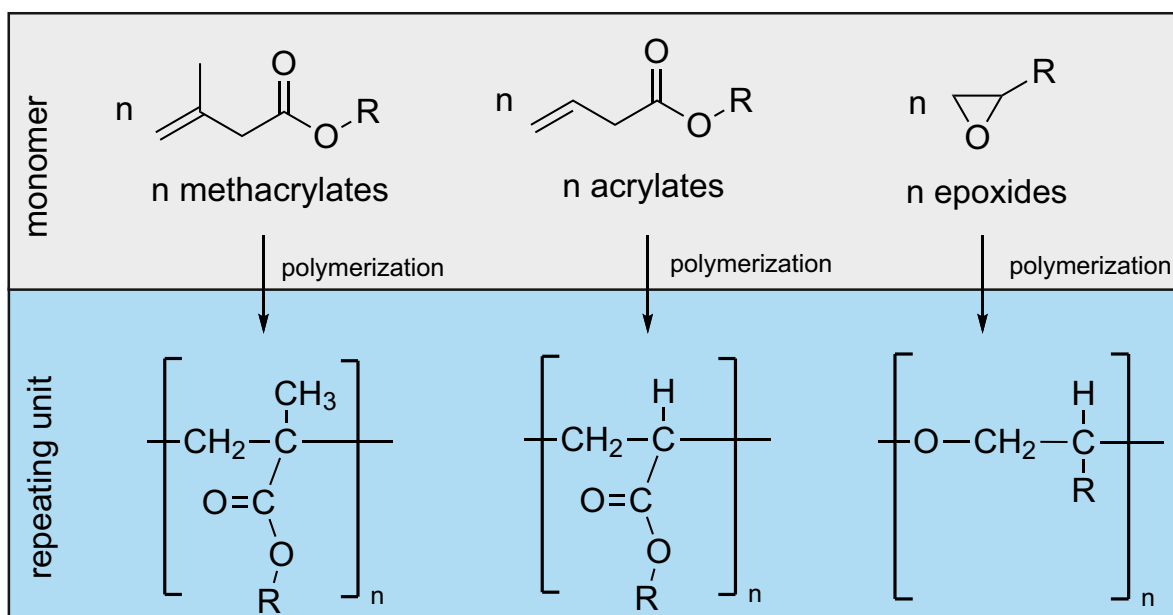


Figure 7.: (Meth-)acrylates and epoxy monomers with their corresponding repeating units in the polymer chain.

Figure 7 shows methacrylate, acrylate and epoxy monomers and their repeating unit in the polymer after polymerization. The only difference between methacrylates and acrylates is the methyl group at the alpha position of the vinyl group (C=C). This causes a steric hindrance and is the reason why the reaction rate of methacrylates is slower than the reaction rate of acrylates [33]. The rapid curing speed of acrylates can lead to distortions in the printed object. Murphy et al. [49] found that a system that contains both slow-curing methacrylates and fast-curing acrylates achieves a better result compared to using only one monomer type. Of course, the monomers can also be multifunctional, i.e. have more than one functional group. If the same functional group exists two, three or four times in the same molecule, they are di-, tri- or tetra-(meth-)acrylates. The amount of functional groups of the monomers has an important influence on the curing behavior and the formation of crosslinks. Generally, the higher the amount of functional groups, the higher the number of crosslinks. Furthermore, an increase in crosslinking density leads to increased tensile strength with simultaneous decrease in the maximum elongation at break, i.e. the brittleness increases [50]. Anastasio et al. [51] found out that for methacrylates cured with low UV light intensities, a thermal postcure can increase the mobility of dangling chains, which can then further react in the network and thus increase also the yield stress. However, unlike the DLS feedstock, the tested material was only UV reactive.

Another important characteristic of the monomer is its molecular weight or molar mass, as it directly affects the viscosity of the resin. Higher molecular weight oligomers are often needed to achieve sufficient green strength and reduced shrinkage after UV-curing, while low-weight monomers are used to improve processability and increase print speed by reducing viscosity.

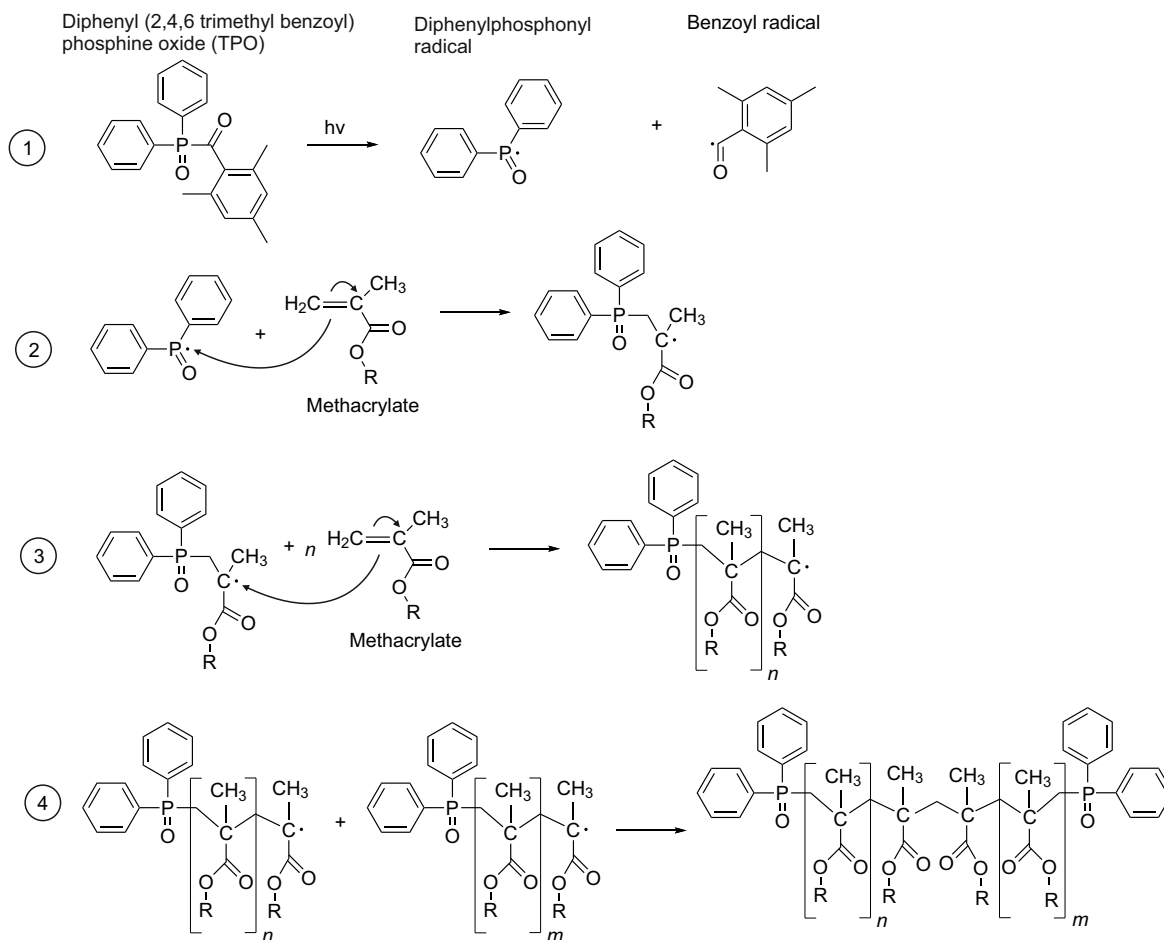


Figure 8.: Chemical reaction steps of a free radical photopolymerization.

The increased viscosity can be compensated by heating the resin. Some companies and research groups specialize in the field of hot lithography. There, resin formulations are processed with such a high proportion of heavy oligomers that the feedstock might be even solid at room temperature [52]. However, these materials are also only UV- and not thermally reactive.

The last group from Figure 7 are sulphur-containing thiol-en systems, which are generally subject to lower polymerization shrinkage compared to acrylate-based systems and are less brittle [53, 54]. Hybrid systems of (meth-)acrylates with thiols show less shrinkage and produce sharper structures [55]. They are also not as prone to oxygen inhibition as acrylates, which is usually a good property. However, this makes them unusable for DLS, as they would polymerize on the oxygen transparent window.

1.2.1. Radical Photopolymerization

The tradename of some DLS materials, such as EPX 81, may be misleading, as one might assume that the underlying reaction model is cationic due to the reference to epoxides. Although the resin system contains hybrid molecules that have both epoxy and (meth-)acrylate functional groups, the reaction system is neither cationic nor hybrid, as the photo differential scanning calorimetry (photo-DSC) results will show in the results section [31, 56]. The tradename of EPX 81 refers to the second thermal curing step in which the reaction between epoxides and amines is initiated by heat. This second reaction step, will be explained in more detail in the next section.

All DLS resin systems undergo radical photopolymerization, as shown in Figure 8, which takes place directly above the oxygen dead zone (see Figure 3). In most DLS resins, the PI is diphenyl (2,4,6 trimethyl benzoyl) phosphine oxide (TPO). The first step of the radical photopolymerization is the initiation (1): UV-light ($h\nu$) causes a homolytic cleavage at the phosphor position of TPO, which leads to the formation of two radicals. The diphenylphosphonyl radical is more than twice as reactive as the benzoyl radical [57, 58]. The second step is the chain start (2), in which the phosphonyl radical reacts with the vinyl double bond (C=C) of the methacrylate, which leads to a new methacrylate radical. In the same way, the chain grows monomer by monomer. This step is called chain propagation (3). When two radical chains react with each other, this terminates the polymerization by recombination (4). Chain propagation can also end with disproportionation, in which the transfer of an H-atom from one radical to another creates a C=C double bond. [59]

1.2.2. Dual Curing Systems

Dual curing systems are defined as a system in which two curing reactions take place to combine two otherwise distinct polymer networks. These curing reactions can be either simultaneous or sequential [60]. A good example for a simultaneously dual curing is the reaction of hybrid photopolymer systems that cure epoxides and (meth-)acrylates with their corresponding PAG and PI simultaneously [33, 61]. On the other hand, sequential dual curing reactions are well known from adhesives and composites, as the processing of these materials often requires a stable intermediate step. A concrete example of sequential dual curing are acrylates that react with nucleophiles (Michael donors) like amines via an aza-Michael addition before photopolymerization [62–64]. Urethane-methacrylate in DLS also follows a sequential dual curing process: as already mentioned, after radical photopolymerisation, the final material properties of the DLS materials have not yet been achieved. The material state after DLS is sometimes referred to as green state. The printed object must be cleaned of excess resin and removed from the build platform. Afterwards, it is placed in a convection oven with a material-specific temperature profile, e.g. four hours at 120 °C for urethane-methacrylates. The dual curing reaction scheme of DLS resins is described in Figure 9. The material goes through two different states with two different reactions: the first is the UV-initiated photopolymerization, which converts the liquid phase (A) to the solid green state (B), the second is the thermally activated crosslinking reaction that results in the final

solid state (C). In order to understand both the UV and thermally activated reaction of a



Figure 9.: Consecutive UV and thermal curing of DLS materials.

DLS photopolymer, it is necessary to take a look at the composition, since it is important to know which molecules are involved in which reaction. The composition of the urethane-methacrylate is given in Figure 10. It consists of two parts: part A and part B, which are mixed in the ratio 10:1 and dispensed into the DLS cassette before printing. Part A of the urethane-methacrylate consists of TPO (photoinitiator, 0.1 % to 2 %), urethane dimethacrylate (UDMA) (difunctional oligomer, 1 % to 20 %), methacrylate blocked polyurethane (MABPU) and methacrylate blocked diisocyanate (MABDI) (blocked prepolymer synthesised with diisocyanates, 10 % to 70 %), isobornyl methacrylate (IBOMA) (reactive diluent, 10 % to 50 %) and neopentyl glycol dimethacrylate (NPGDMA) (difunctional monomer, < 0.3 %). Part B of the urethane-methacrylate consists of trimethylolpropane tris [poly (propylene glycol) amine terminated] ether (Chain extender, 20 % to 100 %). [65, 66] The rather small molecules with

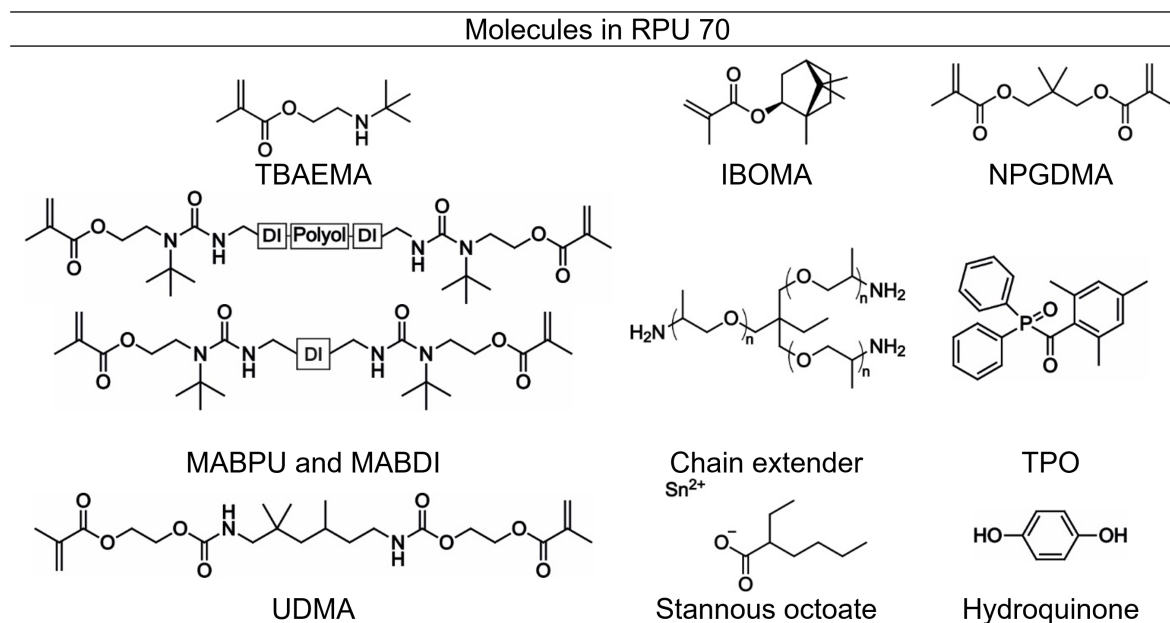


Figure 10.: Composition of the urethane-methacrylate. Adopted from Bachmann et al. [67]

low molecular weight IBOMA, NPGDMA and tert-butylaminoethyl methacrylate (TBAEMA) are reactive diluents as they participate in step (2) and (3) of Figure 8 and reduce the overall viscosity of the resin. The molecules NPGDMA, UDMA, MABDI and MABPU are difunctional, as they have two methacrylate groups at both ends and thus can crosslink two polymer chains during polymerization. TBAEMA has a special role, as it is both reactive

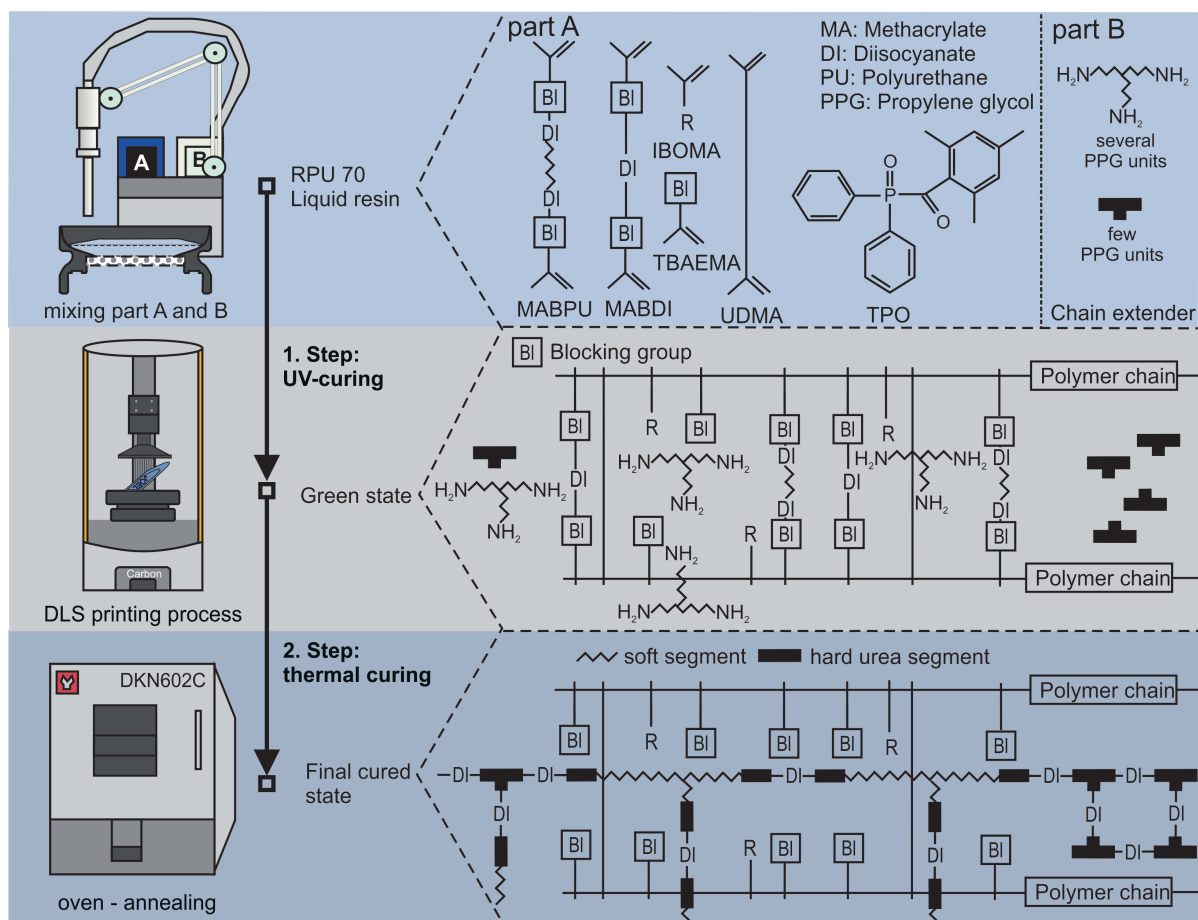


Figure 11.: Dual curing reaction mechanism of a urethane-methacrylate during DLS. Adopted from Bachmann et al. [67]

diluent and the blocking unit of MABDI and MABPU, to which it is connected by a blocked isocyanate group. A detailed analysis of the MABDI and MABPU molecules can be found in the result part of this dissertation [67]. Here it suffices to know that MABDI and MABPU are special synthesized oligomers consisting of one polyol, two diisocyanate and two TBAEMA or one diisocyanate with two TBAEMA, respectively. Both contain the characteristic thermally unstable urea group with the blocking unit TBAEMA. At elevated temperatures, this chemical bond is dissolved and the deblocked isocyanate reacts with the primary amine group of the chain extender from part B. This results in an IPN consisting of the UV polymerized and the thermally created polymer networks. A schematic representation of the DLS process steps, the material states and the IPN can be seen in Figure 11. The additional degree of freedom of the thermal post curing step for Carbon's dual curing formulations enables a wide range of material classes, such as elastomeric polyurethanes (e.g., EPU 40), silicone-like materials (e.g., SIL 30), epoxides (e.g., EPX 82), polyurethanes (e.g., RPU 70), and cyanate esters (e.g., CE 221). [56]

1.2.3. Characterization Methods for Photopolymers

Now that both the process of DLS and the ongoing chemical reactions have been explained, this section summarizes the test methods that are used to characterize photopolymers. Table 1.2 lists various target values that can be found by using the appropriate characterization methods. The corresponding test category, i.e. thermal, rheological, chemical, optical and mechanical is also listed. The most common analyzing methods for characterizing the

Target figure	Testing category	Characterization method
Evaporation behavior	Thermal	Thermogravimetric analysis (TGA)
Reaction heat	Thermal	Differential scanning calorimetry (DSC)
Heat, strength and speed of photopolymerization	Thermal	Photo-DSC
Viscosity	Rheological	Viscometer
Chemical bonding	Chemical	Fourier-transform infrared spectroscopy (FT-IR)
Molar mass	Chemical	Quadrupole / time-of-flight mass spectrometer (Q-TOF MS)
Density differences	Optical	Computed tomography (CT)
cross-section	Optical	Microscope
Tensile strength, -modulus and elongation at break	Mechanical	Tensile testing
Impact strength	Mechanical	Impact testing
Storage-, loss modulus and loss factor	Mechanical	Dynamic mechanical analysis (DMA)

Table 1.2.: Testing methods used to characterize photopolymers.

transition from liquid photopolymer resin to solid, crosslinked thermoset are the fourier-transformed infrared spectroscopy (FT-IR) and the photo-DSC method. The former provides information about the chemical bonds, such as C=C double bond conversion, while the latter provides thermal information about the heat and strength of polymerization. Decker et al. [33] proved by the aid of real-time FT-IR that acrylate monomers polymerize faster than epoxy monomers. By the aid of the photo-DSC, Rusu et al. [68] found out that higher temperatures and higher UV light intensities lead to a higher reaction rate and to faster polymerization conversion. Several other photo-DSC studies investigated radical, cationic and hybrid photopolymers [68–75]. Some focus on the reactivity [71, 76] others on the influence of oxygen inhibition [77, 78]. In these studies, liquid samples are used with small sample masses to ensure isothermal conditions. However, one often neglected aspect of photo-DSC measurements is the sample shape, which can either be drop or film. Almost all mentioned studies use a film sample shape, as it offers a large contact area from the sample to the crucible, which ensures good heat transfer. However, a uniform sample thickness is often difficult to achieve because the resin is pulled upwards at the walls of the crucible. The latter phenomenon can be avoided if the drop shape is used, which offers an interesting

alternative in sample shape preparation, because this shape also reduces surface effects. The downside, however, is that there is also no uniform film thickness. Another neglected aspect of photo-DSC measurements is the time between sample preparation and measurement start (dwell time), which is also an important time for the processing of dual curing photopolymers in DLS. There, the two part resins are first mixed prior to printing. Several hours can pass before the mixed material is UV cured in the process. The influence of prior oxygen diffusion into the resin, evaporation of volatile components from the resin, prior UV- or thermal curing due to environmental influences can not be ruled out.

1.3. Multimaterial AM Technologies

A new multi-material VPP technology will be presented in the result part of this dissertation. In order for this new technology to be adequately discussed in the overall discussion chapter, the state of the art for multi-material AM technologies is presented here.

Multi-material AM is the spatially controlled printing of at least two different materials within a 3D object. Demand for such parts often comes from improved functionalities such as embedded sensors, improved shock absorption, crack resistance, damping, elasticity, actuation and structural electronics [66]. In general, the approaches for multi-material AM can be divided into three main categories: the first category uses multi-material feedstocks, the second category utilizes only one feedstock, but at least two different reactions are initiated, or the production parameters are modified to convert the feedstock into an object that has at least two different material properties and functionalities. The last category is any variant of a combination of the first two categories. The multi-material feedstock approach is used primarily with extrusion-based AM [79–86] and Polyjet [87, 88] as these technologies often provide multiple printing nozzles that are beneficial when printing different materials. However, these methods lack the precision and dimensional accuracy of VPP.

Therefore, there are now a variety of multi-material VPP approaches. Sampson et al. [21] have divided these approaches into six different categories that can be seen in Table 1.3. In the first

Nr.	Multi-Material Approach	VPP Technology	References
1	Manually switching resins / resin vats	SLA, DLP, 2PP, DLS	[89–110]
2	Mechanically switching resins / resin vats	SLA, DLP, 2PP	[111–124]
3	Printing over pre-existing object	CAL	[28]
4	Curing of hybrid resin with two wavelengths	DLP	[125–127]
5	Varying the degree of polymerization	DLP	[89, 105, 128–133]
6	Combination of approaches Nr. 1 - 5	SLA, DLP	[105, 128, 129]

Table 1.3.: Multi-material VPP approaches according to Sampson et al. [21].

two categories, the resin or resin vat is switched manually [89–110] or mechanically [111–124]. With some examples of this approach, only the next to-be-printed layer is injected into the resin vat [102, 103]. From the moment the resin is replaced, the object is further printed with another material. This approach is relatively simple and can be implemented with any

number of materials and for all VPP technologies. One of the challenges is that the already cured object and the resin container must be washed and rinsed to prevent contamination. This makes the entire printing process much slower. Furthermore, the adhesion between the layers of different materials is often problematic and the different curing behavior can lead to different shrinkage, which may require specific programming of the printing process. For the mechanical switching of resins/resin vats approach, one or more of these components are needed: a rotating vat carousel, an automatic (syringe) pump that dispenses the resin into the vat, and a cleaning system with compressed air. Of course, the advantage of having the process more automated goes in hand with the drawback of needing several custom made printer modifications.

The third approach for multi-material VPP is the so-called "overprinting", which describes the printing of a 3D structure around an existing shape. According to Sampson et al. [21], this approach is only made possible by CAL technology. However, 2PP also allows "overprinting", as the example of the printing of a submicroscopic castle on the top of a pencil shows [30]. With 2PP, the laser can penetrate deep into the resin before initiating polymerization [21]. The unique advantage of this approach is that the existing shape, which is "overprinted", can be produced by any manufacturing technology. Kelly et al. [28], for example, demonstrated with CAL the overprinting of a metal shaft of a screwdriver with a personalized polymer handle in less than a minute. The print speed is another advantage. However, CAL requires a highly viscous resin, non-trivial optical alignments, and additional programming to synchronize the sliced projected images with the rotational speed of the vat.

The fourth approach describes the dual curing of hybrid resins (see Table 1.1) with two different wavelengths. One wavelength ensures the initiation and curing of the PI and (meth)acrylates and the other wavelength the curing of the PAG and epoxides. Thus, within a printed layer, an XY-material-heterogeneity can be generated using only one resin. The obvious drawback of this approach is the large hardware as well as software effort involved in installing a second light source. Additionally, this approach is only possible with DLP. Two examples of this approach are solution mask liquid lithography (SMaLL) [125, 126] and multimaterial actinic spatial control (MASC) [127].

The fifth approach is to influence the degree of cure by using grayscale light projections and / or changing exposure times. Both have a direct impact on the crosslinking density and thus on the tensile modulus. With this approach, an XY-material-heterogeneity can be implemented within a layer with only one resin. Additionally, a material-gradient within a layer is possible. However, additional manipulation of the projection images is also required in order to implement grayscale light or a special exposure times strategy.

The sixth approach describes the combination of one or more of the previous approaches. One of the most interesting examples in this category is described by Kuang et al. [128], who used a dual curing resin (UV + thermal) comparable to the Carbon materials (see section 1.2.2). There, an XY-material-heterogeneity within a projection plane is achieved during UV-curing via grayscale light. In the subsequent thermal curing step, an amine cross-linkers react with unreacted epoxides to achieve the final material properties.

1.4. Research Gaps and Questions

In summary, the two main research gaps (RG) and research questions (RQ) that will be the focus of this work are as follows:

- **RG 1:** First, previous photo-DSC studies have not addressed the issue of sample shape and its effects on the measurement. Furthermore, most photo-DSC studies have failed to convert the light intensity of the light source to the actual light intensity on the sample surface during measurement. In addition to light intensity, surrounding gas composition and temperature, other relevant parameters of the 3D printing process or environmental factors such as dwell time, wavelength and relative humidity (RH) have not yet been studied.
- **RQ 1:** How do sample shape, dwell time, wavelength, and RH affect photo-DSC measurements, and how can the light intensity be calibrated in order to replicate VPP process parameters?
- **RG 2:** Secondly, the literature on VPP materials curing with UV and heat is still very limited, so the influence of temperature on the reaction mechanism and process is not yet well understood. The preheating of the resin and its influence on the viscosity, the printing process and the final mechanical properties have not yet been studied.
- **RQ 2:** How do increasing temperatures affect thermal curing, how can the influence be characterized, and what happens to the viscosity of the resin?

1.5. Objective of this work

The main objective of this work is to gain a deeper understanding of the chemistry of dual-curing photopolymers, i.e. UV and thermal curing, using a suitable and reproducible photo-DSC method, to improve the processing of the material in DLS and to find new ways to use dual cure chemistry for additive manufacturing. The objective of this work is divided into three sub goals:

1. The first goal of this work is to develop a reproducible and standardized photo-DSC test method for dual curing photopolymers and to identify the most important influencing factors on the testing method as well as on the material.
2. The second goal is to investigate the thermal influence on a dual curing urethane-methacrylate in order to characterize the ongoing chemical reactions and to understand temperature-dependent challenges in the processing of the material.
3. The third research goal is to use the dual curing reaction to develop a new multi-material VPP technology.

The methodological approach for achieving the objectives of this work can be seen in Figure 12. The next chapter summarizes the results of each publication and outlines the author’s individual contribution on one page. This is followed by the cumulative integration of four accepted journal publications (full papers in international, English language, peer-reviewed journals).

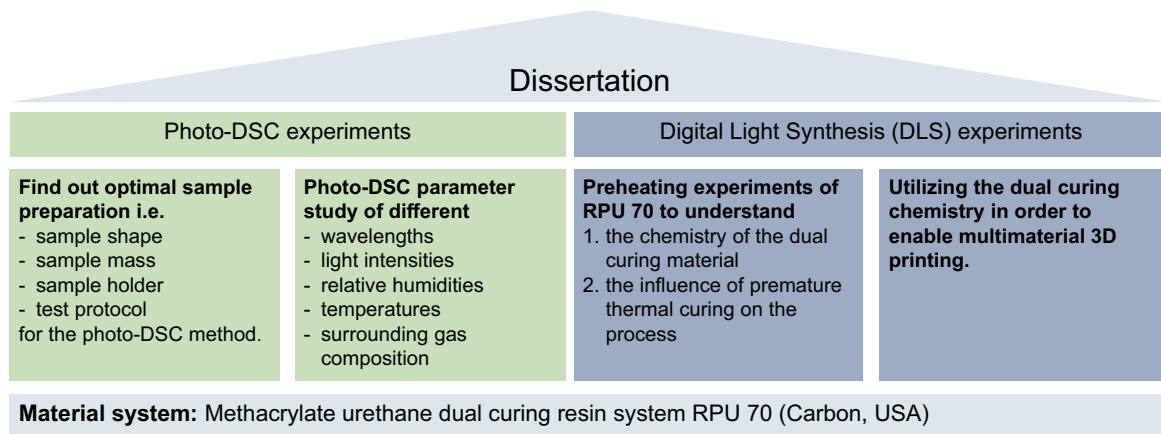


Figure 12.: Methodological approach and structure of results chapter to achieve the objectives of this work.

2. Summary of Publications

The graphical abstracts for the four publications can be seen in Figure 13. The first two publications focus on the photo-DSC method [31, 56], while the last two focus on the temperature dependent chemical reaction in a urethane-methacrylate [66, 67].

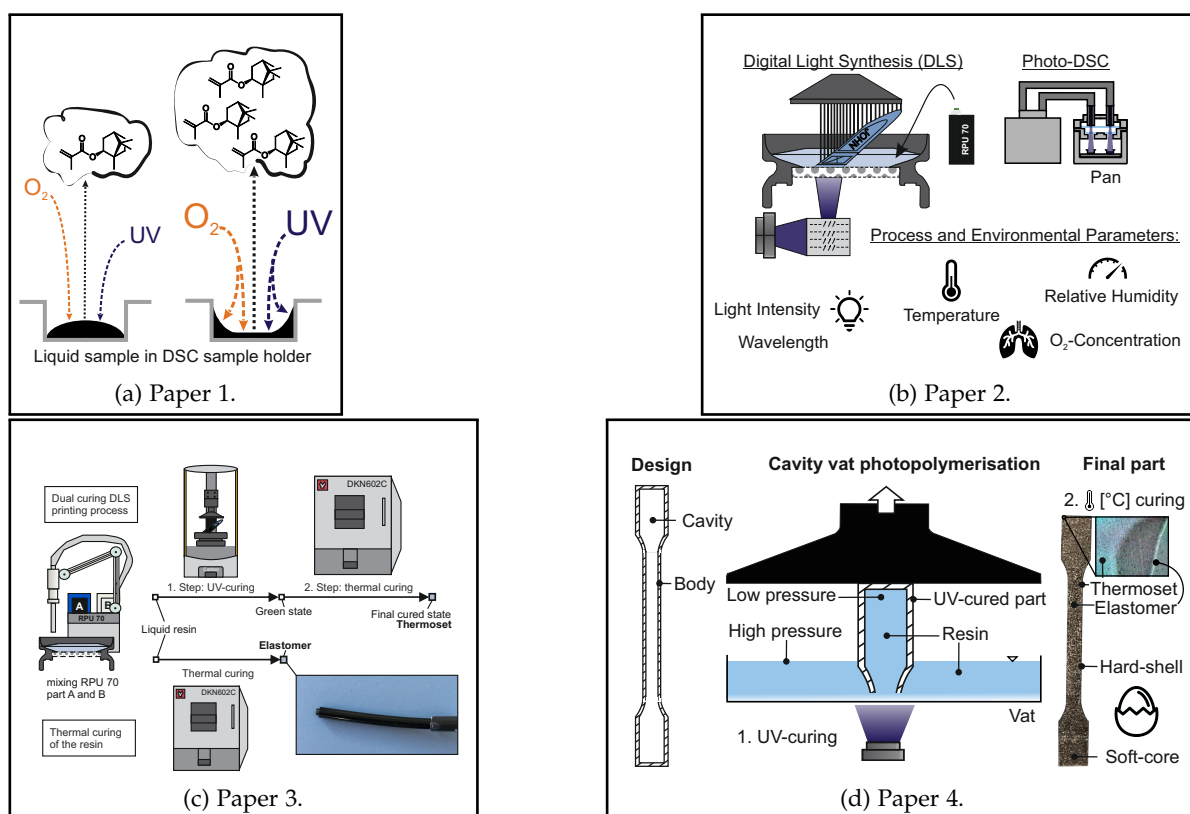


Figure 13.: Graphical summary of the four publications:
 Paper 1: Photo-DSC Fundamentals,
 Paper 2: Photo-DSC Parameter Study,
 Paper 3: Temperature Influence on a Dual Curing Urethane-Methacrylate in DLS,
 Paper 4: A New Additive Manufacturing Technology.

2.1. Photo-DSC Method for Liquid Samples Used in Vat Photopolymerization in *Analytica Chimica Acta*

Summary of the Publication

In the first publication, photo-DSC is presented as a suitable method for characterizing photopolymers in AM. Especially because important process parameters such as the target UV-exposure time and the resulting reaction heat can be determined with it. For the photo-DSC to deliver reliable and meaningful results, careful sample preparation and an appropriate test protocol are required. The selection of a suitable sample shape, sample mass and sample holder (crucible) plays a decisive role. In addition, different reactivity of different resins may require different types of test protocols.

The comparison of two different photo-DSC exposure profiles showed that a preexisting test protocol can be shortened from 42 min to 24 min without losing measuring accuracy. The two two-part DLS resin systems, the methacrylate urethane and the acrylate epoxy, were investigated both part by part as well as in the mixed state at different temperatures and O₂-concentrations using the photo-DSC method. This not only identified the part with the photoinitiator and the type of reaction system (radical or cationic), but it also identified a difference in the curve between methacrylates and acrylates. Although EPX 82 contains epoxy acrylates, it does not follow a hybrid reaction during UV-curing, but a radical reaction. In order to investigate the influence of surface effects such as oxygen-diffusion, prior UV-curing through ambient radiation and evaporation of volatile components on the photo-DSC method the following sample preparations parameters were compared: sample shape (drop, spread), sample mass (1.0 mg, 2.8 mg and 5.0 mg) and dwell time (0 h, 4 h and 7 h). According to the surface-to-volume ratio, the 2.8 mg drop shape offers the most robust sample preparation with the fewest surface effects. The 1.0 mg spread sample shape, on the other hand, offers the thinnest film thickness (40 μm) and thus the closest comparability to high resolution print jobs. Different covers were placed on different crucibles, to further reduce surface effects. These samples were tested over different duration in the automated sample changer (ASC) that enables automated and consecutive measurements. The lowest mass loss of below 1 % for up to 10 h was achieved by the combination of a cold pressed 85 mL crucible covered with a 300 mL Al₂O₃ crucible, which is removed shortly before the actual measurement. [31]

Individual Contributions of the Candidate

One of the contributions of the candidate to this publication were preparatory photo-DSC measurements, which served to investigate and conceptualize the scope of this publication. Two-thirds of the experiments were carried out by Elisabeth Gleis. The other third of the experiments were carried out by the candidate together with Dr. Stefan Schmölder. The formal analysis, the writing of the original manuscript and the project management, which included the organization of resources and equipment for the experiments in two different thermal analysis laboratories, were also carried out by the candidate.

2.2. Photo-DSC Parameter Study of Photopolymers Used in Digital Light Synthesis (DLS) in SPE Polymers

Summary of the Publication

The first publication showed the optimal sample shape and mass for reliable and reproducible photo-DSC results as well as the need to correct the reaction heat due to evaporation during the measurement with a mass correction factor. Building on these results, the second publication focuses to achieve comparability between the photo-DSC method and the DLS process. Therefore, a calibration setup was used to convert the light intensity of the light source of the photo-DSC to the light intensity, which is applied in the DLS process. Furthermore, process and environmental parameters such as wavelength, light intensity, temperature, O_2 -concentration, and relative humidity were investigated to study their influences on the UV-curing behavior of a urethane-methacrylate material system.

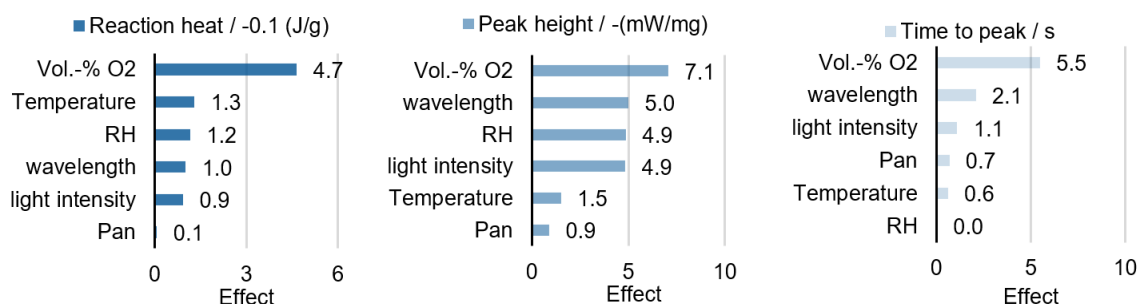


Figure 14.: Main effects from environmental and process related parameter groups on the curing behavior of a urethane-methacrylate [56].

The calibration setup yielded a linear equation between the light intensity of the light source and the light intensity that hits the sample surface. Figure 14 shows the effect of the different parameter groups on the curing behavior of the used material. In this case, the effect was defined as the largest minus the smallest mean within a parameter group. Oxygen inhibition has the largest effect on the three target values ($\Delta H_{R,pc,mc}$, t_p and t_p). For instance, it takes twice as long to reach t_p for the used material in 100% O_2 (10.9 s) as compared to a complete inert gas composition (5.4 s). The conditioning of the used material at 100% RH compared to 24.3% RH had an effect on the reaction heat similar to that of a temperature difference of 20 K, a light intensity difference of 18 mW cm^{-2} , and the change from a 400 nm to 500 nm (bad overlap with photoinitiator) to a 320 nm to 390 nm (good overlap with photoinitiator) wavelength.

Individual Contributions of the Candidate

The experiments were carried out together with Dr. Stefan Schmölder, everything else was done by the candidate.

2.3. Investigation of the Temperature Influence on a Dual Curing Urethane-Methacrylate in Digital Light Synthesis (DLS) in Additive Manufacturing

Summary of the Publication

The third publications focuses on the thermal crosslinking reaction of the urethane-methacrylate in DLS that takes place during the thermal curing step and which builds an IPN in the UV-cured part. The dual curing chemistry is described in the introduction of this publication. A preheating step (1 h at 30 °C, 40 °C, 50 °C and 60 °C) was added at the beginning of the two step DLS process in order to see the immediate effects that temperature has on the viscosity, as well as the effect it has on the mechanical properties of the final part. In addition to this test series a second experiment was performed, in which the resin was put in an oven at 60 °C for different time spans. With Fourier-transform infrared spectroscopy (FT-IR), viscosity measurements, weighing and photo-DSC measurements the used material was analysed before and after the oven time. As described in the first two publications, the evaporation of volatile compounds plays an important role in the photo-DSC measurement. In this study, thermogravimetric analysis (TGA) and gas chromatography mass spectrometry (GC-MS) were carried out in order to further examine the evaporation behavior as well as to determine the chemical identity of the volatile compounds. Furthermore, differential scanning calorimetry (DSC) was performed on the UV-cured parts to identify if the premature thermal curing has a visible impact on the DSC signal.

The evaporating compounds in the urethane-methacrylate are primarily IBOMA followed by TBAEMA. After the preheating experiments increased temperature lead to an increase in viscosity. While the mass loss of the used material for 1 h at 60 °C in the TGA is 3.39 %, it is no proof that the increased viscosity solely derives from the loss of the relatively small molecules IBOMA and TBAEMA. On the contrary, the assumption for the viscosity increase is that the thermal crosslinking reaction results in the formation of larger molecules that increase the viscosity. This assumption was confirmed with the observation that at 60 °C for 1 h with a mass loss of only 0.68 %, the viscosity of the used material more than doubled. After 15 h at 60 °C the liquid urethane-methacrylate solidifies into an elastomer with a negligible mass loss. This ongoing conversion from liquid resin to solid elastomer can be analyzed by the photo-DSC method, which was developed in the first and second publication. The tensile tests showed that with a preheating at 60 °C elongation at break and tensile modulus improved by 47.61 % and 5.54 % respectively, while at the same time tensile strength dropped –5.02 % compared to no preheating. [67]

Individual Contributions of the Candidate

The contribution of the candidate to this publication included conceptualization, investigation of the topic, conducting all experiments, data analysis and writing of the original manuscript. Since several measurements had to be done in a timely manner or sometimes even simultaneously Elisabeth Gleis helped carrying out these measurements.

2.4. Cavity Vat photopolymerization for Additive Manufacturing of Polymer-Composite 3D Objects *in Communications Materials*

Summary of the Publication

The last publication of this cumulative dissertation presents a new vat photopolymerization 3D printing technology, namely cavity vat photopolymerization. The general principle is that one photopolymer resin produces a composite material of an elastomer and thermoset. Cavities are purposefully designed in the solid object, which are then filled with liquid resin during printing due to the negative pressure. As known, from the previous publication, thermal curing solidifies the resin in the cavities into an elastomer. A distinct interface is formed, which is held together by strong covalent bonds. Hybrid specimens indicate improved damping, reduced fragmentation upon fracture and increased local elasticity. Figure 15 shows a few application examples.

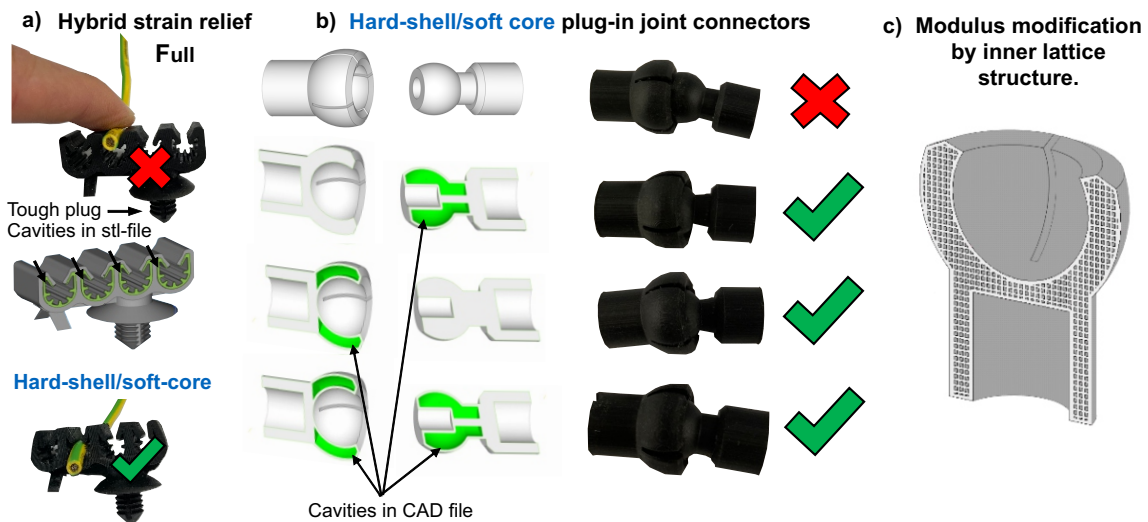


Figure 15.: Application examples of parts that can be produced with cavity vat photopolymerization [66].

Individual Contributions of the Candidate

The contribution of the candidate to this publication included the early investigations into the dual curing mechanism. Philip Obst and Lukas Knorr contributed to the conceptualization of the new process. The candidate carried out the experiments, analyzed the data and wrote the original manuscript.

3. Discussion

In summary, the three main objectives of this work were attained:

1. The first goal of this work was achieved to develop a reproducible and standardized photo-DSC test method for dual curing photopolymers and to identify the most important influencing factors on both the test method and the material.
2. The second objective of investigating the thermal influence on a dual curing urethane-methacrylate resin in order to characterize the ongoing chemical reactions and to understand temperature-dependent challenges in the processing of the material was also attained.
3. The final goal of developing a new multimaterial VPP technology harnessing the dual curing chemical reaction was also realized.

To 1.:

The photo-DSC method can be used to quantify the exothermic character and the heat of reaction of the radical photopolymerization of photopolymers. It was thus possible to distinguish between fast-curing acrylates and slower-curing methacrylates. However, with photo-DSC it is not possible to identify, distinguish or characterize parallel or sequential chemical reaction steps within the multi-step photopolymerization. Also with FT-IR, it is not possible to identify individual reaction steps when several (meth)acrylates are simultaneously involved in the polymerization. According to the ICTAC kinetics committee [134], the identification of the exact reaction steps would be beneficial for the creation of specific kinetic models of polymerization, which would contribute to a better understanding of the ongoing chemical reactions and conversions.

The influence of sample shape and mass on photo-DSC proved to be very important for long residence times, especially when the surface area to volume ratio of the sample is high, more sample mass evaporates from the sample. Evaporation can be reduced by using a lid on the crucible, which is removed just before the start of the measurement. Another suggestion to mitigate this effect in future photo-DSC measurements is to correct the total mass-specific reaction heat (J/g) with the mass loss factor. In addition, the results of this work advocate for a uniform approach, i.e., the use of the same sample pan, mass, shape, and overall test protocol and its documentation.

A major limitation of photo-DSC studies is that the results have limited transferability to the actual DLS process. The main differences between photo-DSC and DLS are twofold: first, the light spectra used in DLS and in photo-DSC are not the same. Even if a calibration method is presented to match the light intensities, it cannot guarantee that the UV light will

have the same wavelength distribution. Since the photoinitiators are very sensitive to certain wavelengths, this could have an impact on the curing behavior and needs to be investigated in more depth. The use of single wavelength filters representing the wavelength of the VPP technology could be a good start to increase comparability.

Second, the material sample for the photo-DSC measurement is relatively small, is exposed to a gas flow, and is placed in a metal crucible that has good heat transfer. Unlike in the DLS process, where the material is cured in a polymerization gradient and is constantly surrounded by uncured, liquid, mobile resin. It can be assumed that the heat transport to the liquid resin in the process looks very different compared to the heat transport to the metal crucible in the measurement method. Under these circumstances, the actual reaction behavior in the DLS may look differently.

To 2.:

The preheating experiments of a dual curing urethane-methacrylate show that increasing the temperature leads to an increase in viscosity. This means that the thermal crosslinking reaction already takes place. Though, the resin remained liquid enough to be processed, the final mechanical properties change significantly with a preheating temperature of 60 °C. Therefore, this work shows that temperature is one of the key parameters in processing dual curing photopolymers. As prior CFD model studies show [35–38], the viscosity of the resin is one of the main limiting factors for VPP technologies. High viscosities reduce the flowability, processability and print speed of the material. Additionally, high viscosities increase the adhesion forces between cured and uncured material, which becomes especially limiting for geometries with large cross-sections. A standard method to reduce the viscosity is to increase the temperature. For dual curing formulations, however, this approach will have the reverse effect, as the higher temperatures would initiate thermal crosslinking and thus also increase the viscosity. It would only work if the onset of the thermal curing is shifted to higher temperatures, which would require a complete new material formulation and maybe also investigations into new deblocking units and molecules apart from isocyanates.

The thermal crosslinking during preheating also results in a different UV curing behavior during photopolymerization, which can be made evident by the photo-DSC test method.

In addition to thermal crosslinking, TGA and GC-MS show that increased temperatures also lead to evaporation of reactive diluents. The influence on viscosity and final mechanical properties is not yet fully understood. Likewise, it is not yet clear whether the evaporation behavior can also be harmful to the operators of the process. Hayes et al. [135] confirmed that in DLS, volatile organic compound (VOC) are highest during post-processing when high temperatures are applied. Therefore, safety measures like proper exhaust and facility air exchange should be in place for further investigations.

A new research question arising from this work can be formulated as follows: Is the heat of polymerization of dual-curing photopolymers during DLS sufficient to cause premature thermal curing. If so, the viscosity of the resin and the adhesion forces would steadily increase during DLS, which would require dynamic adjustment of the process parameters, especially the printing speed, to avoid delamination of the part from the platform. The photo-DSC

method is not the right method to answer this question. Rather, in-depth rheological investigations are required that can detect viscosity changes with temperature changes and UV light.

The thermal crosslinking of the liquid resin went so far as to transform it into an elastomer. The first attempt was made to produce hard-shell, UV cured parts, which are filled with liquid resin and thermally curing in an oven to produce parts with hybrid functionalities [136]. However, manual filling of the cavities with liquid resin proved to be very tedious, as filling was very slow and complete filling without trapped air bubbles could not be guaranteed. These problems led to the invention of cavity vat photopolymerization (CVPP).

To 3.:

CVPP creates hard-shell/soft-core polymers by trapping liquid resin into purposefully designed cavities during the printing process due to negative pressure. Therefore, no additional manual step between UV- and thermal curing is required. As a new multimaterial VPP technology, CVPP offers many advantages over the other multimaterial approaches described in Section 1.3 and Table 1.3. Compared to manually or mechanically switching resins or resin vats, the obvious advantage is that no switching of material is needed, because the two different material properties are derived from one starting material. Since no other material is involved, there is no possible contamination, which would require additional cleaning of the vat. Because the two different material states in CVPP have the same chemical composition, adhesion is better than for multimaterial VPP approaches that attempt to combine two very different materials. In addition, XY-material-heterogeneity can be achieved by CVPP, which is not possible for the first two approaches described in Table 1.3. CVPP also does not delay printing times because no additional manual or mechanical steps are required during the manufacturing process. On the contrary, the build time of the build job from the CVPP publication was 17% shorter than the almost identical build job from the temperature effects publication. Because the cavities produce smaller cross sections, adhesion forces are reduced and faster print speed can be applied. Compared to the two wavelength approach, CVPP does not require hardware modifications and can be used with all top-down and continuous bottom-up VPP processes. One of the disadvantages of CVPP is that it is not possible to overprint existing objects. Another downside of CVPP is that the soft material state contains unreacted photoinitiators and these can diffuse outwards which is noticeable by a strong, characteristic, (meth-)acrylate odor. This disadvantage is shared with all multimaterial VPP approaches, in which the photopolymer is only partially cured. However, so far this issue has been little considered in literature and should be examined more deeply, especially for health reasons. Similarly, the long-term stability of the material properties for only partially cured materials is not yet fully known. The multimaterial VPP approach by Kuang et al. [128] has a high similarity to CVPP. There, the UV curing step is carried out with grayscale DLP, which enables the design of material gradients. Afterwards, the dual curing material is also thermally cured to achieve its final properties. A not insignificant argument could be that CVPP is only an extreme case of this approach, namely when the grayscale is set to 100% (full dark compared to 0% = full intensity), so that cavities in the object are also created, which are

then filled with resin. However, the original research objective of Kuang et al. [128] was to produce functionally graded materials, not to use cavities for to enable hybrid functionalities. The unambiguous difference between these two approaches is that in CVPP the cavities are implemented as part of the part design by the preparation software, whereas if the same cavity is designed with the approach of Kuang et al., it would have to be programmed by grayscale patterns. For the ordinary VPP user, the first variant would be much easier to implement than the second. The advantage of the grayscale DLP approach, however, is that the area of no illumination (cavity) can be exposed with a fraction of the light intensity to chemically bound at least the photoinitiators and a few monomers. This could help to reduce monomer diffusion from the elastic state. Another way to improve CVPP is to formulate of resins that lead to a stable thermally cured elastic state. The invention of CVPP has also launched new research projects that investigate the long-term stability of the material as well as optimal part design for the process. New patents have been filed, which describe the use of CVPP for the production of hybrid lattice structures, self-healing-, electricity conducting- and smart materials.

4. List of Publications

Peer Reviewed Journal Publications

- Photo-DSC method for liquid samples used in vat photopolymerization
J Bachmann, E Gleis, S Schmörlzer, G Fruhmann, O Hinrichsen
Analytica Chimica Acta 1153, 338268 [31]
DOI: <https://doi.org/10.1016/j.aca.2021.338268>
- Photo-differential scanning calorimetry parameter study of photopolymers used in digital light synthesis
J Bachmann, S Schmörlzer, MA Ruderer, G Fruhmann, O Hinrichsen
SPE Polymers 3 (1), 41-53 [56]
DOI: <https://doi.org/10.1002/pls2.10063>
- Investigation of the temperature influence on the dual curing urethane-methacrylate resin Rigid Polyurethane 70 (RPU 70) in digital light synthesis (DLS)
J Bachmann, E Gleis, G Fruhmann, J Riedelbauch, S Schmörlzer, O Hinrichsen
Additive Manufacturing 37, 101677 [67]
DOI: <https://doi.org/10.1016/j.addma.2020.101677>
- Cavity vat photopolymerisation for additive manufacturing of polymer-composite 3D objects
J Bachmann, P Obst, L Knorr, S Schmörlzer, G Fruhmann, G Witt, K Wudy, O Hinrichsen
Communications Materials 2 (1), 1-9 [66]
DOI: <https://doi.org/10.1038/s43246-021-00211-5>

Patents

- DE102020103257A1, 3D-Druck von harten Gehäusen mit elastischem Kern durch zweistufiges Aushärten, Anmeldetag 10.02.2020, B29C 64/124
J Bachmann [137]
- DE102020103255A1, Druckluftbeaufschlagung bei Harz-Bad basierten 3D-Druck Verfahren, Anmeldetag 10.02.2020, B29C 64/124
J Bachmann [136]
- DE102020130690A1, Herstellung von hart/weich-2K-Bauteilen mittels harzbasierter additiver Fertigung, Anmeldetag 20.11.2020
P Obst, J Bachmann, L Knorr [138]

- DE102021131637A1, Selbstheilende Materialien, Anmeldetag 07.07.2021
L Knorr, P Obst, J Bachmann [139]

Patent Applications

- DE102021131634.0 (pending), Hybride Gitterstrukturen und Oberflächenveredelung von Gitterstrukturen, Anmeldetag 07.07.2021
L Knorr, P Obst, J Bachmann
- DE102021131395.3 (pending), Herstellung von leitenden multifunktionalen Werkstoffen durch ein Harzbad- und Hohlraumbasiertes Fertigungsverfahren, Anmeldetag 13.08.2021
J Bachmann, L Knorr, P Obst
- DE102021130981.6 (pending) Multimaterialstrukturen: Belastungsgesteuerte, variable oder irreversible Beeinflussung der mechanischen Eigenschaften von additiv gefertigten Bauteilen durch Multimaterial-Funktionsintegration (Smart Materials), Anmeldetag 14.10.2021
P Obst, L Reusch, F Martin, L Knorr, J Bachmann

A. Original Peer-Reviewed Publications

A.1. Photo-DSC Method for Liquid Samples Used in Vat Photopolymerization

Authors who contribute a journal article in an Elsevier Journal such as Analytical Chimica Acta do not need formal permission to reproduce the material contained in this article. The prerequisite is that the reproduced material is reproduced correctly.

Home ? Help Live Chat Sign in Create Account



Photo-DSC method for liquid samples used in vat photopolymerization

Author: Joel Bachmann, Elisabeth Gleis, Stefan Schmölder, Gabriele Fruhmann, Olaf Hinrichsen

Publication: Analytica Chimica Acta

Publisher: Elsevier

Date: 8 April 2021

© 2021 Elsevier B.V. All rights reserved.

Journal Author Rights

Please note that, as the author of this Elsevier article, you retain the right to include it in a thesis or dissertation, provided it is not published commercially. Permission is not required, but please ensure that you reference the journal as the original source. For more information on this and on your other retained rights, please visit: <https://www.elsevier.com/about/our-business/policies/copyright#Author-rights>

BACK

CLOSE WINDOW

© 2021 Copyright - All Rights Reserved | [Copyright Clearance Center, Inc.](#) | [Privacy statement](#) | [Terms and Conditions](#)
Comments? We would like to hear from you. E-mail us at customer-care@copyright.com



Contents lists available at ScienceDirect

Analytica Chimica Acta

journal homepage: www.elsevier.com/locate/aca

Photo-DSC method for liquid samples used in vat photopolymerization



Joel Bachmann^{a, b, *}, Elisabeth Gleis^c, Stefan Schmöler^d, Gabriele Fruhmann^b,
Olaf Hinrichsen^a

^a Technical University of Munich, Department of Chemistry, Lichtenbergstraße 4, 85748, Garching, Germany

^b BMW Group FIZ, Knorrstraße 147, 80788, Munich, Germany

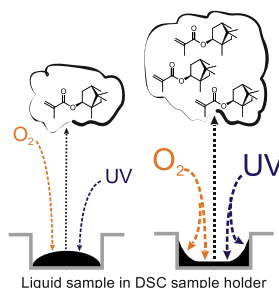
^c Technical University of Munich, Department of Aerospace and Geodesy, Boltzmannstr. 15, 85748, Garching, Germany

^d NETZSCH-Gerätebau GmbH, Wittelsbacherstraße 42, 95100, Selb, Germany

HIGHLIGHTS

- The 1.0 mg spread sample shape has shortest times to peak.
- The 2.8 mg drop sample shape is more robust towards time-dependent surface effects.
- EPX 82 follows a radical not a cationic or hybrid reaction system.
- The reaction heat of EPX 82 is almost twice as much compared to RPU 70.
- Sample preparation for reduced mass loss with the ASC of the DSC is presented.

GRAPHICAL ABSTRACT



ARTICLE INFO

Article history:

Received 8 December 2020

Received in revised form

25 January 2021

Accepted 28 January 2021

Available online 6 February 2021

Keywords:

Vat photopolymerization

Photo DSC

Digital light synthesis (DLS)

Continuous liquid interface production (CLIP)

Sample preparation

Photo-DSC method

ABSTRACT

The photo differential scanning calorimetry (photo-DSC) is an appropriate method to characterize photopolymers used in additive manufacturing (AM). Important process parameters such as optimal ultraviolet (UV) exposure time and reaction heat can be attained by this method. However, achieving reliable and meaningful results from photo-DSC experiments requires careful sample preparation, i.e. the selection of a suitable sample shape, sample mass and sample holder (crucible). The sample shapes drop and spread with 1.0 mg and 2.8 mg sample masses were investigated in this study. Three different times from sample preparation until the start of the measurement (0, 4 and 7 h) were tested, in order to investigate different surface effects such as oxygen-diffusion, prior UV-curing through ambient radiation and evaporation of volatile components. While the 1.0 mg spread sample shape offers the thinnest film thickness (40 μm) and thus the closest comparability to high resolution print jobs, the 2.8 mg drop shape offers a more robust sample preparation with minimized surface effects. To further reduce time-dependent surface effects, this study shows how a preexisting test protocol was shortened from 42 min to 24 min without losing measuring accuracy. Furthermore, to reduce evaporation, different covers were placed on different crucibles, which were tested over time in the device's automated sample changer (ASC) that enables automated and consecutive measurements. The combination of a cold pressed 85 μL crucible covered with a 300 μL Al_2O_3 crucible, which is removed shortly before the actual measurement, provides the best sample preparation for the ASC since mass loss remains below 1% for up to 10 h. Finally, two two-part resin systems, namely a methacrylate-urethane and an acrylate-epoxy based resin that are used in Digital Light Synthesis (DLS) are characterized part by part as well as in

* Corresponding author. Technical University of Munich, Department of Chemistry, Lichtenbergstraße 4, 85748, Garching, Germany.

E-mail addresses: joel.bachmann@tum.de, joel.bachmann@bmw.de (J. Bachmann), elisabeth.gleis@tum.de (E. Gleis), stefan.schmoelzer@netzsch.com (S. Schmöler), gabriele.fruhmann@bmw.de (G. Fruhmann), olaf.hinrichsen@ch.tum.de (O. Hinrichsen).

mixed state. Together with the investigation of different temperatures and atmospheres, it was possible to identify not only the part with the photoinitiator and the type of system (radical or cationic), but also a difference between methacrylates and acrylates with the aid of the photo-DSC method.

© 2021 Elsevier B.V. All rights reserved.

1. Introduction

Photopolymers play an important role in many industries such as adhesives, varnishes on various substrates, paints and composites [1]. New and rapidly expanding industries for photopolymers include food packaging, interior and exterior design, biomedical implants and additive manufacturing (AM) [2]. In the latter, liquid photopolymers are converted, i.e. cured, into a solid state by a point-shaped (stereolithography (SLA) [3]) or an area (digital light processing (DLP)) light exposure from above (top down) or from the bottom (bottom up). Most new technologies for AM such as volumetric polymerization inhibition patterning [4], computed axial lithography (CAL) [5], 4D-printing [6] and printing of fully functional electronic devices [7] are associated with materials printed by photopolymerization approaches [8]. One of these more recent technologies is Digital Light Synthesis (DLS) (formerly known as Continuous Liquid Interface Production (CLIP)), which was presented in 2015 by Carbon, Inc. (Redwood, CA) [9]. DLS works very similar to the bottom-up digital light processing (DLP) technology. A graphical representation of the DLS printing process can be seen in Fig. 1. DLS differs from DLP in that not only light, but also oxygen can pass through the window at the bottom of the resin cassette. A so-called “O₂-dead zone” is created in which polymerization is inhibited by high oxygen concentration. Consequently, the bottom layer does not polymerize and does not adhere to the window, which allows a continuous resin flow into the “O₂-dead zone” as well as a continuous, instead of a layer-by-layer, production. This invention enables much faster production times compared to conventional DLP, since the separation and realignment steps become obsolete [10].

Ligon et al. [11] describe four types of photopolymerization systems in detail that are generally used in AM: radical systems, cationic systems, hybrid formulations and two photon initiators. The latter is not of interest to this study. The general scheme of UV-initiated radical photopolymerization with oxygen interference can

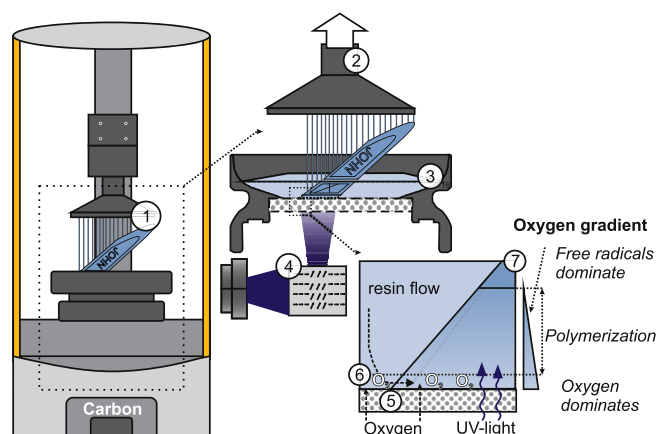


Fig. 1. Schematic illustration of DLS for the production of a personalized product. ① Part with support structures ② Continuous elevation of the build platform ③ Cassette filled with liquid resin ④ DLP system ⑤ Oxygen and light permeable window ⑥ “O₂-dead zone” ⑦ UV-crosslinked part.

be seen in Fig. 2. The absorption of light of a photoinitiator (PI) with an appropriate wavelength creates a photo-excited photoinitiator I^{*}, which is quenched with oxygen or cleaved to form a radical R^{*}. The radical then either reacts to a peroxide with oxygen or initiates and propagates polymerization with (meth)acrylates. A detailed description of the reaction steps during the radical photopolymerization of a methacrylate system can be seen in Fig. A. 1. The cationic system on the other hand requires a photoacid generator (PAG) that reacts with epoxy monomers in a cationic chain growth mechanism. Hybrid formulations contain both radical and cationic monomers and initiators; together they form a so-called interpenetrating network (IPN). Decker et al. [12] observed radical and cationic-type PIs and PAGs by in-situ real-time infrared spectroscopy. They showed that acrylate monomers polymerize faster and more extensively than the epoxy monomers, which makes them suitable for spatial and temporal control. Furthermore, they can be easily modified to obtain desired mechanical properties. Due to the living character of the cationic polymerization, the epoxy monomers polymerize even if the light source is switched off (“dark cure”). In air, the radical polymerization of acrylates is strongly inhibited by oxygen (see Fig. 2), while the cationic polymerization of the epoxy monomers is amplified by the humidity in the atmosphere.

The photo-DSC method is suitable to characterize photopolymers used in DLS due to its comparability to the actual process. Two crucibles are exposed simultaneously with UV light. One crucible contains the sample and the other empty crucible serves as a reference. When the light reaches the resin, photopolymerization starts in the sample. Due to the exothermicity, heat is released in the sample. The heat flow is detected by the sensors underneath the reference and the sample and the difference in heat flow is displayed as a signal over time. Fig. 3 shows the general set up of a photo-DSC.

Several photo-DSC studies have been conducted to study radical, cationic and hybrid resin systems [14–22]. Liquid resin samples are used in these studies, but only the sample weight and sometimes the film thickness are mentioned. Usually, small sample

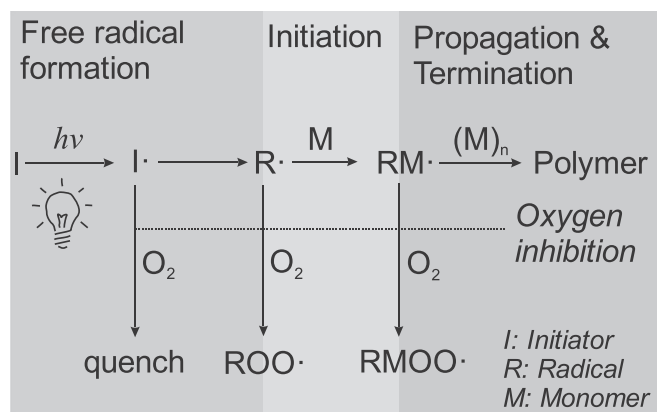


Fig. 2. General scheme of UV-initiated ($h\nu$) radical photopolymerization with oxygen interference [13].

masses are used to ensure isothermal conditions. However, one neglected aspect of photo-DSC measurements is the sample shape. A large contact area from the sample to the crucible is usually desirable since this provides improved heat transfer. However, a uniform sample thickness for liquid samples can only be achieved in the middle of the crucibles, while the resin pulls upwards on the walls on the sides of the crucible, see Fig. 4. The latter phenomenon can be avoided when the drop shape is used. This offers an interesting alternative in sample shape preparation, because the reduced surface reduces effects such as oxygen-inhibition, prior UV-curing or evaporation. The downside, however, is that there is no uniform film thickness.

Another neglected aspect of photo-DSC measurements is the use of the automatic sample changer (ASC) that can automatically place and remove the samples, which for example enables overnight measurements. The ASC is often used for DSC measurements with solid samples, but the effect of long times between sample preparation and start of the measurement (dwell times) has not yet been investigated for liquid photopolymers. This investigation might be of particular significance for the two-part resins used in DLS, which crosslink not only by UV- but also through thermal activation [23,24]. Dwell time experiments with the ASC could reveal the impact of a thermally established network on the photopolymerization, which would be beneficial to develop optimal processing conditions for resins that are exposed to long dwell times. While earlier photo-DSC studies focus on kinetic investigations [15–19,22], interactions between the UV initiators and the absorber [14,20] and the influences of temperature, UV intensity [21] and oxygen inhibition [18], the scope of this study is to investigate the influences of sample shape and sample mass on the photo-DSC measurement. Furthermore, different dwell times as well as different crucibles are studied in order to examine the above-mentioned possible surface effects and to discuss appropriate sample preparations for liquid photo-DSC samples for long, intermediate and short dwell times. Finally, the temperature and oxygen sensitivity of a two-part urethane-methacrylate and a two part epoxy-acrylate resin used in DLS are investigated.

2. Experimental

2.1. Materials

The two-part resin systems rigid polyurethane 70 (RPU 70) and epoxy 82 (EPX 82) used in this study are manufactured by Carbon, Inc. (Redwood, CA). Both materials are delivered as two-part-systems and need to be mixed in the designated ratio before the printing process. In addition to the UV curing step, two-part resin systems like RPU 70 and EPX 82 also need to be thermally post-cured in order to achieve their final properties. In their final state, both materials indicate promising mechanical and thermal



Fig. 4. Spread, drop and invalid liquid sample shape applied in open DSC crucible.

properties (see Table A 1), which is why they are used for engineering purposes, e.g. in the automotive industry. Their chemical composition as well as their mixing ratio can be seen in Table 1. According to the safety data sheets (SDS), both resins have the same photoinitiator TPO, as well as several (meth)acrylates in their composition. Therefore, both materials indicate a radical system. However, EPX 82 contains two hybrid molecules (see Table 1), which have acrylate as well as epoxy groups. Because the exact resin composition is proprietary and the information on the SDS is not exhaustive, the possibility remains that EPX 82 contains a photoacid generator (PAG). If so, it would represent a hybrid formulation with a radical and cationic initiated polymerization. However, it is also possible that the epoxy groups of the hybrid molecules solely serve the purpose of thermal curing with the amine groups of DMA, DADPS and DAP (see Table 1). Both resins indicate a black color in the mixed state and might contain additional stabilizers, dye or passive absorbers, which are not mentioned in the SDS. For some investigations, only part A of RPU 70 was used, which contains the photoinitiator as well as all reactive molecules that take part in photopolymerization. For the experiments in which the mixed resin system was used, the mixing ratio (part A: part B) was achieved by utilizing the Cordless Multi-Component Cartridge Gun (10:1) and (1:1) suggested by Carbon from Albion® Dispensing Solutions (Moorestown, NJ) with the corresponding mixing tips and speeds according to Table 1. The first 10 s of the mixed resin were disposed in order to achieve high mixing quality.

2.2. Photo-DSC method

The photo-DSC signal with four UV-exposures followed by isothermal segments without exposure can be seen in Fig. 5 (a). Obst et al. [27] used four exposure units to ensure complete UV crosslinking for RPU 70. Thus, the fourth peak can be subtracted from the first peak, which creates the subtracted signal in Fig. 5 (b) with the target values peak area (A_p), peak height (h_p) and time to peak (t_p). In general, A_p equals the reaction heat caused by the photopolymerization. However, the DSC signal also depends on the type of crucible and the DSC device for which the heat flow calibration has been performed. Table 2 shows open crucibles with their names, abbreviations and dimensions, which will also be referred to as pans in this study. In order to achieve a reaction heat that is independent of the type of crucible, the peak area is multiplied by a correction factor from Table A 2. The latter can be calculated as the ratio of the literature value for the melting of indium to the peak area of the third heating of indium in the desired crucible (see Fig. A. 2). For this research, A_p corrected by the pan correction factor equals the pan corrected reaction heat $\Delta H_{R,pc}$.

Obst et al. [27] used the photo-DSC settings from Table 3 (second column) to study the reaction heat of RPU 70 for different exposure times. For this study, the same test protocol from Obst et al. [27] with four exposures is used as a starting point. One interesting side issue is whether this test protocol can be shortened to two exposure times, see Table 3 (third column) without the loss of measurement accuracy for all target values.

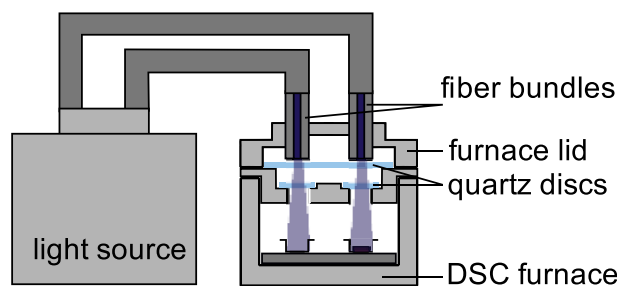
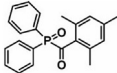
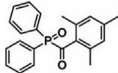
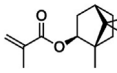
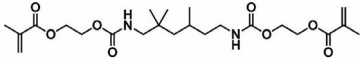
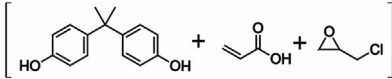
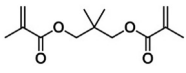
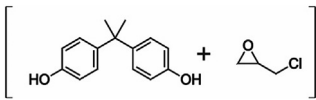
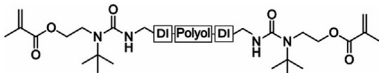
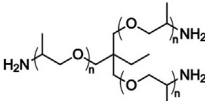
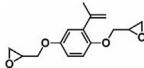
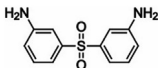
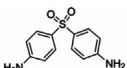


Fig. 3. Sectional drawing of the UV-exposure of the reference crucible and the sample in a photo-DSC setup.

Table 1

Composition of two part resin systems RPU 70 and EPX 82 according to the safety data sheets (SDS) from 2017 [25,26]. The molecule structure is followed by the short name of the molecule, the CAS number and the percentage in the corresponding part.

RPU 70 (black) Cartridge Gun (10:1) Orange tip, Speed 1	Part A Photoinitiator		EPX 82 (black) Cartridge Gun (1:1) White tip, Speed 2
 TPO 75980-60-8 0.1–2%	 TPO 75980-60-8 1–4%		
 IBOMA 7534-94-3 10–50%	Reactive monomers and oligomers		
 UDMA 72869-86-4 1–20%	 DMA 2680-03-7 5–15%	 ED 20 acrylate 55818-57-0 10–30%	
 NPGDMA 1985-51-9 <0.3%	 Araldite 527 25068-38-6 45–80%		
 MABPU n.a. 10–70%			
 Chain extender 39423-51-3 20–100%	Part B		 DS-002683 25085-99-8 5–15%
	 DMA 2680-03-7 30–50%	Urethane Acrylate n.a. n.a. 25–40%	
	 DADPS 599-61-1 5–15%	 DAP 80-08-0 5–15%	

2.3. Sample preparation

In Fig. 6, a schematic description of the sample preparation process for the photo-DSC is given. The total time from mixing to the start of the measurement varies between 10 and 20 min. For the first experiments glass pasteur pipettes were used to transfer the resin to the crucible. Later, a paper clip was used for this step because of an improved ease of use. With the tip of a paper clip, very small amounts of resin can be transferred to and from the crucible, which allows a very precise weighing of the sample. After

each application, the paper clip is rinsed with isopropanol. After the sample shape was set in the crucible, the sample mass was determined by a Cubis® Ultra Micro Balance from Sartorius (Göttingen, Germany). Three different sample masses, 1.0 ± 0.1 mg, 2.8 ± 0.1 mg and 5.0 ± 0.1 mg, were used in this study. For 1.0 mg and 2.8 mg, it was possible to test both shapes, see Fig. 7. The sample shape spread was achieved by spreading the drop in the pan with a plastic cable tie (282×4.8 mm). Afterwards, the sample was placed in the automated sample changer (ASC) of a NETZSCH DSC 204 F1 (device 1, Munich, Germany). The film thickness was measured by a caliper

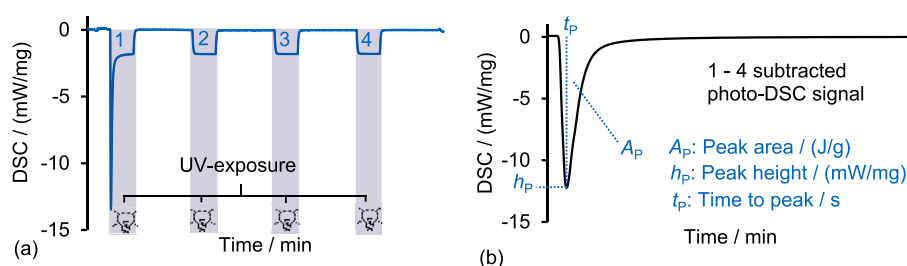


Fig. 5. Photo-DSC signal with four UV-exposures, followed by isothermal segments without exposure (a). Subtracted photo-DSC signal with target values (b).

Table 2

NETZSCH crucible names, abbreviations and dimensions.

CAD-sectional drawing of crucible	Name of open crucible	Abbreviation	Inner bottom diameter / mm	Inner height to lid / mm	Nominal Volume / μL
	Concavus Al	conc	4.40	2.25	40
	Pan Al	std	5.07	1.38	40
	Al 85 μL	85 μL	6.26	2.58	85
	Al SFI	sfi	4.40	2.28	80
	Al ₂ O ₃ 300 μL	300 μL	7.00	7.70	300

Table 3

Existing (old) and new photo-DSC test protocols with parameter settings. Segments with UV-exposure in parentheses means that it only refers to the isothermal segment of the test protocol (old).

Name	Existing test protocol from Obst et al. [27]	New test protocol
Short name	old	new
Exposure times	4	2
Peak subtraction	P1–P4	P1–P2
Irradiation time/min	2	3
Segment 1 (SEG. 1):	25 °C/00:10/25 °C	25 °C/00:10/25 °C
SEG. 2:	25 °C/2.0(K/min)/30 °C	25 °C/2.0(K/min)/30 °C
SEG. 3:	30 °C/00:01/30 °C	30 °C/00:01/30 °C
SEG. 4: UV-exposure	30 °C/00:07/30 °C	30 °C/00:05/30 °C
SEG. 5: UV-exposure	30 °C/00:07/30 °C	30 °C/00:05/30 °C
SEG. 6: (UV-exposure)	30 °C/00:07/30 °C	30 °C/00:05/30 °C
SEG. 7: (UV-exposure)	30 °C/00:07/30 °C	30 °C/10.0(K/min)/25 °C
SEG. 8:	30 °C/10.0(K/min)/25 °C	
Time between irradiation/min	5	2
Total time/min	42	24

from Sylvac SA (Yverdon, Switzerland). For the drop shape, only the maximum height was determined, since the sample shape does not have a uniform film thickness.

2.4. Experimental procedure

An overview of all photo-DSC measurements conducted in this study can be seen in Table 4. The OmniCure® S2000 from Excelitas (Waltham, MA) with a 200 Watt UV lamp with a light intensity of 0.5 W/cm² and no bandpass filter and a transparent quartz glass

were used for the photo-DSC set up. The light emitting spectrum of the OmniCure® S2000 as well as the absorption spectrum of the photoinitiator TPO and the radiometer RM22 with the UVA + sensor from Opsytec Dr. Gröbel GmbH (Ettlingen, Germany) can be seen in Fig. A. 3 (a). Fig. A. 3 (b) shows how a screwdriver was used to determine the distance the light must travel from the end of the light guide to the surface of the surface of the sample. In this case, the distance is 2.7 cm. The lowest light intensity setting for the OmniCure® S2000 is 0.5 W/cm². With a distance of 2.7 cm to the RM22 UVA + sensor, an intensity of 11.60 mW/cm² (see Fig. A. 3 (c))

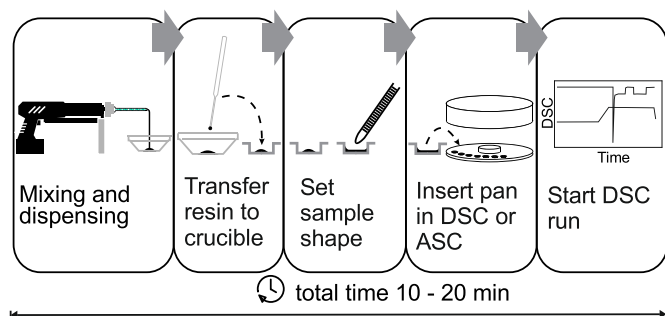


Fig. 6. Schematic depiction of the sample preparation process for photo-DSC measurements.

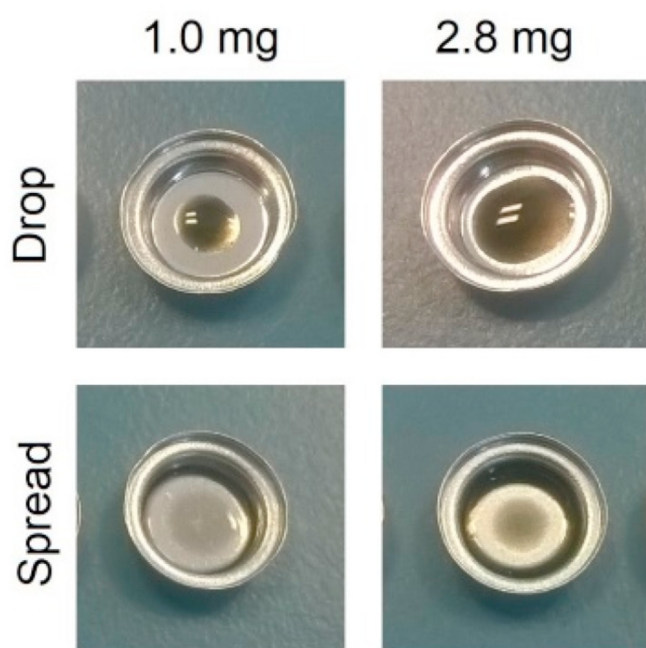


Fig. 7. Different sample preparations with two different shapes and masses.

results on the sample surface, which is comparable to the operating settings of the carbon printers (9 mW/cm^2). The same radiometer RM22 with the UVA + sensor was used to measure the ambient

radiation in the lab. A purge gas flow of 20 ml/min nitrogen was set for all experiments with the exception of the study of different atmospheres, for which oxygen and air atmosphere was used (see Table 4). The applied photo-DSC test protocol, material, sample mass, sample shape, dwell time, temperature, atmosphere and sample size (N) for each experiment can be read from Table 4. For the experiment with the 5.0 mg sample mass, only the spread form could be investigated, since the drop shape cannot be realized with this mass. For another experiment, the ASC was covered with aluminum foil to prevent UV-curing by ambient radiation see Fig. A. 4. The experimental plans were randomized, with an exception of the dwell time, which was blocked to avoid complexity.

In order to investigate if the evaporation can be reduced by different kind of coverings, the experiment set up from Table 5 was conducted. In Table 5, the short names are built up with the used material, followed by the crucible and the utilized cover. All short names represent a test series of N measurements performed sequentially with the ASC. The first column was examined separately with the DSC device 1. For columns 2–4, DSC device 2 was used and all samples were first prepared with the given material and crucibles. Afterwards, these were placed in the ASC. The sequence was set so that the second measurement of a test series takes place only after the completion of the first measurement of the other test series. With the latest version of the DSC 204 F1 Phoenix® (device 2, NETZSCH, Selb), the ASC is able to move in two dimensions so that a sample and its crucible can be covered and this cover can be removed automatically before the measurement. For these experiments, the $300 \mu\text{L}$ Al_2O_3 -crucible was used as a cover because it is large enough to be placed over both the std and $85 \mu\text{L}$ crucibles, see Table 2. The pan calibration for DSC-device 2 can be seen in Fig. A. 2. Furthermore, the weight loss in these experiments was determined for each sample after the measurement.

3. Results

3.1. Comparison of two different photo-DSC exposure profiles with RPU 70 - part A and EPX 82 (1:1)

The comparison of the existing (old) and new test protocols can be seen in Fig. 8. The target values for both test protocols: the pan-corrected reaction heat ($\Delta H_{R,pc}$), peak height (h_p) and time to peak (t_p) were determined with the subtracted signal. The Tukey test for equal means and the Leven test for equal variances show that the means and variances of test protocol old and new for $\Delta H_{R,pc}$, h_p and t_p , are not significantly different at the significance level of 0.05 (see Fig. 9). This means that reducing the exposure segments from

Table 4

Parameters for photo-DSC experiments conducted in this study.

Nr.	Experiments	Photo-DSC test protocol	Material	Sample mass / mg	Sample shape	Dwell time / h	Temperature / °C	vol. % O_2	N
1	Test protocol comparison	old, new	RPU 70 - part A	1.0	drop	0	30	0	9
		old, new	EPX 82 (1:1)	2.8	spread	0	30	0	3
2	Resin characterization	new	RPU 70 (1:1), part A, part B	2.8	spread	0	30	0	1
		new	EPX 82 (1:1), part A, part B	2.8	spread	0	30	0	1
3	Temperature variation	new	RPU 70 (10:1)	2.8	spread	0	30, 40, 50, 60	0	1
		new	EPX 82 (1:1)	2.8	spread	0	30, 40, 50, 60	0	1
4	Atmosphere variation	new	RPU 70 (10:1)	2.8	spread	0	30	0, 80, 100	1
		new	EPX 82 (1:1)	2.8	spread	0	30	0, 80, 100	1
5	Shape – Mass – Dwell time	new	RPU 70 - part A	1.0, 2.8	drop, spread	0, 4, 7	30	0	3
		new	RPU 70 - part A	5.0	spread	0, 4, 7	30	0	3
6	UV-protected ASC	new	RPU 70 - part A	1.0, 2.8	spread	0, 4, 7	30	0	3
7	ASC with different pans	See Table 5							

Table 5

Sample mass before the photo-DSC measurement with different crucibles and covers. In order to obtain the same drop shape as part A, a higher sample mass was needed for the RPU 70 measurements. The use of a paper clip for sample preparation was very efficient compared to the use of a glass pipette. The standard deviation for sample mass was reduced by a factor of 10 and the preparation time was also reduced.

Short name	part A, std, no-lid	part A, std, PET-lid	part A, 85 μ L, Al ₂ O ₃ -lid	part A, sfi, Al ₂ O ₃ -lid	rpu70, sfi, Al ₂ O ₃ -lid
Material	RPU 70 part A	RPU 70 part A	RPU 70 part A	RPU 70 part A	RPU 70 (10:1)
DSC device	1	2	2	2	2
Crucible	std	std	85 μ L	sfi	sfi
Shape	spread	spread	spread	drop	drop
Cover	No lid	PET-lid	Al ₂ O ₃ -lid	Al ₂ O ₃ -lid	Al ₂ O ₃ -lid
Preparation with	Glass pipette	Paper clip	Paper clip	Paper clip	Paper clip
N	12	9	10	10	11
Sample mass mean / mg	2.87	2.78	2.81	2.78	3.95
Sample mass std. dev. / mg	0.14	0.02	0.01	0.02	0.02

4 \times 2 min to 2 \times 3 min has no significant effect on the photo-DSC measurement of RPU 70 – part A. The total time of the photo-DSC test protocol can thus be shortened from 42 min (old) to 24 min (new) while maintaining the same measurement accuracy. Thus, a reduction of the total photo-DSC measuring time can be achieved while maintaining the same curing behavior.

Given the very similar results, means and standard deviations are calculated for all 18 experiments (see Table 6). The latter can be used to qualify a further shortening or modification of the photo-DSC test protocol for RPU 70 – part A measurements. For example, the isothermal holding time at the beginning and/or the time between measurements of the test protocol could be further shortened. These changes are statistically legitimate if the values $\Delta H_{R,pc}$, h_p and t_p do not differ significantly from the means and standard deviations given in rows A + B of Table 6.

In order to verify whether the shortening of the test protocol can also be applied to another resin system, Fig. 10 shows the results for the same experiment with EPX 82. The differences in the EPX 82 measurement were that the two part resin system was mixed in a 1:1 ratio prior to testing, and a higher sample mass of 2.84 mg \pm 0.08 mg was used. Additionally, the sample shape spread was used in the std crucible. Since $\Delta H_{R,pc}$, h_p and t_p do not show a strong deviation after three measurements, the sample size was reduced to N = 3. The Tukey test for equal means and the Leven test for equal variances show that the means and variances of test protocol old and new for $\Delta H_{R,pc}$, h_p and t_p are not significantly different for all three comparisons at the significance level of 0.05. The one exception is the variances for the t_p comparison, because the three measurements for test protocol old all had the exact same value and thus had a variance of zero. However, the means of test protocol old and new for t_p are even closer compared to the t_p of RPU 70. Thus, the shortening of the test protocol without the loss of accuracy can be verified for a much more reactive resin system such

as EPX 82.

The overall higher values for $\Delta H_{R,pc}$ and h_p and lower values for t_p compared to RPU 70 – part A are due to the resin composition (compare Figs. 9 and 10). Even though both resins have the same photoinitiator (PI), EPX 82 consists of highly reactive acrylates, while the composition of RPU 70 – part A indicates only methacrylates, which are less reactive due to the steric hindrance at the reactive C=C double bond.

3.2. Investigation of RPU 70 and EPX 82 via photo-DSC

The subtracted photo-DSC curves of the two resin systems are compared in Fig. 11, which is a good example of how photo-DSC measurements can be used to generally characterize photopolymers used in AM. It shows that only part A of RPU 70 and EPX 82 reacts upon exposure, which means that part A can be identified as the part containing the PI. Part B shows no signs of reaction for both resin systems. Very interestingly, the exposure of the mixed EPX 82 resin leads to a much stronger exothermic reaction compared to only part A of EPX 82, while the photo-DSC signal for the mixed RPU 70 decreases compared to part A of RPU 70. This leads to the assumption that the UV-reactive methacrylates are only present in part A of RPU 70, whereas the faster-reacting acrylates are present in both parts of EPX 82. This supposition can be confirmed by Table 1, which shows that there are no methacrylates in part B of RPU 70, but that acrylates can be found in part B of EPX 82.

Another important investigation for processing photopolymers in AM is the study of the influence of temperature and oxygen on the UV-reaction. The photo-DSC provides a good method to investigate these issues. Fig. 12 (a) and Table 7 show the results of the investigation of the temperature on the curing process. The peak height (h_p) of RPU 70 is only one third compared to that of h_p of EPX 82. Additionally, t_p is only 3.2 s for the acrylate containing

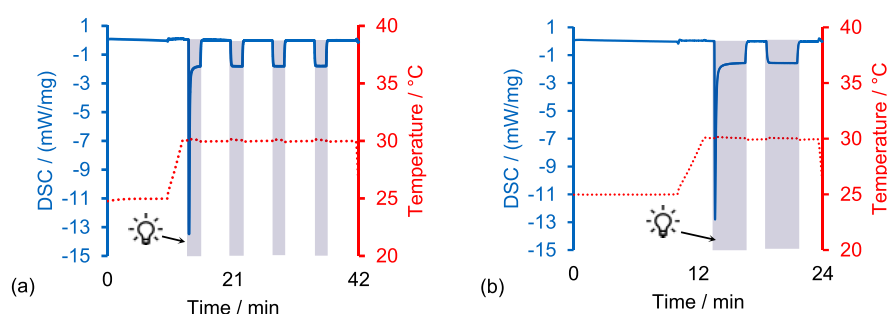


Fig. 8. Change from existing test protocol (old) from Obst et al. [27] (a) to new test protocol (new) by reducing the exposure profile from 4 \times 2 min to 2 \times 3 min (b).

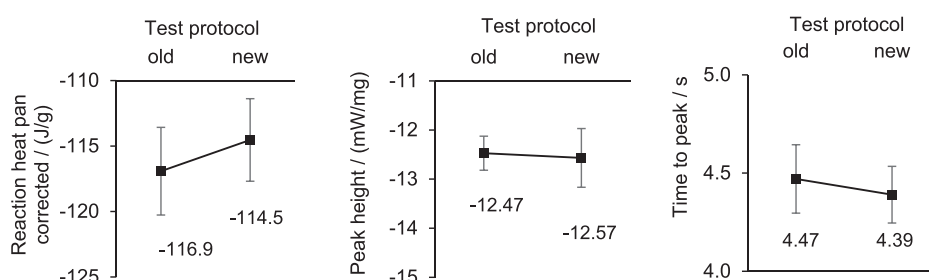


Fig. 9. Mean and standard deviation comparisons of an RPU 70 – part A, 1.0 mg, drop sample with the existing (old) and new isothermal (30 °C) test protocols. The sample size for each test protocol is N = 9.

Table 6

Mean and standard deviations for test protocol old and new. Because their means do not significantly differ, the **total mean** and **standard deviations** of both test protocols are given in rows old + new as a reference point for further changes on the photo-DSC test protocol for RPU 70 – part A.

RPU 70 – part A	Test protocol	N total	Mean	Standard Deviation
Reaction heat pan corrected / (J/g)	old	9	-116.9	3.35
	new	9	-114.5	3.15
	old + new	18	-115.7	3.29
Peak height / (mW/mg)	old	9	-12.47	0.35
	new	9	-12.57	0.60
	old + new	18	-12.52	0.46
Time to peak / s	old	9	4.47	0.17
	new	9	4.39	0.14
	old + new	18	4.43	0.16

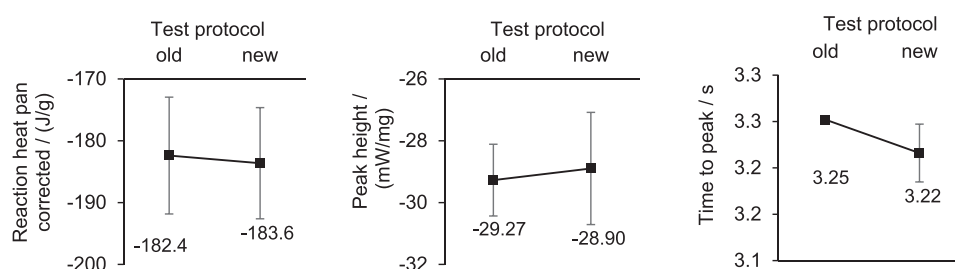


Fig. 10. Mean and standard deviation comparisons of an EPX 82, 2.8 mg, spread sample with the existing (old) and new isothermal (30 °C) test protocols. The sample size is N = 3. The standard deviation for the t_p of test protocol old is not missing but all three measurements had the same value.

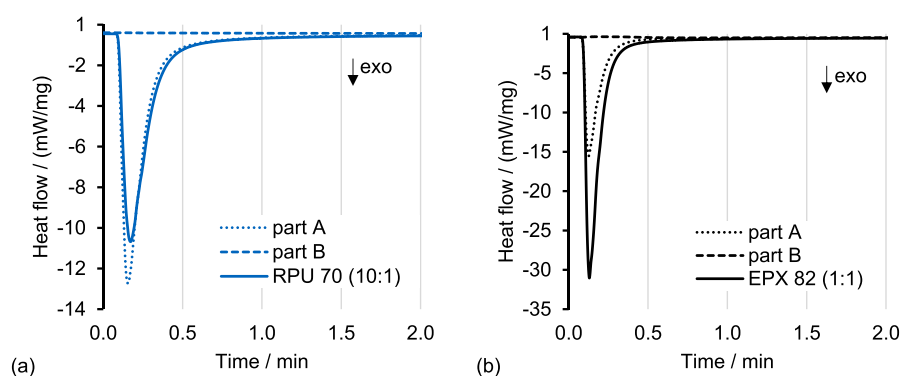


Fig. 11. Comparison of the photo-DSC measurements of the two parts of RPU 70 (a) and EPX 82 (b) as well as the mixed resins with their corresponding mixing ratios (part A: part B) RPU 70 (10:1) and EPX 82 (1:1).

EPX 82 compared to 5.4 s for the methacrylate containing RPU 70 and the peak area of EPX 82 is almost two times as big as the peak area of RPU 70. These observations match with the widespread

knowledge that acrylates react faster and more exothermic than methacrylates [28,29]. Because of the fast curing behavior of EPX 82, also followed by a fast termination of the reaction that can be

identified by the steep decline after the peak, it is very unlikely that EPX 82 contains a PAG. Furthermore, the influence of temperature on the photopolymerization of RPU 70 is much greater than on EPX 82. Higher temperatures increase the mobility in the resin, and this effect might be more significant for the sterically hindered methacrylates compared to the already highly reactive acrylates. On the other hand, both resins show a decrease in reaction heat with rising oxygen concentrations (see Fig. 12 (b)). This is mainly due to the effect of oxygen inhibition (see Fig. 2), which is known to have a decreasing effect on the photopolymerization rate and delays the reaction [30,31]. The strong influence of oxygen on the UV curing reaction in EPX 82 suggests that solely a free radical mechanism is involved in the photocuring reaction and that there is no cationic curing of epoxides, since the latter would not show oxygen inhibition [32]. In DLS, in which both resins are processed, oxygen inhibition is used to create a so-called oxygen "dead zone" in which no polymerization occurs and a steady resin flow is possible. Above this area, a continuous polymerization gradient develops in which the free radicals dominate, see introduction Fig. 1.

3.3. Investigation of the influences of sample shape, sample mass and dwell time on the photo-DSC measurement of RPU 70 - part A

The results in Fig. 13 show the effects of the different sample shapes, i.e. drop and spread, the different sample masses, i.e. 1.0 mg and 2.8 mg and different dwell times 0 h, 4 h and 7 h on the values $\Delta H_{R,pc}$, h_p and t_p . The main observation for $\Delta H_{R,pc}$ (see Fig. 13 (a)) is that with longer dwell times, $\Delta H_{R,pc}$ decreases. Additionally, the decrease of $\Delta H_{R,pc}$ with longer dwell times is much stronger for the 1.0 mg sample compared to the 2.8 mg samples and the strongest decrease can be seen for the 1.0 mg spread. The following three effects can occur and reduce $\Delta H_{R,pc}$ with longer dwell times:

1. Prior UV-curing in the open sample holder due to ambient UV-radiation (0.021 mW/cm^2).
2. Evaporation of volatile, reactive diluents that accelerate UV-initiated photopolymerization.
3. O_2 -diffusion from the ambient air into the sample that inhibits photopolymerization.

If the last effect, the O_2 -diffusion into the sample, takes place, t_p would be increased with longer dwell times because oxygen inhibition delays the reaction (see Fig. 12 (b)) [30,31]. However, Fig. 13 (c) shows that the trend for t_p is rather decreasing with longer dwell times. Therefore, only the first two effects remain. All effects are dependent on the surface-to-volume ratio (S/V) depicted in Fig. 14, since a larger surface area leads to an enhanced O_2 -diffusion, UV-

Table 7

Comparison of target values between RPU 70 and EPX 82 for four different temperatures from Fig. 12 (a).

T/°C	Peak area / (J/g)		Peak height / (mW/mg)		Time to peak / s	
	RPU 70	EPX 82	RPU 70	EPX 82	RPU 70	EPX 82
30	-124.6	-209.1	10.21	30.63	5.4	3.2
40	-135.8	-203.1	11.84	29.43	5.2	3.2
50	-148.6	-204.5	13.96	29.58	5	2.6
60	-157.3	-217.9	14.47	30.94	5.2	2.8

exposure and evaporation.

The drop shape resembles the form of a hemisphere and since the spherical shape is known to have the lowest surface of all geometric shapes, the S/V for the drop is lower than for the spread form. As the mass of the drop shape increases, the surface increases by the power of two, but volume by the power of three. Hence, the 2.8 mg drop with the higher mass, has a smaller S/V than the 1.0 mg drop. The 1.0 mg spread sample has the largest S/V, which means the largest area for evaporation and/or premature UV-curing. Therefore, the 1.0 mg spread sample shows the strongest reduction of $\Delta H_{R,pc}$ with increasing dwell times. The spread shape creates a much larger exposure area for the UV-light and a larger contact area to the crucible and temperature sensor. Furthermore, the 1.0 mg spread sample has the shortest t_p for all dwell times (see Fig. 13 (c)). The sample film is thinner ($40 \mu\text{m}$) compared to the same sample mass in drop shape ($<230 \mu\text{m}$). With increasing film thickness, the UV radiation is delayed and attenuated because the overlying resin absorbs the photons. For thicker samples, this means that the illuminated regions at the top, closer to the irradiation source, are already curing, while the remaining photons are still migrating to the bottom regions. Thus, the decomposition of the photoinitiator as well as the entire reaction slows down. The increase of t_p with sample thickness in photo-DSC measurements is also reported by Ruiz et al. [30]. Additionally, the 1.0 mg spread sample shows the highest values for h_p at 0 h. As already mentioned, the layer thickness of the resin in the crucible for these samples is very small and consequently almost the entire resin is irradiated simultaneously. This leads to a high mass-specific exothermal heat flow and high absolute values for the peak height shortly after the start of the UV exposure. In the case of thick samples, the delaying and attenuated effect also contributes to a lower mass-specific heat flow. During DLS, the penetration depth of UV-light, which solidifies the resin, is also referred to as cured thickness. The latter becomes proportionally larger with increasing light intensity, longer exposure time and greater absorption height of the resin. The absorption height describes how deep the UV light

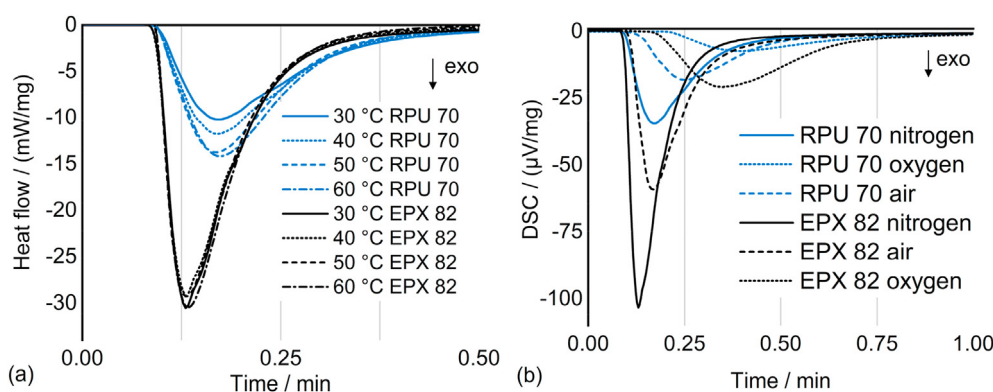


Fig. 12. Influence of temperature (a) and oxygen concentrations (b) on UV-reaction of RPU 70 and EPX 82.

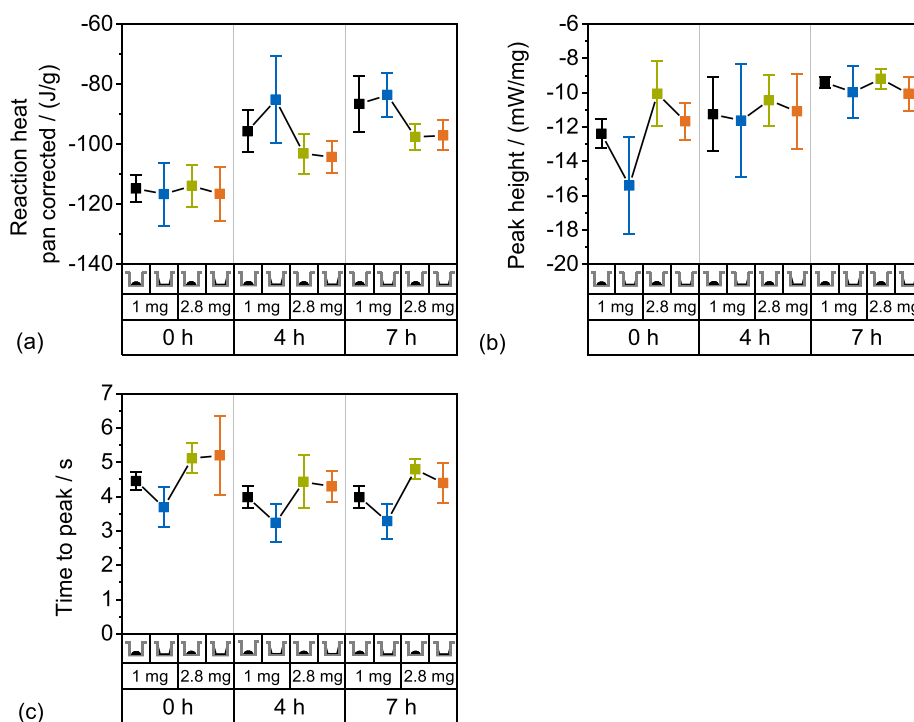


Fig. 13. Influence of sample shape (drop or spread), sample mass (1 or 2.8 mg) and time to measurement also known as dwell time (0, 4 or 7 h) on reaction heat pan corrected ($\Delta H_{R,pc}$), peak height (h_p) and time to peak (t_p) with the sample size $N = 3$.

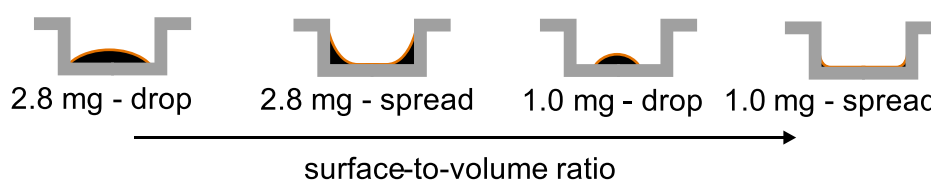


Fig. 14. Schematic depiction of the cross sections of a DSC crucible and the investigated sample mass and shape regarding their surface-to-volume ratio (S/V). The surface, where interactions with atmospheric oxygen, UV-light or the evaporation of volatile components is expected is colored in orange for better visualization. (For interpretation of the references to color in this figure legend, the reader is referred to the Web version of this article.)

can penetrate into the resin. This size is characteristic of the resin as it depends on how much light is absorbed by the photoinitiator and by passive absorbers such as dye or soot. Tumbleston et al. [9] showed how the absorption height for a resin was reduced by a gradual increase in dye loading from 700 μm to 360 μm and finally to 140 μm . However, the same cured thickness could still be achieved for each resin by adjusting the UV exposure parameters. The DLS user can also determine the vertical resolution, i.e. slicing, that determines how many layers the CAD model should be divided into. Normally, the slicing is 100 μm . Parts with fine or very fine vertical resolution are build up with a slicing of 50 μm and 25 μm respectively. Januszewicz [10] even presented 0.4 μm slicing. In order to achieve different slicing with the same resin (absorption height), the exposure parameters must be adjusted. In terms of sample preparation for the photo-DSC, this means that the 1.0 mg sample preparation, which has the thinnest film thickness, seems to be particularly comparable to print jobs with high vertical resolutions, i.e. low slicing thickness (0.04–50 μm). However, as described above, this sample preparation has the highest S/V and is therefore the most susceptible to the decrease of $\Delta H_{R,pc}$ with longer dwell times. The more robust sample preparation is the 2.8 mg drop, since it has the lowest S/V , which means that with longer dwell times, $\Delta H_{R,pc}$ decreases not as much as for samples with higher S/V . In order to investigate whether an even lower S/V

makes the measurement even more robust, an additional experiment was conducted with a 5.0 mg spread sample preparation, which can be seen in Fig. A. 5. However, the increased sample mass did not reduce the decreasing effect of longer dwell times on $\Delta H_{R,pc}$. On the contrary, the 5.0 mg samples show slightly smaller values for $\Delta H_{R,pc}$ compared to the 2.8 mg samples for all dwell times. One possible explanation might be that the film thickness is increased so much that the UV-light cannot fully penetrate the sample. This means that although the S/V is larger for 5.0 mg compared to 2.8 mg, better measurement results are achieved with the 2.8 mg sample weight. Furthermore, it is not possible to create the drop shape with the 5.0 mg sample, since this is too much liquid material for the crucible and the drop itself would spread to the walls of the crucible. This raises a general problem for both shapes: the extent to which the resin moves up on the walls is unknown for the spread shape, while the film thickness for the drop shape is not consistent across the entire contact area of the crucible. A closer look at the surface structure of the crucibles (see Fig. A. 6) reveals that it determines the direction of self-spreading of the drop. In terms of the sample preparation, the drop shape is less prone to error, since the additional preparation step of distributing the drop evenly over the crucible surface is omitted. To find out whether the decrease of $\Delta H_{R,pc}$ with prolonged dwell times comes from a prior curing due to ambient UV-radiation, an additional experiment was conducted in

which aluminum foil was used to shield the autosampler from ambient UV-radiation (see Fig. A. 4). The spread sample shape was used due to the higher S/V compared to the drop shape. The results with the UV-shielded [UV] autosampler were compared with the non-shielded [-] autosampler and can be seen in Fig. 15.

Fig. 15 (a) shows that the shielding of the autosampler from ambient UV-radiation does not show a significant influence on the target values reaction heat pan corrected ($\Delta H_{R,pc}$), peak height (h_p) and time to peak (t_p). Sample shape spread was used for this comparison because of the higher S/V . Furthermore, $\Delta H_{R,pc}$ for the UV-shielded autosampler with longer dwell times is reduced almost as much as for the non-shielded samples. This means that the main effect of dwell time does not result from the UV-curing of the sample by ambient UV-light, but from the evaporation of reactive molecules, which is examined in the next section. However, in general it is advisable to reduce UV-exposure during sample preparation in order to avoid a possible source of error. This is particularly advisable for measurements of resin systems containing photoinitiators that are activated by visible light.

3.4. Investigation of the influence of mass loss for different crucibles and dwell times on the photo-DSC measurement of RPU 70

As described above, the effect of O_2 -diffusion into the sample as well as ambient UV-radiation does not have a great effect on the decrease of $\Delta H_{R,pc}$ over time. It seems that mass loss due to the evaporation of reactive molecules plays a much greater role. In order to investigate if evaporation can be reduced by different kinds of coverings, the experiments from Table 2 were conducted. As long as the sample is in the ASC covered by the Al_2O_3 -crucible, it is protected from UV-radiation and air flow, even for longer dwell times. Due to the reduced air flow around the sample, a significant reduction in evaporation is expected. Since not all ASCs are able to remove a cover from the prepared sample, it was also investigated whether a transparent PET-lid over a std crucible can likewise reduce evaporation. While the airflow is likely to be reduced by the

PET-lid, the transparent cover allows the sample to be cured by the UV light during the photo-DSC measurement. Comparing an 85 μL - and a sfi crucible allows a comparison of sample shapes. One characteristic of the sfi pan is that it preserves the drop shape of the sample even for long dwell times. The sfi crucible is an 85 μL pan, which is cold-pressed by a crucible pressing tool. In the 85 μL crucible, on the other hand, the sample was spread across the surface. Since the sample mass in the pan was determined before and after each measurement, the mass loss could be calculated and the pan and mass corrected reaction heat $\Delta H_{R,pc,mc}$ was calculated by multiplying the peak area with the ratio of sample mass before the measurement to the sample mass after the measurement. The sample shape for all crucibles except the sfi pan was spread and the experiments were carried out with the sample masses from Table 5. The results from the photo-DSC measurement over a dwell time of almost 15 h can be seen in Fig. 16.

Fig. 16 (a) shows that if an ASC without any covering is used, the mass loss of the part A sample in a std pan can reach 7.42% in 4.6 h. When a PET-lid is used, it considerably reduces the mass loss to 4.32% in 12.2 h. However, the highest reduction in mass loss, i.e. evaporation, can be observed for the samples that used Al_2O_3 -crucibles as a cover. For RPU 70 in the sfi pan, the maximum mass loss is 1.31% after more than 13 h. Using gas chromatography mass spectrometry (GC-MS), a preceding study with RPU 70 showed that mainly the reactive diluents IBOMA from Table 1 and 2-(tert-Butylamino)ethyl methacrylate (TBAEMA) evaporate from the resin [23]. One possible explanation for why the part A, std, PET-lid measurements have the highest fluctuations and generally have higher mass loss values compared to the Al_2O_3 -covers might be that the PET-lids were handmade and did not show perfect fitting accuracy. On the other hand, the Al_2O_3 -crucibles were all manufactured industrially and there was only a minimal gap through which free convection could reach the sample. Because the sfi pan maintained the drop shape throughout the 13 h, the mass loss was lower compared to that in the 85 μL pan. The mixed RPU 70 resin has an even lower mass loss than part A in the Al_2O_3 -covered sfi

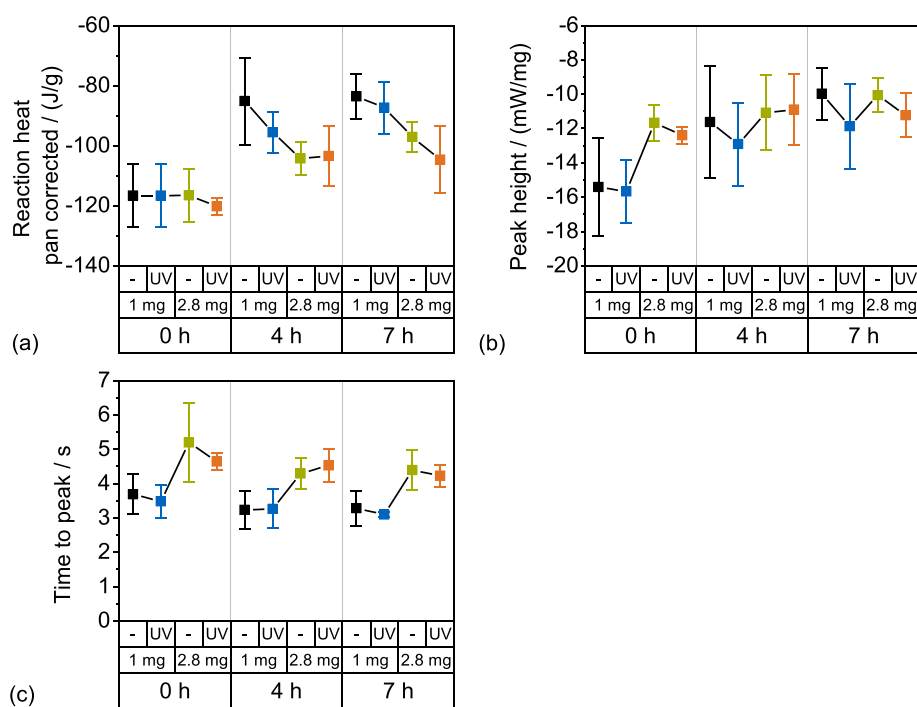


Fig. 15. [UV] and [-] indicate that the autosampler was shielded [UV] or non-shielded [-] from UV radiation during dwell time (see Fig. A. 4).

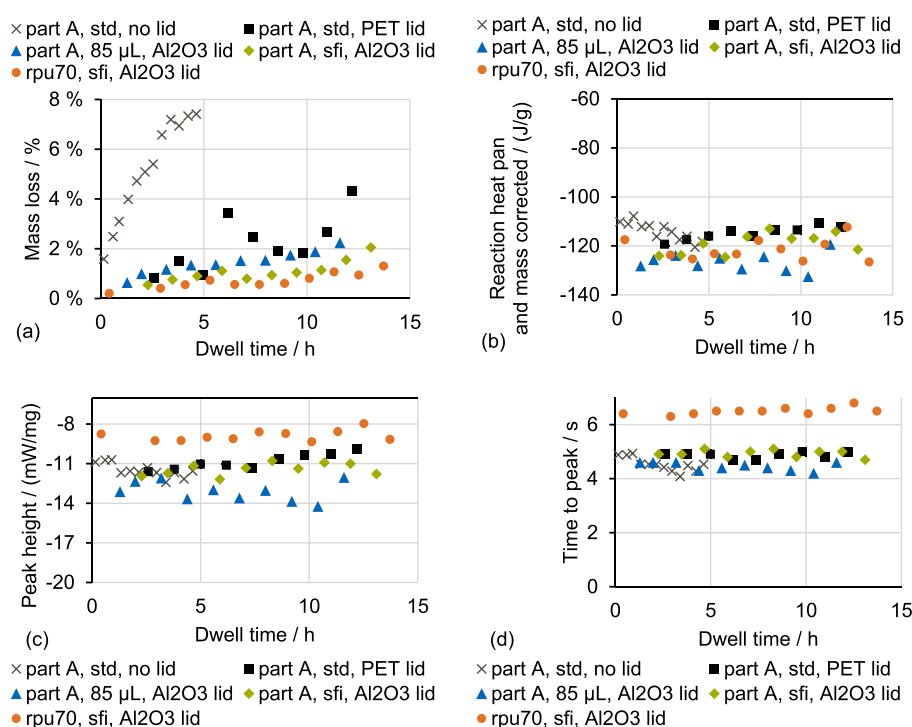


Fig. 16. Results of dwell time experiment with RPU 70 and part A in std, 85 µL and sfi crucibles.

pan. An explanation might be that the amines of part B create hydrogen bridge bonds to the carbonyl group of the volatile methacrylates, which would make them less mobile and volatile.

The most important observation from Fig. 16 (b) is that the pan- and mass-corrected reaction heat does not decrease as much over time as in the previous experiments (see Figs. 13 (a) and Fig. 15 (a)). This might either derive from the reduced mass loss or from the mass correction. Since, *part A, std, no lid* also shows that $\Delta H_{R,pc,mc}$ does not decrease for almost 5 h, even though no cover has been used, the stabilizing effect on the reaction heat can be attributed to the mass correction of the reaction heat. The explanation is that regardless of the initial sample mass, the total reaction heat, which is specified in J/g, should always have the same value. However, because of the mass loss over long dwell times, the initial sample mass is higher than the sample mass at the time of UV-exposure. The DSC uses the initial, higher mass to create the signal, which means that the given area below the exothermic UV-polymerization peak, i.e. the reaction heat, becomes much smaller for longer dwell times (compare Figs. 13 (a) and Fig. 15 (a)). For some covered samples, $\Delta H_{R,pc,mc}$ still decreases marginally for longer dwell times. A possible explanation for why the total reaction heat might decrease, even with mass correction, is that evaporation changes the resin composition, since the small reactive molecules evaporate predominately, while the larger less reactive oligomers remain in the resin. For *part A, std, no lid*, $\Delta H_{R,pc,mc}$ increases slightly over time. Of course, it is very unlikely that the reactivity in the resin will increase over time. Thus, the source of error might derive from the mass correction factor, which depends on the weight of the sample before and after the measurement. Peak height and time to peak remain constant for almost all test series (see Fig. 16 (c) and Fig. 16 (d)). Since the effect of the dwell time was minimized, Fig. A. 7 shows the statistic of the collected data from Fig. 16. Fig. A. 7 (a) shows that a higher sample mass of 3.95 mg was used for RPU 70 to ensure the drop shape in the sfi pan

because the density of part B is much lower compared to part A. This increase in sample mass and film thickness leads to longer t_p and reduced h_p for *rpu70, sfi, Al₂O₃-lid* compared to the other test series (compare Fig. 13 and Fig. A. 5). Additionally, part B in the mixed RPU 70 does not contain reactive components and does not take part in the UV reaction, which also results in a lower h_p and longer t_p (compare Fig. 11 (a)). In Fig. A. 7 (b), the 85 µL pan shows the overall highest $\Delta H_{R,pc,mc}$. The explanation is the overall thinner film thickness of the sample in an 85 µL pan compared to a sfi pan because the sample shape is spread instead of drop. An explanation of why $\Delta H_{R,pc,mc}$ is higher for the sfi and the 85 µL pan compared to the std pan might be the higher walls of the 85 µL pan, which enable more wall reflections and thus generate an increased light intensity on the sample. One reason for comparing RPU 70 and part A in the same crucible and covering was to find out if a reaction between part A and part B takes place, which would result in larger molecules and a reduction in reaction heat, peak height and longer times to peak [23]. However, no conversion is detectable for longer dwell times at room temperature via photo-DSC.

4. Discussion

This study demonstrates how a test protocol was shortened from 42 min to 24 min without losing measuring accuracy for part A of RPU 70 (see Fig. 9). The shorter test protocol was also applicable for the more reactive two-part resin system EPX 82 (see Fig. 10). Further potentials to shorten the test protocol are to reduce the isothermal holding time at the beginning and/or the time between measurements. Given the very similar results, means and standard deviations are calculated for all 18 experiments (see Table 6). The latter can be used to qualify a further shortening or modification of the photo-DSC test protocol for RPU 70 – part A measurements. For example, the isothermal holding time at the beginning and/or the time between measurements of the test

protocol could be further shortened. These changes are statistically acceptable if the values $\Delta H_{R,PC}$, t_P and t_P do not differ significantly from the means and standard deviations given in rows A + B of Table 6.

It was possible to determine that for RPU 70 and EPX 82, part A contains the photoinitiator. In addition, part B of RPU 70 does not and part B of EPX 82 does contain molecules, which participate in the photopolymerization reaction (see Fig. 11). These results show that the photo-DSC is useful for identifying the photo-reactive components in two-part resin systems in addition to the SDS. Additionally, it is reasonable to conclude that EPX 82 during DLS follows only a radical and not a cationic photopolymerization. Even though, EPX 82 contains hybrid molecules with acrylates as well as epoxy groups, the small t_P , the highly exothermic reaction, the fast and steep decline after the peak maximum and the oxygen inhibition indicate that EPX 82 follows solely a radical mechanism during DLS. The epoxy groups react with the amine groups in the thermal post process. Furthermore, two important influences on the DLS printing process, temperature and oxygen concentration, were investigated: a temperature increase during the measurement significantly increases the reactivity of the urethane-methacrylate containing RPU 70 and decreases t_P for the epoxy-acrylate containing EPX 82 (see Fig. 12 (a) and Table 7). The increase in O_2 -concentration reduces the reactivity for both resins equally (see Fig. 12 (b)), which is a requirement for them to be processed via DLS, using the so-called “ O_2 -dead zone” (see Fig. 1) to ensure continuous polymerization. In summary, not only the part with the photoinitiator and the type of system (radical or cationic), but also a difference between methacrylates and acrylates can be identified with the aid of photo-DSC measurements. However, achieving reliable and meaningful results from photo-DSC experiments requires careful sample preparation, i.e. the selection of a suitable sample shape, sample mass and crucible. If only the total reaction heat is of interest, it is not important which sample shape and sample mass is used as long as the measurement is carried out within the first hour (see Fig. 13 (a)). If process-close parameters like the optimal UV-exposure time for print jobs with high resolution, i.e. low penetration depth, are searched, then the 1.0 mg spread sample shape provides the thinnest film thickness (40 μm) and offers adequate comparability (see Fig. 13 (b,c)). However, it is important to note that the 1.0 mg spread sample shape also has the highest S/V, which is why it is the most susceptible to surface effects like evaporation and UV-curing from ambient UV-light (see Fig. 14). The higher the proportion of volatile components in the resin composition, the better to choose a more robust sample preparation like the 2.8 mg drop sample shape. The latter has a low S/V, while the film thickness at the same time is not too thick (230 μm). It is also one of the easiest ways to prepare the sample, because the additional step of spreading the sample uniformly is omitted. Initially, a glass pipette was used to extract the resin sample and place it in the crucible, however by using a paper clip, the weighing accuracy was improved by a factor of 10 (see Table 5). The major impact of prolonged dwell times is not the O_2 -diffusion into the sample or a pre-reaction caused by ambient UV-light, but the evaporation of volatile components. Most commercially available resin systems for 3D-printing use reactive monomers to adjust viscosity. The mass loss should therefore be tracked and the total reaction heat needs to be corrected by the ratio of initial to final

sample mass (see Fig. 13 (b)). Because of the mass loss, the consecutive and automated measurement of several samples with the ASC is not recommended. One result from studying the use of the ASC was that the lowest mass loss is achieved with the sfi crucibles that are covered by 300 μL Al_2O_3 -crucibles that are removed shortly before the measurement (see Fig. 16 (a)).

5. Conclusion

This study introduces a new photo-DSC test protocol that is 18 min shorter compared to the predecessor test protocol. It can be used to characterize liquid two-part photopolymers like RPU 70 and EPX 82, which are commonly used in DLS. Even though, EPX 82 includes epoxy in its name, it follows not a hybrid but a radical reaction system during UV-curing. Furthermore, the difference between slower methacrylates and faster acrylates can be identified with the photo-DSC. The 1.0 mg spread sample shape is the optimal sample preparation for process close investigations like wavelength, light-intensity, exposure time and atmosphere. The 2.8 mg drop sample shape on the other hand is optimal if the effects of long dwell times is of interest. For example to track the effect of a thermal conversion, between the two resin parts, on the UV-reaction. If the ASC is used and the resin system contains volatile components, the lowest mass loss can be achieved by using sfi-crucibles that are covered by 300 μL Al_2O_3 -crucibles that are removed shortly before the measurement.

CRedit authorship contribution statement

Joel Bachmann: Conceptualization, Formal analysis, Investigation, Writing - original draft, Writing - review & editing, Visualization, Project administration. **Elisabeth Gleis:** Conceptualization, Formal analysis, Investigation, Visualization, Project administration. **Stefan Schmörlzer:** Methodology, Investigation, Resources. **Gabriele Fruhmann:** Supervision. **Olaf Hinrichsen:** Writing - review & editing.

Declaration of competing interest

The authors declare that they have no known competing financial interests or personal relationships that could have appeared to influence the work reported in this paper.

Acknowledgements

The authors acknowledge the provided proofreading services sponsored by the TUM Graduate School, which was carried out by KERN Corporation. Additionally, the authors are thankful for Johannes Roth and Birgit Hoenisch at the thermal analysis lab at BMW for their help in installing the photo-DSC device. Finally, we would like to thank Opsytec Dr. Gröbel GmbH and Qioptiq Photonics GmbH & Co. KG for providing the spectrum of the radiometer and the light source, respectively.

Appendix

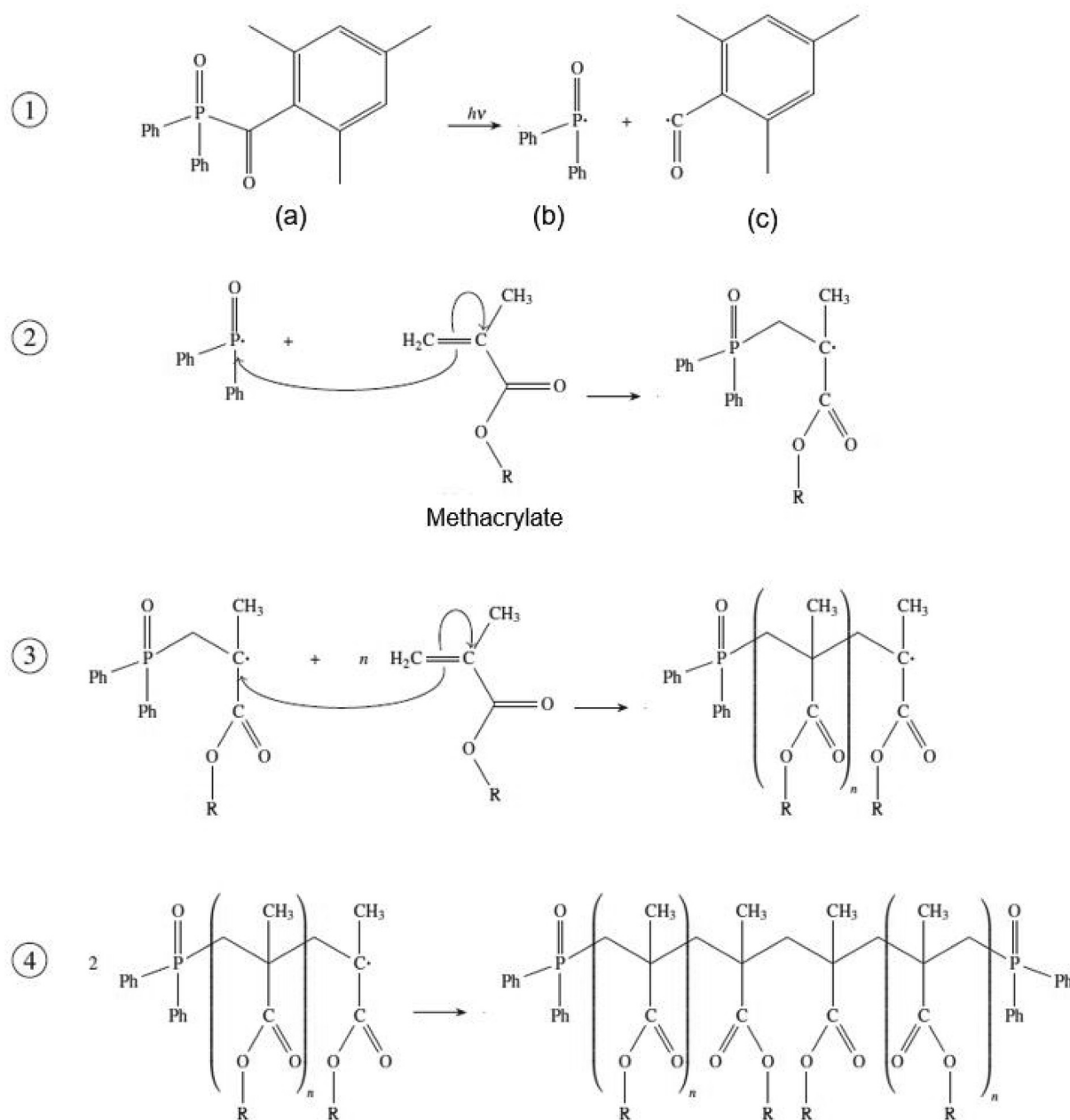


Fig. A.1. Reaction pathway of radical photopolymerization with TPO as photoinitiator and methacrylates as reactive monomers. With free radical formation ①, initiation ②, propagation ③ and termination by recombination ④. Ph stands for a phenyl ring.

The photoinitiator depicted in ① is Diphenyl(2,4,6-trimethylbenzoyl)phosphine oxide (a), which is homolytically cleaved by UV-radiation and thus produces two free radicals – Diphenyl-phosphonyl (b) and 2,4,6-Trimethylbenzoyl (c). Phosphoryl radicals are one to two times as reactive as benzoyl radicals [33,34]. Both the initiation ② and the propagation step ③ follow

the same mechanism. Termination can either happen by recombination with another radical, as shown in ④, or by disproportionation. In disproportionation, a radical is neutralized by a hydrogen atom of another radical. The latter experiences an electron surplus and forms a double bond.

Table A.1

The mechanical and thermal properties of the two-part carbon materials RPU 70 and EPX 82 according to the technical data sheets (TDS) after DLS thermal post processing [35,36].

Property	RPU 70	EPX 82
General	High-strength, functional toughness and high ductility	High-strength, excellent long-term durability, functional toughness
Comparable to	ABS	20% glass filled PBT
Ultimate Tensile Strength / MPa	40	80
Tensile Modulus / MPa	1700	2800
Elongation at Break / %	100	5
Impact Strength / (J/m)	15	45
Heat Deflection Temperature / °C	60	130

Table A.2

Correction factors to calculate the pan corrected reaction heat $\Delta H_{R,pc}$ for various crucibles and devices.

Device	Pan (open)	Onset temperature / °C	Peak area of third heating / (J/g)	Pan correction factor: Literature value/peak area third heating
1	std	156.1	30.80	0.929
2	std	156.6	31.85	0.898
2	85 μ L	156.6	31.28	0.914
2	sfi	156.6	31.71	0.902
Literature		156.6	28.6	

DSC / (mW/mg)

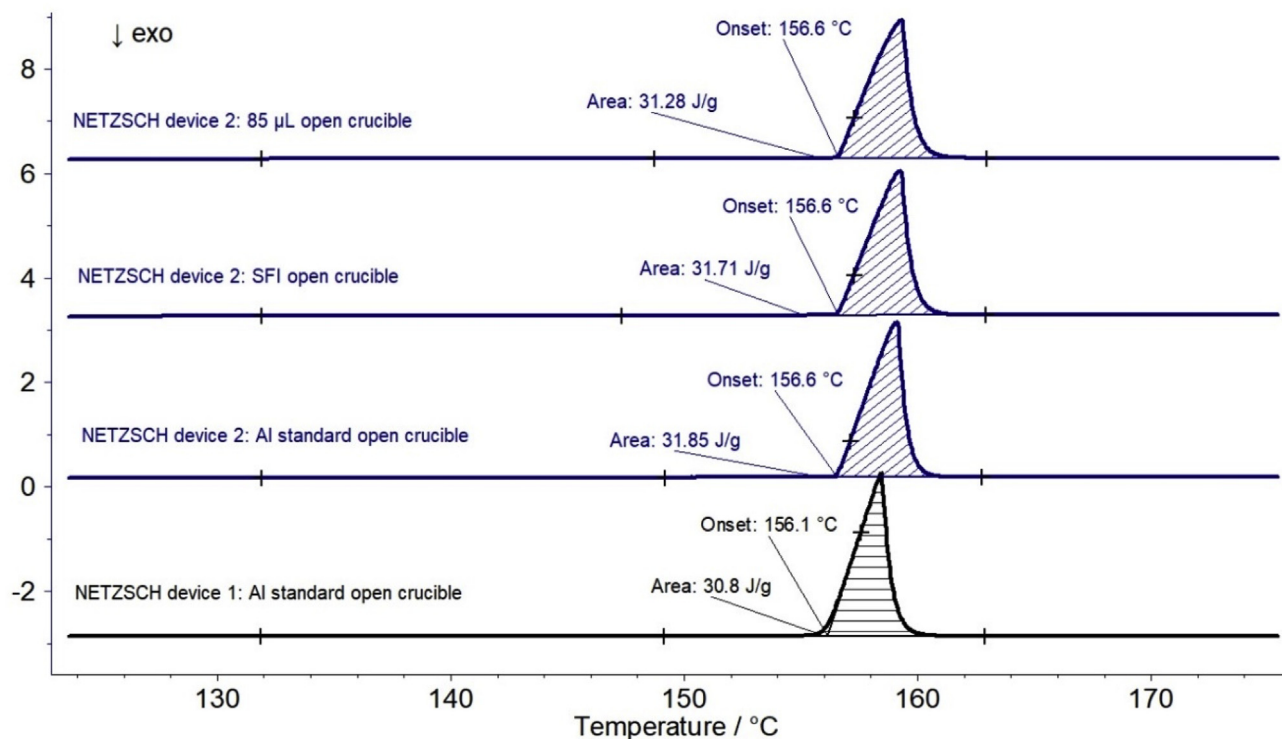


Fig. A.2. Third heating of Indium for various open crucibles and DSC devices with onset temperature and peak area.

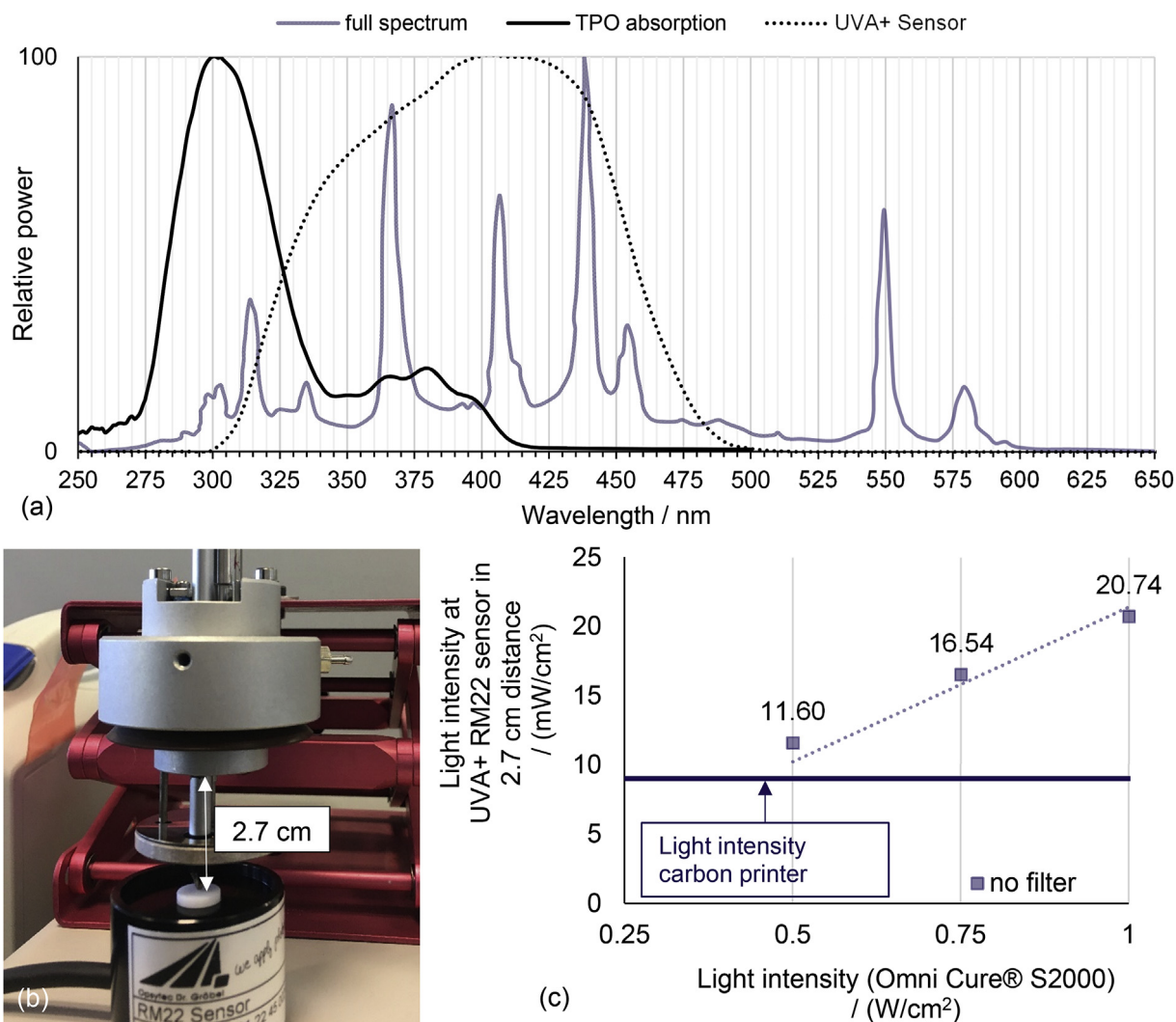


Fig. A.3. (a) Emitting light spectrum of the Omni Cure® S2000 light source without wavelength filter depicted with the absorption spectrum of the photoinitiator TPO and the absorption spectrum of the RM22 UVA + sensor. (b) A lifting platform that holds the photo-DSC head at a fixed distance to the radiometer. (c) Calibration curve to identify the light intensity on the sample surface.

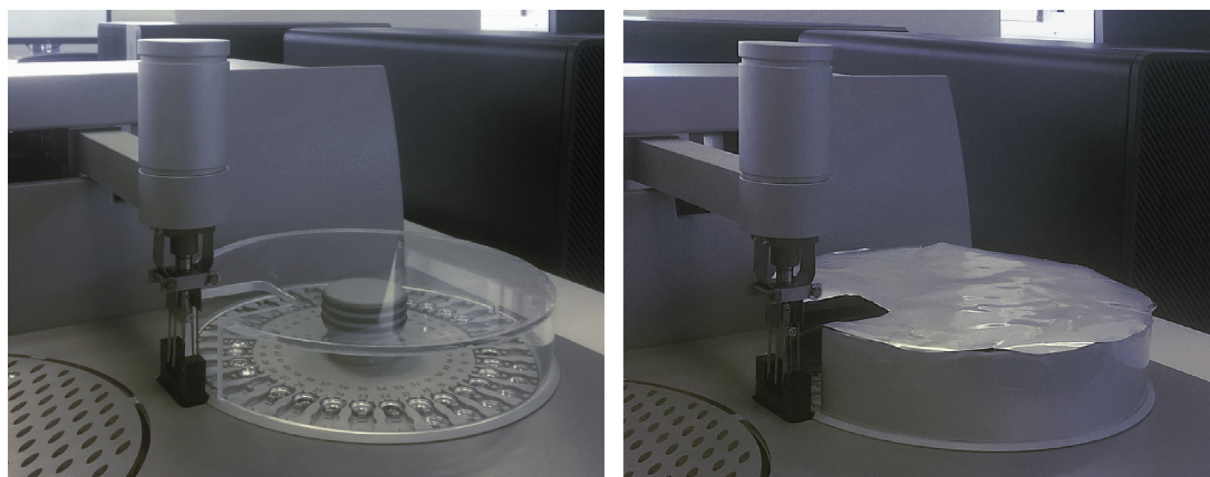


Fig. A.4. Automated sample changer (ASC) of the DSC (left) and modified version to shield the samples via aluminum foil from ambient UV-radiation (right).

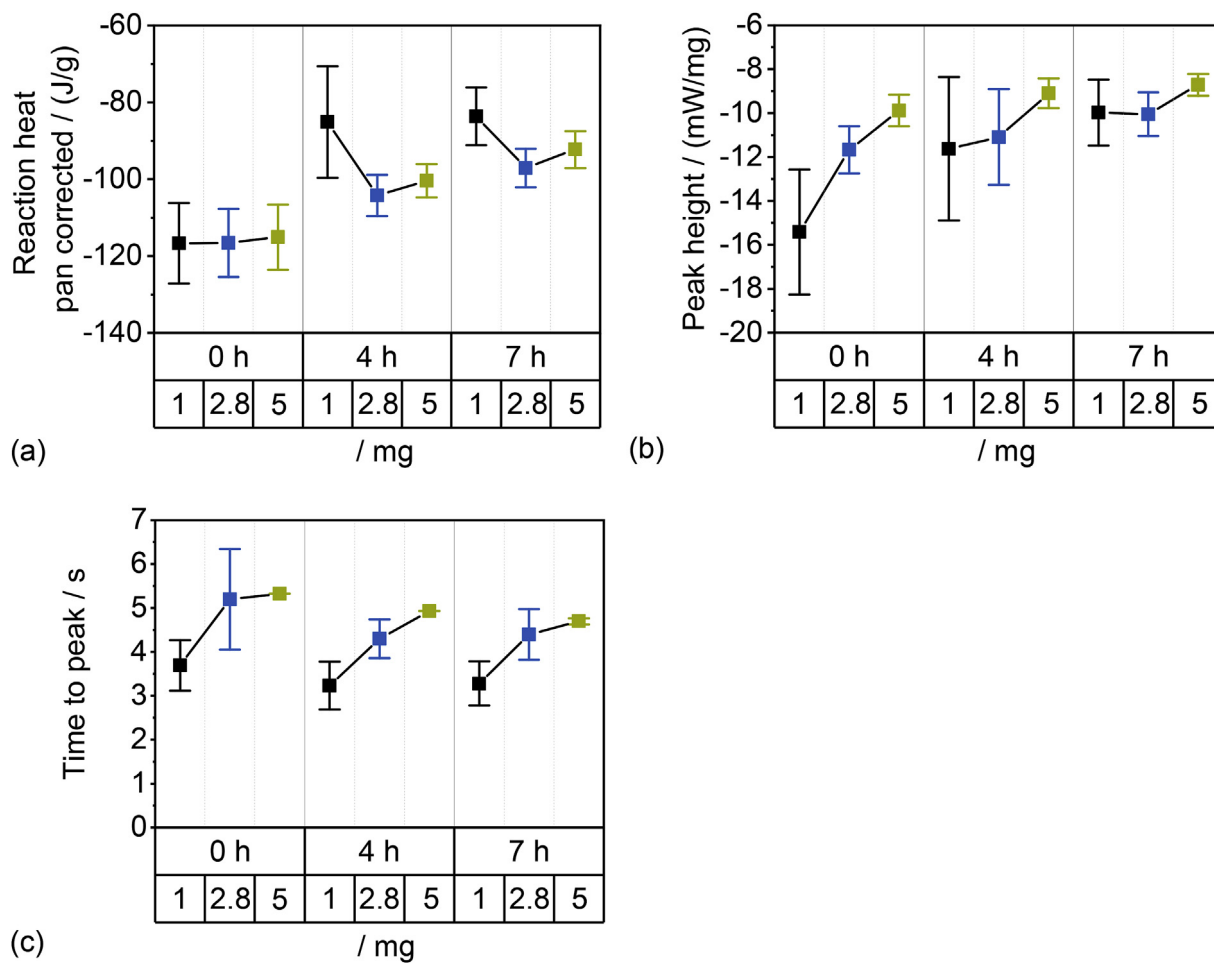


Fig. A.5. Influence of sample weight (1, 2.8 and 5 mg) and time to measurement (0, 4 or 7 h) on reaction heat pan corrected (a), peak height (b) and time to peak (c) with the sample size N = 3 and sample shape spread.

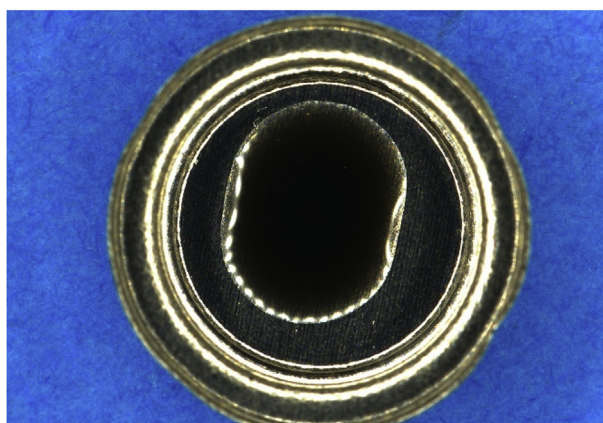


Fig. A.6. Bird's eye perspective on a 2.8 mg drop sample in a standard aluminum crucible. The texture of the crucible determines the direction of the spreading of the drop shape.

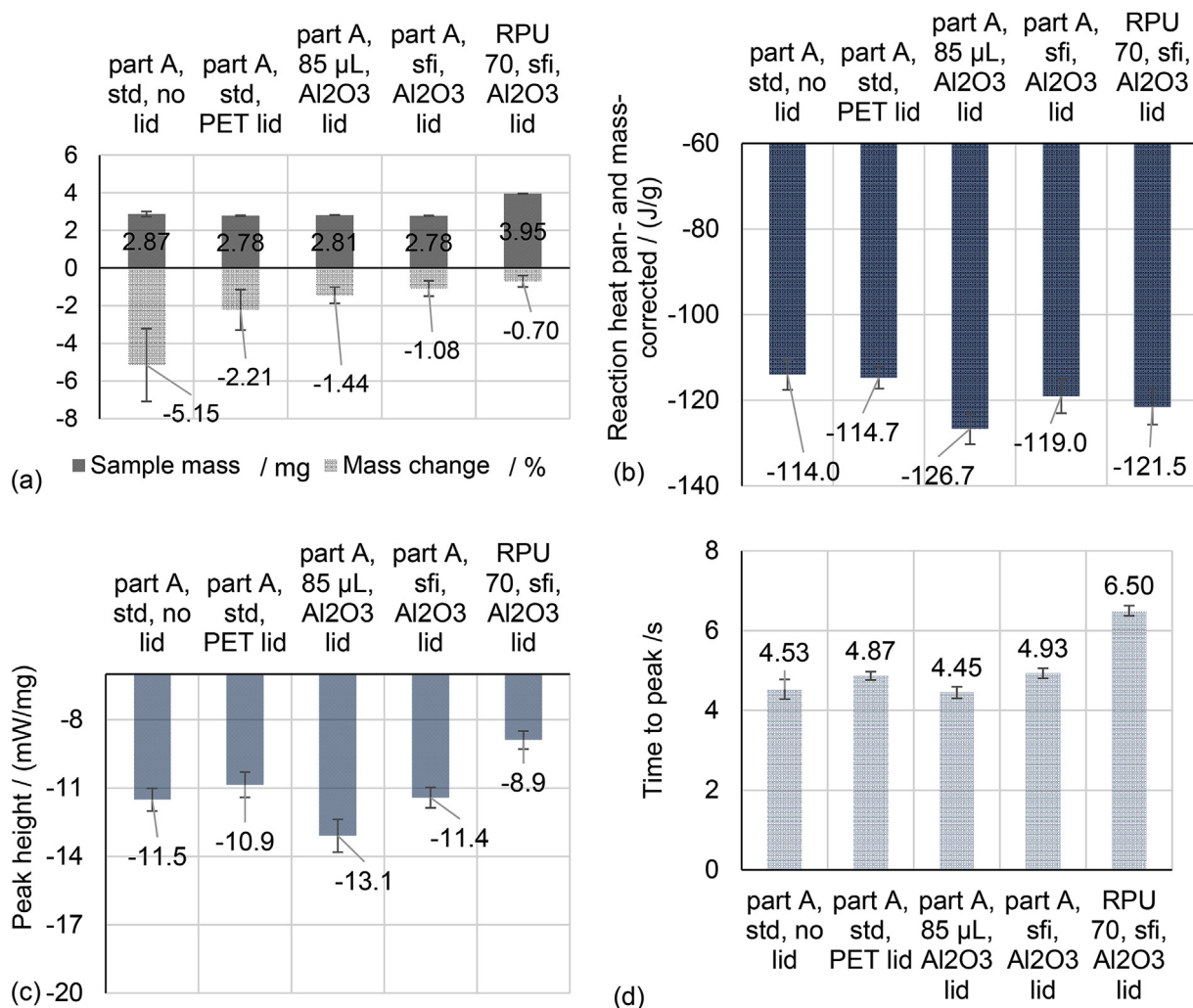


Fig. A.7. Summary of the data points from Fig. 16.

References

- J.P. Fouassier, X. Allonas, D. Burget, Photopolymerization reactions under visible lights: principle, mechanisms and examples of applications, *Prog. Org. Coating* 47 (2003) 16–36, [https://doi.org/10.1016/S0300-9440\(03\)00011-0](https://doi.org/10.1016/S0300-9440(03)00011-0).
- J.V. Crivello, E. Reichmanis, Photopolymer materials and processes for advanced technologies, *Chem. Mater.* 26 (2014) 533–548, <https://doi.org/10.1021/cm402262g>.
- J.W. Allison, J. Richter, C.M. Childers, D.R. Smalley, C.W. Hull, P.F. Jacobs, Method of Making a Three-Dimensional Object by Stereolithography, US5256340 (A), 3D SYSTEMS INC [US, 1992.
- M.P. de Beer, H.L. van der Laan, M.A. Cole, R.J. Whelan, M.A. Burns, T.F. Scott, Rapid, continuous additive manufacturing by volumetric polymerization inhibition patterning, *Sci. Adv.* 5 (2019), <https://doi.org/10.1126/sciadv.aau8723>.
- B.E. Kelly, I. Bhattacharya, H. Heidari, M. Shusteff, C.M. Spadaccini, H.K. Taylor, Volumetric additive manufacturing via tomographic reconstruction, *Science* (New York, N.Y.) 363 (2019) 1075–1079, <https://doi.org/10.1126/science.aau7114>.
- X. Kuang, D.J. Roach, J. Wu, C.M. Hamel, Z. Ding, T. Wang, M.L. Dunn, H.J. Qi, Advances in 4D printing: materials and applications, *Adv. Funct. Mater.* 29 (2019), 1805290, <https://doi.org/10.1002/adfm.201805290>.
- C. Mendes-Felipe, J. Oliveira, I. Etxebarria, J.L. Vilas-Vilela, S. Lanceros-Mendez, State-of-the-Art and future challenges of UV curable polymer-based smart materials for printing technologies, *Adv. Mater. Technol.* 4 (2019), 1800618, <https://doi.org/10.1002/admt.201800618>.
- M. Layani, X. Wang, S. Magdassi, Novel materials for 3D printing by photopolymerization, *Adv. Mater.* (Deerfield Beach, Fla.) 30 (2018), e1706344, <https://doi.org/10.1002/adma.201706344>.
- J.R. Tumbleston, D. Shirvanyants, N. Ermoshkin, R. Januszewicz, A.R. Johnson, D. Kelly, K. Chen, R. Pinschmidt, J.P. Rolland, A. Ermoshkin, E.T. Samulski, J.M. DeSimone, Additive manufacturing. Continuous liquid interface production of 3D objects, *Science* (New York, N.Y.) 347 (2015) 1349–1352, <https://doi.org/10.1126/science.aaa2397>.
- R. Januszewicz, J.R. Tumbleston, A.L. Quintanilla, S.J. Mecham, J.M. DeSimone, Layerless fabrication with continuous liquid interface production, *Proc. Natl. Acad. Sci. Unit. States Am.* 113 (2016) 11703–11708, <https://doi.org/10.1073/pnas.1605271113>.
- S.C. Ligon, R. Liska, J. Stampfl, M. Gurr, R. Mülhaupt, Polymers for 3D printing and customized additive manufacturing, *Chem. Rev.* 117 (2017) 10212–10290, <https://doi.org/10.1021/acs.chemrev.7b00074>.
- C. Decker, T. Nguyen Thi Viet, D. Decker, E. Weber-Koehl, UV-radiation curing of acrylate/epoxide systems, *Polymer* 42 (2001) 5531–5541, [https://doi.org/10.1016/S0032-3861\(01\)00065-9](https://doi.org/10.1016/S0032-3861(01)00065-9).
- Prof Lechner, M.D. Dr, Prof Dr K. Gehrke, Prof Dr E.H. Nordmeier, *Makromolekulare Chemie: Ein Lehrbuch für Chemiker, Physiker, Materialwissenschaftler und Verfahrenstechniker*, second ed., Birkhäuser Basel, Basel, 1996.
- K. Ikemura, K. Ichizawa, M. Yoshida, S. Ito, T. Endo, UV-VIS spectra and photoinitiation behaviors of acylphosphine oxide and bisacylphosphine oxide derivatives in unfilled, light-cured dental resins, *Dent. Mater.* J. 27 (2008) 765–774, <https://doi.org/10.4012/dmj.27.765>.
- C. Esposito Corcione, G. Malucelli, M. Frigione, A. Maffezzoli, UV-curable epoxy systems containing hyperbranched polymers: kinetics investigation by photo-DSC and real-time FT-IR experiments, *Polym. Test.* 28 (2009) 157–164, <https://doi.org/10.1016/j.polymertesting.2008.11.002>.
- C. Esposito Corcione, M. Frigione, A. Maffezzoli, G. Malucelli, Photo – DSC and real time – FT-IR kinetic study of a UV curable epoxy resin containing o-Boehmites, *Eur. Polym. J.* 44 (2008) 2010–2023, <https://doi.org/10.1016/j.eurpolymj.2008.04.030>.
- C. Esposito Corcione, A. Greco, A. Maffezzoli, Photopolymerization kinetics of an epoxy-based resin for stereolithography, *J. Appl. Polym. Sci.* 92 (2004)

- 3484–3491, <https://doi.org/10.1002/app.20347>.
- [18] C.E. Corcione, R. Striani, M. Frigione, UV-cured methacrylic-silica hybrids: effect of oxygen inhibition on photo-curing kinetics, *Thermochim. Acta* 576 (2014) 47–55, <https://doi.org/10.1016/j.tca.2013.11.028>.
- [19] R.V. Ghorpade, S.M. Bhosle, S. Ponrathnam, C.R. Rajan, N.N. Chavan, R. Harikrishna, Photopolymerization kinetics of 2-phenylethyl (meth)acrylates studied by photo DSC, *J. Polym. Res.* 19 (2012) 1155, <https://doi.org/10.1007/s10965-011-9811-3>.
- [20] Y. Irmouli, B. George, A. Merlin, Study of the polymerization of acrylic resins by photocalorimetry: interactions between UV initiators and absorbers, *J. Therm. Anal.* 96 (2009) 911–916, <https://doi.org/10.1007/s10973-009-0061-0>.
- [21] M.C. Rusu, C. Block, G. van Assche, B. van Mele, Influence of temperature and UV intensity on photo-polymerization reaction studied by photo-DSC, *J. Therm. Anal.* 110 (2012) 287–294, <https://doi.org/10.1007/s10973-012-2465-5>.
- [22] F. Jiang, D. Drummer, Curing kinetic analysis of acrylate photopolymer for additive manufacturing by photo-DSC, *Polymers* 12 (2020), <https://doi.org/10.3390/polym12051080>.
- [23] J. Bachmann, E. Gleis, G. Fruhmann, J. Riedelbauch, S. Schmölder, O. Hinrichsen, Investigation of the temperature influence on the dual curing urethane-methacrylate resin Rigid Polyurethane 70 (RPU 70) in Digital Light Synthesis (DLS), *Addit. Manuf.* (2020), 101677, <https://doi.org/10.1016/j.addma.2020.101677>.
- [24] A. Redmann, P. Oehlmann, T. Scheffler, L. Kagermeier, T.A. Osswald, Thermal curing kinetics optimization of epoxy resin in Digital Light Synthesis, *Addit. Manuf.* 32 (2020), 101018, <https://doi.org/10.1016/j.addma.2019.101018>.
- [25] Carbon Inc, SDS Germany RPU 70 Part A and B, Redwood City, CA 94063, USA, 2017.
- [26] Carbon Inc, SDS US EPX 82 Part A and B, Redwood City, CA 94063, USA, 2017.
- [27] P. Obst, J. Riedelbauch, P. Oehlmann, D. Rietzel, M. Launhardt, S. Schmölder, T.A. Osswald, G. Witt, Investigation of the influence of exposure time on the dual-curing reaction of RPU 70 during the DLS process and the resulting mechanical part properties, *Addit. Manuf.* 32 (2020), 101002, <https://doi.org/10.1016/j.addma.2019.101002>.
- [28] C. Decker, Photoinitiated curing of multifunctional monomers, *Acta Polym.* 45 (1994) 333–347, <https://doi.org/10.1002/actp.1994.010450501>.
- [29] D.E. Roberts, Heats of polymerization. A summary of published values and their relation to structure, *J. Res. Natl. Bur. Stand.* 44 (1950) 221–232.
- [30] C.S.B. Ruiz, L.D.B. Machado, J.E. Volponi, E.S. Pino, Oxygen inhibition and coating thickness effects on uv radiation curing of weatherfast clearcoats studied by photo-DSC, *J. Therm. Anal. Calorim.* 75 (2004) 507–512.
- [31] E. Andrzejewska, Photopolymerization kinetics of multifunctional monomers, *Prog. Polym. Sci.* 26 (2001) 605–665.
- [32] M. Sangermano, Advances in cationic photopolymerization, *Pure Appl. Chem.* 84 (2012) 2089–2101, <https://doi.org/10.1351/PAC-CON-12-04-11>.
- [33] J.E. Baxter, R.S. Davidson, H.J. Hageman, T. Overeem, Photoinitiators and photoinitiation. 8† the photoinduced α -cleavage of acylphosphine oxides. Identification of the initiating radicals using a model substrate, *Makromol. Chem.* 189 (1988) 2769–2780, <https://doi.org/10.1002/macp.1988.021891206>.
- [34] G.W. Sluggett, C. Turro, M.W. George, I.V. Koptuyug, N.J. Turro, (2,4,6-Trimethylbenzoyl)diphenylphosphine oxide photochemistry. A direct time-resolved spectroscopic study of both radical fragments, *J. Am. Chem. Soc.* 117 (1995) 5148–5153, <https://doi.org/10.1021/ja00123a018>.
- [35] Carbon Inc, Rpu 70: high-strength, functional toughness, and moderate heat-resistance. <https://www.carbon3d.com/materials/rpu-70/>, 2020. (Accessed 27 October 2020).
- [36] Carbon Inc, Epx 82: high-strength, excellent long-term durability, functional toughness. <https://www.carbon3d.com/materials/epx-82/>, 2020. (Accessed 27 October 2020).

A.2. Photo-Differential Scanning Calorimetry Parameter Study of Photopolymers Used in Digital Light Synthesis

This publication was published open access under the terms of the Creative Commons Attribution 4.0 International License, which permits use and distribution in any medium. The prerequisite is that the original work is properly cited, the use is non-commercial and no modifications or adaptations are made.



WILEY

Photo-differential scanning calorimetry parameter study of photopolymers used in digital light synthesis

Author: Joel Bachmann, Stefan Schmolzer, Matthias A. Ruderer, et al

Publication: Spe Polymers

Publisher: John Wiley and Sons

Date: Dec 25, 2021

© 2021 The Authors. SPE Polymers published by Wiley Periodicals LLC on behalf of Society of Plastics Engineers.

Open Access Article

This is an open access article distributed under the terms of the [Creative Commons CC BY](#) license, which permits unrestricted use, distribution, and reproduction in any medium, provided the original work is properly cited.

You are not required to obtain permission to reuse this article.

For an understanding of what is meant by the terms of the Creative Commons License, please refer to [Wiley's Open Access Terms and Conditions](#).

Permission is not required for this type of reuse.

Wiley offers a professional reprint service for high quality reproduction of articles from over 1400 scientific and medical journals. Wiley's reprint service offers:

- Peer reviewed research or reviews
- Tailored collections of articles
- A professional high quality finish
- Glossy journal style color covers
- Company or brand customisation
- Language translations
- Prompt turnaround times and delivery directly to your office, warehouse or congress.

Please contact our Reprints department for a quotation. Email corporatesaleseurope@wiley.com or corporatesalesusa@wiley.com or corporatesalesDE@wiley.com.

Photo-differential scanning calorimetry parameter study of photopolymers used in digital light synthesis

Joel Bachmann^{1,2}  | Stefan Schmölder³ | Matthias A. Ruderer² |
Gabriele Fruhmann²  | Olaf Hinrichsen^{1,4}

¹Department of Chemistry, Technical University of Munich, Garching, Germany

²BMW Group, FIZ, Munich, Germany

³NETZSCH-Gerätebau GmbH, Selb, Germany

⁴Catalysis Research Center, Technical University of Munich, Garching, Germany

Correspondence

Joel Bachmann, BMW Group, FIZ, Knorrstraße 147, 80788 Munich, Germany.

Email: joel.bachmann@bmw.de

Funding information

TUM; Technical University of Munich

Abstract

Photopolymers for 3D printing belong to the largest material group used in additive manufacturing. One suitable characterization method is the photo-differential scanning calorimetry (DSC) method, since UV light is used both as a probe in photo-DSC measurements and for the curing process in digital light synthesis (DLS). The photo-DSC method determines the speed and heat of the photopolymerization reaction, so it is an excellent method for characterizing the chemical process in DLS. In addition, the setup has been optimized in such a way that the photo-DSC parameters used meet typical DLS process conditions. In particular, both the overlapping of the wavelengths of the light source and the photoinitiator and the similarity of the light intensities are very important. In this study, the commonly used dual curing, urethane methacrylate, DLS resin RPU 70 is thoroughly characterized. Several photo-DSC experiments demonstrate the influence of wavelength, light intensity, temperature, relative humidity, and oxygen concentration in the atmosphere used on the curing process. Using the typical DLS parameters for light intensity and wavelength, the chemical reaction is mainly influenced by the oxygen concentration. The exposure time for vat photopolymerization processes decreases with decreasing oxygen concentration, which is why inert printing processes could have a positive effect on printing times. Additionally, it is shown that this method is also suitable for other DLS resins.

KEYWORDS

additive manufacturing, digital light synthesis, photo-DSC, photopolymers, relative humidity, RPU 70, vat photopolymerization

1 | INTRODUCTION

Photopolymers for additive manufacturing (AM) are used in vat photopolymerization (VPP)^[1] technologies. Photopolymers are cured either with a point-based laser, as in

stereolithography (SLA), or with an area-wise exposure, as in digital light processing (DLP). This polymer group belongs to one of the largest material groups used in AM.^[2] Typical applications can be found in the fields of prototyping, biomedicine, individualization, engineering,

This is an open access article under the terms of the Creative Commons Attribution License, which permits use, distribution and reproduction in any medium, provided the original work is properly cited.

© 2021 The Authors. *SPE Polymers* published by Wiley Periodicals LLC on behalf of Society of Plastics Engineers.

and 4D printing.^[3–6] Highly crosslinked thermosets or low crosslinked elastomers can be produced with these technologies. The great advantage of photopolymers compared to other 3D printing materials is the production of dense parts having an excellent surface quality. In this respect, they outperform the powder or filament AM materials used in powder bed fusion or material extrusion, respectively.^[7]

The polymerization mechanism for photopolymers is either a radical chain growth or a cationic step growth. These two reaction pathways require different initiating and propagating molecules. Photoinitiators with (meth-)acrylates monomers follow a radical photopolymerization; photoacid generators with epoxy monomers follow a step growth polymerization. Other components, like pigments, passive absorbers, and stabilizers are also part of the resin composition.^[8]

One of the newer VPP methods is digital light synthesis (DLS),^[9] which uses UV light projection and oxygen to enable continuous area-wise polymerization, in which UV light passes through the UV and oxygen transparent window at the bottom of the resin vat. The light causes a homolytic cleavage of the photoinitiator, which leads to the formation of two radicals. The latter react with C=C double bond of the (meth-)acrylate molecules and thereby form further radicals. The polymer is created by the continuous addition of a new monomer to the chain. Oxygen also enters through the window and inhibits radical photopolymerization at the bottom of the vat. Therefore, this area is called the “O₂ dead zone” and is only a few micrometers thick. Above it, a continuous polymerization gradient is formed. Since no resin polymerizes in the “O₂ dead zone,” the surrounding resin can flow continuously into the polymerization zone. The typical realignment step with a slider is thus made obsolete.^[10]

DLS uses two-part resins which are thermally post-cured after the shape-giving UV curing step. These two-part resins form a second, interpenetrating network during thermal post-processing.^[11–14] The additional degree of freedom of the thermal post curing and the resulting modification of the material enables the processability of a wide range of material classes, such as elastomeric polyurethanes (e.g., EPU 40), silicone-like materials (e.g., SIL 30), epoxides (e.g., EPX 82), polyurethanes (e.g., RPU 70), and cyanate esters (e.g., CE 221). These resins contain even more different kinds of molecules than typical VPP formulations. Many molecules having various functions are present in one composition. Not only is a small variation of their concentration in the resin, but also process and environmental parameters such as light intensity, wavelength, temperature, atmosphere, and relative humidity (RH) can easily change the reaction behavior of the entire resin. The term “atmosphere” is

used as a synonym for the surrounding gas phase composition. Since the series production of components requires high reproducibility, it is crucial to be able to control the influencing parameters. To ensure this, a systematic approach is needed to identify the main influencing factors and their impact on key outcome values.

The three most appropriate analyzing methods used to characterize photopolymers are Fourier transform infrared, Raman spectroscopy, and photo-differential scanning calorimetry (DSC).^[15–21] The former two provide information about the chemical identity during the conversion from monomers to polymer, such as double bond conversion, while the third provides thermal information about the strength and speed of polymerization. These can be characterized by the following photo-DSC values: reaction heat, peak height, and time to peak.

A recent photo-DSC study on RPU 70 and EPX 82^[22] showed that, due to the evaporation tendency of their volatile monomers, a robust and reproducible sample preparation is the drop sample shape with ~2.8 mg sample weight and a short total measuring and preparation time (~1 h). Kardar et al.^[23] studied the influence of temperature (25, 45, 65, and 85°C) and light intensity (2, 20, 40, and 80 mW/cm²) on a pigmented and an unpigmented epoxy acrylate system. Rusu et al.^[24] investigated the effect of temperature (–10, 0, 10, 20, 30, 40, and 50°C), light intensity (2, 4, 6, 8, and 10 W/cm²), and various reaction atmospheres (nitrogen and air) on a proprietary photopolymer. Other photo-DSC publications have focused on reactivity^[16,25] and the influence of oxygen inhibition.^[26,27]

However, most photo-DSC studies have not converted the light intensity from the light source to the actual light intensity applicable in the 3D printing process and on the sample surface during the measurement. In addition to light intensity, atmosphere, and temperature, other relevant 3D printing process parameters or environmental factors such as wavelengths and RH have rarely been considered. Finally, the various effects on the chemical reaction are often analyzed in isolation and are not compared with each other.

Therefore, the scope of this study is a systematic approach to investigating and comparing the effects of the following five parameter groups on the UV curing behavior of RPU 70: wavelength (365, 320–390, and 400–500 nm), light intensity (9, 18, and 27 mW/cm²), temperature (20, 30, and 40°C), atmosphere (0, 20, and 100 vol % O₂), and RH (24.3% and 100%). All of these parameter groups can affect the DLS process and thus affect the quality of the final part. Additionally, this method demonstrated robustness against the influence of different sample pans and is also suitable for the characterization of other photopolymer classes such as EPX 82 and CE 221.

2 | EXPERIMENTAL

2.1 | Material and sample preparation

The individual components of RPU 70, EPX 82, and CE 221 (part A or part B) are listed in Table S1 according to the safety data sheets (SDS) from 2017^[28–30] with their short name, CAS number, volume percentage in the corresponding part, and molecule structure. The following section specifies the full chemical name of the component, followed by the short name and the volume percentage in the corresponding part.

RPU 70 (Carbon, United States) with the lot number 19AP1191 is a black two-part resin which was mixed in a 10:1 ratio and dispensed at a speed of 1 mm/s using an Albion Dispenser (Albion Engineering, United States) and a mixing head. Part A of RPU 70 consisted of the photoinitiator diphenyl (2,4,6-trimethylbenzoyl) phosphine oxide (TPO, 0.1%–2%), urethane dimethacrylate (UDMA, 1%–20%), methacrylate blocked polyurethane/diisocyanate (MABPU and/or MABDI, 10%–70%), isobornyl methacrylate (IBOMA, 10%–50%), and neopentyl glycol dimethacrylate (NPGDMA, <0.3%). Part B of RPU 70 consisted of trimethylolpropane tris [poly(propylene glycol) amine terminated] ether (chain extender, 20%–100%).

EPX 82 (Carbon) with the lot number 19CP1419 is a black two-part resin which was mixed in a 1:1 ratio and dispensed at a speed of 2 mm/s using an Albion Dispenser (Albion Engineering) and a mixing head. Part A of EPX 82 consisted of bisphenol A-epichlorohydrin polymer (Araldite 527, 45%–80%), bisphenol A-acrylate epichlorohydrin (ED 20 acrylate, 10%–30%), *N,N*-dimethylacrylamide (DMA, 5%–15%), and the photoinitiator diphenyl(2,4,6-trimethylbenzoyl)phosphine oxide (TPO, 1%–4%). Part B of EPX 82 consisted of *N,N*-dimethylacrylamide (DMA, 30%–50%), urethane acrylate (proprietary, 25%–40%), 3,3'-sulfonyldianiline (DADPS, 5%–15%), 4,4'-sulfonylbisbenzamine (DAP, 5%–15%), and a reaction product of bisphenol A & epichlorohydrin (DS-002683, 5%–15%).

CE 221 (Carbon) with the lot number 17HP4876 is a yellow two-part resin which was mixed in a 1:1 ratio and dispensed at a speed of 2 mm/s using an Albion Dispenser (Albion Engineering) and a mixing head. Part A of CE 221 consisted of 4,4'-ethylidenediphenyl dicyanate (bisphenol E cyanate ester, 100%). Part B of CE 221 consisted of (1-methylethylidene)bis[4,1-phenyleneoxy (2-hydroxy-3,1-propanediyl)]ester (BisGMA, 20%–60%), trimethylolpropane trimethacrylate (TMPTMA, 20%–50%), exo-1,7,7-trimethylbicyclo[2.2.1]hept-2-yl methacrylate (IBOMA, 1%–25%), dicyclopentadienedimethanol diacrylate (T-ACRYLATE, 1%–20%), and the photoinitiator phenylbis(2,4,6-trimethylbenzoyl)-phosphine oxide (BAPO, 0.1%–4%).

For the measurement of two components resins, a static mixing head was attached to the opening of the two component outputs. The cartridge and the mixing head were then inserted into the resin mixing gun and the corresponding mixing speed set. The first 10 s of the mixed resin were rinsed and disposed of in a glass container. After the rinsing process, the resin was collected in a UV-protected container. For measurements in which only a single part (e.g., part A) was examined, a commercially available uncoated paper clip was used to draw the resin out of the cartridge. The liquid resin was positioned centrally and in the form of a drop shape in the open pan. A Cubis[®] Ultra Micro Balance (Sartorius, Germany) was used to determine the sample weight, which was $2.326 \text{ mg} \pm 0.093 \text{ mg}$ for all experiments ($N = 75$). Either a standard 40 μl volume aluminum pan (std) or a cold-pressed 85 μl (sfi) pan was used (see Table S2). The time between sample preparation and the start of the measurement was always $13 \pm 2 \text{ min}$.

2.2 | Photo-DSC method and measured values

The photo-DSC setup consisted of a NETZSCH DSC 204 F1 Phoenix dynamic differential scanning calorimetry with a NETZSCH CC300 cooling controller and a OmniCure[®] S2000 light source (Excelitas Technologies[®] Corp., Canada). The default offset for the light source was 5 s. The corresponding NETZSCH Proteus 8.0 software was used for the evaluations. Before each measurement, the DSC device was set to the corresponding temperature and atmosphere settings (offset) at which the experiment was then performed. Table 1 shows the temperature and UV-exposure profile for a photo-DSC measurement at 30°C under a 100% nitrogen atmosphere (20 ml/min for rinsing and 60 ml/min inert gas during the measurement). As soon as the desired temperature and atmosphere had been constantly displayed for 5 min, the open sample and the open reference pan were positioned on the corresponding measuring sensors. The quartz disc in the path of the UV light was checked for transparency before the measurement (see Figure S1). The measuring cell was then closed and the measurement started.

Figure 1A shows the photo-DSC signal from the method presented in Table 1. UV exposure caused the two peaks P1 and P2. Figure 1B shows the subtracted photo-DSC signal of P1 minus P2 with the measured values peak area A_p , peak height h_p and time to peak t_p . The value for t_p was subtracted by 5 s due to the light source offset. Additionally, A_p must be multiplied by the pan and by the mass correction factor to attain the reaction heat ΔH_R .

TABLE 1 Photo-DSC method with parameter settings: Temperature, UV-exposure, and atmosphere

No.	Mode	Temperature (°C)	Duration (min)	UV-exposure	Duration UV-exposure (min)	Atmosphere (vol% N ₂)
0	Initial	30	-	-	-	100
1	Isotherm	30	3	-	-	100
2	Isotherm	30	6		3	100
3	Isotherm	30	6		3	100

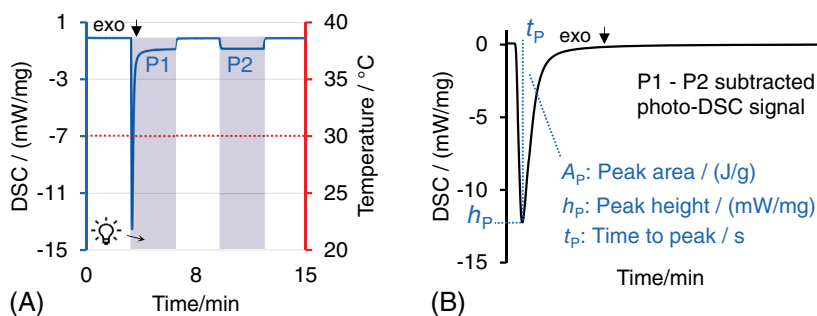


FIGURE 1 (A) Photo-differential scanning calorimetry (DSC) signal with two exposure segments with 3-min radiation at 30°C. (B) The subtraction of P2 of P1 results in the subtracted photo-DSC signal with the corresponding measured values

The pan correction factor pc is necessary so that the results can be analyzed and compared independently of the choice of pan.^[22] This factor was calculated by the value found in the literature^[31] for the melt enthalpy of indium (28.6 J/g) divided by the melting peak area of the third heating of indium with the pan used. The third heating process was used to avoid measurement errors due to impurities that may occur more frequently during the first and second heating processes. In general, the melt enthalpy of indium in each pan should come close to the value from the literature, so the pc factor should be not less than 0.8 and not higher than 1.2. It must be redefined after each calibration of the DSC device.

$$0.8 < pc = \frac{28.6 \text{ J/g}}{\text{Melting peak area of indium in reference pan}} < 1.2$$

The mass correction factor mc is necessary because photopolymers contain many volatile monomers, and a strong mass decrease by evaporation takes place in some cases.^[22] For different photopolymers to be comparable, the reaction enthalpy was corrected with the mass after the measurement. The mc factor results from the reweighing of the sample in the pan after the photo-DSC measurement.

$$mc = \frac{m_{\text{sample before measurement}}}{m_{\text{sample after measurement}}}$$

The calculation of the pan and the mass corrected reaction enthalpy ($\Delta H_{R,pc,mc}$) thus results in:

$$\Delta H_{R,pc,mc} = A_p \cdot pc \cdot mc$$

Regarding photopolymerization, t_p describes the time between the onset of photopolymerization to the time when the maximum heat flow rate is reached.^[24] This time is also used to set the optimal UV exposure time in 3D printing.^[12] The h_p value corresponds to the maximum photopolymerization rate, and A_p correlates with the reaction heat released during photopolymerization.^[24]

2.3 | Parameter study—Photo-DSC settings

Table 2 shows 15 different measurement settings for the parameter study. The seven parameter groups of wavelength, light intensity, pan, material, temperature, atmosphere, and RH are provided as columns in the table. The last column contains the short name for the measurement. The measurements from the first and sixth rows were used in the results section for more than one comparison, so there are several short names in the last column. For the sfi pan measurements, the reference pan was also changed from std to sfi. The temperatures (20, 30, and 40°C) and atmospheres (0, 20, and 100 vol% O₂) were changed correspondingly for all four segments from Table 1. The RHs of 100% and 24.3% were achieved by placing the sample pan in an airtight glass jar with and without water inside at room temperature for

TABLE 2 Photo-DSC settings for parameter study with short names

Material	Pan	Wavelength filter (nm)	Light intensity (mW/cm ²)	Temperature (°C)	Vol% O ₂	RH	Short name
Part A	std	365	9	30	0	-	1st 365 nm; 2nd 9 mW/cm ² ; 3rd RPU 70 part A
Part A	std	320–390	9	30	0	-	320–390 nm
Part A	std	400–500	9	30	0	-	400–500 nm
Part A	std	365	18	30	0	-	18 mW/cm ²
Part A	std	365	27	30	0	-	27 mW/cm ²
RPU 70	std	365	9	30	0	-	std; RPU70; 30°C; 0 vol% O ₂
RPU 70	sfi	365	9	30	0	-	sfi
CE 221	std	365	9	30	0	-	CE221
EPX 82	std	365	9	30	0	-	EPX82
RPU 70	std	365	9	20	0	-	20°C
RPU 70	std	365	9	40	0	-	40°C
RPU 70	std	365	9	30	20	-	20 vol% O ₂
RPU 70	std	365	9	30	100	-	100 vol% O ₂
RPU 70	std	365	9	30	0	100%	100% RH
RPU 70	std	365	9	30	0	24.3%	24.3% RH

Note: Five measurements were made for each parameter.

24 h. The RH was measured with a Traceable[®] memory-card humidity/temperature/dew point meter (VWR International, United States).

2.3.1 | Setup for light intensity calibration

Figure 2 shows the experimental setup used to convert the light intensity of the OmniCure[®] light source into the light intensity on the surface of the sample. One light guide of the photo-DSC was removed. When the oven was closed, a commercially available screwdriver was inserted through the opening until the tip of the screwdriver touched the measurement platform of the pans. Afterwards, the screwdriver was fixed with the same screw that fixes the light guide (see Figure 2A), and the photo-DSC head was placed on a special lab boy setup which allows a leveled horizontal alignment and an ascent or descent. Beneath the photo-DSC head, a radiometer RM22 with the UVA+ sensor (Opsytec Dr. Gröbel GmbH, Germany) was placed in such a way that the tip of the screwdriver touched the surface of the UVA+ sensor (see Figure 2B). The screwdriver was then removed, and the light guide was set at the correct position. Using the setup from Figure 2C, the calibration of the light intensities was performed using various wavelength filters.

3 | RESULTS AND DISCUSSION

3.1 | Light source calibration

One important process parameter for all vat-based AM technologies is the applied light intensity. For RPU 70 in DLS, the processing light intensity in the default print script is 9 mW/cm².^[12] The wavelength used in the production process is unknown. In photo-DSC, however, only the light intensity emitted from the tip of the light guide can be set. The distance from the sample surface to the tip of the light guide is 2.7 mm. In addition, the light must pass through a sapphire glass protecting the light source. The use of wavelength filters further reduces the light intensity. Therefore, the calibration device from Figure 2 was created in order to identify the light intensity striking the sample surface. Figure 3 shows the light spectra without and with four different wavelength filters. The absorption spectrum of the photoinitiator TPO and the absorption spectrum of the UVA+ sensor of the radiometer for each light spectrum are also displayed. Apart from the *empty filter* setting, the UVA+ sensor can cover the spectra emitted with the various wavelength filters.

In Figure 4, seven different light intensities (0.5, 0.75, 1.0, 1.5, 2.0, 3.0, and 4.0 W/cm²) of the light source were measured using the UVA+ sensor of the radiometer at a distance of 2.7 mm for five different wavelength settings.



FIGURE 2 Setup for light intensity calibration

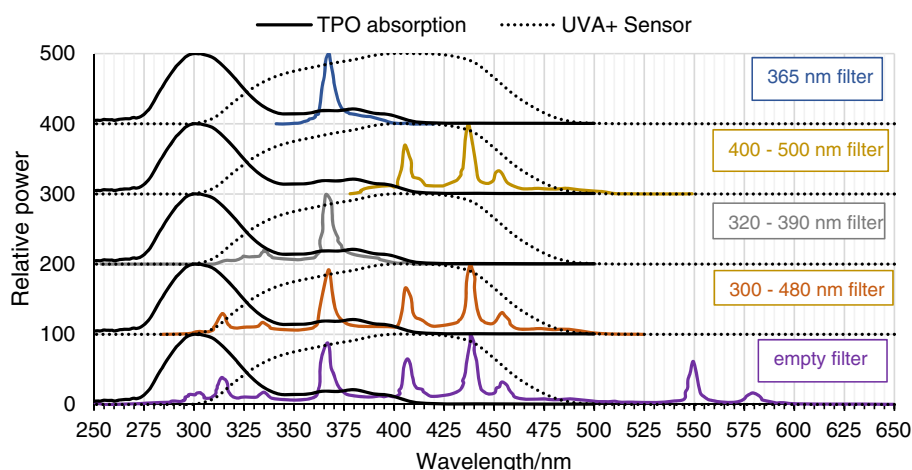


FIGURE 3 Light spectrum for five different wavelength settings, plotted with the absorption spectrum of the photoinitiator TPO and the absorption spectrum of the UVA+ sensor of the radiometer

A linear behavior was discovered. Therefore, a non-linear influence of the used filters can be excluded. The desired target light intensity on the sample surface for the respective filter can be set from the resulting linear equations. The minimum adjustable light intensity of the Omni Cure lamp is 0.50 W/cm^2 . This setting results in a light intensity on the sample surface of 14.02 or 13.31 mW/cm^2 for the *empty* or the $300\text{--}480 \text{ nm}$ filter. Accordingly, a typical process-related setting of 9 mW/cm^2 cannot be achieved for these filter settings (see also Figure S2). The other filters, 365 , $320\text{--}390$, and $400\text{--}500 \text{ nm}$ can reach 9 mW/cm^2 . The corresponding light source settings can be seen in Table 3. Since various light intensities on the sample surface were also investigated for the parameter study, the conversion values for 18 and 27 mW/cm^2 are provided for the 365 nm filter.

3.2 | Results from parameter study

This section shows the influence of various influencing factors on the chemical reaction. These influencing factors are also 3D printing process-related or environmental factors. The parameter set was tested according to Table 2. The subtracted photo-DSC signals for the various influencing factors can be seen in Figure 5, and the comparison of the three measured values of the photo-DSC measurement $\Delta H_{R,pc,mc}$, h_P , and t_P can be seen in Figure 6. To ensure a good level of comparability among the three different measured values in Figure 6, the results for $\Delta H_{R,pc,mc}$ and h_P were divided by -10 and -1 , respectively. All displayed error bars represent the SD. Figure S3 compares all measured values of all influencing factors in one diagram, and Figure S7

FIGURE 4 Calibration lines for five wavelength settings at a distance from the top of the light source to the surface of the UVA+ sensor of 2.7 mm. The SDs are too small to be seen at this resolution

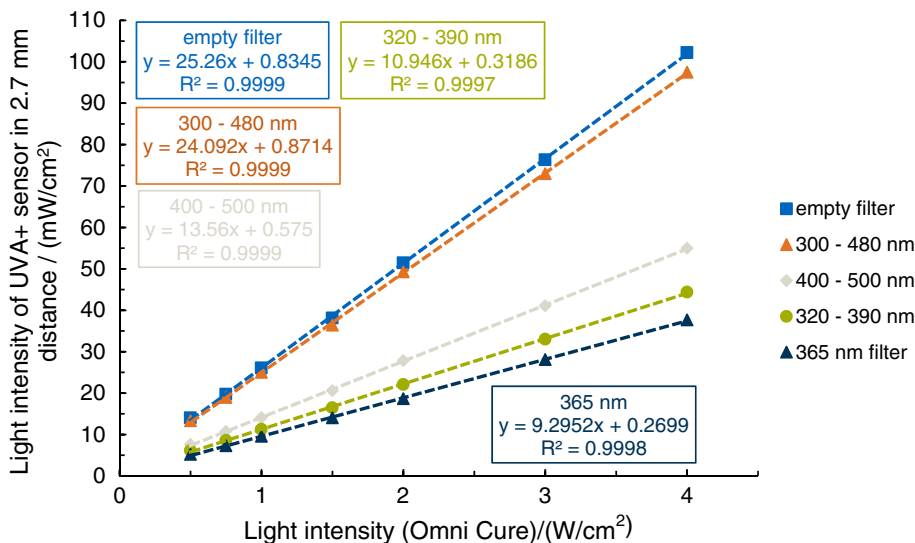


TABLE 3 Light intensity conversion values for different wavelengths and light intensities

Light intensity on sample surface	Light intensity for light source with different wavelengths		
	365 nm	320–390 nm	400–500 nm
9 mW/cm ²	0.94 W/cm ²	0.79 W/cm ²	0.62 W/cm ²
18 mW/cm ²	1.91 W/cm ²	-	-
27 mW/cm ²	2.88 W/cm ²	-	-

compares the effects of the various parameter groups on the individual measured photo-DSC values.

The sample weight before the measurement was constant for all parameter groups except the RH group. In the latter, the mass increased during the conditioning time due to water absorption. After conditioning and during the measurement, the mass decreased sharply again due to water evaporation (see Figure S6). The means of the measured sample weight and mass loss for all parameter groups are shown in Figure S4. The mass change refers only to the mass lost during the experiment. In the following discussion, each of the seven parameter groups is analyzed and interpreted separately.

3.2.1 | Influence of wavelength

The wavelength is not changed during DLS. However, other VPP technologies use different light engines with different wavelengths, and a typical question during application is whether the material can also be processed on other 3D printers.

As depicted above, the calibration line (see Figures 4 and S2) shows that the process-relevant light intensity of 9 mW/cm² can only be reached using three wavelength filters, that is, 320–390 nm, 400–500 nm, and 365 nm.

Figure 6A shows the comparison of these three filters at a light intensity on the sample surface of 9 mW/cm². The 400–500 nm filter has the lowest $\Delta H_{R,pc,mc}$ (−113.5 J/g) and h_p (−8.1 mW/mg) and the longest t_p (6.5 s) in comparison to the other filters. The light spectrum of the 400–500 nm filter has the smallest overlap with the absorption spectrum of the photoinitiator (see Figure 3). As a result, photopolymerization cannot proceed as strongly and quickly as with the other filters. The 320–390 nm filter has a higher h_p (−13.1 mW/mg) and a shorter t_p (4.42 s) than the 365 nm filter (−11.6 mW/mg and 4.96 s). However, $\Delta H_{R,pc,mc}$ is very similar for the 320–390 nm (−123.6 J/g) and the 365 nm wavelength (−121.2 J/g). The reason for the faster and higher peak of the 320–390 nm filter might be that a more reactive absorption range of TPO is covered by the broader emission spectrum. The photoinitiation process is intensified as a result.

3.2.2 | Influence of light intensity

In DLS, UV light is transmitted from the light engine via a digital micromirror device to the bottom of the vat. These micromirrors project the layer information into the vat with a pixel size of $\sim 75 \times 75 \mu\text{m}$. However, small

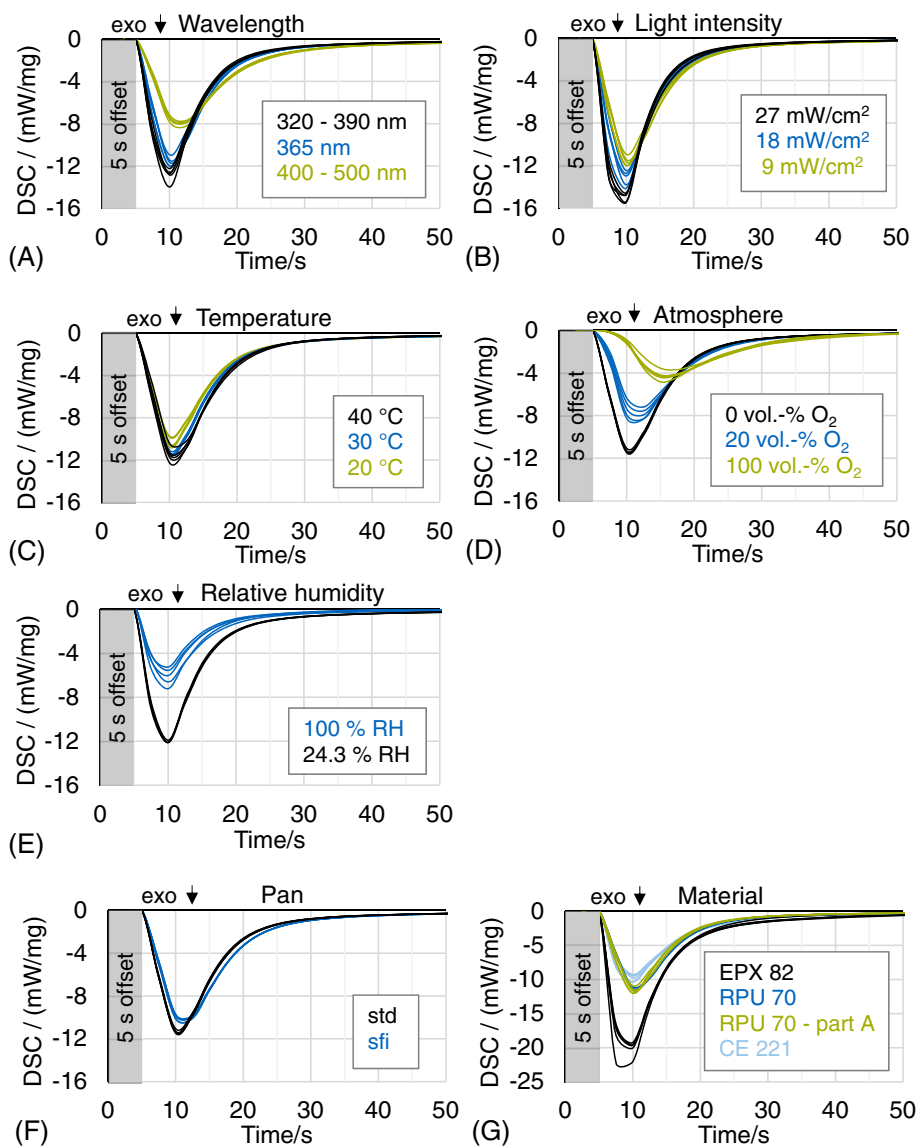


FIGURE 5 Subtracted photo-DSC signals for seven different parameter groups (A–G) with $N = 5$

variations in light intensity can occur within a pixel and over the projection area.

The 365 nm filter was used for the 9, 18, and 27 mW/cm^2 light intensity investigations because the overlap with the reactive absorption range of TPO is good, and the reaction occurred in a manner very similar to that of the 320–390 nm wavelength range (see Section 3.2.1). In addition, most light engines in DLP and DLS commonly use a narrow wavelength range of 365, 385, or 405 nm. Figure 6B, with a wavelength of 365 nm, shows that the difference in $\Delta H_{R,pc,mc}$ between 9 (-121.2 J/g) and 18 mW/cm^2 (-122.4 J/g) lies within the SE of the DSC device ($\sim 3\%$). At a light intensity of 27 mW/cm^2 , $\Delta H_{R,pc,mc}$ increases significantly to -130.5 J/g . Both h_p and t_p indicated a linear behavior with increasing light intensity (see Figure 7). The light intensity describes the energy of the photons per area. The more photons with the corresponding wavelength,

the more homolytic cleavages of TPO. As a result, photopolymerization intensifies, which is made clear by a shorter t_p and higher h_p . These observations can be confirmed by other photo-DSC studies from the literature.^[24,32] Figure S4 shows a slight increase in mass loss as the light intensity increased. This might have occurred because, at an increased light intensity, more reaction heat dissipates into the sample, thus increasing the temperature of the sample and leading to more evaporation.

3.2.3 | Influence of temperature

Since the photopolymerization during DLS is strongly exothermic, the surrounding resin is continuously heated by the released heat. Parts with a large cross-section generate more heat as more resin is irradiated simultaneously by UV light. At the beginning of the print job,

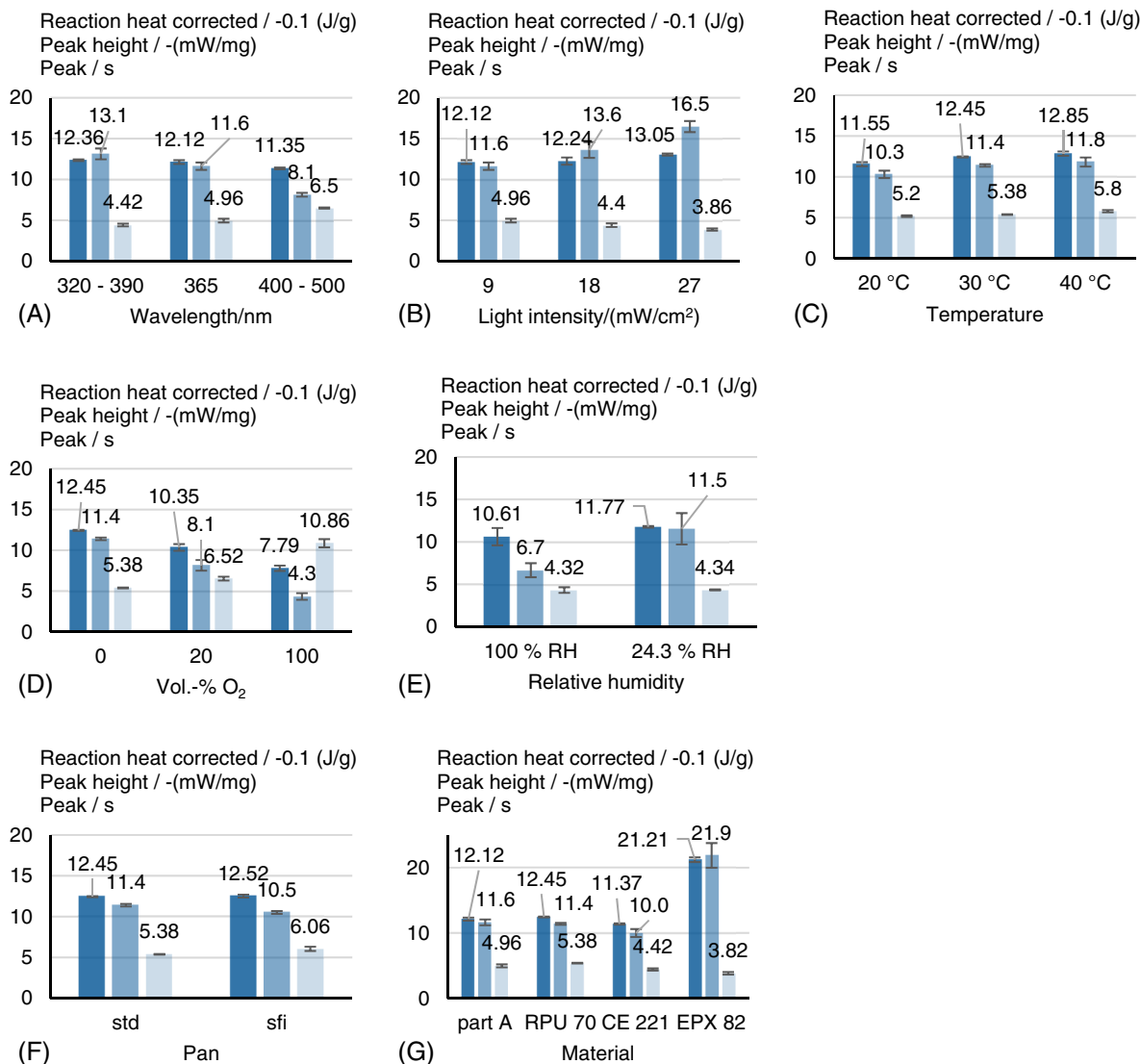
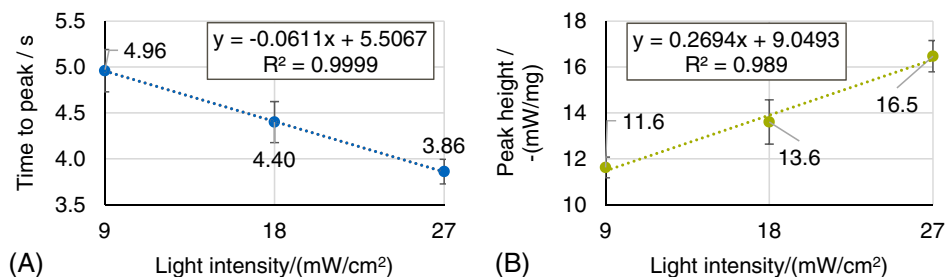


FIGURE 6 Means of measured values $\Delta H_{R,pc,mc}$, h_P and t_P for the seven different parameter groups (A–G)

FIGURE 7 Linear correlation between light intensity and (A) t_P and (B) h_P



the resin in the vat is still at room temperature (20–30°C). After a number of exposures, the temperature of the resin can already be significantly above room temperature (~40°C or higher^[12]). Therefore, temperature is an important process parameter—especially in two-part DLS resins—since the reaction between part A and part B may also take place at elevated temperatures.

Figure 6C shows that $\Delta H_{R,pc,mc}$ of RPU 70 increased with rising temperatures (20°C: –115.5 J/g, 30°C: –124.5 J/g and 40°C: –128.5 J/g). The increase of reaction heat for (meth-)acrylates at higher temperatures is well documented in the literature.^[24] In addition, all three photo-DSC measured exhibited a weak linear dependence with respect to temperature. However, the

relatively low increase in t_p at rising temperatures is in contrast to that expected from the literature.^[24] One possible explanation is that RPU 70, unlike most of the (meth-)acrylate photo-DSC materials studied, is a dual-curing resin, and a temperature increase also causes the formation of a polymer network between part A and part B.^[11] Increased viscosity reduces the mobility of methacrylates during photopolymerization and thus increases t_p . The mass loss during the measurement even showed a linear correlation with temperature (see Figure 8). The latter clearly resulted from the tendency of volatile components in the resin to evaporate more strongly at higher temperatures.

3.2.4 | Influence of O₂ concentration

As mentioned in the introduction, oxygen is a very important process parameter for DLS because it generates the “O₂ dead zone” which enables continuous polymerization.

Figure 6D shows that this is also one of the most significant influences on the photopolymerization of RPU 70. The well-known oxygen inhibition of methacrylates increases t_p and greatly reduces $\Delta H_{R,pc,mc}$ from -124.5 J/g at 0 vol% O₂ to -77.9 J/g at 100 vol% O₂ and h_p from -11.4 mW/mg at 0 vol% O₂ to -4.3 mW/mg at 100 vol% O₂. Furthermore, Figure 9 displays a linear increase in t_p at a rising oxygen concentration.

3.2.5 | Influence of RH

The environmental parameter of RH plays a critical role for DLS because it varies considerably, depending on the weather, season, or country.

The result from Figure 6E compares a sample conditioned at 100% with one conditioned at 24.3% RH for 24 h at 25°C. The samples were then weighed again after the conditioning time. For the 100% RH samples, no stable sample weight was achieved prior to the photo-DSC

measurement due to a heavy mass loss. The mass loss due to water evaporation continued during the measurement. The evaporated water corresponds to the amount absorbed during the 24-h conditioning. Even though the measured values $\Delta H_{R,pc,mc}$ and h_p were significantly reduced from 24.3% RH (-117.7 J/g and -11.5 mW/mg) to 100% RH (-106.1 J/g and -6.7 mW/mg), there was almost no effect on t_p (24.3% RH: 4.34 s and 100% RH: 4.32 s).

3.2.6 | Influence of material

In addition to the effect of process and environmental parameter groups on the reaction behavior of RPU 70, the EPX 82 and CE 221 materials were also investigated using the photo-DSC method. Although all the photopolymers investigated underwent radical photopolymerization, their composition differed according to the photoinitiators (TPO for RPU 70 and EPX 82; BAPO for CEE 221), monomers, oligomers, and chain extenders used (see Table S1). Figure 6G shows that $\Delta H_{R,pc,mc}$ and h_p of EPX 82 (-212.1 J/g, -21.9 mW/mg) were almost twice as large as for the other DLS resins. Furthermore, Figure S4 shows that EPX 82 had the highest mass loss during the photo-DSC measurement (at 1.64%) compared to all other experiments. The high percentage of acrylates in EPX 82 appears to be the reason for the lowest t_p (3.82 s), a higher h_p and $\Delta H_{R,pc,mc}$, and a higher mass

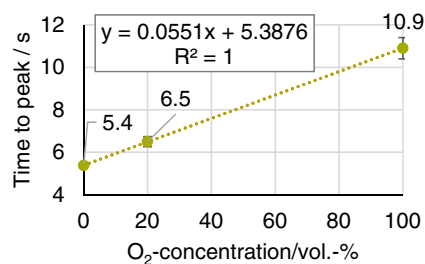


FIGURE 9 Linear correlation between t_p and O₂-concentration

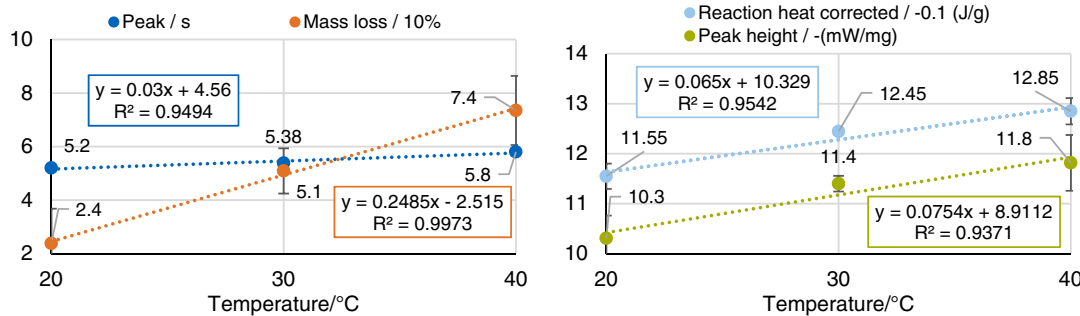


FIGURE 8 Linear correlation of photo-differential scanning calorimetry (DSC) measured values and mass loss with temperature

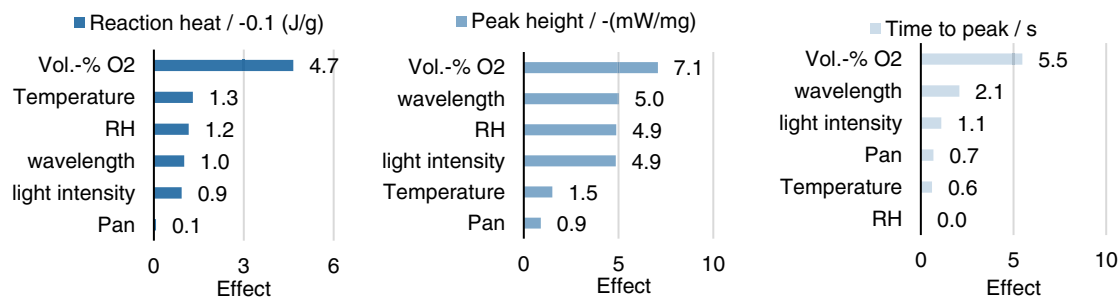


FIGURE 10 Main effects from process and environmental related parameter groups on the curing behavior of RPU 70

loss. It is known from the literature that acrylates react much faster than methacrylates. The latter are sterically hindered by a methyl group, so they react slower than acrylates and are the predominant components of RPU 70 and CE 211. This means that EPX 82 needs the lowest exposure time during DLS in comparison to RPU 70 and CE 221. The mass loss of RPU 70 and CE 221 is 0.51% and 0.06%, respectively. Since different 3D-printing resins have vastly different compositions with different volatile diluent monomers, and they also exhibit differences in their evaporation behavior. To be able to compare the reaction heat of different materials, the mass change during the measurement should always be considered, and the reaction heat needs to be corrected, as explained in the method chapter. Whereas $\Delta H_{R,pc,mc}$ and h_p are almost the same for the mixed RPU 70 (-124.5 J/g, -11.4 mW/mg) and part A (-121.2 J/g, -11.6 mW/mg), the non-UV-reactive species in part B influences only t_p . Compared to part A (4.96 s), RPU 70 has a lower volume percentage of reactive monomers, so it needs more time to reach the peak maximum (5.38 s). Although the values found in the literature^[33,34] show that BAPO has a higher local light absorption than TPO at 365 nm, CE 221 shows the lowest values for the values $\Delta H_{R,pc,mc}$ (-113.7 J/g) and h_p (-10.0 mW/mg) of all materials, and t_p is with 4.42 s between EPX 82 and RPU 70. Higher molar absorptivity means that a lower photoinitiator concentration is needed for equal curing. However, the precise concentration of the photoinitiators is unknown. Overall, all three material systems can be distinctly identified by their subtracted photo-DSC signal (see Figure 5G).

3.2.7 | Influence of the pan

The design of the pan is also crucial to the photo-DSC measurement. The pan comparison of $\Delta H_{R,pc,mc}$ of RPU 70 between *std* (-124.5 J/g) and *sfi* (-125.2 J/g) in Figure 6F showed no significant difference. However, the photopolymerization reaction was intensified using *std* (-11.4 mW/mg, 5.38 s) instead of *sfi* sample pans

(-10.5 mW/mg, 6.06 s), which can be represented by the shorter t_p and higher h_p described above. One possible explanation for this phenomenon could be the differing sample shapes of the resin in the pan after measurement (see Figure S5). Although a drop shape was used in both cases, the *sfi* pan provided a more uniform drop shape, which can be better obtained through the cold-pressed edge. Whereas the drop in the *std* pan spills toward the pans surface structure and toward the wall of the pan. Thereby, it increases its surface area, which is exposed to UV light and at the same time it reduces its film thickness, which is a very important sample preparation parameter for photo-DSC measurements.^[22] A thicker film delays and attenuates the UV reaction because the migration of the photons through the resin takes more time.

4 | CONCLUSION

Photo-DSC is an excellent characterization technique for the photopolymers used in AM. In this study, a calibration setup (see Figure 2) was used to enable typical DLS process conditions for the photo-DSC method. The resulting linear equations (see Figure 4) allow the light intensity of the light source at a certain wavelength to be converted into the light intensity that hits the sample surface and thus corresponds to the light intensity of the DLS process. These settings were used to study the effects of the process and environmental parameters such as wavelength, light intensity, temperature, atmosphere, and RH on the urethane methacrylate material system RPU 70.

Figure 10 shows the parameter group having the largest effect on the curing behavior of RPU 70. In this case, the effect was defined as the largest minus the smallest mean within a parameter group. The largest effect on the reaction heat ($\Delta H_{R,pc,mc}$), the maximum photopolymerization rate (h_p), and the time until the latter was reached (t_p) is caused by oxygen inhibition. It takes twice as long to reach t_p for RPU 70 in 100 vol% O₂ (10.9 s) as

compared to a completely inert environment (5.4 s). In an air-like atmosphere with ~20 vol% O₂, it still takes 1.1 s longer to reach t_p . A longer t_p correlates with longer exposure times for each projection layer in DLS, and longer exposure times accumulate to longer total print times. The conditioning of RPU 70 at 100% RH compared to 24.3% RH had an effect on the reaction heat similar to that of a temperature difference of 20 K, a light intensity difference of 18 mW/cm², and the change from a 400–500 nm (bad overlap with photoinitiator) to a 320–390 nm (good overlap with photoinitiator) wavelength. The effect of about 10 J/g difference of reaction heat from these parameter groups is remarkable, so it is recommended that these influencing factors be regularly checked, for example, before and after each DLS printing process. A further reasonable consideration based on the results of this study is to consider the use of oxygen- and humidity-controlled printing environments for VPP technologies. In addition, the moisture absorption of the resins before printing should be avoided.

Although the chosen geometry of the pan is an influencing factor that is not transferable to DLS, it has been included in order to show that the method is robust against this influence. Given the reaction heat and the maximum heat flow rate of RPU 70, the selection of pans has a negligible influence. However, the choice between a *sfi* and *std* pan is significant for t_p . Therefore, kinetic investigations should always be performed using the same pan.

Furthermore, it was shown that this characterization procedure is also suitable for other photopolymer classes, such as EPX 82 (epoxy acrylate) and CE 221 (cyanate ester). These different vat photopolymerization resins display different evaporation behaviors. Therefore, it is recommended that the total reaction heat be corrected by taking the mass loss during the measurement into account. A pan correction for the total reaction heat values is also suggested. Finally, for future standardization of the photo-DSC for VPP applications, it is important to consider the conversion of light intensity.

ACKNOWLEDGEMENTS

The authors are grateful that the Technical University of Munich is bearing the costs of the article processing charge (APC), as TUM participates in the nationwide DEAL contract with the scientific publisher Wiley. Proofreading was sponsored by the TUM Graduate School and conducted by KERN Corporation. The authors would like to thank Johannes Roth from BMW's Thermal Analysis Lab, who helped set up the light intensity calibration. Finally, we would like to thank Opsytec Dr Gröbel GmbH and Qioptiq Photonics GmbH & Co. KG for providing the spectrum of the radiometer and the light source. Open Access funding enabled and organized by Projekt DEAL.

CONFLICT OF INTEREST

All the authors declare no conflict of interest.

CRediT STATEMENT

Joel Bachmann: conceptualization, formal analysis, investigation, writing – original draft, writing – review and editing, visualization, project administration. **Stefan Schmölder:** conceptualization, investigation, resources. **Matthias A. Ruderer:** conceptualization **Gabriele Fruhmann:** supervision. **Olaf Hinrichsen:** writing – review and editing.

DATA AVAILABILITY STATEMENT

The data that support the findings of this study are available from the corresponding author upon reasonable request.

ORCID

Joel Bachmann  <https://orcid.org/0000-0001-5416-6493>

Gabriele Fruhmann  <https://orcid.org/0000-0003-2993-6024>

REFERENCES

- [1] ISO 52900, *Additive manufacturing — General principles — Terminology* **2017**.
- [2] W. Wohlers, *Report 2019: 3D Printing and Additive Manufacturing State of the Industry*, Wohlers Associates, Fort Collins, CO **2019**.
- [3] J. Zhang, P. Xiao, *Polym. Chem.* **2018**, *9*, 1530.
- [4] G. A. Appuhamillage, N. Chartrain, V. Meenakshisundaram, K. D. Feller, C. B. Williams, T. E. Long, *Ind. Eng. Chem. Res.* **2019**, *58*, 15109.
- [5] X. Kuang, D. J. Roach, J. Wu, C. M. Hamel, Z. Ding, T. Wang, M. L. Dunn, H. J. Qi, *Adv. Funct. Mater.* **2019**, *29*, 1805290. <https://doi.org/10.1002/adfm.201805290>
- [6] M. Layani, X. Wang, S. Magdassi, *Adv. Mater.* **2018**, *30*, e1706344. <https://doi.org/10.1002/adma.201706344>
- [7] R. Berger, *Polymer Additive Manufacturing - Market Today and in the Future*, 2020, <https://www.rolandberger.com/en/Insights/Publications/Polymer-additive-manufacturing-Market-today-and-in-the-future.html#!#&gid=1&pid> (accessed: July 2021).
- [8] S. C. Ligon, R. Liska, J. Stampfl, M. Gurr, R. Mülhaupt, *Chem. Rev.* **2017**, *117*, 10212.
- [9] J. R. Tumbleston, D. Shirvanyants, N. Ermoshkin, R. Januszewicz, A. R. Johnson, D. Kelly, K. Chen, R. Pinschmidt, J. P. Rolland, A. Ermoshkin, E. T. Samulski, J. M. DeSimone, *Science* **2015**, *347*, 1349.
- [10] R. Januszewicz, J. R. Tumbleston, A. L. Quintanilla, S. J. Mechem, J. M. DeSimone, *PNAS* **2016**, *113*, 11703.
- [11] J. Bachmann, E. Gleis, G. Fruhmann, J. Riedelbauch, S. Schmölder, O. Hinrichsen, *Addit. Manuf.* **2020**, *37*, 101677. <https://doi.org/10.1016/j.addma.2020.101677>
- [12] P. Obst, J. Riedelbauch, P. Oehlmann, D. Rietzel, M. Launhardt, S. Schmölder, T. A. Osswald, G. Witt, *Addit. Manuf.* **2020**, *32*, 101002. <https://doi.org/10.1016/j.addma.2019.101002>

- [13] A. Redmann, P. Oehlmann, T. Scheffler, L. Kagermeier, T. A. Osswald, *Addit. Manuf.* **2020**, *32*, 101018. <https://doi.org/10.1016/j.addma.2019.101018>
- [14] J. Bachmann, P. Obst, L. Knorr, S. Schmölder, G. Fruhmann, G. Witt, T. Osswald, K. Wudy, O. Hinrichsen, *Commun. Mater.* **2021**, *2*, 107. <https://doi.org/10.1038/s43246-021-00211-5>
- [15] S. Asmussen, W. Schroeder, I. Dell'Erba, C. Vallo, *Polym. Test.* **2013**, *32*, 1283.
- [16] C. Esposito Corcione, M. Frigione, A. Maffezzoli, G. Malucelli, *Eur. Polym. J.* **2008**, *44*, 2010.
- [17] C. Esposito Corcione, G. Malucelli, M. Frigione, A. Maffezzoli, *Polym. Test.* **2009**, *28*, 157.
- [18] C. Esposito Corcione, A. Greco, A. Maffezzoli, *J. Appl. Polym. Sci.* **2004**, *92*, 3484.
- [19] C. Decker, *Acta Polym.* **1994**, *45*, 333.
- [20] C. Decker, T. Nguyen Thi Viet, D. Decker, E., *Polymer* **2001**, *42*, 5531.
- [21] B. Martin, J. Puentes, L. Wruck, T. A. Osswald, *Polym. Eng. Sci.* **2018**, *58*, 228.
- [22] J. Bachmann, E. Gleis, S. Schmölder, G. Fruhmann, O. Hinrichsen, *Anal. Chim. Acta* **2021**, *1153*, 338268. <https://doi.org/10.1016/j.aca.2021.338268>
- [23] P. Kardar, M. Ebrahimi, S. Bastani, *J. Therm. Anal. Calorim.* **2014**, *118*, 541.
- [24] M. C. Rusu, C. Block, G. van Assche, B. van Mele, *J. Therm. Anal. Calorim.* **2012**, *110*, 287.
- [25] C. A. Gracia-Fernández, P. Davies, S. Gómez-Barreiro, J. López Beceiro, J. Tarrío-Saavedra, R. Artiaga, *J. Therm. Anal. Calorim.* **2010**, *102*, 1057.
- [26] S. C. Ligon, B. Husár, H. Wutzel, R. Holman, R. Liska, *Chem. Rev.* **2014**, *114*, 557.
- [27] C. S. B. Ruiz, L. D. B. Machado, J. E. Volponi, E. S. Pino, *J. Therm. Anal. Cal.* **2004**, *75*, 507.
- [28] SDS Germany, RPU 70 Part A and B, Carbon Inc., Redwood City, CA 94063, USA, SDS Germany RPU 70 Part A and B **2017**.
- [29] SDS Germany, CE 221 Part A and B, Carbon Inc., Redwood City, CA 94063, USA, SDS Germany, CE 221 Part A and B **2017**.
- [30] SDS US, EPX 82 Part A and B, Carbon Inc., Redwood City, CA 94063, USA, SDS US EPX 82 Part A and B **2017**.
- [31] D. G. Archer, S. Rudtsch, *J. Chem. Eng. Data* **2003**, *48*, 1157.
- [32] F. Jiang, D. Drummer, *Polymers* **2020**, *12*, 1080. <https://doi.org/10.3390/polym12051080>
- [33] C. S. Sodr , P. P. A. Albuquerque, C. P. Isolan, R. R. Moraes, L. F. Schneider, *Int. J. Adhes. Adhes.* **2015**, *63*, 152.
- [34] B. Steyrer, P. Neubauer, R. Liska, J. Stampfl, *Materials* **2017**, *10*, 1445. <https://doi.org/10.3390/ma10121445>

SUPPORTING INFORMATION

Additional supporting information may be found in the online version of the article at the publisher's website.

How to cite this article: J. Bachmann, S. Schmölder, M. A. Ruderer, G. Fruhmann, O. Hinrichsen, *SPE Polym.* **2021**, *1*. <https://doi.org/10.1002/pls2.10063>

A.3. Investigation of the Temperature Influence on on a Dual Curing Urethane Methacrylate in Digital Light Synthesis (DLS)

Authors who contribute a journal article in an Elsevier Journal such as Additive Manufacturing do not need formal permission to reproduce the material contained in this article. The prerequisite is that the reproduced material is reproduced correctly.





Investigation of the temperature influence on the dual curing urethane-methacrylate resin Rigid Polyurethane 70 (RPU 70) in digital light synthesis (DLS)

Author: Joel Bachmann, Elisabeth Gleis, Gabriele Fruhmann, Julius Riedelbauch, Stefan Schmölzer, Olaf Hinrichsen

Publication: Additive Manufacturing

Publisher: Elsevier

Date: January 2021

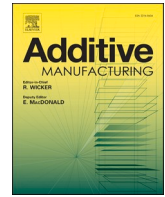
© 2020 Elsevier B.V. All rights reserved.

Journal Author Rights

Please note that, as the author of this Elsevier article, you retain the right to include it in a thesis or dissertation, provided it is not published commercially. Permission is not required, but please ensure that you reference the journal as the original source. For more information on this and on your other retained rights, please visit: <https://www.elsevier.com/about/our-business/policies/copyright#Author-rights>

[BACK](#) [CLOSE WINDOW](#)

© 2021 Copyright - All Rights Reserved | Copyright Clearance Center, Inc. | Privacy statement | Terms and Conditions
Comments? We would like to hear from you. E-mail us at customercare@copyright.com



Research Paper

Investigation of the temperature influence on the dual curing urethane-methacrylate resin Rigid Polyurethane 70 (RPU 70) in digital light synthesis (DLS)

Joel Bachmann^{a,b,*}, Elisabeth Gleis^{a,b}, Gabriele Fruhmann^a, Julius Riedelbauch^a, Stefan Schmörlzer^c, Olaf Hinrichsen^b

^a BMW Group FIZ, Knorrstraße 147, 80788 Munich, Germany

^b Technical University Munich (TUM), Department of Chemistry, Lichtenbergstraße 4, 85748 Garching, Germany

^c NETZSCH-Gerätebau GmbH, Wittelsbacherstraße 42, 95100 Selb, Germany



ARTICLE INFO

Keywords:

Dual curing resin
Thermal crosslinking
Post processing
Digital light synthesis (DLS)
Rigid Polyurethane 70 (RPU 70)

ABSTRACT

The two part urethane-methacrylate resin RPU 70, used in DLS, seems to have superior material properties. These properties are achieved by a dual curing process of ultraviolet (UV) and thermal curing. The temperature influence on the processability of the mixed resin and the resulting mechanical properties are still unknown. It was possible to solidify the liquid RPU 70 resin into an elastomer at 60 °C for 15 h without the influence of UV light by solely harnessing the temperature sensitive crosslinking reaction between part A and part B. The ongoing thermal conversion of the liquid resin into an elastomer was analyzed with viscosity measurements, Fourier-transform infrared spectroscopy (FT–IR), differential scanning calorimetry (DSC) and Photo-DSC. The latter method proved to be effective in tracking the thermal conversion and to identify optimal exposure times for preheated resins. Furthermore, thermogravimetric analysis (TGA) showed a linear evaporation of reactive diluents in RPU 70 over time. In order to investigate the processability and to understand the effects of the thermal curing on mechanical properties, the resin was preheated to 30 °C, 40 °C, 50 °C and 60 °C for one hour before the dual curing DLS process. Even though, the viscosity of the resin was increased by preheating and additionally by the released reaction heat of the photopolymerization during DLS, the build job could be produced with the same part quality as the unheated resin. Tensile tests were conducted on dual cured specimen and the results showed that with a preheating of the resin for one hour at 50 °C, the tensile modulus of RPU 70 increased 19.56%, while tensile strength and elongation at break values remained in the standard deviation range of the comparison group. The preheating at 60 °C improved elongation at break and tensile modulus 47.61% and 5.54% respectively, while at the same time tensile strength dropped –5.02% compared to no preheating. Apart from the possibility to slightly modify the mechanical properties by preheating the resin before DLS, there are two temperature-dependent challenges for RPU 70 during the DLS process, namely evaporation and undesirable thermal curing. However, there are also new innovative ways to utilize the result of this study that RPU 70 resin can be thermally solidified into an elastomer: the creation of parts that have a hard shell and a soft core. The hard shell can be produced by using DLS, the soft core by pouring the liquid resin in the shell and thermally curing both.

1. Introduction

In recent years photopolymers for vat photopolymerization technologies have seen a tremendous development in mechanical, optical,

chemical and thermal properties [1]. In 2016, they accounted for the largest share of total sales of AM products [2]. One of the more recent developed techniques is Digital Light Synthesis (DLS) (formerly known as Continuous Liquid Interface Production, i.e. CLIP) from Carbon, Inc.

Abbreviations: RPU 70, Rigid Polyurethane 70; DLS, digital light synthesis; TGA, thermogravimetric analysis; FT–IR, Fourier-transform infrared spectroscopy; DSC, differential scanning calorimetry; UV, ultraviolet.

* Corresponding author at: BMW Group FIZ, Knorrstraße 147, 80788 Munich, Germany.

E-mail addresses: joel.bachmann@tum.de, joel.bachmann@bmw.de (J. Bachmann).

<https://doi.org/10.1016/j.addma.2020.101677>

Received 24 July 2020; Received in revised form 16 October 2020; Accepted 19 October 2020

Available online 22 October 2020

2214-8604/© 2020 Elsevier B.V. All rights reserved.

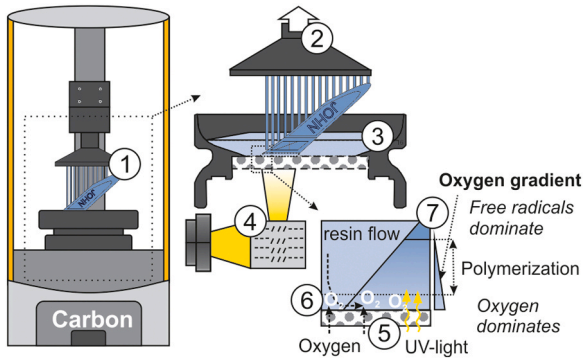


Fig. 1. Schematic illustration of DLS for the production of a personalized MINI side scuttle. ① Part with support structures ② Continuous elevating of the build platform ③ Cassette filled with liquid resin ④ DLP system ⑤ Oxygen and light permeable window ⑥ Oxygen “death zone” ⑦ UV-crosslinked part. End product can be seen in Fig. 2.



Fig. 2. Personalized MINI turn signal housing also known as side scuttle. Source: BMW press club [5].

(Redwood, CA). DLS basically works very similar to the bottom-up digital light processing (DLP) technology.

However, it differs in that not only light, but also oxygen passes through the window at the bottom of the resin cassette. This creates a so-called “dead zone” in which the polymerization is inhibited by the high oxygen concentration. As a result, the bottom layer does not polymerize and does not adhere to the window. Therefore, a continuous flow of resin into this “dead zone” is possible, enabling continuous, rather than layer-by-layer, production (see Fig. 1). This innovation allows much faster production times compared to conventional DLP, as the separation and realignment steps become obsolete [3,4]. Fig. 2.

Another not so well-known, but no less pioneering invention of carbon are the two-part, namely part A and part B, resin systems. These are initially mixed in a predefined mixing ratio and attain their dimensional stability through ultraviolet (UV)-curing during DLS. However, their final mechanical properties are reached by the sequential thermal curing in a convection oven. There, molecules from part A and part B, which require thermal activation, are crosslinking. In this research, this combination of UV- and thermal curing is called dual curing, as first described by Velankar et al., characterized by Decker et al. and later utilized by Rolland et al. for DLS [6–9]. A graphical scheme of the dual curing process is shown on the left side in Fig. 3, the right side explains the ongoing chemistry, which will be explained in the subsection 1.2 of this introduction. At this point, it is important to distinguish that the dual curing in this study does not relate to the combined UV-curing of epoxy-acrylate blends with different wavelengths [10], nor to the sequential curing of a two-part resin system, in which acrylates first react via an aza-Michael addition with amines before photopolymerization [11–13].

An advantage of the dual curing mechanism is that Carbon can offer a wide range of materials such as elastomer-like polyurethanes (e.g. EPU 40), epoxies (e.g. EPX 82), silicones (e.g. SIL 30), cyanate esters (e.g. CE 221) and rigid polyurethanes (e.g. RPU 70). On the other hand, one disadvantage is that the total processing time of these dual curing resins is increased by the additional thermal post-processing step in the oven that can take several hours to achieve complete cure. Redmann et al. demonstrated the possibility of reducing the thermal curing time of EPX

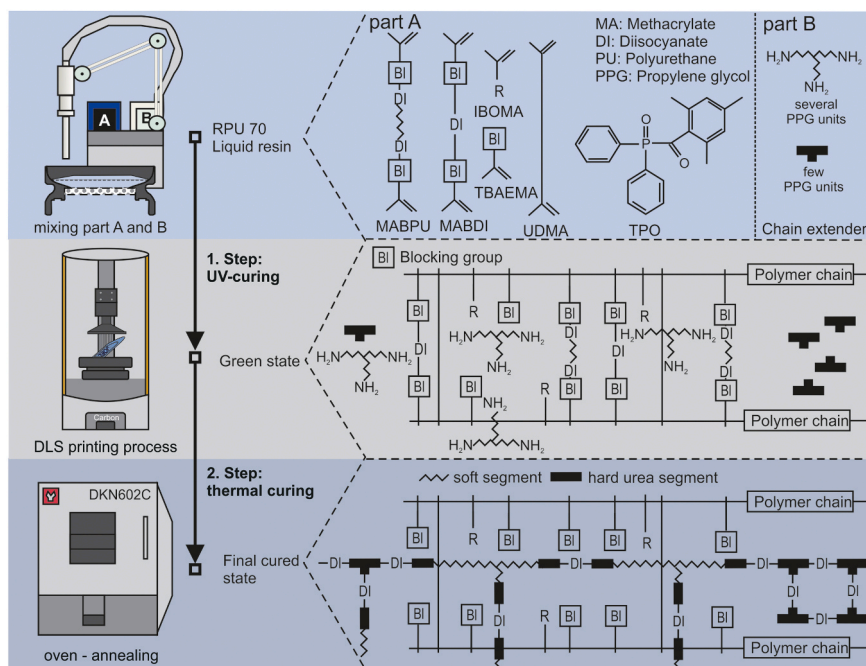


Fig. 3. Dual curing steps of Carbon’s two-part resin RPU 70 with the corresponding chemical compositions of the three different material stages. BI stands for the blocked urea group in the oligomers MABPU and MABDI and for the sterically hindered amine in the TBAEMA monomer. DI describes a molecule with two isocyanate groups. According to [8,9].

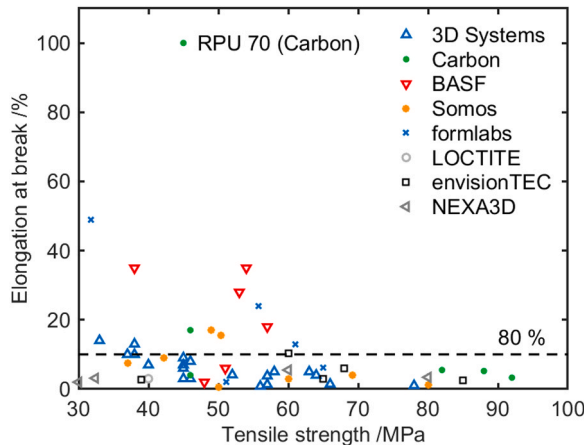


Fig. 4. Overview of tensile strength and elongation at break of commercially available 3D-printing photopolymers in the final state, which was compiled by a TDS screening in April 2020. Only materials with a tensile modulus over 1000 MPa are displayed. Values should be considered with the awareness that different machines and testing standards have been utilized.

82 with an optimized kinetics calculation by more than 9 h from 12.5 to 3.4 h, while achieving the same mechanical properties [14]. Nonetheless, the additional processing step might be the reason that the dual curing, two-part resins are almost unique to Carbon. Competitors try to meet the material requirements of the industries mainly with one-part resins, which are only UV-cured and occasionally subjected to a short UV-post cure in a UV-chamber in order to reach a higher degree of conversion of the UV-cured network. In processes where the final properties are reached after an AM post-process, the intermediate state is often referred to as a green state.

The overall challenge for AM photopolymers is to make the leap from prototyping to series production and to ensure highly consistent and reproducible properties. Despite good surface quality, a major challenge of photopolymers is their brittleness. As shown in Fig. 4, commercially available AM photopolymers have a tensile strength between 30 and 100 MPa, wherein in 80% of cases the elongation at break is less than 10%. Tough (i.e. tensile modulus above 1000 MPa) AM photopolymers are thermosets because they contain multifunctional molecules such as di- and tri(meth-)acrylates or epoxies, which form a tight thermoset network upon reaction. In contrast to thermoplastics with no crosslinking or elastomers, where the crosslinking density is very low, the

high crosslinking density of thermosets is the reason for high tensile strength and low elongation at break [15]. According to the technical data sheet (TDS), RPU 70 is a tough and rigid material that is a good choice for parts that require strength, toughness and moderate heat resistance [16]. The material exhibits properties comparable to conventional acrylonitrile butadiene styrene (ABS) plastic and was used by BMW for the production of personalized MINI side scuttles (see Fig. 2). RPU 70 was chosen because of its superior surface quality, while at the same time having good mechanical properties. Just like conventional thermoplastic polyurethanes (TPUs), RPU 70 also consists of hard and soft segments (depicted in Fig. 3 in the “final cured state”) [17]. Compared to elastomeric polyurethanes (EPUs) like EPU 40, the amount of hard segments is higher for RPU 70, which results in a far higher tensile modulus 1700 MPa > 8 MPa, tensile strength 35 MPa > 9 MPa but lower elongation at break 100% < 300% [16,18,19]. As depicted in Fig. 4, RPU 70 shows the highest elongation at break of 100%, i.e. the length of the sample has doubled at the time of breakage, of all commercially available AM photopolymers with a tensile modulus above 1000 MPa. This remarkable improvement in toughness is achieved by utilizing the dual curing reaction mechanism explained in Fig. 3 and subsection 1.2.

1.1. Research questions and objective

Reproducibility and process stability are imperative for a material to become a manufacturing standard. As described above, thermal curing and thus temperature is a decisive factor for dual curing resin systems. However, little is known so far about the consequences of increased temperatures, e.g. due to the strong exothermic reaction heat caused by the radical photopolymerization during DLS or higher room temperatures.

The following research questions arise:

1. Can the thermal curing be triggered with a preheating of the mixed resin before DLS?
 - a. If so, what happens to the viscosity, does the resin remain printable for DLS?
 - b. If so, which characterization methods can track the thermal curing reaction?
2. What happens to the material properties when the resin is preheated before DLS?

For the investigation of the temperature impact on processing RPU 70 in DLS and on the final mechanical properties the following

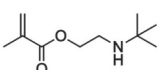
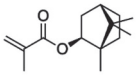
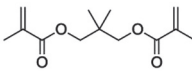
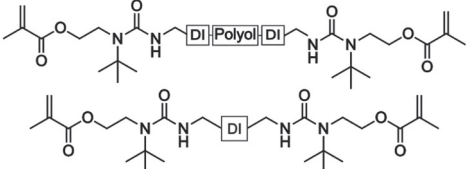
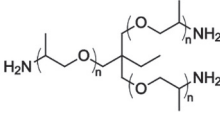
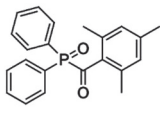
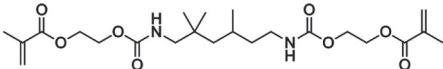
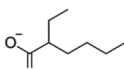
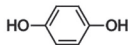
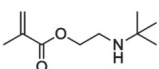
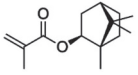
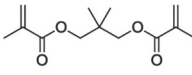
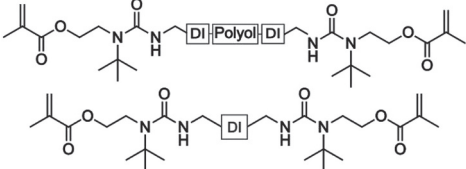
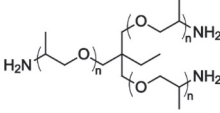
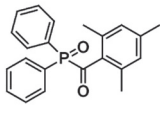
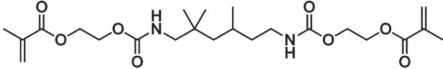
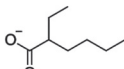
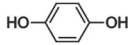
Table 1
RPU 70 components of part A and part B from safety data sheet (SDS) [22].

Short name	Full name	% in RPU 70	CAS-number	Category
RPU 70 part A (black color)				
TPO	Diphenyl (2,4,6 trimethylbenzoyl) phosphine oxide	0.1–2	75980–60–8	Photoinitiator
UDMA	Diurethane dimethacrylate	1–20	72869–86–4	Difunctional oligomer
MABPU and / or MABDI	Methacrylate Blocked Polyurethane/Diisocyanate	10–70	n.a.	Modified prepolymer synthesized with blocking units and diisocyanates.
IBOMA	Isobornyl methacrylate	10–50	7534–94–3	Reactive diluent – monomer
TBAEMA ^a	2-(tert-Butylamino)ethyl methacrylate	n.a.	3775–90–4	Reactive diluent – monomer and blocking unit in MABPU and MABDI
NPGDMA	Neopentylglycol dimethacrylate	<0.3	1985–51–9	Difunctional monomer
Tin catalyst ^b	Stannous octoate	0.1 – 0.3 ^b	301–10–0	Tin catalyst for MABPU and MABDI synthesis
Stabilizer ^b	Hydroquinone	100 – 500 ppm ^b	123–31–9	Stabilizes reactive methacrylates
Passive UV-absorbers	Sooth (black color)	n.a.	n.a.	Limit the UV-penetration depth and thus regulate the printing speed and part resolution
RPU 70 part B (colorless)				
Chain extender	Trimethylolpropane tris [poly (propylene glycol) amine terminated] ether	20 – 100	39423–51–3	Primary amine with repeating propylene glycol (PPG) units. Reacts with deblocked isocyanate during thermal curing

^a Has been found in RPU 70 part A via Quadrupole/time-of-flight mass spectrometer analysis see appendix Fig. A.2.

^b Not part of the SDS but related to the synthesis of the MABPU and MABDI [8,9].

Table 2
Chemical structure of molecules in RPU 70.

Molecules in RPU 70		
 TBAEMA	 IBOMA	 NPGDMA
 MABPU and MABDI	 Chain extender Sn ²⁺	 TPO
 UDMA	 Stannous octoate	 Hydroquinone
Molecules in RPU 70		
 TBAEMA	 IBOMA	 NPGDMA
 MABPU and MABDI	 Chain extender Sn ²⁺	 TPO
 UDMA	 Stannous octoate	 Hydroquinone

treatment sequence was applied to the resin:

1. Heat treatment of RPU 70 for 1 h at 30, 40, 50 and 60 °C
2. DLS with default print script on Carbon M1 printer
3. Default thermal curing profile (0.5 h ramp up from RT + 4 h at 120 °C)

Therefore, the objective of this paper is to characterize the influence of temperature on the dual curing resin RPU 70 via DSC, TGA, Photo-

DSC, viscosity and FT-IR analysis and to provide a deeper understanding of the chemical reaction mechanism of RPU 70 in the dual curing process. The latter is important in order to understand temperature dependent challenges during processing as well as to comprehend the new innovative way, in which RPU 70 might be utilized.

1.2. Reaction mechanism of RPU 70 during dual curing

In this subsection the reaction mechanism of RPU 70 in the dual

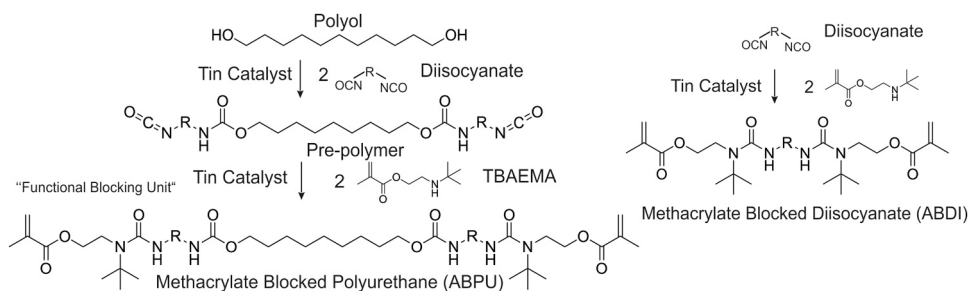


Fig. 5. Synthesis of MABPU and MABDI with two blocked isocyanate groups according to [8].

Table 3

Experimental set up with preheating of the mixed RPU 70 resin in an oven for one hour before DLS.

Experiment	Oven temperature
E1	Comparison group – no preheating
E2	30 °C
E3	40 °C
E4	50 °C
E5	60 °C

curing process is explained and can be followed with the right side of Fig. 3. The composition of RPU 70 is listed in Table 1, whereas Table 2 shows the chemical structure of the molecules.

The first step is the UV-initiated photopolymerization: UV-light causes a homolytic cleavage at the phosphor position of TPO. The photoinitiator (PI) breaks into two radicals. Preferably, the phosphonyl radical reacts with the vinyl double bond of the monomers and oligomers to form a polymer chain [20]. The small and low molecular weight molecules IBOMA, TBAEMA and NPGDMA are reactive diluents as they participate in the radical chain growth reaction and reduce the viscosity of the resin, which is important for the resin's reflow and thus for the printing speed and possible designable cross-sections. Difunctional molecules like NPGDMA, UDMA, MABDI and MABPU have two methacrylate groups at both ends and can thereby crosslink two polymer chains. Furthermore, they can rotate around the polymer chain axis and in this way create three dimensional crosslinks. TBAEMA is both a reactive diluent and the blocking unit of the MABDI and MABPU molecules to which it is connected by a blocked isocyanate group.

The centerpiece of the RPU 70 formulation is a confidential oligomer that participates in the UV- and thermal curing. In patent [8] three different types of oligomers are presented:

1. Methacrylate Blocked Polyurethane (MABPU)
2. Methacrylate Blocked Diisocyanate (MABDI)
3. Methacrylate Blocked Chain Extender (MABCE)

Through FT-IR analysis no methacrylates were found in part B of RPU 70, which contains the chain extenders, therefore the third possibility of MABCE oligomer can be dismissed. However, it is uncertain whether only MABPU, MABDI or a combination of both is used in RPU 70. MABPU and MABDI are special synthesized prepolymers that have two blocking units at both ends. They differ in the middle of the structure, where MABDI has only one diisocyanate and is therefore much shorter than MABPU. The central structure of the latter consists of a polyol and two diisocyanates. The synthesis can be seen in Fig. 5. The

characteristic group of MABPU and MABDI is the thermally labile, blocked urea bond with the blocking unit TBAEMA. High temperatures cleave this group and the deblocked isocyanate can react with the chain extender from part B to a crosslinked, thermoset polyurea within the UV-crosslinked network (see also appendix Fig. A.1) [6].

The trifunctional chain extender has primary amines at the end and repeating propylene glycol (PPG) units with different lengths in the middle. The chain extender has no reactive (C=C) double bond and thus cannot participate in the UV-curing reaction. During thermal curing, the primary amines of the chain extender react with the deblocked isocyanate of the MABPU and / or MABDI to a urea bond, which is thermally more stable than the previous urea bond.

Obst et al. observed with DSC that a shorter UV-exposure time increased the thermal curing reaction enthalpy of the UV-cured RPU 70 parts. In addition, the corresponding final parts showed a higher elongation at break at lower exposure times. In their study, tensile strength increased by more than 100% from green to final state for all exposure times. At the same time, the elongation at break of the final parts was 8–20% higher compared to the green parts, with the exception of the longest exposure time of 8 s, where the elongation at break decreased by –39.7%. [21].

The doubling of the tensile strength from the green to the final state indicates that the formation of the secondary polymer network, which is created by the thermal curing, further toughens the material. The already high elongation at break of around 70% for the green parts for all exposure times shows that a high elasticity is already produced during UV- and not only during thermal curing. Since the MABPU molecule is much larger than the MABDI molecule, the expected cross-linking density for MABPU after UV-curing is lower and the expected elongation at break is higher than for the MABDI molecule. Although a high elongation at break is an indication of the MABPU oligomer, it cannot be completely excluded that the MABDI oligomer or even a mixture of both oligomers is used.

2. Material and methods

The following Sections 2.1–2.9 describe the materials and methods used in this research.

2.1. Material

RPU 70 with its part A and part B and their corresponding components from Table 1 was used for all five experiments E1–E5 described in Table 3. The EQ MM38 Resin Mix System (MMD) from Henkel LOCTITE was used to mix the two parts. The mixing ratio was 10:1 (part A: part B),



Fig. 6. Build job of the 21 printed tensile specimen (ISO 3167 Type A) and specimen for Charpy impact testing (ISO 179-1eU) as a CAD file (a), in the M1 printer (b) and spread on a grid with parchment paper in a Yamato DKN612C oven (c) [23,24].

the flow rate was 180 ml/min and a total of 500 ml per print job was dispensed. The first 40 ml of mixed volume were disposed in order to rinse the MMD and achieve good mixing quality.

2.2. Build job setup

In order to investigate the influence of a preheated vat on tensile and impact strength, the print job from Fig. 6 is used. The build job includes 21 printed tensile specimen (ISO 3167 Type A) and specimen for Charpy impact testing (ISO 179-1eU) [23,24]. The latter were elevated on the build platform by support structures, so that the area of mechanical testing lies within the same build range for the two different specimen. The support structures were constructed densely and even overlapping, so that DSC samples could be cut from the extended centerline of the test specimens after DLS. The consecutive numbering from A1–C7 was used for evaluation purposes. The arrangement and numbering of the tensile specimen allows the build area position to be considered as well. Additionally, a large number of specimen per build job are required to achieve statistically representative data. The filling degree, which is defined as the ratio of printed volume to build area times the maximum z value of the print, is 12.67%. Although, Carbon already distributes M2 and L1 printers with larger build platforms 189 × 118 × 326 mm for the M2 and the L1 with five times the build area of the M2, a Carbon M1 printer with a maximum build volume of 141 × 79 × 326 mm is used. The cassette and build platform were cleaned with isopropyl before and after each build job.

2.3. Preheating the resin

In the comparison group (E1), the resin was not preheated (see Table 3). For the other experiments (E2–E5), 500 ml of RPU 70 was filled into a 1000 ml SCHOTT DURAN® beaker with an inner diameter of 105 mm and covered with a petri dish from DUROPLAN [25,26]. Afterwards, the beaker was placed for an hour in a preheated Memmert oven with fan level 5 [27]. Afterwards, the temperature of the resin was measured in the middle of the beaker with a Testo 905-T1 thermometer [28]. The surface-to-volume ratio SA/V (see Eq. (1)) can be calculated using the volume of resin in the cup V and the surface area SA , which is obtained from the inner diameter d of the beaker. The SA/V_{E2-E5} ratio for the resin in the beaker for the experiments (E2–E5) is 0.017.

$$SA/V = (d^2\pi/4)/V \quad (1)$$

2.4. Viscosity measurements

Viscosity measurements were carried out with the rectangular slit viscometer μ VISC™ with a C20 Chip from RHEOSENSE, INC. [29]. The width ($w = 2.31$ mm) of the flow channel is much greater than the depth $..$ and height ($h = 204.1$ μ m), so the flow effects from the edges of the channel are negligible. The geometry of the sensor also ensures a fully developed laminar flow and a linear pressure drop along the pressure sensor array. Thus, the sensor can be treated as an ideal two-dimensional system, and the viscosity can be calculated with the flow rate Q , the apparent shear rate $\dot{\gamma}_{app}$ and the shear stress τ according to Eq. (2) [30].

$$\eta = \frac{\tau}{\dot{\gamma}_{app}} \quad \text{with} \quad \dot{\gamma}_{app} = \frac{6Q}{wh^2} \tau = -slope \frac{wh}{(2w + 2h)} \quad (2)$$

For Newtonian fluids, the apparent shear rate does not need to be corrected and the automatic mode can be used, which used a shear rate of 59.6 s^{-1} and a flow rate of 57.5 μ L/min. The viscosity was measured three times in the vat before and after every print job. After three measurements, the flow channel was rinsed three times with acetone. In the DLS process the resin remains mainly unloaded and only minor shear stress occurs when the resin flows to the bottom of the vat. Additionally, for some print jobs the pumping mode can be activated, which consists of an up and down movement of the build platform in order to improve



Fig. 7. Thermal treatment with RPU 70 cartridge material, which was mixed with an Albion E18T400×10 Cartridge Gun from Albion Dispensing Solutions with a 10:1 ratio. The μ VISC™ pipette was filled and put in a preheated oven at 60 °C for various time lengths before different analysis were performed. UV-exposure was avoided during all stages of the experiment.

Table 4
Photo-DSC settings.

Photo-DSC testing device	NETZSCH 204 F1 phoenix
Light intensity – OmniCure® S2000 /(W/cm ²)	0.5
Wavelength filter	365 nm
Exposure time/s	180
Temperature/°C	30
Nitrogen flow /(ml/min)	20
Crucible	SFI
Correction factor	0.95
Sample weight/mg	3.5
Measurement per preheating time	1

the flow of the resin to the printing area. In this case the shear stress might also be increased.

2.5. DLS, cleaning and thermal curing

After preheating, the resin was filled into the thoroughly cleaned (IPA) cassette of the Carbon M1 and the build job began immediately afterwards. The default print script (April 2019) was used with a layer thickness of 100 μ m, 6.8 s exposure time and a light intensity of 9 mW/cm². The total printing time was 6:28 h. The SA/V_{DLS} ratio during DLS is approximately 22.278 for the required print job volume of 500 ml. The surface area for the resin changes over the course of the print job and was approximated with the print area of the M1 printer (141 mm × 79 mm).

After printing, the build job was left in the printer for a few more minutes so that excess resin could drain (see Fig. 6(b)). The entire build platform was then plugged into the Smart Part Washer from Carbon Inc., which operated in default wash mode with seven minutes of cleaning time. Two chemicals of the solvent inside the part washer are indicated: CAS 138495–42–8 and CAS 67–56–1. After washing, the tensile rods and support structures were removed with a scraper. All green parts were placed in a Yamato DKN612C oven on a grid with parchment paper (see Fig. 6(c)) [31]. Carbon’s recommended default curing cycle for RPU 70 was used: during the first 30 min, the oven heats up to 120 °C. After that, the temperature profile remains constant at 120 °C for four hours. All specimens were checked after thermal curing, wrapped and stored in a standard atmosphere for at least 24 h before mechanical testing.

2.6. Differential scanning calorimetry (DSC) of green parts and resin

5 mg of the densely packed support structures of the impact test specimen at position B4 was taken at a height of 25 mm, placed in an

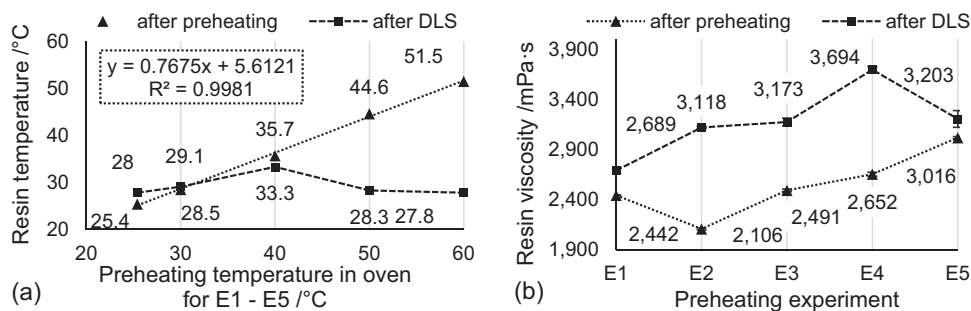


Fig. 8. (a) Temperature and (b) viscosity of the RPU 70 resin after preheating and after DLS for E1–E 5.

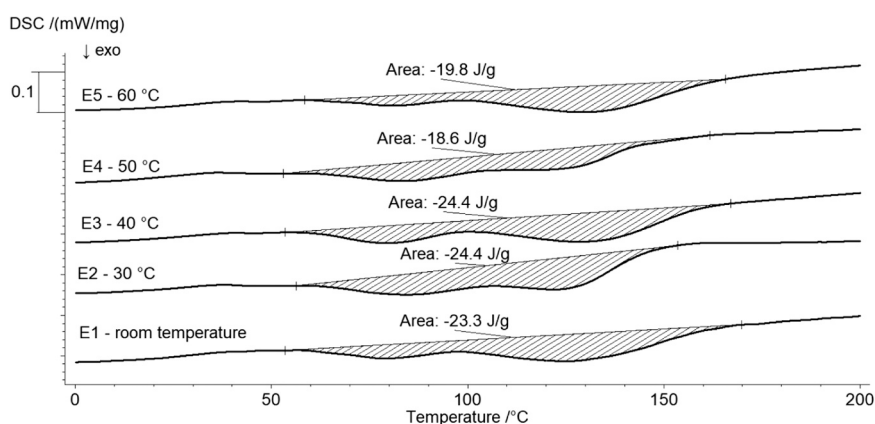


Fig. 9. DSC signal of first heating of UV-cured RPU 70 (green state) for the experiments E1–E5 with a heating rate of 10 K/min.

aluminum crucible with a pierced lid and analyzed using a NETZSCH DSC 204 F1 device [32]. The recorded temperature range was -80 – 220 °C with a heating and cooling rate of 10 K/min. The thermal response of the liquid RPU 70 and part A resin was determined by the mean of three first heatings with the same DSC device, heating rate and sample mass, but with closed, low pressure crucibles and a temperature range between 20 °C and 225 °C. A constant nitrogen flow of 20 ml/min was used for all DSC experiments.

2.7. Tensile and impact testing

For tensile testing a Zwick Roell Z020 machine was used with Type A tensile specimen geometry according to ISO 3167 [33,34]. First a test speed of 1 mm/min was used between 0% and 0.25% strain. The tensile modulus was calculated as the slope of the stress and strain curve according to ISO 527–1 between 0.05% and 0.25% strain [35]. Then, the test speed was increased to 50 mm/min because high nominal strain at break, later referred to as elongation at break, was expected and thus the time to reach the point of breakage was reduced with a faster testing speed. The tensile strength value is the stress at the first local maximum observed during the tensile test and the nominal strain was calculated without the aid of extensometers with method A from the tensile testing standard ISO 527–1 [35]. The testing climate was set according to ISO 291–23/50 (class 2) with $23 (\pm 2)$ °C and $50 (\pm 10\%)$ relative humidity [36].

Rectangular impact specimens with a length of $80.0 (\pm 2.0)$ mm, width of $10.0 (\pm 0.2)$ mm and a thickness of $4.0 (\pm 0.2)$ mm were used for the unnotched ISO 179–1eU impact testing [24]. An INSTRON® CEAST 9050 machine with a four-joule pendulum was used [37]. The testing climate conditions were the same as with the tensile testing.

In order to verify if the preheating of the resin has an effect on

mechanical properties via analysis of variance, the data set is first tested at normal distribution. The elongation at break values have to be transformed by Johnson Transformation in order to achieve normal distribution. In the Pearson correlation, these values are called elongation at break (JT) and are dimensionless. For the tensile strength values, an outlier was replaced by the mean value.

2.8. Thermogravimetric analysis (TGA)

A NETZSCH TG 209 F1 Libra was used in an isothermal experiment to see how much mass is lost due to evaporation [38]. Under nitrogen atmosphere, 10 mg RPU 70 was heated to 25 °C, 30 °C, 40 °C, 50 °C and 60 °C with a heating rate of 10 K/min. The total mass loss of the resin was calculated for one hour. The Al_2O_3 crucibles had an inner diameter of 6.8 mm. According to the TDS, the density of RPU 70 resin is 1.01 g/cm^3 [16]. Therefore, the surface-to-volume ratio for the TGA experiments SA/V_{TGA} , according Eq. (1), is 3.632, which is 210 times higher than SA/V_{E2-E5} and 163 times higher than the SA/V_{DLS} .

2.9. Thermal treatment of RPU 70 resin with viscosity, FT–IR and photo-DSC analysis

Since the change in viscosity from E1 to E5 can also derive from the evaporation of smaller molecules from the vat, the additional experiment shown in Fig. 7 was performed, in which the effect of evaporation was minimized. The surface-to-volume ratio was reduced by using the μ VISC™ pipettes with an orifice diameter of 0.8 mm, which were filled consecutively with approx. 300 μ L of the liquid resin Part A, Part B and RPU 70. Therefore, the surface-to-volume ratio for the μ VISC pipette experiment $SA/V_{\mu VISC}$ was approximately 0.002. Eq. (3) shows that the μ VISC pipette has the smallest surface-to-volume ratio of all

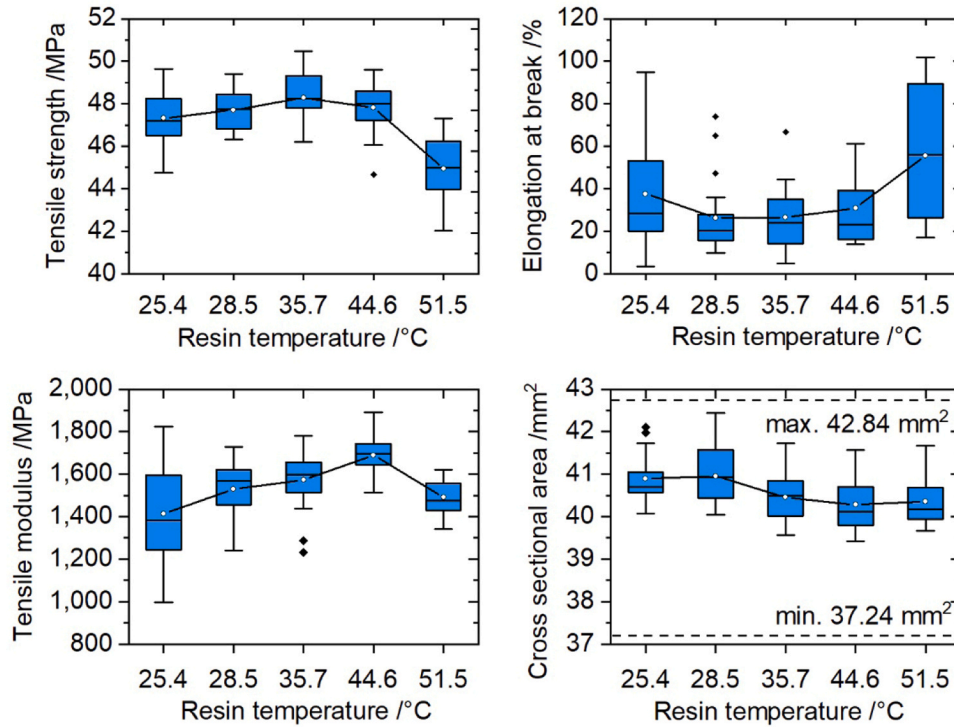


Fig. 10. Boxplots of tensile strength, elongation at break, tensile modulus and cross sectional area (solidified) in correlation with increasing preheating. Connecting line shows the mean development. Single dots indicate the outliers. Min. and max. (—) show the permissible cross sectional area according to ISO 3167 [23].

experiments. The viscosity measurements were carried out in the same way as described above in 2.4. In order to find the best method to track the thermal conversion in the resin, Photo-DSC measurements as well as FT-IR analysis were performed before and after the preheating. The settings for the Photo-DSC analysis can be seen in Table 4. The light intensity setting of 0.5 W/cm² was chosen because it is the lowest possible setting and nearly leads to a surface exposure intensity of 9 mW/cm², which is the light intensity during DLS. FT-IR analysis was conducted using 16 scans on an ATR-unit in the mid-infrared region on a Perkin Elmer Frontier device.

$$SA/V_{\mu\text{VISC}} < SA/V_{E2-E5} < \text{approx. } SA/V_{\text{DLS}} \ll SA/V_{\text{TGA}}$$

$$\text{approx. } 0.002 < 0.017 < \text{approx. } 0.022 \ll 3.632 \quad (3)$$

3. Results and discussions

3.1. Influence of preheating on viscosity, reaction heat and mechanical properties

3.1.1. Influence of preheating on resin temperature and viscosity

After preheating, the temperature of the resin rises linearly with increasing oven temperatures see Fig. 8(a). The viscosity of the resin decreases after preheating of 30 °C, but rises again above 30 °C see Fig. 8(b). In general, viscosity is a function of temperature, pressure, shear rate and molecule size distribution. When pressure and shear rate remain constant, higher temperatures usually reduce the viscosity of viscous photopolymers by increasing the mobility of the molecules [39]. Contrary to this expectation, the viscosity of RPU 70 increases at temperatures above 30 °C. There are two possible explanations for the behavior: first, the loss of small molecules by evaporation could change the resin composition to such an extent that it shifts the molecule size distribution to larger molecules, which would make the resin more viscous. Likewise, higher temperatures might start the thermal

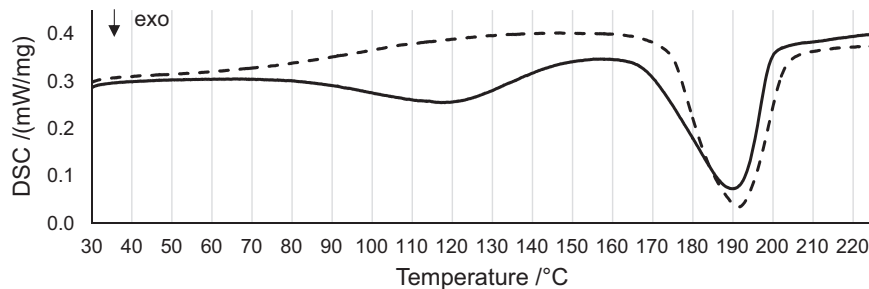


Fig. 11. Mean of three DSC measurements of first heating from RPU 70 resin (—) and part A resin (---) with a heating rate of 10 K/min. .

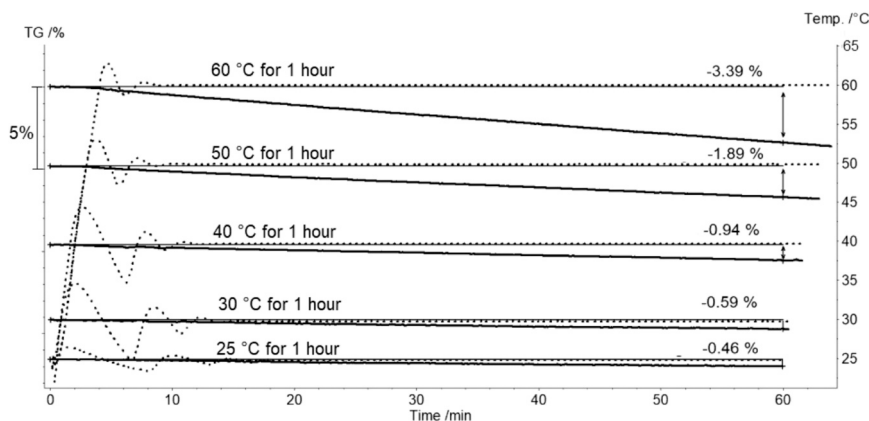


Fig. 12. Isothermal TGA of RPU 70 for one hour at different temperatures.

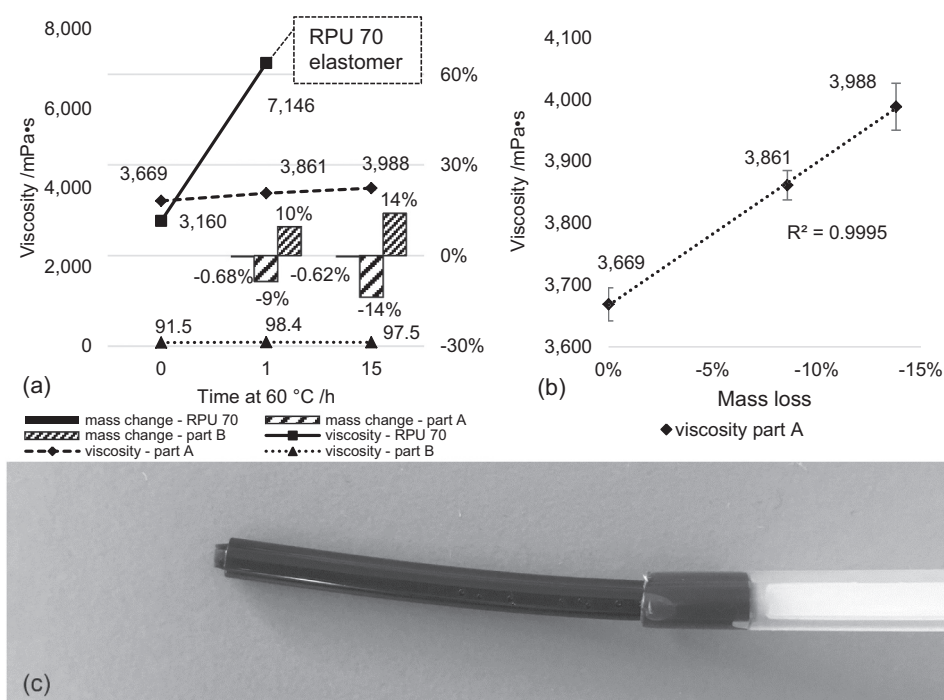


Fig. 13. (a) Viscosity and mass loss correlation to heat treatment of RPU 70, part A and part B. The mixing ratio of part A to part B in RPU 70 is 10:1. (b) Linear correlation of viscosity of part A with corresponding mass loss. (c) RPU 70 resin thermally solidified into an elastomer at 60 °C for 1 h and squeezed out of a μ VISC™ pipette. .

crosslinking reaction between part A and part B of RPU 70, which would also produce larger molecules and increase the viscosity. In order to investigate the main reason for the increased viscosity, the experiment described in Section 2.9 was added.

During the 6:28 h in which the build job is produced by DLS, the resin is expected to cool down to room temperature ($25.4 \text{ }^\circ\text{C} \pm 0.5 \text{ }^\circ\text{C}$). The latter remained constant throughout the day for all experiments. Yet, for all experiments, even for the comparison group E1, in which the resin was not preheated, the temperature of the resin after DLS is at least 2 °C warmer than room temperature (see Fig. 8(a)). Additionally, the viscosity after DLS is further increased for all experiments (see Fig. 8(b)). This means that the radical photopolymerization during DLS, which is very exothermic, constantly releases heat to the surrounding resin. Consequently, the temperature of the resin is increased, which causes the increase in viscosity, as described above.

At this point, the first part of the first research question from the

introduction can be answered (see 1.1): the viscosity of the resin is increased by preheating, however, all build jobs can be produced while the quality of the parts remains unchanged.

3.1.2. Influence of preheating on reaction heat of green state

Fig. 9 shows the DSC signal of the first heating of RPU 70 green parts after preheating and processing by DLS. The exothermic two-peak DSC signal consists of a smaller peak around 55–110 °C and an overlapping larger peak from 100 °C to over 150 °C. In order to interpret the DSC signal exhaustively, a lot of knowledge about the confidential resin composition and the reaction mechanism is required. Since this knowledge is not completely at hand, two possible interpretations for the two peaks remain: first, they might indicate the thermal crosslinking of two types of oligomers such as MABPU and MABDI, with the first reacting at lower and the second at higher temperatures. The second explanation for the two-peak DSC signal is that only one peak

Table 5
Molecule interactions in RPU 70 and their corresponding FT-IR signals.

Letter	Interaction	From/ cm ⁻¹	To/ cm ⁻¹	Peak/ cm ⁻¹	Reference
A, a	N-H stretching	3450	3200	3385	[40-42]
B, b	C=O stretching	1750	1678	1714	[40,41,43]
C, c,	C=O stretching urea	1679	1649	1658	[40,41]
D, d	(unbonded) C=C stretching	1649	1619	1637	[40,44]
	C=O stretching urea	1649	1619	1630	[40]
e	(bonded) N-H bending of primary amines	1677	1523	1591	[45]
E, f	Amide II vibration (C-N stretching combined with N-H bending)	1600	1471	1519	[41,43,46]
F	C-O stretching (ester)	1307	1281	1297	[47]
G, g	C-O-C stretching	1189	1132	1160	[43]
	C-O stretching (ether)	1132	1067	1109	[40,44,45]
H	Reference peak	1068	1029	1053	
J, h	C=C bending	830	796	814	[40,44,48]

characterizes the thermal curing and the other represents a post-polymerization of unreacted monomers. It is well known that conversion rates during photopolymerization do not reach 100% and some reactive molecules remain trapped in the UV-cured network. Heat exposure to the UV-crosslinked photopolymers can lead to higher degrees of conversion, as the mobility of the system is increased and thus enclosed reactive groups can proceed to polymerize and to crosslink.

The assumption for this experiment was that with a preheating at higher temperatures the thermal curing between part A and part B is

already triggered, which would reduce the exothermic DSC signal linked to the thermal crosslinking reaction. However, only a small decreasing trend with higher preheating temperatures is visible. The peak areas of E4 and E5 are both below -20 J/g and the strongest decrease in reaction heat can be observed from E3 to E4. Yet, the trend is not unambiguous, because the reaction heat from E4 to E5 slightly increases. This might also be due to the small deviations in the shape of the DSC signals, which influence the evaluated reaction heat.

3.1.3. Influence of preheating on mechanical properties

The results of the mechanical testing can be seen in the appendix Table A.1. Pearson correlation coefficients and p-values were calculated to determine which mechanical properties are most sensitive to the preheating of the resin, see appendix Table A.2. The Pearson correlation coefficient shows how strong the linear correlation between two parameters is (positive or negative) on a scale from -1-1. The corresponding p-value, if below 0.05 (bold number), determines the significance of the correlation. In terms of preheating the resin before the dual curing process, the test shows a medium, negative correlation of -0.434 with a high significance ($p = 0.000$) for tensile strength, a small, positive correlation of 0.239 ($p = 0.014$) for tensile modulus, a small, negative correlation of -0.387 ($p = 0.000$) for cross sectional area (solidified) and a small positive correlation of 0.261 with also a high significance ($p = 0.007$) for elongation at break (JT). For impact strength the effect can be neglected because the p-value is 0.985. Presented in a boxplot see Fig. 10 and Fig. A.3 for impact strength, these correlations become more obvious.

With a preheating of the resin for one hour at 50 °C, the tensile modulus of RPU 70 increases 19.56%, while tensile strength and

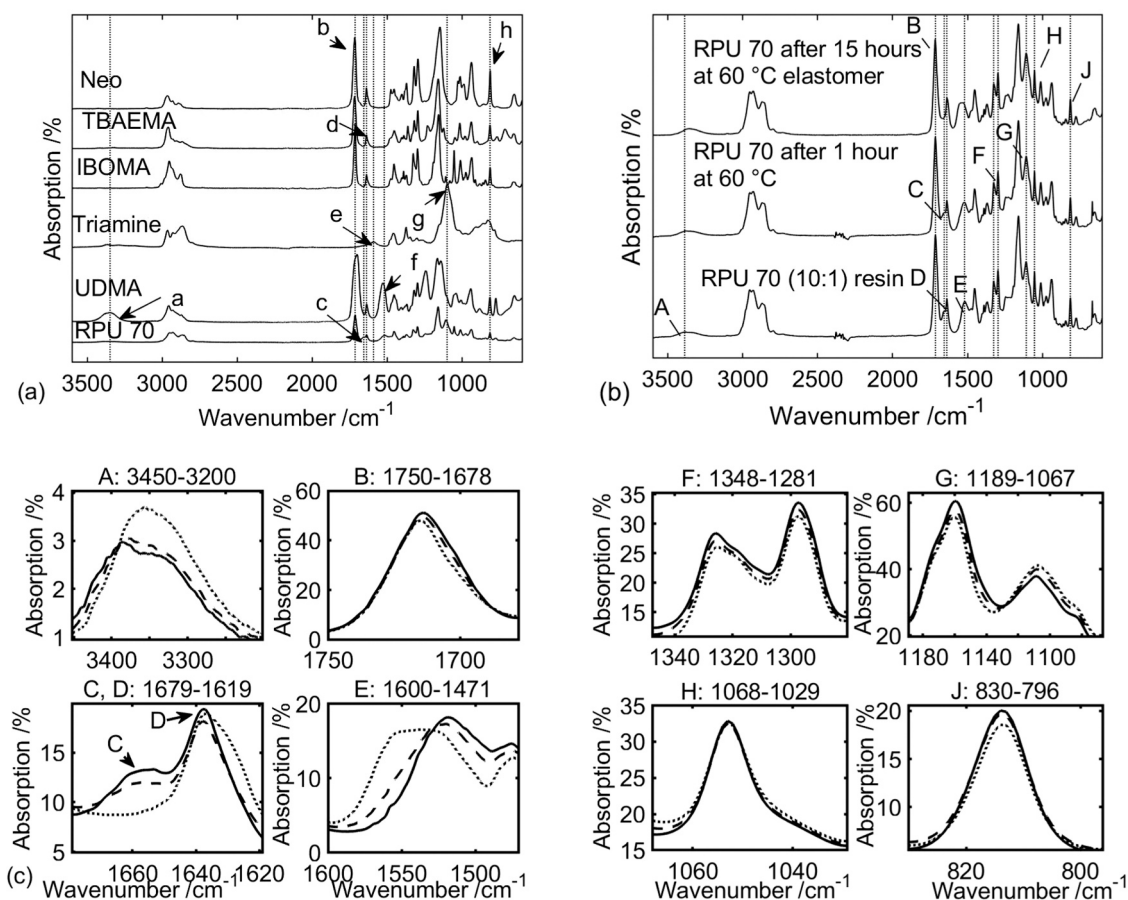


Fig. 14. (a) FT-IR spectra of RPU 70 and its components. (b) Temperature influence on RPU 70 FT-IR spectra. (c) Temperature influence on RPU 70 resin (—), heated for one hour at 60 °C (—) and RPU 70 heated for 15 h at 60 °C, which transformed into an elastomer (---).

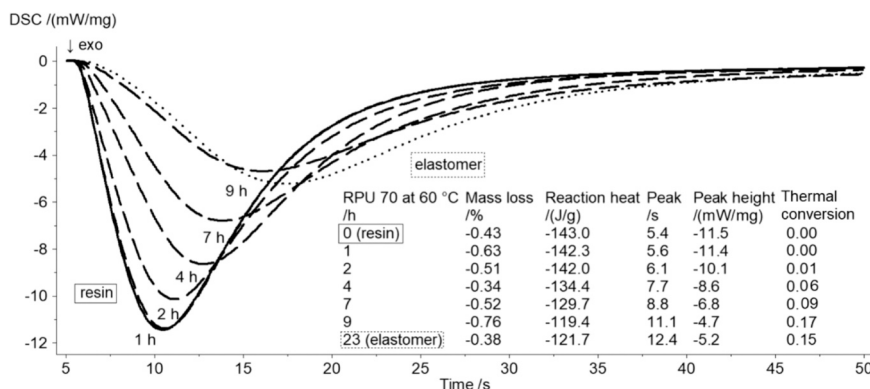


Fig. 15. Photo-DSC signals of the UV-curing reaction of RPU 70 resin (—), preheated for different times (—) at 60 °C. After 23 h at 60 °C the thermal cure transformed the resin into an elastomer with the dotted (···) UV-curing signal. Exposure starts after a 5 s offset. The thermal conversion is calculated by one minus the fraction of reaction heat at the corresponding preheating time to the reaction heat of the untreated resin (−143.0 J/g).

elongation at break values remained in the standard deviation range of the comparison group. The preheating at 60 °C improved elongation at break and tensile modulus 47.61% and 5.54% respectively, while at the same time tensile strength dropped −5.02% compared to no preheating. The biggest one time change in mechanical properties lies between E4 and E5, where tensile strength and modulus drop −6.02% and −11.72% respectively and elongation at break increases 79.61%. Since the resin has the highest viscosity after the E5 preheating (see Fig. 8(b)), the mobility of the molecules in the resin is impaired. The increased viscous behavior of the system worsens the formation of UV-crosslinks during the radical photopolymerization, which results in the above mentioned mechanical changes in the final part. Even though the viscosity after DLS for E4 is higher than for E5 (see Fig. 8(b)), the impact on mechanical properties is not as strong. Therefore, the effect of the viscosity of the resin at the beginning of DLS on the mechanical properties might be greater than the increase in viscosity caused by the heat release during DLS. The overall high deviations, especially for elongation at break, also compared to the TDS values, are mainly due to sample position in the build area, see appendix Fig. A.4.

3.2. Influence of temperature – characterization methods

3.2.1. DSC of RPU 70 and part A resins

Fig. 11 shows the first heating from RPU 70 and part A resin. For both resins, the DSC signal shows a very strong exothermic reaction of comparable size around 190 °C. This might indicate a thermal activation of the radical polymerization. The first exothermic effect of RPU 70 resin between 50 °C and 160 °C is not seen in the DSC signal of part A. This means that the thermal effect only takes place when part A and part B are present at the same time, which clearly indicates the thermal crosslinking. It also shows that the thermal crosslinking in the resin is represented as a single exothermic peak. Furthermore, the peak maximum is at 120 °C, which is also the peak maximum of the second peak of the UV-cured RPU 70 parts from Fig. 9. This means that the two-peak DSC signal from Fig. 9 can be further interpreted: the second peak can be clearly attributed to the thermal crosslinking. The first peak is unique to the green state. This might indicate that the thermal curing requires an additional step in the green state compared to the resin. Another assumption is that the first peak does not characterize the thermal curing but a thermal post-polymerization of unreacted monomers that have not reacted during UV-curing.

3.2.2. Isothermal TGA of RPU 70 for one hour at different temperatures

The isothermal TGA analysis from Fig. 12 shows how much mass RPU 70 loses within an hour at different temperatures. The mass loss is

linear for each temperature and can be attributed to the evaporation of smaller molecules. The total mass loss within one hour almost doubles for every temperature increase of 10 °C. The mass loss for preheating the resin in the oven and during DLS can be estimated lower, since the surface-to-volume ratio for the TGA tests is significantly greater (compare Eq. 3). Appendix Table A.3 shows the vapor pressure for the components of RPU 70 at 20 °C and 25 °C. The reactive diluent IBOMA and TBAEMA have the highest values with 7.5 Pa at 20 °C and 12 Pa at 25 °C and 5.986 Pa at 20 °C respectively. In an additional experiment, the evaporation gases of RPU 70 at 35 °C were analyzed using gas chromatography mass spectrometry (see appendix Fig. A.5), where fragments of IBOMA and TBAEMA were found. Therefore, it can be concluded that the mass loss is mainly caused by the evaporation of the volatile monomers IBOMA and TBAEMA.

3.2.3. Temperature-viscosity correlation of RPU 70, parts A and B without UV-curing

Fig. 13 shows the results for a thermal curing without UV-influence, as described in Section 2.9. The viscosity of the RPU 70 resin more than doubles from 3160 mPa·s to 7146 mPa·s with only one hour at 60 °C, while mass loss remains below 1%. Thus, the viscosity increase results from the ongoing thermal curing rather than from evaporation. After 15 h, the viscosity of RPU 70 could no longer be measured, as the thermal curing widely crosslinked the resin into an elastomer without any residual liquid resin.

Despite the very low surface-to-volume ratio for the μ VISC™ pipettes, the mass change for part A and B was very high compared to the RPU 70 mixture. The viscosity of part A shows a linear correlation with the corresponding mass loss. In this case, the increase in viscosity can be attributed to the evaporation of the volatile monomers TBAEMA and IBOMA. The same experiment with part B shows a mass increase. The polar primary amines of the chain extender probably cause water absorption from air humidity. This hydrophilic behavior of part B was verified by weighing 2.143 mg in a DSC crucible. After one hour at room temperature the sample mass increased by 3.78% to 2.224 mg.

3.2.4. Tracking the thermal conversion via FT-IR

The molecular interactions and the corresponding wavelength signals for RPU 70 are summarized in Table 5. There are two ways to identify the ongoing thermal curing of RPU 70 using FT-IR analysis:

1. The decrease of the (N–H) bending of the primary amines of the chain extender at 1591 cm^{-1} .
2. Conversion of the blocked urea group of MABPU and or MABDI to the unblocked urea group with chain extender.

3. The frequency shift of (N–H), (C=O) and (C–O–C) groups due to different hydrogen bridge bonds in RPU 70 resin and elastomer.

In Fig. 14(a), the (N–H) bending (ϵ) of the primary amines of the chain extender is not visible in the RPU 70 spectrum. This might be due to the small amount of part B in the mixed resin. Therefore, the conversion cannot be tracked by the first option. The second possibility is even harder to detect because the blocked and unblocked urea groups have almost identical chemical structures namely (–NH–CO–NC–) and (–NH–CO–NH–) respectively.

However, there is third indicator of conversion: the urethane and urea groups, which have a hydrogen bridge bond, are identified by a frequency shift to lower frequencies, compared to those that do not have a hydrogen bridge bond [40,49]. Therefore, the shift in (N–H) stretching (A) in Fig. 14(b) and (c) to lower wavenumbers might be due to the increased formation of unblocked urea groups, since these can better form hydrogen bridge bonds than blocked urea groups. The peak at 1658 cm^{-1} (C) might indicate the H-bond free (C=O) stretching of the blocked urea group, which is reduced by thermal curing. The steric hindered urea group might not be able to form hydrogen bonds in the resin. Furthermore, the shoulder at (D) that is only visible for the elastomer, might indicate the formation of hydrogen bridge bonded (C=O) stretching of the unblocked urea. The carbonyl (C=O) group of the urethanes and methacrylates (B) is reduced and shifts to higher frequencies, which indicates fewer hydrogen bridge bonds. Since, hydrogen bridge bonding is competitive between (C=O) and (C–O–C) towards (–N–H) (see also appendix Fig. A.6), the decrease might derive from the rise of the (C–O–C) stretching at 1109 cm^{-1} (G) in the elastomer [40].

Since, the shoulder at 1630 cm^{-1} is overlapping with the (C=C) stretching vibration (D) at 1637 cm^{-1} , the double bond conversion (DBC), according to Eq. (4), is calculated with the peak height of the (C=C) bending (J) at 814 cm^{-1} and is corrected with the reference peak height (H) at 1053 cm^{-1} . The DBC after 1 and 15 h is 0.69% and 6.53% respectively. There are two possibilities for the intensity of the (C=C) bond to decrease: First the (C=C) bonds either react with each other, or with the primary amines of the chain extender in an Aza-Michael addition as described by González et al. and Konuray et al. [11–13]. Secondly, volatile methacrylates might evaporate and thus decrease the overall (C=C) concentration. For the first hour at $60\text{ }^\circ\text{C}$ the 0.68% mass loss correlates perfectly with the 0.69% DBC. However, for 15 h at $60\text{ }^\circ\text{C}$ the mass loss remains at low 0.62% while DBC increases to 6.53%.

$$DBC_t = \left[1 - \frac{(\text{peakheight}_{814}/\text{peakheight}_{1053})_t}{(\text{peakheight}_{814}/\text{peakheight}_{1053})_0} \right] \cdot 100\% \quad (4)$$

3.2.5. Tracking the conversion via photo-DSC

In Fig. 15 the influence of thermal curing on the radical polymerization becomes visible. The reaction heat of the elastomer is only reduced by 15% compared to the RPU 70 resin while the mass loss remains constant below 1%. The loss of reaction heat therefore does not result from a higher degree of evaporation of the reactive diluents, but from a mobility restriction due to the increasing thermal crosslinking, which is made visible by the flattening of the curve and the increased time to reach the peak maximum. The results show that the elastomer can still be UV-cured, but longer exposure times are required to attain the maximum reaction rate. To process preheated RPU 70 resin, the results could be useful to adjust the exposure time during DLS to ensure complete UV-curing.

4. Conclusions

One of the main observations of this research is that the viscosity of the RPU 70 resin increases with higher temperatures. At first, this phenomenon seems counterintuitive, as higher temperatures are often used to reduce the viscosity of one part resin systems like for example in Hot-Lithography [50]. Similarly, for one of the latest, double-curing materials of carbon, namely RPU 130, which is also the successor of RPU 70, a heatable cassette is used to improve the processability by reducing the viscosity. Carbon's unique dual curing resins are first UV-cured in DLS and then thermally cured in a post-process. Thermal curing causes a crosslinking between part A and part B. This crosslinking can already take place in the liquid resin and is the reason for the increased viscosity with rising temperatures (see Fig. 8(b)). In order to confirm the assumption that the increased viscosity results from the thermal crosslinking reaction and does not derive from the evaporation of the reactive diluents, Fig. 13(a) shows that even with a mass loss $<1\%$, the viscosity of RPU 70 more than doubles after one hour at $60\text{ }^\circ\text{C}$. Consequently, the increase in viscosity can be attributed to the crosslinking reaction. Usually, low viscosities are intended because the resin reflow becomes faster and thus printing time can be reduced. This consideration is more important for print jobs with big cross-sections, where the reflow of the resin to the middle takes longer than for lattice structures that have only small cross-sections. Moreover, photopolymerization during DLS generates reaction heat, which is released into the surrounding resin. For a 6:28 h build job, this increases the temperature of RPU 70 by more than $2\text{ }^\circ\text{C}$ and the viscosity, even if RPU 70 is not preheated, by 10% (see Fig. 8(a)). Especially for big cross-sections, in which large areas are irradiated, a lot of reaction heat is generated. In these places, the thermal crosslinking is already taking place and the viscosity increase could be even higher. This study shows that RPU 70 resin can be preheated for one hour at $60\text{ }^\circ\text{C}$ and that the increased viscosity, after preheating and DLS, does not negatively affect the print quality of the test specimen from Fig. 6.

In general, this study shows that the mechanical properties can be adjusted by processing RPU 70 with the curing order: thermal–UV–thermal (see Fig. 10). The biggest change in mechanical properties lies between E4 and E5, where the material becomes more viscoelastic: tensile strength and modulus drop -6.02% and -11.72% respectively and elongation at break increases 79.61%. An important criterion that determines whether a photopolymer becomes brittle or viscoelastic is the UV-crosslinking density produced during photopolymerization [15]. Therefore, the changes in mechanical properties between E4 and E5 indicate that the increased viscosity due to the ongoing thermal curing impairs the crosslinking mechanism that takes place during photopolymerization. Furthermore, the effect of higher viscosities at the beginning of DLS on the mechanical properties seems to be bigger than the effect of increased viscosities caused by the heat release during DLS (compare Fig. 8(b) and Fig. 10). Moreover, Fig. 15 shows that a preheating of more than one hour at $60\text{ }^\circ\text{C}$ flattens the photo-DSC signal and shifts the reaction maximum to higher exposure times. Hence, preheated resins might require different exposure parameters such as longer exposure times and higher light intensities to achieve the same UV-crosslinking densities as an untreated resin.

The ongoing thermal curing with higher preheating temperatures is not so clearly visible for the two-peak exothermic DSC signals from Fig. 9 compared to the viscosity measurements from Fig. 8(b). Nevertheless, a small decreasing trend with higher preheating temperatures is recognizable. Furthermore, the first exothermic DSC signal of the RPU 70 resin from Fig. 11 with the peak maximum at $120\text{ }^\circ\text{C}$ clearly characterizes the thermal curing reaction between part A and part B in the

resin, since this peak is not visible in the DSC signal of part A.

It is concluded that the change in material properties is largely due to ongoing thermal curing and that the evaporation of the volatile components IBOMA and TBAEMA plays only a minor role. The reason for this consideration is that the surface to volume ratio for TGA is 210 and 163 times higher than for DLS and the experiments (E2–E5) respectively. Thus, the evaporation of the reactive diluents during DLS and the experiments (E2–E5) is likely to be much lower than for the TGA shown in Fig. 12. However, evaporation plays a central role for all characterization methods such as DSC, FT–IR and viscosity measurements. Therefore, the mass loss should always be taken into account.

The liquid resin solidified into an elastomer after 15 h at 60 °C without UV-irradiation. This conversion from liquid resin to widely crosslinked elastomer was best tracked via Photo-DSC (see Fig. 15). The flattening of the exothermic UV-curing reaction peak from resin to elastomer indicates the formation of the thermally cured network. The FT–IR analysis of RPU 70 from Fig. 14 and of the individual components shows the high proportion of different methacrylates, but the overlapping effect of different molecules in the FT–IR makes it difficult to track the thermal curing.

5. Outlook

In order to achieve high process stability and production standards, this study concludes that for dual curing DLS resin systems such as RPU 70 methods and means need to be investigated to monitor, control or eliminate the chain extension reaction and the evaporation of the reactive diluents. For the latter two possible solutions might be applying a separating agent on the resins surface or to use pressurization. An

innovative application of the results of this study could be the creation of parts that have a hard shell and a soft core. The hard shell can be produced by using DLS, the soft core by pouring the resin in the shell and thermally curing both.

Declaration of Competing Interest

The authors declare that they have no known competing financial interests or personal relationships that could have appeared to influence the work reported in this paper.

Acknowledgements

The authors acknowledge the provided proofreading services sponsored by the TUM Graduate School, which was carried out by Kern. Additionally, the authors are thankful for Martin Friedrich at the BMW Additive Manufacturing Center for providing the necessary printer and material, as well as Johannes Roth and Birgit Hoenisch at the thermal analysis lab at BMW for providing the TGA.

Conflict of interest

This research did not receive any specific grant from funding agencies in the public, commercial, or not-for-profit sectors.

Appendix

See Figs. A1–A6 and Tables A1–A3.

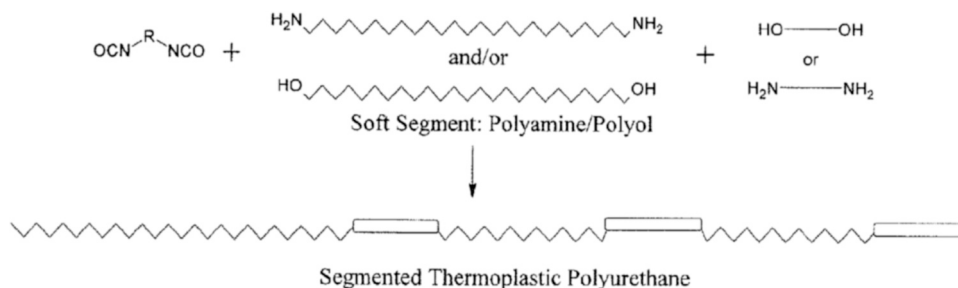


Fig. A.1. Synthesis of a segmented thermoplastic polyurethane and polyurea with soft and hard segments [8].

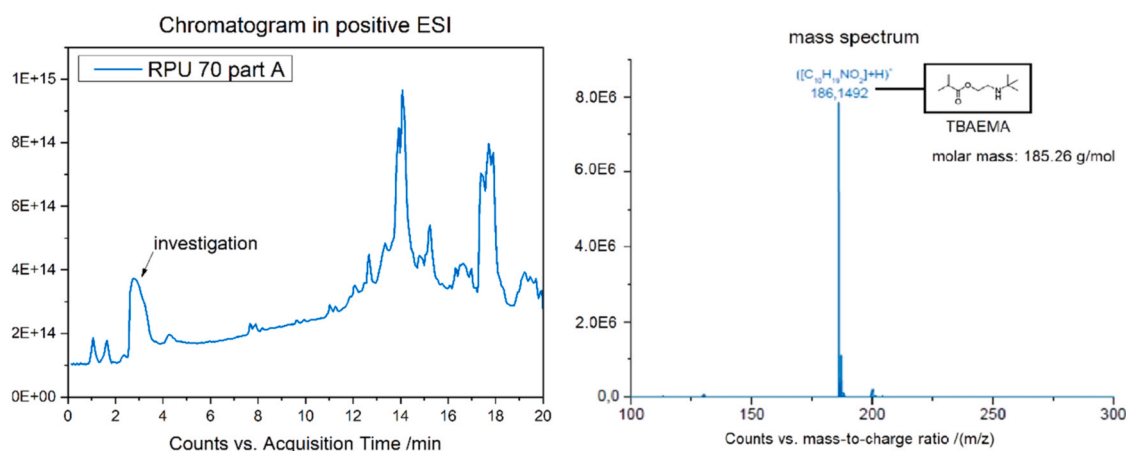


Fig. A.2. Quadrupole/time-of-flight mass spectrometer analysis of RPU 70 part A in positive Electrospray Ionization (ESI). Peak at around 3 min acquisition time in chromatogram indicates a protonated molecule with a molecular weight of 186.1492. Subtracted by the proton, the number is close enough to verify the molecular weight of TBAEMA 185.26 g/mol.

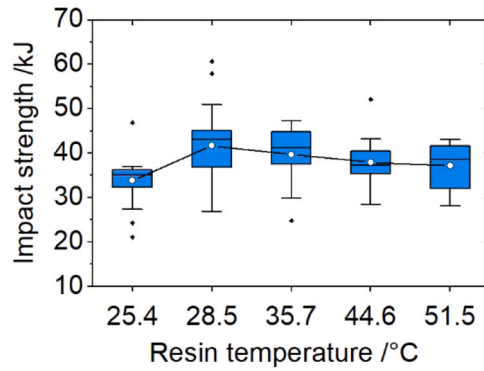


Fig. A.3. Boxplots of impact strength in correlation with increasing preheating temperatures. Connecting line shows the mean development. Single dots indicate the outliers.

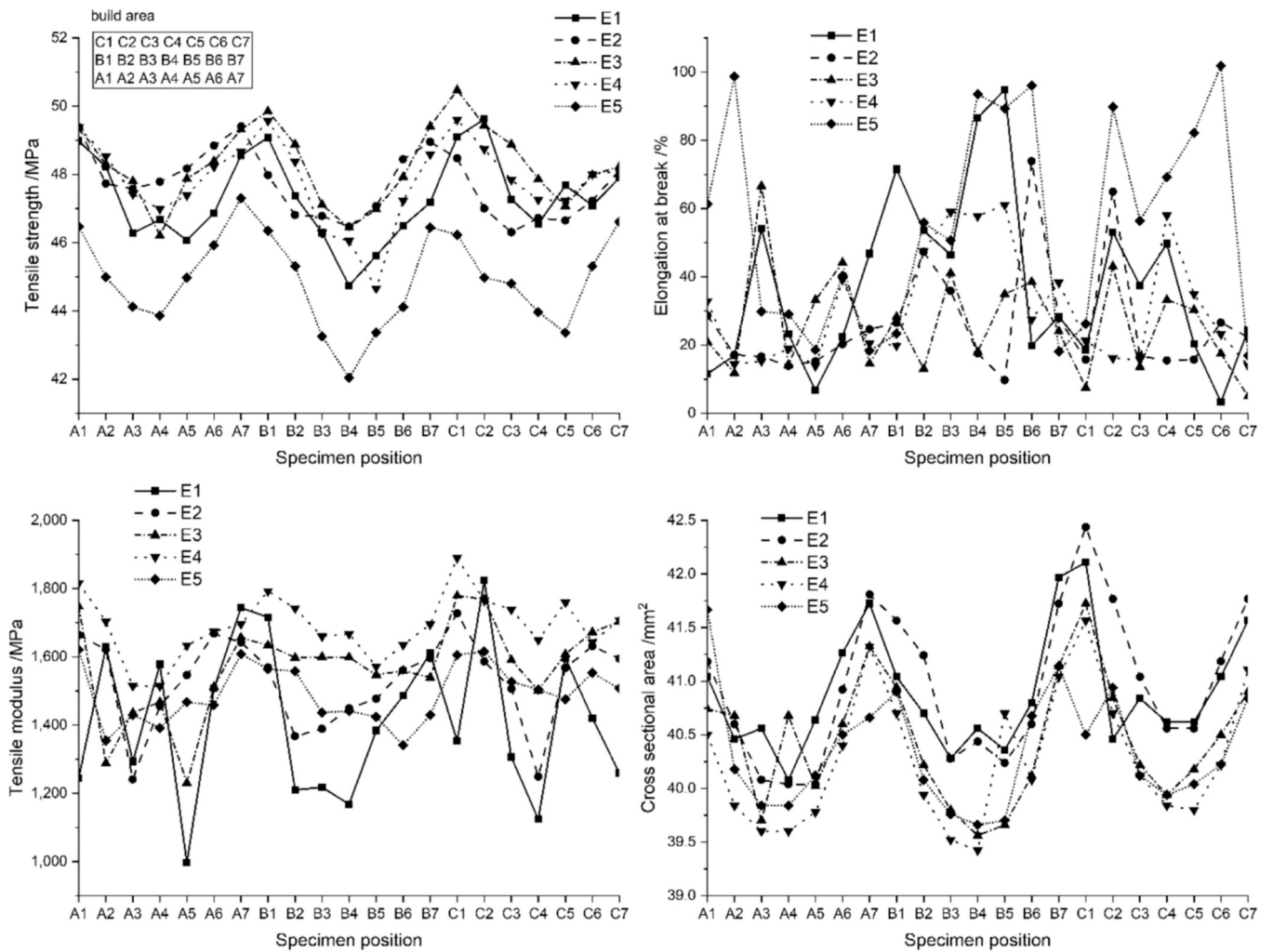


Fig. A.4. Mechanical properties in correlation to specimen position in the build area for all five experiments with different preheating temperatures.

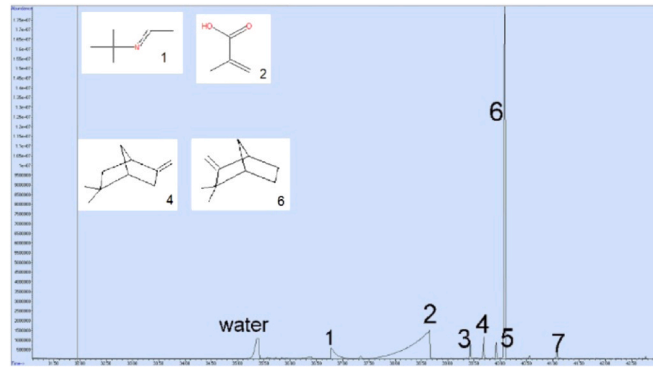


Fig. A.5. Fragments of IBOMA and TBAEMA Monomers found in the vapor of RPU 70 at 35 °C analyzed via gas chromatography mass spectrometry.

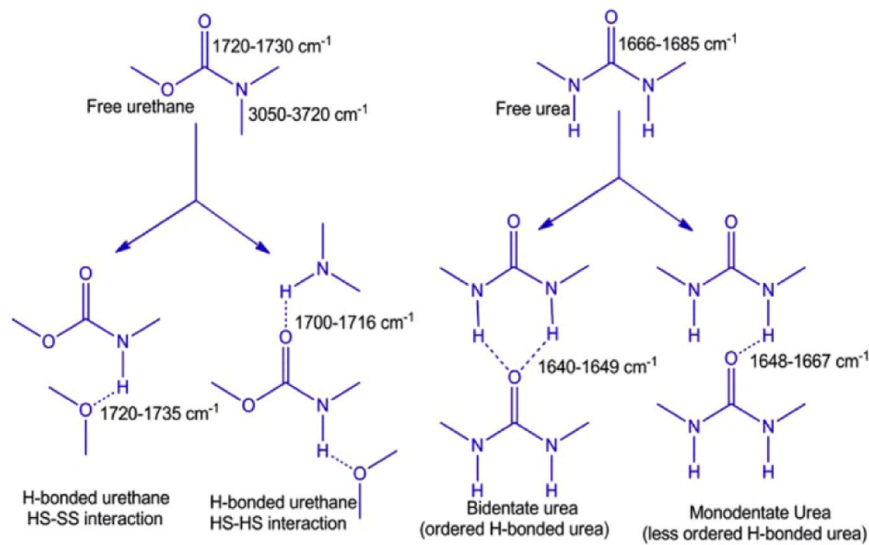


Fig. A.6. The different types of hydrogen bonding for urethane and urea [49].

Table A.1
Mechanical properties of RPU 70 after preheating of the resin, DLS and thermal curing.

Variable	Resin temperature/°C	N	Mean	StDev	Minimum	Median	Maximum
Tensile modulus/MPa	25.4	21	1412.7	224.6	996.9	1383.9	1823.7
	28.5	21	1529.0	131.8	1240.9	1567.5	1727.2
	35.7	21	1573.2	140.0	1230.3	1598.0	1779.6
	44.6	21	1689.0	92.1	1514.0	1695.1	1889.7
	51.5	21	1491.1	85.2	1340.6	1475.2	1620.9
Tensile strength/MPa	25.4	21	47.316	1.272	44.741	47.176	49.620
	28.5	21	47.709	0.963	46.308	47.733	49.408
	35.7	21	48.276	1.137	46.214	48.233	50.471
	44.6	21	47.816	1.214	44.659	48.005	49.603
	51.5	21	44.941	1.371	42.039	44.972	47.300
Elongation at break/%	25.4	21	37.60	25.31	3.26	28.34	94.86
	28.5	21	26.30	16.71	9.67	20.26	73.85
	35.7	21	26.35	15.17	4.94	24.04	66.53
	44.6	21	30.90	16.81	13.83	23.20	61.08
	51.5	21	55.50	31.21	16.95	55.90	101.88
Cross sectional area (solidified)/mm ²	25.4	21	40.892	0.555	40.079	40.700	42.110
	28.5	21	40.956	0.695	40.039	40.922	42.437
	35.7	21	40.452	0.583	39.561	40.500	41.725
	44.6	21	40.276	0.628	39.422	40.120	41.566
	51.5	21	40.349	0.536	39.661	40.179	41.666
Impact strength/kJ	25.4	20	33.89	5.34	21.07	35.08	46.83
	28.5	21	41.63	8.92	26.79	43.11	60.61
	35.7	21	39.70	5.97	24.80	41.21	47.26
	44.6	21	37.95	4.72	28.34	37.22	52.04
	51.5	21	37.15	4.94	28.17	38.62	43.00

Table A.2

Pearson correlation with p-value of mechanical properties and resin temperature. Cell contents: Pearson correlation (up) and p-value (down).

	Tensile modulus	Tensile strength	Cross sectional area (solidified)	Elongation at break (JT)	Impact strength
Tensile strength	0.462 0.000				
Cross sectional area (solidified)	0.130 0.187	0.436 0.000			
Elongation at break (JT)	-0.068 0.488	-0.429 0.000	-0.206 0.035		
Impact strength	0.124 0.210	0.130 0.189	-0.076 0.444	-0.087 0.377	
Resin temperature	0.239 0.014	-0.434 0.000	-0.387 0.000	0.261 0.007	-0.002 0.985

Table A.3

Vapor pressure according to the European Chemicals Agency.

Molecule	20 °C	25 °C
Jeffamine T403 (Chain extender)	0.002 Pa	0.004 Pa
UDMA	0 Pa	0 Pa
TBAEMA	5.986 Pa	-
IBOMA	7.5 Pa	12 Pa
TPO	0 Pa	0 Pa
Stannous octoate	0.3 Pa	-

References

- [1] S.C. Ligon, R. Liska, J. Stampfl, M. Gurr, R. Mülhaupt, Polymers for 3D printing and customized additive manufacturing, *Chem. Rev.* 117 (2017) 10212–10290, <https://doi.org/10.1021/acs.chemrev.7b00074>.
- [2] T.T. Wohlers, Wohlers report: 3D-printing and additive manufacturing state of the industry, Wohlers Associates, Fort Collins (2017).
- [3] J.R. Tumbleston, D. Shirvanyants, N. Ermoshkin, R. Januszewicz, A.R. Johnson, D. Kelly, K. Chen, R. Pinschmidt, J.P. Rolland, A. Ermoshkin, E.T. Samulski, J. M. DeSimone, Continuous liquid interface production of 3D objects, *Science* 347 (2015) 1349–1352, <https://doi.org/10.1126/science.aaa2397>.
- [4] R. Januszewicz, J.R. Tumbleston, A.L. Quintanilla, S.J. Mecham, J.M. DeSimone, Layerless fabrication with continuous liquid interface production, *Proc. Natl. Acad. Sci. U. S. A.* 113 (2016) 11703–11708, <https://doi.org/10.1073/pnas.1605271113>.
- [5] BMW Group, Germany, BMW Group small series production with 3D-printers: turn signal housing aka MINI side scuttle, 2016. (<https://www.press.bmwgroup.com/deutschland/photo/search/additive,manufacturing/>) (Accessed 17 September 2020).
- [6] S. Velankar, J. Pazos, S.L. Cooper, High-performance UV-curable urethane acrylates via deblocking chemistry, *J. Appl. Polym. Sci.* 62 (1996) 1361–1376, [https://doi.org/10.1002/\(SICI\)1097-4628\(19961128\)62:9<1361::AID-APP6>3.0.CO;2-F](https://doi.org/10.1002/(SICI)1097-4628(19961128)62:9<1361::AID-APP6>3.0.CO;2-F).
- [7] C. Decker, F. Masson, R. Schwalm, Dual-curing of waterborne urethane-acrylate coatings by UV and thermal processing, *Macromol. Mater. Eng.* 288 (2003) 17–28, <https://doi.org/10.1002/mame.200290029>.
- [8] J.P. Rolland, K. Chen, J. Poelma, J. Goodrich, R. Pinschmidt, J.M. DeSimone, L. Robeson, inventors. Carbon Inc., Redwood City, CA (US) assignee. Polyurethane resins having multiple mechanisms of hardening for use in producing three-dimensional objects. International WO patent 2015/200201 A1. 2015 Dec 30.
- [9] J.P. Rolland, K. Chen, J. Poelma, J. Goodrich, R. Pinschmidt, J.M. DeSimone, L. Robeson, inventors. Carbon Inc., Redwood City, CA (US) assignee. Methods of producing three-dimensional objects from materials having multiple mechanisms of hardening. US patent 2017/0239887 A1. 2017 Aug 27.
- [10] C. Tosto, E. Pergolizzi, I. Blanco, A. Patti, P. Holt, S. Karmel, G. Cicala, Epoxy based blends for additive manufacturing by liquid crystal display (LCD) printing: the effect of blending and dual curing on daylight curable resins, *Polymers (Basel)* 12 (2020), <https://doi.org/10.3390/polym12071594>.
- [11] G. González, X. Fernández-Francos, A. Serra, M. Sangermano, X. Ramis, Environmentally-friendly processing of thermosets by two-stage sequential aza-Michael addition and free-radical polymerization of amine-acrylate mixtures, *Polym. Chem.* 6 (2015) 6987–6997, <https://doi.org/10.1039/C5PY00906E>.
- [12] A.O. Konuray, X. Fernández-Francos, A. Serra, X. Ramis, Sequential curing of amine-acrylate-methacrylate mixtures based on selective aza-Michael addition followed by radical photopolymerization, *Eur. Polym. J.* 84 (2016) 256–267, <https://doi.org/10.1016/j.eurpolymj.2016.09.025>.
- [13] A.O. Konuray, A. Ruiz, J.M. Moranchó, J.M. Salla, X. Fernández-Francos, A. Serra, X. Ramis, Sequential dual curing by selective Michael addition and free radical polymerization of acetoacetate-acrylate-methacrylate mixtures, *Eur. Polym. J.* 98 (2018) 39–46, <https://doi.org/10.1016/j.eurpolymj.2017.11.003>.
- [14] A. Redmann, P. Oehlmann, T. Scheffler, L. Kagermeier, T.A. Osswald, Thermal curing kinetics optimization of epoxy resin in digital light synthesis, *Addit. Manuf.* 32 (2020), 101018, <https://doi.org/10.1016/j.addma.2019.101018>.
- [15] S.C. Ligon-Auer, M. Schwentenwein, C. Gorsche, J. Stampfl, R. Liska, Toughening of photo-curable polymer networks: a review, *Polym. Chem.* 7 (2016) 257–286, <https://doi.org/10.1039/C5PY01631B>.
- [16] Carbon Inc., Redwood City, CA 94063, USA, RPU 70 Technical Data Sheet (2020).
- [17] H.J. Qi, M.C. Boyce, Stress-strain behavior of thermoplastic polyurethanes, *Mech. Mater.* 37 (2005) 817–839, <https://doi.org/10.1016/j.mechmat.2004.08.001>.
- [18] M. Hossain, R. Navaratne, D. Perić, 3D printed elastomeric polyurethane: Viscoelastic experimental characterizations and constitutive modelling with nonlinear viscosity functions, *Int. J. Non-linear Mech.* 126 (2020), 103546, <https://doi.org/10.1016/j.ijnonlinmec.2020.103546>.
- [19] Carbon Inc., Redwood City, CA 94063, USA, EPU 40 Technical Data Sheet (2020).
- [20] G.W. Sluggett, C. Turro, M.W. George, I.V. Koptuyug, N.J. Turro, (2,4,6-trimethylbenzoyl)diphenylphosphine oxide photochemistry. A direct time-resolved spectroscopic study of both radical fragments, *J. Am. Chem. Soc.* 117 (1995) 5148–5153, <https://doi.org/10.1021/ja00123a018>.
- [21] P. Obst, J. Riedelbauch, P. Oehlmann, D. Rietzel, M. Launhardt, S. Schmolzer, T. A. Osswald, G. Witt, Investigation of the influence of exposure time on the dual-curing reaction of RPU 70 during the DLS process and the resulting mechanical part properties, *Addit. Manuf.* 32 (2020), 101002, <https://doi.org/10.1016/j.addma.2019.101002>.
- [22] Carbon Inc., Redwood City, CA 94063, USA, SDS Germany No. 933780: RPU 70 Part A and B (2017).
- [23] ISO 3167, Plastics – multipurpose test specimens, 2014 (accessed 23 July 2020).
- [24] ISO 179–1, Plastics – determination of Charpy impact properties, 2010 (accessed 23 July 2020).
- [25] Schott AG, Germany, Duran® beaker, 2017. (<https://www.duran-group.com/en/products-solutions/laboratory-glassware/products/boiling-flasks-and-general-laboratory-glassware/beaker.html>) (accessed 23 July 2020).
- [26] Merck KGaA, Germany, Duroplan Petri dish, glass, 2020. (<https://www.sigmaaldrich.com/catalog/search?term=Duroplan&interface=All&N=0&mode=match%20partially&lang=de®ion=DE&focus=product>) (accessed 23 July 2020).
- [27] Memmert GmbH & Co. KG, Germany, Memmert drying oven U, 2020. (<https://www.memmert.com/products/heating-drying-ovens/universal-oven/#!filters=%7B%7D>) (accessed 23 July 2020).
- [28] Farnell GmbH, Germany, Testo 905-T1, 2019. https://de.farnell.com/testo/testo-905-t1/einstech-thermometer-50-bis-350/dp/2678091?gclid=Cj0KCQjw6uT4BRD5ARIsADwJQ19wIxpqsiIRDEcqpGz3F2tAWP52XsanYkzgnb-z7UCfTCyAJIE4rbgaAgthEALw_wcB&mckv=sNITv1syu_dc=pcrid|427606605497|kword=testo%20905-t1|match=p|plid|slid|product|pgrid|100970574138|ptaid=kwd-351376341307|&CMP=KNC-GDE-GEN-SKU-MDC-Test111A-Category-Bidding (accessed 23 July 2020).
- [29] RheoSense Inc., USA, μVISC™ – portable, small sample viscometer, 2020. (<https://www.rheosense.com/microvisc.html>) (accessed 23 July 2020).
- [30] K. Walters. Rheometry, Chapman and Hall, London, 1975.
- [31] Yamato Scientific Co., Ltd, Japan, Forced convection oven DKN612, 2020. (https://www.yamato-scientific.com/product/show/dkn612_2/) (accessed 23 July 2020).
- [32] NETZSCH-Gerätebau GmbH, Germany, DSC 204 F1 Phoenix®, 2020. (<https://www.netzsch-thermal-analysis.com/de/produkte-loesungen/dynamische-differenzkalorimetrie-differenz-thermoanalyse/dsc-204-f1-phoenix/>) (accessed 23 July 2020).
- [33] Zwick Roell, Germany, Zwick Roell Z20, 2020. (<https://www.zwickroell.com/en>) (accessed 23 July 2020).
- [34] DIN EN ISO Norm 3167, Vielzweckprobekörper, 2014.
- [35] ISO 527–1, Plastics – determination of tensile properties, 2019.
- [36] ISO 291, Plastics – standard atmospheres for conditioning and testing, 2008 (accessed 23 July 2020).
- [37] Instron®, USA, Pendelschlagwerk CEAST 9050, 2020. (<https://www.instron.ch/de-ch/products/testing-systems/impact-systems/pendulums/9050-pendulum>) (accessed 23 July 2020).
- [38] NETZSCH-Gerätebau GmbH, Germany, TG 209 F1 Libra®, 2020. (<https://www.netzsch-thermal-analysis.com/de/produkte-loesungen/thermogravimetrie/tg-209-f1-libra/>) (accessed 23 July 2020).
- [39] G. Menges, E. Haberstroh, W. Michaeli, E. Schmachtenberg, Menges Werkstoffkunde Kunststoffe, first. Aufl., Carl Hanser Fachbuchverlag, 2014.
- [40] E. Yilgör, E. Burgaz, E. Yurtsever, I. Yilgör, Comparison of hydrogen bonding in polydimethylsiloxane and polyether based urethane and urea copolymers, *Polymer* 41 (2000) 849–857.

- [41] T. Buruiana, V. Melinte, L. Stroea, E.C. Buruiana, Urethane dimethacrylates with carboxylic groups as potential dental monomers. Synthesis and properties, *Polym. J.* 41 (2009) 978–987, <https://doi.org/10.1295/polymj.PJ2009131>.
- [42] E. Delebecq, J.-P. Pascault, B. Boutevin, F. Ganachaud, On the versatility of urethane/urea bonds: reversibility, blocked isocyanate, and non-isocyanate polyurethane, *Chem. Rev.* 113 (2013) 80–118, <https://doi.org/10.1021/cr300195n>.
- [43] T.-C. Wen, J.-C. Fang, H.-J. Lin, C.-H. Yang, Characteristics of PPG-based thermoplastic polyurethane doped with lithium perchlorate, *J. Appl. Polym. Sci.* 82 (2001) 389–399.
- [44] K. Sahre, M.H. Abd Elrehim, K.-J. Eichhorn, B. Voit, Monitoring of the synthesis of hyperbranched poly(urea-urethane)s by real-time attenuated total reflection (ATR)-FT-IR spectroscopy, *Macromol. Mater. Eng.* 291 (2006) 470–476, <https://doi.org/10.1002/mame.200500358>.
- [45] A. Erdem, F.A. Ngwabebhoh, U. Yildiz, Fabrication and characterization of soft macroporous Jeffamine cryogels as potential materials for tissue applications, *RSC Adv.* 6 (2016) 111872–111881, <https://doi.org/10.1039/C6RA22523C>.
- [46] C. Tan, T. Tirri, C.-E. Wilen, Investigation on the influence of chain extenders on the performance of one-component moisture-curable polyurethane adhesives, *Polymers (Basel)* 9 (2017), <https://doi.org/10.3390/polym9050184>.
- [47] L. Guo, J. Guan, X. Zhao, B. Lin, H. Yang, Design, synthesis, and photosensitive performance of polymethacrylate-positive photoresist-bearing o -nitrobenzyl group, *J. Appl. Polym. Sci.* 132 (2015), <https://doi.org/10.1002/app.41733>.
- [48] J. Deng, Z. Dai, J. Yan, M. Sandru, E. Sandru, R.J. Spontak, L. Deng, Facile and solvent-free fabrication of PEG-based membranes with interpenetrating networks for CO₂ separation, *J. Membr. Sci.* 570–571 (2019) 455–463, <https://doi.org/10.1016/j.memsci.2018.10.031>.
- [49] T. Gurunathan, S. Mohanty, S.K. Nayak, Isocyanate terminated castor oil-based polyurethane prepolymer: synthesis and characterization, *Prog. Org. Coat.* 80 (2015) 39–48, <https://doi.org/10.1016/j.porgcoat.2014.11.017>.
- [50] B. Steyrer, B. Busetti, G. Harakály, R. Liska, J. Stampfl, Hot lithography vs. room temperature DLP 3D-printing of a dimethacrylate, *Addit. Manuf.* 21 (2018) 209–214, <https://doi.org/10.1016/j.addma.2018.03.013>.

A.4. Cavity Vat Photopolymerisation for Additive Manufacturing of Polymer-Composite 3D Objects

This publication was published open access under the terms of the Creative Commons Attribution 4.0 International License, which permits use and distribution in any medium. The prerequisite is that the original work is properly cited, the use is non-commercial and no modifications or adaptations are made.



Springer Nature

Cavity vat photopolymerisation for additive manufacturing of polymer-composite 3D objects

Author: Joel Bachmann et al
Publication: Communications Materials
Publisher: Springer Nature
Date: Oct 26, 2021

Copyright © 2021, The Author(s)

Creative Commons

This is an open access article distributed under the terms of the [Creative Commons CC BY](#) license, which permits unrestricted use, distribution, and reproduction in any medium, provided the original work is properly cited.

You are not required to obtain permission to reuse this article.

To request permission for a type of use not listed, please contact [Springer Nature](#)

© 2021 Copyright - All Rights Reserved | [Copyright Clearance Center, Inc.](#) | [Privacy statement](#) | [Terms and Conditions](#)
Comments? We would like to hear from you. E-mail us at customer-care@copyright.com



<https://doi.org/10.1038/s43246-021-00211-5>

OPEN

Cavity vat photopolymerisation for additive manufacturing of polymer-composite 3D objects

Joel Bachmann ^{1,2}, Philip Obst², Lukas Knorr ², Stefan Schmölder³, Gabriele Fruhmann ², Gerd Witt⁴, Tim Osswald⁵, Katrin Wudy⁶ & Olaf Hinrichsen^{1,7}

Vat photopolymerisation describes resin-based additive manufacturing processes in which ultraviolet light is used to layer-wise solidify liquid resin into a desired 3D shape. If the starting resin is a dual-curing formulation the object is also thermally cured to attain its final properties, obtaining either an elastomer or a thermoset. Here, we introduce cavity vat photopolymerisation, in which one photopolymer resin produces a composite material of an elastomer and thermoset. Cavities of any geometry are purposefully designed in the solid object and then filled with liquid resin during printing due to negative pressure. Thermal curing then solidifies the resin in the cavities into an elastomer, forming a distinct interface held together by strong covalent bonds. Hybrid specimens indicate improved damping, reduced fragmentation upon fracture and increased local elasticity, and we suggest several hard-shell/soft-core applications that might benefit.

¹Department of Chemistry, Technical University of Munich, Lichtenbergstraße 4, 85748 Garching, Germany. ²BMW Group FIZ, Knorrstraße 147, 80788 Munich, Germany. ³NETZSCH-Gerätebau GmbH, Wittelsbacherstraße 42, 95100 Selb, Germany. ⁴Department of Engineering, University Duisburg, Lotharstraße 1, 47057 Duisburg, Germany. ⁵Polymer Engineering Center, Department of Mechanical Engineering, University of Wisconsin-Madison, Madison, WI 53706, USA. ⁶Technical University of Munich, Professorship of Laser-based Additive Manufacturing, Boltzmannstraße 15, 85748 Garching, Germany. ⁷Catalysis Research Center, Technical University of Munich, Ernst-Otto-Fischer-Str. 1, 85748 Garching, Germany. ✉email: joel.bachmann@bmw.de

Vat photopolymerisation (VPP, official abbreviation according to ISO/ASTM 52900¹) processes hold the largest material market share in additive manufacturing (AM)². An advantage of resin-based AM approaches is the high accuracy, precision and void-free, completely dense parts with a good surface quality even on the submillimetre scale. Stereolithography (SLA) and digital light processing (DLP) are the best known VPP technologies, but new approaches also have emerged in recent years, such as Digital Light Synthesis (DLS)³, volumetric polymerisation inhibition patterning⁴ and tomographic volumetric printing^{5,6}. In addition, tremendous research efforts are performed on 4D-printing^{7,8}, smart materials, and printing materials with hybrid functionalities^{9–29}. The big interest in enabling multi-functional materials stems from numerous examples often inspired by nature, such as the resilience in the nacre of the *Pinna nobilis* shell that is achieved by a brick and mortar nanostructure³⁰, elastic joints in rigid skeletons that enable flexibility and movement, or other natural products and animals that are tough on the outside though soft on the inside, for example, nuts and crustaceans. From the engineering perspective, qualities like spatially controlled areas with improved shock absorption, crack resistance, damping, elasticity, and hardness are driving the search for AM processes that can produce advanced composites of two different polymer (hard polymer – soft polymer) materials. To create materials designed with spatially different chemical and mechanical properties, one of two approaches is usually followed: either multi-material feedstocks are used in combination with extrusion-based AM^{14–22}, Polyjet^{24,25}, VPP^{11–13} or a combination of different AM processes²³. Another possibility is that a second orthogonal chemical crosslinking reaction beside the photopolymerisation takes place and creates an interpenetrating network (IPN). The other reaction can be another photopolymerisation, which is initiated by a different wavelength^{26,27}; it can also be a catalysed condensation reaction³¹ or—as presented in this study—a heat-activated reaction initiated by temperature. However, many approaches to multi-functional, polymer–polymer composites are very difficult to implement because they require additional modifications of existing AM processes, which typically increase the complexity of the already complex process-parameter environment of AM. This makes most of the current approaches slow, expensive and only applicable for minimal build volumes. Moreover, much work needs to be put into the design process, and additional software-specific and process-specific coding is required. For example, Kuang et al.²⁹ use a code to create a

grayscale distribution that can adjust the modulus of the polymer by generating different light intensities. Finally, one of the biggest challenges in the field of multi-material parts or the composition of two materials is the bonding zone. Typically, this area is the weak point due to material combinations that are chemically often incompatible. In this study, the authors present an AM method called cavity vat photopolymerisation (CVPP), which can produce hard-shell/soft-core polymer composites with a dual-curing resin as a prerequisite. Dual-curing resins are two-part resins that are mixed before printing, UV-cured during vat photopolymerisation and thermally post-cured to attain their final properties. A recent study shows that if the first step of photopolymerisation is omitted and the resin is only thermally cured, this will lead to a fully developed elastomer³². The idea behind CVPP is the following: Before printing, cavities are specifically created during the design process in the part where, for example, higher shock absorption or damping is required. Typically, all unvented volumes should be avoided in DLS, as the resin is trapped there by negative pressure. For CVPP, however, the resin inclusion in the cavities serves as an enabler for creating composite 3D objects without any additional processing step. After designing the cavities, CVPP follows the same steps of the dual-curing process known from DLS: printing, post-processing with cleaning, removal of support structures and thermal curing in an oven with a specific temperature profile. In the final post-processing step of thermal curing, the resin is solidified into an elastomer and chemically bonds to the thermoset shell. The application of CVPP does not require any additional processing steps, modification of the process, multi-material feedstock or extra wavelength. It can be broadly applied to all top-down and continuous bottom-up VPP processes (see Fig. 1a). In non-continuous, bottom-up VPP processes that use realignment steps where the part is pulled out of the vat, the resin does not remain in the cavity due to the pressure compensation. However, a modification of CVPP can also be applied for non-continuous, bottom-up VPP by designing inlets to the cavities and injecting dual-curing, liquid resin after the printing process. The sole prerequisite here is the creation of a closed cavity filled with the dual-curing photopolymer resin. For showcasing CVPP, DLS is used as a VPP process, as it provides a continuous bottom-up process and an above-average printing speed through continuous polymerisation, which is enabled by an oxygen-permeable window and a so-called “O₂-dead zone” (see Fig. 1b). The commercially available and scientifically studied^{32–34} DLS material RPU 70 is used as a dual-curing resin formulation. This study

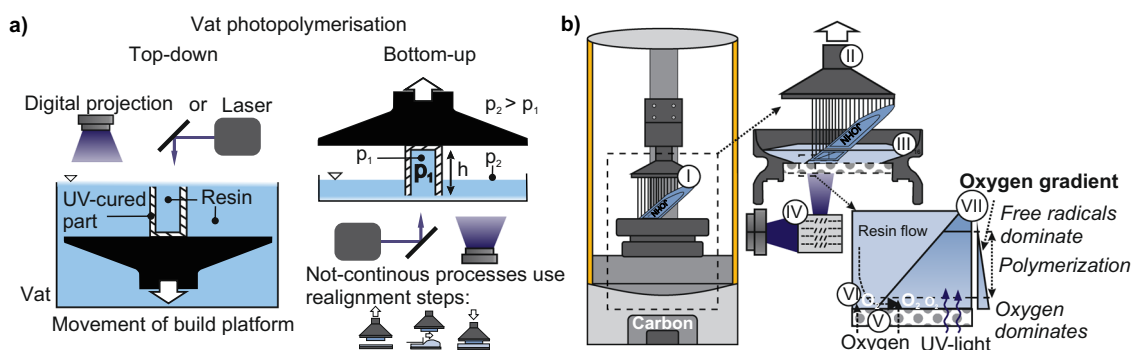


Fig. 1 Vat photopolymerisation (VPP) technologies suitable for cavity vat photopolymerisation (CVPP). **a** Top-down VPP process, in which resin is solidified on the resin surface and cavities are naturally filled with resin. Bottom-up VPP processes solidify the resin at the bottom of the vat either with UV-laser or digital projection of UV light. Continuous bottom-up VPP processes do not need realignment steps and are suitable for CVPP because cavities are automatically filled with resin because the atmospheric pressure p_2 is greater than the weight pressure p_1 of the resin in the cavity. **b** Graphic depiction of the continuous bottom-up VPP process DLS. (I) Personalised geometry (II) Constant elevation of the build platform (III) Resin-filled vat (IV) DLP system with micro-mirrors (V) Light and oxygen penetrable window (VI) Zone of no polymerisation (VII) UV-cured object.

investigates a print job that is spread over the whole build area to demonstrate that CVPP is simultaneously applied to the entire build area. Even though CVPP can produce complex soft-hard composites in the micrometre range, long uninterrupted and uniform cavities were chosen to demonstrate that the negative pressure keeps the resin in tall geometries (resin-filled cavity height = 15.5 cm in the z-direction) during printing. The scope of this study is to prove that CVPP can take advantage of all benefits of the DLS process like one-step, continuous production of different geometries spread over the build platform and that the resin-filled cavity geometries can be produced with no delay in print time. CT scans and thin-section microscopy of hybrid parts are conducted to investigate the two different phases. To investigate the mechanical and damping properties, tensile, impact testing and dynamic mechanical analysis (DMA) are performed on regular, dense RPU 70 parts (full) and compared to hard-shell/soft-core, thermoset—elastomer parts (hybrid). This study concludes by presenting possible applications of composite 3D objects produced by CVPP.

Results and discussion

Printing resin-filled parts and producing hard-shell/soft-core test specimens by CVPP. Figure 2 shows the printing process steps and specimen produced by the CVPP method. Tensile and impact test specimens from Fig. 2a with a thickness of 4.0 mm were designed as dense parts (series A1-B5) and modified CVPP test specimens with a wall thickness of 1.0 mm (series C1-D5). The specimens were successfully printed (see Fig. 2b), washed and thermally cured. Figure 2c shows a resin-filled impact bar, cut with a scalpel after DLS. The shell releases the enclosed resin. Of course, this step is not the desired result, but it does show that the resin is trapped inside when printing unvented volumes with DLS. The result of CVPP is revealed after thermally curing (see Fig. 2d) the resin-filled specimens. Figure 2e shows the tensile bar C1, cut vertically, revealing its hybrid nature with a hard thermoset shell and a soft elastomer core.

Furthermore, the vertical cross-section of the tensile bar proves that the entire cavity has been filled with resin from top to bottom

during printing. For top-down VPP processes (see Fig. 1a), it seems quite intuitive that liquid resin flows into the cavities. However, for continuous bottom-up processes such as DLS, it seems initially counterintuitive that the resin remains in the cavities, especially when it is drawn out of the vat. Nevertheless, on a second glance, we see this how this principle works in the well-known mercury barometer from Evangelista Torricelli (1608–1647). In his famous experiment, the atmospheric pressure (atm) at sea level keeps mercury in a glass tube at the height of 760 mm (1 atm = 760 mm Hg = 1 torr). The same principle applies to unvented volumes during DLS: the resin in the cavity is exposed only to its own weight pressure p_1 , which is defined by the density of the resin ρ_{resin} times gravity g times the height of the uninterrupted resin-filled cavity h :

$$p_1 = \rho_{resin} \cdot g \cdot h \tag{1}$$

The vat, on the other hand, is exposed to the atmospheric pressure p_2 :

$$p_2 = p_{atm} \tag{2}$$

According to the observation during printing, the resin stays in the cavities, which means:

$$p_1 \leq p_2 \tag{3}$$

$$\rho_{resin} \cdot g \cdot h \leq p_{atm} \tag{4}$$

The hydrostatic pressure would have to overcome the air pressure. Assuming an air pressure of $p_{atm} = 1013.25$ hPa, the pressure at sea level and the density of the resin used in this study of $\rho_{resin} = 1010$ kg m⁻³, this leads to:

$$h \leq \frac{p_{atm}}{\rho_{resin} \cdot g} = \frac{101325\text{Pa}}{1010\text{kgm}^{-3} \cdot 9.81\text{ms}^{-2}} = 10.23\text{m} \tag{5}$$

The resin column in the cavity must, therefore, not exceed 10.23 metres. For DLS, the maximum z-direction height for print jobs is

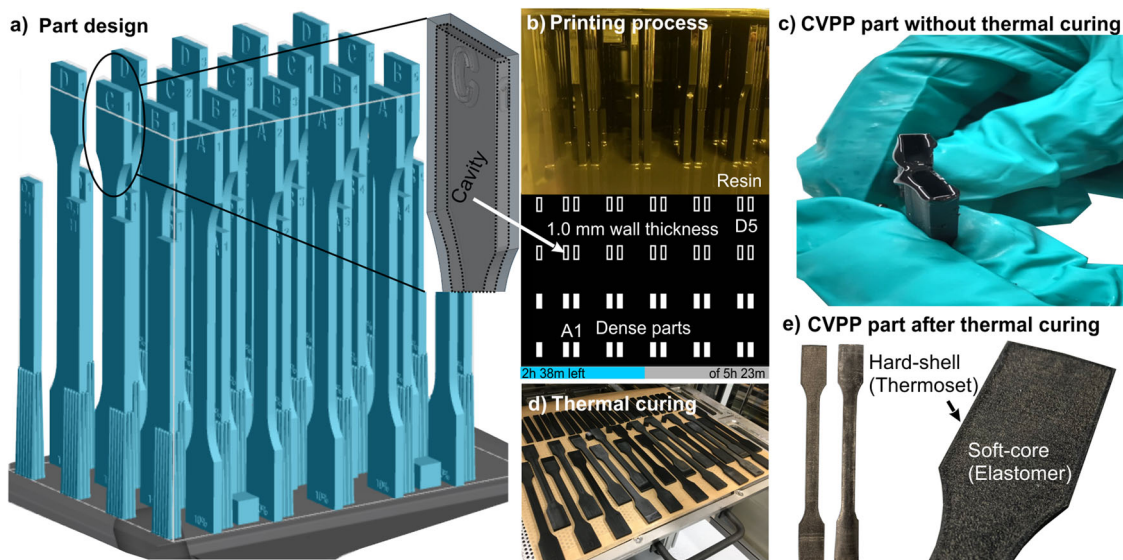


Fig. 2 Printing resin-filled test specimen and printing hybrid parts via CVPP. **a** DLS print job with 10 full (A1 - B5) and 10 hollow (C1 - D5) tensile (Type A, ISO 3167⁴⁰) and impact specimen (80 x 10 x 4 mm, ISO 179-1eU³⁶) on M2 build platform (189 x 118 mm). Maximum z-height of build job = 17.5 cm. Impact specimens are built on support structures to have the testing area at the same height as the tensile test specimen. Magnification shows STL-file of hollow C1 tensile test specimen with a wall thickness of 1.0 mm. **b** Print job during printing (above). Cross-sections of resin-filled and full tensile and impact bars at about 50% (down) **c** Resin-filled impact test specimen after DLS cut open with a scalpel: in cavity trapped liquid resin escapes. **d** Thermal curing of resin-filled and dense UV-cured parts. **e** Hybrid tensile bar (C1) cut vertically in two halves. Magnification shows 1.0 mm wall thickness of thermoset shell and elastomer core.

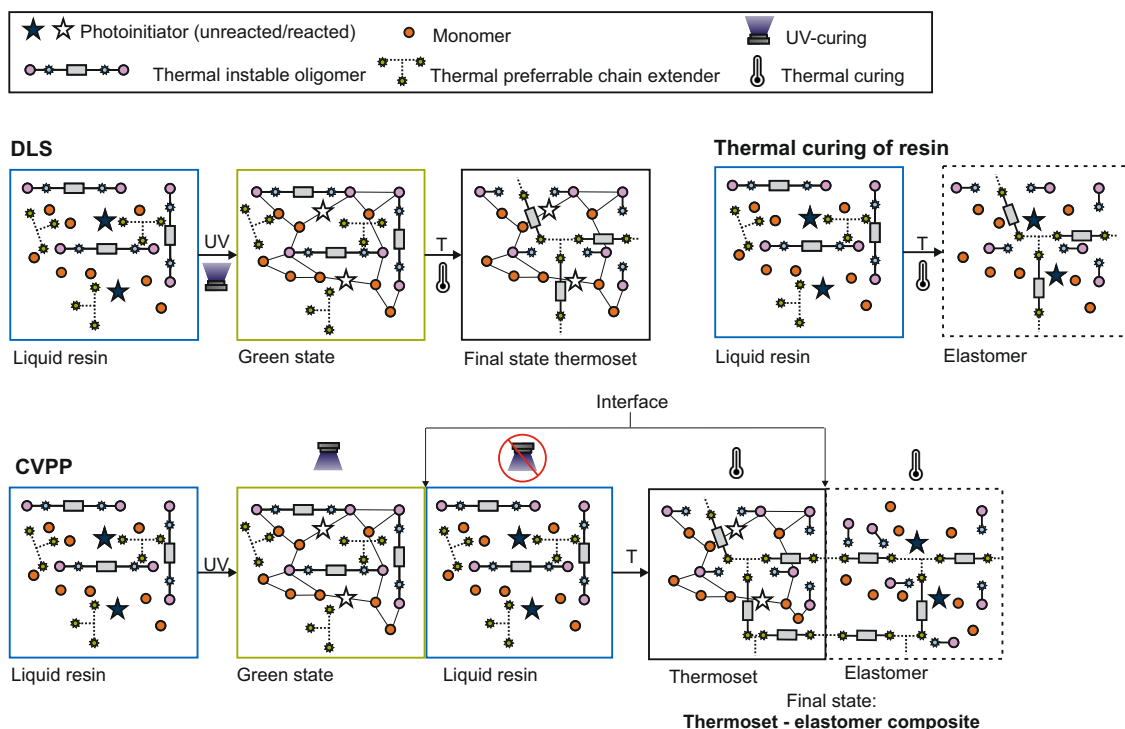


Fig. 3 Chemistry of dual-curing resin during DLS, purely thermal curing and for CVPP. The molecules in the liquid resin state (blue square) can move freely. UV light initiates photopolymerization and the first polymer network is formed, also known as the green state (green square). Thermal curing causes the formation of a second polymer network. If the liquid resin is heated, an elastomer (black dashed square) is formed, if the green part is exposed to heat, a thermoset (black square) is formed. The covalent bonds of this second polymer network are the reason for a strong binding strength between the thermoset and elastomer phase in CVPP.

0.46 m, which L1 printers can achieve. Therefore, even for high-density photopolymers, CVPP is not limited by the weight pressure of the resin but by the maximum printing height of conventional printers.

Dual-curing chemistry as a prerequisite for CVPP. CVPP requires dual curing, i.e. UV and thermal curing resins. Figure 3 shows a schematic representation of the dual-curing chemistry. The starting material is a liquid resin with photoinitiators, reactive monomers, thermal unstable oligomers and a thermal preferable chain extender. The latter is usually mixed to the reactive composition before printing. To explain the basic principle, the diagram does not include other components such as various monomers, oligomers and passive absorbers. The basic two-step DLS process with UV and thermal curing with the corresponding chemical reactions is shown above. During UV-curing, the photoinitiator triggers photopolymerisation of the reactive (meth-)acrylate groups of the monomers and thermally unstable oligomers. The thermal preferable chain extenders do not take part in this reaction but remain unreacted in the network of the UV-cured (green) state. During the thermal post-process, the “pre-determined breaking points” in the thermally unstable oligomer break up and react with the thermal preferable chain extender. Thermally unstable oligomers combined with thermally preferable chain extenders are the focus of dual-curing resins and the CVPP method. The reaction that occurs can be characterised as a displacement reaction between a strong sterically blocked urethane or urea group. These can be easily synthesised by a sterically hindered (meth-)acrylate like tert-butylaminoethyl methacrylate (TBAEMA) with a diisocyanate. A primary amine

or alcohol can displace TBAEMA from its position and form a thermally stable urea or urethane group, respectively³⁵. An in-depth characterisation of the dual-curing chemistry of RPU 70 can be found in the literature³², which also refers to the possibility of a thermal reaction of the dual-curing resin to the elastomer. This reaction is also depicted in Fig. 3. CVPP (see Fig. 3 below) combines these two curing chemistries as the body is exposed to UV, but the resin in the cavity is not. In the second step, both the green state body and the resin within are exposed to the thermal curing reaction. Thus, the final state of the outer shell can be characterised as a thermoset with an IPN with the inner core as an elastomer. The thermoset shell is connected to the elastomer core by the thermally preferable chain extender, which is bonded to urea groups in each phase. These strong covalent chemical bonds are unique to CVPP. Other AM, as well as injection-moulding approaches for multi-materials either rely on partial curing, weaker bonds or adhesives. Since CVPP uses the same material for the two different material states, good bonding between them is obvious. FT-IR analysis of the uncured, UV-cured, thermal cured and UV- and thermal cured RPU 70 resin validates the proposed reaction steps (see Fig. 4).

Non-porous homogeneous phases with a clearly defined interface. The sharp and strong interface can be best observed in the thin-section microscopy image of a horizontal cross-section of a hybrid tensile bar in Fig. 5a. The density of the final thermoset state ($\rho_{thermoset} = 1080 \text{ kg m}^{-3}$) and the elastomer state ($\rho_{elastomer} = 1028 \text{ kg m}^{-3}$) are very similar, which is reflected in only a low contrast in the CT scan (see Fig. 5b), as this imaging technology relies on density differences. Therefore,

it is well suited to identify remaining air-filled cavities. The horizontal cross-section from Fig. 5b indicates that both phases, namely the thermoset shell and elastomer core, are homogeneous and do not indicate any porosity with enclosed air ($\rho_{\text{air}} \approx 1.25 \text{ kg m}^{-3}$). The Supplementary Movie 1 shows all cross-sections through the 17.5 cm high tensile bar from Fig. 5b: No air bubble can be detected in the entire CT scan. This means that no air is left behind or is dragged into the

uninterrupted cavity during printing. Consequently, CVPP can produce two homogeneous, void-free, non-porous phases separated by a well-defined interface.

Mechanical properties of full and hybrid parts. Figure 6 shows the results of the mechanical test between the fully dense thermoset (full) and the hard thermoset shell – soft elastomer core hybrid with a 1.0 mm wall thickness (hybrid). At the breaking point, the total material shows brittle fractures with larger and smaller fragments both during tensile (Fig. 6a) and impact testing (Fig. 6b). The hybrid, on the other hand, exhibits an entirely different material behaviour. The elastic core improves elongation at break. At the same time, it reduces tensile strength, impact strength and internal tension before breakage, thereby preventing fragments and even holding the part together after the impact of the pendulum (see Supplementary Movie 2, 3). All mechanical tests were carried out following ISO standards^{36–38}. However, these standards are specified for homogeneous parts, something which must be considered when examining and comparing the absolute values between full and hybrid parts summarised in Table 1. The dynamic mechanical analysis (DMA) results displayed in Fig. 6c emphasise the difference in material behaviour between the full and hybrid state. Both the storage (E') and the loss (E'') modulus show different curves for the different states.

The hybrid, whose material behaviour is dominated by the elastomer, has a low glass transition temperature (T_g) of -38°C , typical for elastomers. Below, the T_g , the material is hard and brittle comparable to glass. Above the T_g the material demonstrates an elastic or viscoelastic behaviour. The T_g of the hybrid is a mixed T_g because the thermoset and elastomer states are compatible. With the ratio of elastomer to thermoset, it is possible to adjust the mixed T_g and thus also the material behaviour of the hybrid. The full material has a much higher T_g of 50°C , and the storage modulus is always above the storage modulus of the hybrid for the entire temperature range. The loss factor $\tan \delta$, which represents the damping capacity of the material, is defined as the ratio E''/E' . The $\tan \delta$ of the hybrid shows a small shoulder at low temperatures indicating the elastomer and a clear peak at high temperatures, which indicates the thermoset. The elastomer signal in $\tan \delta$ is less noticeable because the elastomer fraction in the hybrid is smaller than the duromer fraction.

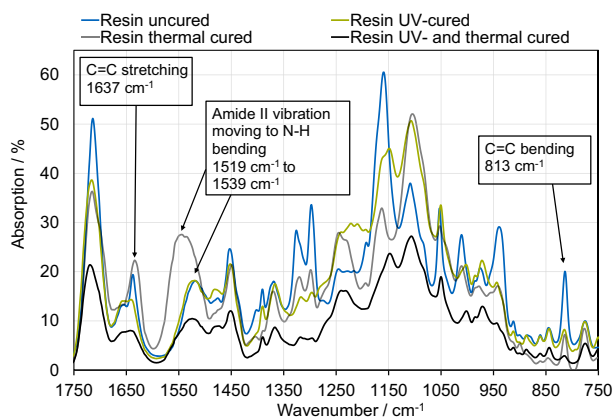


Fig. 4 FT-IR analysis of RPU 70 resin (resin), UV-cured (green), thermally cured (elastomer) and thermoset (final) state. The decrease in C=C stretching (1637 cm^{-1}) and bending (813 cm^{-1}) signal from resin to green and final state indicates that all photoinitiators and reactive monomers and oligomers have reacted during photopolymerization. The elastomer does not show a decrease in C=C concentration. This means that in the elastomer state, the C=C double bonds have not reacted, and the (meth-)acrylates network is not established. On the other hand, the amide II vibration (1519 cm^{-1}), which consists of N-H bending and C-N stretching, moves for the elastomer into the N-H bending direction (1539 cm^{-1}). This behaviour is because the blocking unit (TBAEMA) in the thermally unstable oligomer in the urea group represents a tertiary amine without hydrogen, so no N-H bending is possible. However, the thermal preferable chain extender is a primary amine that replaces the tertiary amine and becomes a secondary amine in the urea group with hydrogen. Therefore, the N-H bending is predominant for the elastomer state and characterizes the thermal reaction.

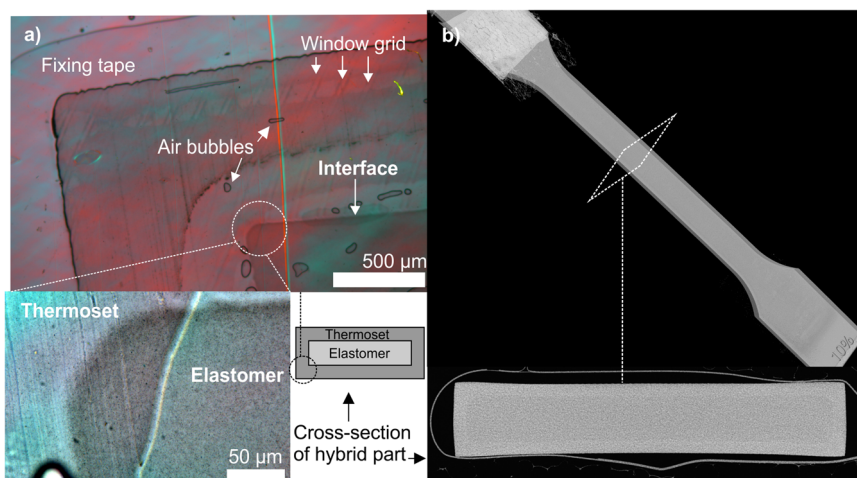


Fig. 5 Hybrid form part with CT and microscopy analysis. **a** Cross-section and thin-section microscopy image of hybrid tensile bar. The trapped air bubbles in the image derive from the rough surface, and the fixing tape and are not pores inherent to the two phases. The red line is from the polarisation filter, while the parallel lines in the thermoset phase come from the window grid during DLS. The magnification shows two homogeneous phases with a clearly defined interface between the 1.0 mm thick thermoset shell and the elastomer core. **b** The CT scan of a hybrid C1 tensile bar with 1.0 mm wall thickness and cross-section of CT scan reveals two homogeneous phases without any porosity.

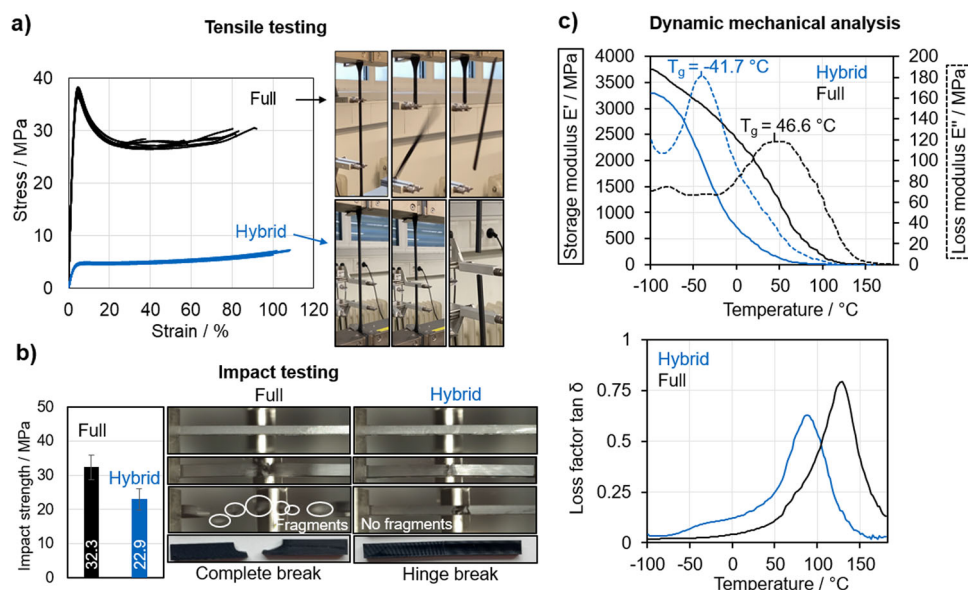


Fig. 6 Mechanical analysis of thermoset (full) and thermoset – elastomer composite (hybrid) parts. **a** Tensile testing with images of full and hybrid parts at the breaking point. **b** Impact testing results with SD as error bars. High-speed images at the moment of the pendulum impact and impact bars after testing. **c** DMA measurements. Diagram **c** (on top): — storage modulus - - - loss modulus.

Table 1 Results of tensile and impact testing without outliers.

Mechanical Testing		State	N	Mean	Std. Dev.	Minimum	Median	Maximum
Tensile Testing	Cross-section /mm ²	full	8	38.65	0.13	38.47	38.66	38.81
		hybrid	10	37.00	0.32	36.39	36.94	37.59
	Tensile modulus /MPa	full	8	1300.02	35.14	1248.86	1294.45	1369.37
		hybrid	10	135.54	5.69	122.76	135.49	142.58
	Tensile strength /MPa	full	8	37.42	0.74	36.33	37.52	38.31
		hybrid	10	4.72	0.13	4.53	4.66	4.96
	Elongation at break /%	full	8	71.28	18.48	37.56	80.50	91.99
		hybrid	10	97.30	10.14	78.11	100.75	108.34
Impact Testing	Cross-section /mm ²	full	10	38.58	0.15	38.33	38.62	38.81
		hybrid	10	40.12	0.16	39.87	40.14	40.36
	Impact strength /MPa	full	10	32.34	3.65	27.15	32.44	38.24
		hybrid	10	22.93	3.22	16.99	22.66	28.71

Furthermore, the hybrid material has superior damping properties up to 100 °C. Therefore, the measurement error, the non-homogeneous sample, is neutralised, and a comparison with the full material is permissible.

Applications of hybrid materials produced by CVPP. Engineering demands on automobile wire harnesses are a growing field of AM applications. Parts such as strain reliefs, plugs, grommets and gaiters often have individual geometries that are also size-suitable for AM. The first application from Fig. 7a shows a typical cable strain relief that consists of a robust plug for attaching the part in a bracket. However, to clamp the cable onto the strain relief, the cable holder must be elastic enough to push the cable through. A DLS-printed RPU 70 part does not fulfil the elastic requirement for mounting the cable. However, the hard-shell/soft-core printed part, manufactured by RPU 70 and CVPP, can guarantee both functionalities: the robust plug on the bracket and the elastic cable mounting. The locally designed cavities, with higher elastic requirements in some places, represent the only change from the earlier production. The second example from Fig. 7b is a plug-in, joint-like connector consisting of a plug and a socket. The DLS-printed RPU 70 connector cannot be plugged

into the socket. However, by increasing the elasticity of either the connector or socket locally at the connection point and by designing cavities in the STL file, the plug-in connection works. Both examples demonstrate that not only can uninterrupted, simple geometries be realised, but that complex hybrid geometries can also be produced by CVPP. Of course, it is not only possible to achieve higher elasticity for hybrid parts; locally improved damping and/or fracture behaviour can also be ensured. The latter could be particularly interesting for parts that require high safety standards, such as head impacts, where fragments could become fatal projectiles upon impact. The latter example Fig. 7c shows the infinite possibilities of designing cavities within the part. Small micrometre lattice structures within the part enable different damping properties, moduli and mixed T_g .

Conclusion

Several AM attempts have been made to produce parts with hybrid functionalities. However, most approaches call for modification of the AM process, which means that they are not ready for general customer use throughout the AM community. This study presents the method CVPP, which can produce hard-shell/soft-core polymer composites without modifying the DLS

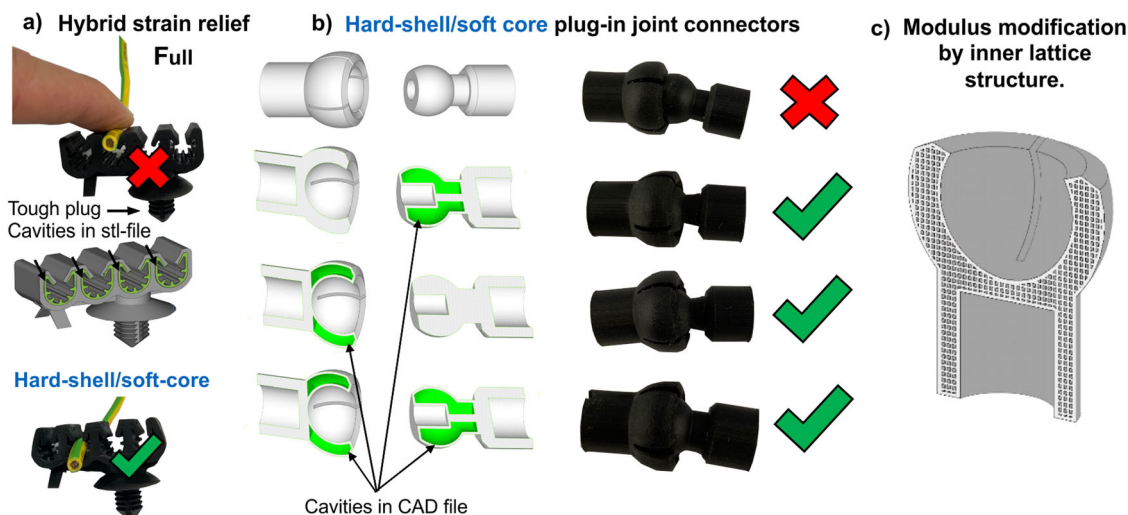


Fig. 7 Possible applications of hybrid parts produced by CVPP. **a** The hybrid strain relief printed with RPU 70 without modification does not allow to mount a cable. The same part, however, with modified cavities in the area of the desired elasticity allows the fixing of the cable. **b** The Hard shell - soft core connector is another good example of how the design of cavities in the CAD file leads to increased elasticity with CVPP. **c** Inner lattice structures are an outlook on how CVPP could be used to change the modulus of a part.

process. The prerequisites for the implementation of CVPP are threefold:

1. The design of cavities in the CAD file.
2. The use of a dual, i.e. UV and thermal, curing resin like RPU 70.
3. Thermal post processing after the UV-curing step.

The cavities should be designed in areas where the final part requires increased local elasticity, shock absorption and/or damping. Prerequisites here are a dual-curing resin formulation and a thermal post-curing step. CVPP can be broadly applied to all top-down and continuous bottom-up VPP processes (see Fig. 1a). The maximum uninterrupted cavity height is not physically limited and can easily reach the maximum printing height of conventional 3D printers. CVPP can produce two hybrid, homogeneous, non-porous, void-free phases of any geometry with a clearly defined interface. One of the main challenges in the field of multi-material parts is the bonding zone. This is typically the weak point due to chemical, often incompatible material combinations. In this approach, the material is chemically equivalent and, during thermal curing, chemical covalent bonds are formed between the two materials, which provide strong cohesion. The material properties of these hard-shell/soft-core parts can be adjusted between elastomer and thermoset behaviour. Improved fracture behaviour without dangerous projectiles has been demonstrated along with improved damping behaviour at up to 100 °C compared to the full thermoset. The hybrid stress relief part is a perfect example of how CVPP permits hybrid functionalities, starting from one individual photopolymer and by locally designing cavities in the CAD geometry. Several parts in automobile wire harnesses require similar hybrid functionalities. Moreover, the click-and-clip function of joint-like plug-in connectors can be realised by locally increasing the elasticity of the part. It is easy to imagine how CVPP allows endless possibilities of constructing different material properties by varying the amount and size of cavities and elastomeric compartments separated by thermoset lattices. Of course, this can also be applied locally on elements in the part that require a more elastic behaviour or better damping. The thickness of the hard-shell is theoretically limited only by the horizontal resolution of the 3D printer. It should be noted, however, that optimal geometric

designs still need to be found to eliminate sagging and curvatures that may result from the different thermal expansions. Although our approach offers significant benefits, long-term mechanical and chemical stability still needs to be addressed. Furthermore, new dual curing resin formulations will expand the spectrum for even more applications.

Methods

Material. RPU 70 (Carbon, USA) with lot number 20DP2641 was used for all experiments. It consists of two parts: part A and part B, which are mixed in the ratio 10:1 and dispensed at a speed of 1 mm s^{-1} into the DLS cassette with an Albion Dispenser (Albion Engineering, USA) before printing. A volume of 460 mL was used for the print job. The volume of the part and support was 287.2 mL. Part A of RPU 70 consists of Diphenyl (2,4,6 trimethyl benzoyl) phosphine oxide (TPO, photoinitiator, 0.1–2%), urethane dimethacrylate (UDMA, difunctional oligomer, 1–20%), methacrylate blocked polyurethane/diisocyanate (MABPU and/or MABDI, blocked prepolymer synthesised with diisocyanates, 10–70%), Isobornyl methacrylate (IBOMA, reactive diluent, 10–50%) and neopentyl glycol dimethacrylate (NPGDMA, difunctional monomer, <0.3%)³⁹. Part B of RPU 70 consists of Trimethylolpropane tris [poly (propylene glycol) amine terminated] ether (Chain extender, 20–100%)³⁹.

3D-printing with digital light synthesis (DLS). The M2 printer (Carbon, USA) with a build volume of $270 \times 160 \times 380 \text{ mm}$ was used for DLS with a customised print script and build job (see Fig. 2a). The total time for the print was 6 h and 21 min. After the print, the specimens were cleaned in the smart part washer (Carbon, USA) in the default washing mode (7 min) with VF1-Solvent (Vertrel™, MS-767-3D-13). For post-processing, the sample specimens were placed with baking paper on a perforated plate, which was placed in the middle of a Memmert UF 260 TS convection oven (Mettmert GmbH & Co. KG, Germany). The standard thermal curing cycle with a 30 min ramp to 120 °C followed by an isothermal hold for 4 h and then left to cool for to room temperature 30 min.

Material characterisation. The weight of the samples was determined by a Cubis® Ultra Micro Balance (Sartorius, Germany). Density measurements of the green and final part were performed by dividing the sample mass by the measured volume of the printed $10 \times 10 \times 10 \text{ mm}$ cubes. These results were compared with density measurements using the ISO 1183-1 immersion method. Tensile testing was performed with a Type A tensile specimen (ISO 3167⁴⁰) according to ISO 527-1³⁶ on a Z020 machine (ZwickRoell GmbH & Co. KG, Germany). Impact testing was done on an INSTRON® CEAST 9050 machine (Illinois Tool Works Inc., USA) with a four-joule pendulum and $10 \times 8 \times 4 \text{ mm}$ unnotched specimen according to ISO 179-1eJ³⁷. Dynamic mechanical analysis (DMA) was performed on an EPLEXOR® 500 N (NETZSCH-Gerätebau GmbH, Germany) with a $10 \times 8 \times 4 \text{ mm}$ rectangular specimen in tensile mode according to ISO 6721-1³⁸. A measure frequency of 10 Hz, a contact force of 1 N, a static load of 0.3%, a dynamic load of 0.05%, a heating rate of 2 K min^{-1} and a temperature range between -70 °C and 180 °C was used. The T_g for the full and hybrid was determined as the peak in the

loss modulus. Fourier transform infrared spectroscopy (FT-IR) was carried out with 16 scans on a mid-infrared ATR unit on a Frontier MIR Spectrometer (PerkinElmer[®] Inc., USA). Eight images were produced via computed tomography (CT) of the hybrid tensile bar C1 using a Phoenix V|tome|x M 240 D|180 NF Micro-CT machine at a 100 kV voltage, 260 μ A current, 500 ms exposure time and 20 μ m isotropic voxel size. A cardboard roll with foam was used to fixate and stabilise the part. Thin-section microscopy images were captured by a PROGRES GRYPHAX[®] NAOS camera (Optische Systeme Jülich GmbH, Germany). A Leica DM LM microscope (Leica Microsystems GmbH, Germany) was used with varying magnifications. To prepare a thin cross-section out of a hybrid impact bar, a rotational HistoCore AUTOCUT automatic microtome (Leica Biosystems Nussloch GmbH, Germany) was used.

Disclaimer for the image integrity: Some images in Figs. 2 and 6 were taken in a laboratory environment with different and sometimes distracting backgrounds. Therefore, the background for these images was cut out.

Data availability

The data that support the findings of this study are available from the corresponding author upon reasonable request.

Received: 10 June 2021; Accepted: 30 September 2021;

Published online: 26 October 2021

References

- ISO 52900 (en). *Additive manufacturing — General principles — Terminology*. (2017).
- Wohlers. Wohlers report 2019. 3D printing and additive manufacturing state of the industry (Wohlers Associates, Fort Collins, Colorado, 2019).
- Tumbleston, J. R. et al. Additive manufacturing. Continuous liquid interface production of 3D objects. *Science* **347**, 1349–1352 (2015).
- Beer, M. P. de et al. Rapid, continuous additive manufacturing by volumetric polymerization inhibition patterning. *Sci. Adv.* **5**, eaau8723 (2019).
- Loterie, D., Delrot, P. & Moser, C. High-resolution tomographic volumetric additive manufacturing. *Nat. Commun.* **11**, 852 (2020).
- Bernal, P. N. et al. Volumetric bioprinting of complex living-tissue constructs within seconds. *Adv. Mater.* **31**, e1904209 (2019).
- Kuang, X. et al. Advances in 4D printing: materials and applications. *Adv. Funct. Mater.* **29**, 1805290 (2019).
- Tibbits, S. 4D printing: multi-material shape change. *Archit. Des.* **84**, 116–121 (2014).
- Deore, B. et al. Direct printing of functional 3D objects using polymerization-induced phase separation. *Nat. Commun.* **12**, 55 (2021).
- Huang, J., Ware, H. O. T., Hai, R., Shao, G. & Sun, C. Conformal geometry and multimaterial additive manufacturing through freeform transformation of building layers. *Adv. Mater.* **33**, e2005672 (2021).
- Chen, D. & Zheng, X. Multi-material additive manufacturing of metamaterials with giant, tailorable negative poisson's ratios. *Sci. Rep.* **8**, 9139 (2018).
- Grigoryan, B. et al. Development, characterization, and applications of multi-material stereolithography bioprinting. *Sci. Rep.* **11**, 3171 (2021).
- Hensleigh, R. et al. Charge-programmed three-dimensional printing for multi-material electronic devices. *Nat. Electron.* **3**, 216–224 (2020).
- Podcast: A rapid, multi-material 3D printer, and a bacterium's role in alcoholic hepatitis. *Nature*. <https://doi.org/10.1038/d41586-019-03507-2> (2019).
- Bundell, S. New 3D printer makes multi-material robots. *Nature*. <https://doi.org/10.1038/d41586-019-03513-4> (2019).
- Hardin, J. O., Ober, T. J., Valentine, A. D. & Lewis, J. A. Microfluidic printheads for multimaterial 3D printing of viscoelastic inks. *Adv. Mater.* **27**, 3279–3284 (2015).
- Li, F., Smejkal, P., Macdonald, N. P., Guijt, R. M. & Breadmore, M. C. One-step fabrication of a microfluidic device with an integrated membrane and embedded reagents by multimaterial 3D printing. *Anal. Chem.* **89**, 4701–4707 (2017).
- Loke, G. et al. Structured multimaterial filaments for 3D printing of optoelectronics. *Nat. Commun.* **10**, 4010 (2019).
- Overvelde, J. T. B. How to print multi-material devices in one go. *Nature* **575**, 289–290 (2019).
- Rutz, A. L., Hyland, K. E., Jakus, A. E., Burghardt, W. R. & Shah, R. N. A multimaterial bioink method for 3D printing tunable, cell-compatible hydrogels. *Adv. Mater.* **27**, 1607–1614 (2015).
- Skyllar-Scott, M. A., Mueller, J., Visser, C. W. & Lewis, J. A. Voxlated soft matter via multimaterial multinozzle 3D printing. *Nature* **575**, 330–335 (2019).
- Zhou, L.-Y. et al. Multimaterial 3D printing of highly stretchable silicone elastomers. *ACS Appl. Mater. Interfaces* **11**, 23573–23583 (2019).
- Alcántara, C. C. J. et al. Mechanically interlocked 3D multi-material micromachines. *Nat. Commun.* **11**, 5957 (2020).
- Zhang, Y.-F. et al. Fast-response, stiffness-tunable soft actuator by hybrid multimaterial 3D printing. *Adv. Funct. Mater.* **29**, 1806698 (2019).
- Zorzetto, L. et al. Properties and role of interfaces in multimaterial 3D printed composites. *Sci. Rep.* **10**, 22285 (2020).
- Schwartz, J. J. & Boydston, A. J. Multimaterial actinic spatial control 3D and 4D printing. *Nat. Commun.* **10**, 791 (2019).
- Dolinski, N. D. et al. Solution mask liquid lithography (SMaLL) for one-step, multimaterial 3D printing. *Adv. Mater.* **30**, e1800364 (2018).
- Dolinski, N. D. et al. Tough multimaterial interfaces through wavelength-selective 3D printing. *ACS Appl. Mater. Interfaces*. <https://doi.org/10.1021/acami.1c06062> (2021).
- Kuang, X. et al. Grayscale digital light processing 3D printing for highly functionally graded materials. *Sci. Adv.* **5**, eaav5790 (2019).
- Gim, J. et al. Nanoscale deformation mechanics reveal resilience in nacre of Pinna nobilis shell. *Nat. Commun.* **10**, 4822 (2019).
- Wallin, T. J. et al. 3D printable tough silicone double networks. *Nat. Commun.* **11**, 4000 (2020).
- Bachmann, J. et al. Investigation of the temperature influence on the dual curing urethane-methacrylate resin Rigid Polyurethane 70 (RPU 70) in digital light synthesis (DLS). *Addit. Manuf.* **37**, 101677 (2021).
- Bachmann, J., Gleis, E., Schmöler, S., Fruhmann, G. & Hinrichsen, O. Photo-DSC method for liquid samples used in vat photopolymerization. *Anal. Chim. Acta.* **1153**, 338268 (2021).
- Obst, P. et al. Investigation of the influence of exposure time on the dual-curing reaction of RPU 70 during the DLS process and the resulting mechanical part properties. *Addit. Manuf.* **32**, 101002 (2020).
- Rolland, J. P. et al. Polyurethane resins having multiple mechanisms of hardening for use in producing three-dimensional objects. (2015).
- ISO 527-1. *Plastics — Determination of tensile properties* (2019).
- ISO 179-1. *Plastics — Determination of Charpy impact properties* (2010).
- ISO 6721-1. *Plastics — Determination of dynamic mechanical properties* (2019).
- Carbon Inc., Redwood City, CA 94063, USA. SDS Germany RPU 70 Part A and B (2017).
- ISO 3167. *Plastics — Multipurpose test specimens* (2014).

Acknowledgements

Proofreading was sponsored by the TUM Graduate School and carried out by KERN Corporation. The authors would like to thank Michael Lieberwirth, Stefan Stiel, Stefan Griesing, Johannes Eschl, Gunter Schroeter, Dirk Schuster, Thomas Schromm and Katrin Röckl from the BMW lab for assisting with the mechanical tests, high-speed recordings, CT scans and thin-section microscopy. The authors also thank Rüdiger Selhing from NETZSCH for supporting the DMA measurements.

Author contributions

J.B.: Conceptualisation, formal analysis, investigation, writing—original draft, writing—review & editing, visualisation, project administration. P.O.: Conceptualisation, Investigation. L.K.: Conceptualisation, Investigation. S.S.: Conceptualisation, Resources. G.F.: Supervision. G.W.: Supervision. T.O.: Supervision. K.W.: Writing—review & editing. O.H.: Writing—review & editing.

Funding

Open Access funding enabled and organized by Projekt DEAL.

Competing interests

P.O., L.K. and J.B. are holders of two pending patents related to this work submitted to the German patent and trademark office (Patent 1: Process for additive manufacturing of a form part (DE 10 2020 103 257.9); Patent 2: Production of hard/soft 2 K parts by resin-based additive manufacturing (DE 10 2020 130 690.3)). The other authors declare no competing interests.

Additional information

Supplementary information The online version contains supplementary material available at <https://doi.org/10.1038/s43246-021-00211-5>.

Correspondence and requests for materials should be addressed to Joel Bachmann.

Peer review information *Communications Materials* thanks the anonymous reviewers for their contribution to the peer review of this work. Primary Handling Editor: John Plummer. Peer reviewer reports are available.

Reprints and permission information is available at <http://www.nature.com/reprints>

Publisher's note Springer Nature remains neutral with regard to jurisdictional claims in published maps and institutional affiliations.



Open Access This article is licensed under a Creative Commons Attribution 4.0 International License, which permits use, sharing, adaptation, distribution and reproduction in any medium or format, as long as you give appropriate credit to the original author(s) and the source, provide a link to the Creative Commons license, and indicate if changes were made. The images or other third party material in this article are included in the article's Creative Commons license, unless indicated otherwise in a credit line to the material. If material is not included in the article's Creative Commons license and your intended use is not permitted by statutory regulation or exceeds the permitted use, you will need to obtain permission directly from the copyright holder. To view a copy of this license, visit <http://creativecommons.org/licenses/by/4.0/>.

© The Author(s) 2021

Acronyms

- 2PP** two-photon polymerization. 4, 17, 18
- AM** additive manufacturing. 1–3, 5, 7, 9, 10, 17, 22
- ASC** automated sample changer. 22
- BJT** binder jetting. 3
- CAD** computer-aided design. 1
- CAL** computed axial lithography. 4, 18
- CDLP** continuous digital light processing. 3
- CLIP** continuous liquid interface production. 2, 5
- CVPP** cavity vat photopolymerization. 28, 29
- DED** direct energy deposition. 3
- DLP** digital light processing. 3–5, 17, 18
- DLS** digital light synthesis. 2, 3, 5–9, 12–17, 19, 21–24, 26, 27
- DMD** digital micromirror device. 3, 5
- DSC** differential scanning calorimetry. 24
- FT-IR** Fourier-transform infrared spectroscopy. 24, 26
- GC-MS** gas chromatography mass spectrometry. 24, 27
- IBOMA** isobornyl methacrylate. 14, 24
- IPN** interpenetrating polymer network. 2, 10, 15, 24
- LCD** liquid crystal display. 3
- MABDI** methacrylate blocked diisocyanate. 14, 15

- MABPU** methacrylate blocked polyurethane. 14, 15
- MASC** multimaterial actinic spatial control. 18
- MEX** material extrusion. 3, 10
- MTJ** material jetting. 2
- NIR** near infrared. 4
- NPGDMA** neopentyl glycol dimethacrylate. 14
- PAG** photoacid generator. 10, 13, 18
- PBF** powder bed fusion. 3, 9, 10
- photo-DSC** photo differential scanning calorimetry. 13, 19, 21–24, 26, 27
- PI** photoinitiator. 10, 13, 18
- RH** relative humidity. 19, 23
- SHL** sheet lamination. 3
- SLA** stereolithography. 3, 5, 17
- SMaLL** solution mask liquid lithography. 18
- TBAEMA** tert-butylaminoethyl methacrylate. 14, 15, 24
- TGA** thermogravimetric analysis. 24, 27
- TPO** diphenyl (2,4,6 trimethyl benzoyl) phosphine oxide. 13, 14
- UDMA** urethane dimethacrylate. 14
- UV** ultraviolet. 2, 3, 5, 7, 9, 11, 13, 14, 18, 19, 22–24
- VAM** volumetric additive manufacturing. 4
- VOC** volatile organic compound. 27
- VPIP** volumetric polymerization inhibition patterning. 3
- VPP** vat photopolymerization. 2–4, 9, 10, 17–19, 26–29

Bibliography

- [1] ASTM International. *Standard Terminology for Additive Manufacturing Technologies*. West Conshohocken, PA, 2012. DOI: 10.1520/F2792-12A.
- [2] Wohlers. *Wohlers report 2019: 3D printing and additive manufacturing state of the industry*. Fort Collins, Colorado: Wohlers Associates, 2019. ISBN: 978-0-9913332-5-7.
- [3] Gregg Profozich. *Top 8 Industries Benefiting from Additive Manufacturing*. 2021. URL: <https://www.cmtc.com/blog/six-industries-benefiting-from-additive-manufacturing> (visited on 10/18/2021).
- [4] Shukantu Dev Nath and Sabrina Nilufar. "An Overview of Additive Manufacturing of Polymers and Associated Composites". In: *Polymers* 12.11 (2020). DOI: 10.3390/polym12112719.
- [5] Samuel Clark Ligon, Robert Liska, Jürgen Stampfl, Matthias Gurr, and Rolf Mülhaupt. "Polymers for 3D Printing and Customized Additive Manufacturing". In: *Chem. Rev.* 117.15 (2017), pp. 10212–10290. DOI: 10.1021/acs.chemrev.7b00074.
- [6] T. T. Le, S. A. Austin, S. Lim, R. A. Buswell, A. G. F. Gibb, and T. Thorpe. "Mix design and fresh properties for high-performance printing concrete". In: *Mater. Struct.* 45.8 (2012), pp. 1221–1232. DOI: 10.1617/s11527-012-9828-z.
- [7] S. Lim, R. A. Buswell, T. T. Le, S. A. Austin, A.G.F. Gibb, and T. Thorpe. "Developments in construction-scale additive manufacturing processes". In: *Autom. Constr.* 21 (2012), pp. 262–268. DOI: 10.1016/j.autcon.2011.06.010.
- [8] Alexander Paolini, Stefan Kollmannsberger, and Ernst Rank. "Additive manufacturing in construction: A review on processes, applications, and digital planning methods". In: *Addit. Manuf.* 30 (2019), p. 100894. DOI: 10.1016/j.addma.2019.100894.
- [9] Chang Liu, Bin Qian, Rongping Ni, Xiaofeng Liu, and Jianrong Qiu. "3D printing of multicolor luminescent glass". In: *RSC Adv.* 8.55 (2018), pp. 31564–31567. DOI: 10.1039/c8ra06706f.
- [10] Reda Mohammed Zaki, Clément Strutynski, Simon Kaser, Dominique Bernard, Gregory Hauss, Matthieu Faessel, Jocelyn Sabatier, Lionel Canioni, Younès Messaddeq, Sylvain Danto, and Thierry Cardinal. "Direct 3D-printing of phosphate glass by fused deposition modeling". In: *Mater. Des.* 194 (2020), p. 108957. DOI: 10.1016/j.matdes.2020.108957.

- [11] Atanu Kumar Das, David A. Agar, Magnus Rudolfsson, and Sylvia H. Larsson. "A review on wood powders in 3D printing: processes, properties and potential applications". In: *J. Mater. Res. Technol.* 15 (2021), pp. 241–255. DOI: 10.1016/j.jmrt.2021.07.110.
- [12] A. Le Duigou, M. Castro, R. Bevan, and N. Martin. "3D printing of wood fibre biocomposites: From mechanical to actuation functionality". In: *Mater. Des.* 96 (2016), pp. 106–114. DOI: 10.1016/j.matdes.2016.02.018.
- [13] Matthew Lanaro, David P. Forrestal, Stefan Scheurer, Damien J. Slinger, Sam Liao, Sean K. Powell, and Maria A. Woodruff. "3D printing complex chocolate objects: Platform design, optimization and evaluation". In: *J. Food Eng.* 215 (2017), pp. 13–22. DOI: 10.1016/j.jfoodeng.2017.06.029.
- [14] Sylvester Mantihal, Sangeeta Prakash, Fernanda Condi Godoi, and Bhesh Bhandari. "Optimization of chocolate 3D printing by correlating thermal and flow properties with 3D structure modeling". In: *Innov. Food Sci. Emerg. Technol.* 44 (2017), pp. 21–29. DOI: 10.1016/j.ifset.2017.09.012.
- [15] Ding Zhao, Anpan Han, and Min Qiu. "Ice lithography for 3D nanofabrication". In: *Sci. Bull.* 64.12 (2019), pp. 865–871. DOI: 10.1016/j.scib.2019.06.001.
- [16] Doron Kam, Michael Chasnitsky, Chen Nowogrodski, Ido Braslavsky, Tiffany Abitbol, Shlomo Magdassi, and Oded Shoseyov. "Direct Cryo Writing of Aerogels Via 3D Printing of Aligned Cellulose Nanocrystals Inspired by the Plant Cell Wall". In: *J. Colloid Interface Sci.* 3.2 (2019), p. 46. DOI: 10.3390/colloids3020046.
- [17] John R. Tumbleston, David Shirvanyants, Nikita Ermoshkin, Rima Januszewicz, Ashley R. Johnson, David Kelly, Kai Chen, Robert Pinschmidt, Jason P. Rolland, Alexander Ermoshkin, Edward T. Samulski, and Joseph M. DeSimone. "Additive manufacturing. Continuous liquid interface production of 3D objects". In: *Science (New York, N.Y.)* 347.6228 (2015), pp. 1349–1352. DOI: 10.1126/science.aaa2397.
- [18] Carbon Inc., Redwood City, CA 94063, USA. *RPU 70 Technical Data Sheet*. 2020.
- [19] Wohlers Terry and Gornet Tim. *History of additive manufacturing*. 2014. URL: <https://www.wohlersassociates.com/history2014.pdf> (visited on 12/21/2021).
- [20] Charles W. Hull. "Apparatus for production of three-dimensional objects by stereolithography". US4575330 (A). 1984.
- [21] Kathleen L. Sampson, Bhavana Deore, Abigail Go, Milind Ajith Nayak, Antony Orth, Mary Gallerneault, Patrick R. L. Malenfant, and Chantal Paquet. "Multimaterial Vat Polymerization Additive Manufacturing". In: *ACS Appl. Polym. Mater.* 3.9 (2021), pp. 4304–4324. DOI: 10.1021/acsapm.1c00262.
- [22] Formlabs. *SLA vs. DLP: 3D-Drucktechnologien für Kunstharze im Vergleich (Leitfaden 2020)*. 2020. URL: <https://formlabs.com/de/blog/vergleich-3d-druck-sla-dlp/> (visited on 12/21/2021).

- [23] Gayan A. Appuhamillage, Nicholas Chartrain, Viswanath Meenakshisundaram, Keyton D. Feller, Christopher B. Williams, and Timothy E. Long. "110th Anniversary : Vat Photopolymerization-Based Additive Manufacturing: Current Trends and Future Directions in Materials Design". In: *Ind. Eng. Chem. Res.* 58.33 (2019), pp. 15109–15118. DOI: 10.1021/acs.iecr.9b02679.
- [24] Xiaoyu Zheng, Howon Lee, Todd H. Weisgraber, Maxim Shusteff, Joshua DeOtte, Eric B. Duoss, Joshua D. Kuntz, Monika M. Biener, Qi Ge, Julie A. Jackson, Sergei O. Kucheyev, Nicholas X. Fang, and Christopher M. Spadaccini. "Ultralight, ultrastiff mechanical metamaterials". In: *Science (New York, N.Y.)* 344.6190 (2014), pp. 1373–1377. DOI: 10.1126/science.1252291.
- [25] A. Bertsch, S. Zissi, J. Y. Jézéquel, S. Corbel, and J. C. André. "Microstereolithography using a liquid crystal display as dynamic mask-generator". In: *Microsyst. Technol.* 3.2 (1997), pp. 42–47. DOI: 10.1007/s005420050053.
- [26] Rima Januszewicz, John R. Tumbleston, Adam L. Quintanilla, Sue J. Mecham, and Joseph M. DeSimone. "Layerless fabrication with continuous liquid interface production". In: *Proc. Natl. Acad. Sci. U.S.A.* 113.42 (2016), pp. 11703–11708. DOI: 10.1073/pnas.1605271113.
- [27] Martin P. de Beer, Harry L. van der Laan, Megan A. Cole, Riley J. Whelan, Mark A. Burns, and Timothy F. Scott. "Rapid, continuous additive manufacturing by volumetric polymerization inhibition patterning". In: *Sci. Adv.* 5.1 (2019), eaau8723. DOI: 10.1126/sciadv.aau8723.
- [28] Brett E. Kelly, Indrasen Bhattacharya, Hossein Heidari, Maxim Shusteff, Christopher M. Spadaccini, and Hayden K. Taylor. "Volumetric additive manufacturing via tomographic reconstruction". In: *Science (New York, N.Y.)* 363.6431 (2019), pp. 1075–1079. DOI: 10.1126/science.aau7114.
- [29] John D. Cuthbert, ed. *Optical/Laser Microlithography V*. SPIE Proceedings. SPIE, 1992.
- [30] TU Wien. *Multiphoton Lithography*. 2020. URL: https://amt.tuwien.ac.at/projects/completed_projects/multiphoton_lithography/EN/ (visited on 12/21/2021).
- [31] Joel Bachmann, Elisabeth Gleis, Stefan Schmölzer, Gabriele Fruhmann, and Olaf Hinrichsen. "Photo-DSC method for liquid samples used in vat photopolymerization". In: *Anal. Chim. Acta* 1153 (2021), p. 338268. DOI: 10.1016/j.aca.2021.338268.
- [32] Joseph DeSimonek. *What if 3D printing was 100x faster?* 2015. URL: https://www.ted.com/talks/joseph_desimone_what_if_3d_printing_was_100x_faster#t-465560 (visited on 12/21/2021).
- [33] C. Decker, T. Nguyen Thi Viet, D. Decker, and E. Weber-Koehl. "UV-radiation curing of acrylate/epoxide systems". In: *Polymer* 42.13 (2001), pp. 5531–5541. ISSN: 00323861. DOI: 10.1016/S0032-3861(01)00065-9.
- [34] Sebastian Seiffert, Kummerlöwe Claudia, and Vennemann Norbert. *Lechner, Gehrke, Nordmeier - Makromolekulare Chemie*. Springer, 2020. ISBN: 978-3-662-61109-8.

- [35] You-Min Huang and Cho-Pei Jiang. "On-line force monitoring of platform ascending rapid prototyping system". In: *J. Mater. Process. Technol.* 159.2 (2005), pp. 257–264. doi: 10.1016/j.jmatprotec.2004.05.015.
- [36] Farzad Liravi, Sonjoy Das, and Chi Zhou. "Separation force analysis and prediction based on cohesive element model for constrained-surface Stereolithography processes". In: *Comput. Aided Des.* 69 (2015), pp. 134–142. doi: 10.1016/j.cad.2015.05.002.
- [37] Yayue Pan, Haiyang He, Jie Xu, and Alan Feinerman. "Study of separation force in constrained surface projection stereolithography". In: *Rapid Prototyp. J.* 23.2 (2017), pp. 353–361. doi: 10.1108/RPJ-12-2015-0188.
- [38] Quandai Wang, Yulong Sun, Bingbing Guo, Pengyang Li, and Yan Li. "CFD analysis and prediction of suction force during the pulling-up stage of the continuous liquid interface production process". In: *AIP Adv.* 9.1 (2019), p. 015225. doi: 10.1063/1.5080516.
- [39] Gabriel Lipkowitz, Tim Samuelsen, Kaiwen Hsiao, Brian Lee, Maria T. Dulay, Ian Coates, Harrison Lin, William Pan, Geoffrey Toth, Lee Tate, Eric S. G. Shaqfeh, and Joseph M. DeSimone. "Injection continuous liquid interface production of 3D objects". In: *Sci. Adv.* 8.39 (2022), eabq3917. doi: 10.1126/sciadv.abq3917.
- [40] O. Weeger, N. Boddeti, S.-K. Yeung, S. Kaijima, and M. L. Dunn. "Digital design and nonlinear simulation for additive manufacturing of soft lattice structures". In: *Addit. Manuf.* 25 (2019), pp. 39–49. doi: 10.1016/j.addma.2018.11.003.
- [41] Carbon Inc. *Carbon software enables digital manufacturing: Software Controlled Chemical Reaction*. 2022. URL: <https://www.carbon3d.com/resources/whitepaper/carbonsoftware/> (visited on 04/16/2022).
- [42] Urs Weber. *Der neue Adidas 4D FWD im Test*. 2021. URL: <https://www.runnersworld.de/ausruetzung/adidas-4dfwd-im-test/> (visited on 11/11/2021).
- [43] Carbon Inc. *Media Hub: Part Images*. 2021. URL: <https://www.carbon3d.com/media-hub/> (visited on 11/01/2021).
- [44] BMW Group and Germany. *BMW Group small series production with 3D-printers: turn signal housing aka MINI side scuttle*. 2021. URL: <https://www.press.bmwgroup.com/deutschland/photo/search/additive,manufacturing/> (visited on 07/21/2021).
- [45] Aaron Borrill. *Best 3D-printed saddle: A Fizik vs Specialized head-to-head*. 2020. URL: <https://www.cyclingnews.com/reviews/best-3d-printed-saddles/> (visited on 11/11/2021).
- [46] Carbon Inc. *Riddell® Speedflex Diamond Helmet*. 2021. URL: <https://www.carbon3d.com/riddell/> (visited on 11/11/2021).

- [47] Philip Obst, Julius Riedelbauch, Paul Oehlmann, Dominik Rietzel, Martin Launhardt, Stefan Schmölzer, Tim A. Osswald, and Gerd Witt. "Investigation of the influence of exposure time on the dual-curing reaction of RPU 70 during the DLS process and the resulting mechanical part properties". In: *Addit. Manuf.* 32 (2020), p. 101002. doi: 10.1016/j.addma.2019.101002.
- [48] Robert W. Peiffer. "Applications of Photopolymer Technology". In: *ACS Symp. Ser.* Vol. 673, pp. 1–14. doi: 10.1021/bk-1997-0673.ch001.
- [49] Edward J. Murphy, Robert E. Ansel, and John J. Krajewski. "Method of forming a three-dimensional object by stereolithography and composition therefore". US4942001 (A). 1990.
- [50] Samuel Clark Ligon-Auer, Martin Schwentenwein, Christian Gorsche, Jürgen Stampfl, and Robert Liska. "Toughening of photo-curable polymer networks: a review". In: *Polym. Chem.* 7.2 (2016), pp. 257–286. doi: 10.1039/C5PY01631B.
- [51] R. Anastasio, W. Peerbooms, R. Cardinaels, and L. C. A. van Breemen. "Characterization of Ultraviolet-Cured Methacrylate Networks: From Photopolymerization to Ultimate Mechanical Properties". In: *Macromolecules* 52.23 (2019), pp. 9220–9231. issn: 0024-9297. doi: 10.1021/acs.macromol.9b01439.
- [52] Bernhard Steyrer, Bernhard Buseti, György Harakály, Robert Liska, and Jürgen Stampfl. "Hot Lithography vs. room temperature DLP 3D-printing of a dimethacrylate". In: *Addit. Manuf.* 21 (2018), pp. 209–214. doi: 10.1016/j.addma.2018.03.013.
- [53] Christopher J. Kloxin, Timothy F. Scott, and Christopher N. Bowman. "Stress relaxation via addition-fragmentation chain transfer in a thiol-ene photopolymerization". In: *Macromolecules* 42.7 (2009), pp. 2551–2556. issn: 0024-9297. doi: 10.1021/ma802771b.
- [54] Hui Lu, Jacquelyn A. Carioscia, Jeffery W. Stansbury, and Christopher N. Bowman. "Investigations of step-growth thiol-ene polymerizations for novel dental restoratives". In: *Dent. Mater.* 21.12 (2005), pp. 1129–1136. doi: 10.1016/j.dental.2005.04.001.
- [55] Ranjana C. Patel, Michael Rhodes, Yong Zhao, and Ranjana Patel. "Photocurable Compositions". US2007205528 (A1). 2007.
- [56] Joel Bachmann, Stefan Schmölzer, Matthias A. Ruderer, Gabriele Fruhmann, and Olaf Hinrichsen. "Photo-differential scanning calorimetry parameter study of photopolymers used in digital light synthesis". In: *SPE Polymers* (2021). issn: 2690-3857. doi: 10.1002/pls2.10063.
- [57] Gregory W. Sluggett, Claudia Turro, Michael W. George, Igor V. Koptuyug, and Nicholas J. Turro. "(2,4,6-Trimethylbenzoyl)diphenylphosphine Oxide Photochemistry. A Direct Time-Resolved Spectroscopic Study of Both Radical Fragments". In: *J. Am. Chem. Soc.* 117.18 (1995), pp. 5148–5153. doi: 10.1021/ja00123a018.
- [58] Gregory W. Sluggett, Peter F. McGarry, Igor V. Koptuyug, and Nicholas J. Turro. "Laser Flash Photolysis and Time-Resolved ESR Study of Phosphinoyl Radical Structure and Reactivity". In: *J. Am. Chem. Soc.* 118.31 (1996), pp. 7367–7372. doi: 10.1021/ja961043b.

- [59] Jane E. Baxter, R. Stephen Davidson, Hendrik J. Hageman, and Ton Overeem. In: *Makromol. Chem.* 189.12 (1988), pp. 2769–2780. DOI: 10.1002/macp.1988.021891206.
- [60] Osman Konuray, Xavier Fernández-Francos, Xavier Ramis, and Àngels Serra. “State of the Art in Dual-Curing Acrylate Systems”. In: *Polymers* 10.2 (2018). DOI: 10.3390/polym10020178.
- [61] Claudio Tosto, Eugenio Pergolizzi, Ignazio Blanco, Antonella Patti, Paul Holt, Sarah Karmel, and Gianluca Cicala. “Epoxy Based Blends for Additive Manufacturing by Liquid Crystal Display (LCD) Printing: The Effect of Blending and Dual Curing on Daylight Curable Resins”. In: *Polymers* 12.7 (2020). DOI: 10.3390/polym12071594.
- [62] Gustavo González, Xavier Fernández-Francos, Àngels Serra, Marco Sangermano, and Xavier Ramis. “Environmentally-friendly processing of thermosets by two-stage sequential aza-Michael addition and free-radical polymerization of amine–acrylate mixtures”. In: *Polym. Chem.* 6.39 (2015), pp. 6987–6997. DOI: 10.1039/C5PY00906E.
- [63] Ali Osman Konuray, Xavier Fernández-Francos, Àngels Serra, and Xavier Ramis. “Sequential curing of amine-acrylate-methacrylate mixtures based on selective aza-Michael addition followed by radical photopolymerization”. In: *Eur. Polym. J.* 84 (2016), pp. 256–267. DOI: 10.1016/j.eurpolymj.2016.09.025.
- [64] Ali Osman Konuray, Anna Ruiz, José M. Morancho, José M. Salla, Xavier Fernández-Francos, Àngels Serra, and Xavier Ramis. “Sequential dual curing by selective Michael addition and free radical polymerization of acetoacetate-acrylate-methacrylate mixtures”. In: *Eur. Polym. J.* 98 (2018), pp. 39–46. DOI: 10.1016/j.eurpolymj.2017.11.003.
- [65] Carbon Inc., Redwood City, CA 94063, USA. “SDS Germany RPU 70 Part A and B”. In: (2017).
- [66] Joel Bachmann, Philip Obst, Lukas Knorr, Stefan Schmölder, Gabriele Fruhmann, Gerd Witt, Tim Osswald, Katrin Wudy, and Olaf Hinrichsen. “Cavity vat photopolymerisation for additive manufacturing of polymer-composite 3D objects”. In: *Commun. Mater.* 2.1 (2021). DOI: 10.1038/s43246-021-00211-5.
- [67] Joel Bachmann, Elisabeth Gleis, Gabriele Fruhmann, Julius Riedelbauch, Stefan Schmölder, and Olaf Hinrichsen. “Investigation of the temperature influence on the dual curing urethane-methacrylate resin Rigid Polyurethane 70 (RPU 70) in digital light synthesis (DLS)”. In: *Addit. Manuf.* 37 (2021), p. 101677. DOI: 10.1016/j.addma.2020.101677.
- [68] Marius Ciprian Rusu, Christophe Block, Guy van Assche, and Bruno van Mele. “Influence of temperature and UV intensity on photo-polymerization reaction studied by photo-DSC”. In: *J. Therm. Anal. Calorim.* 110.1 (2012), pp. 287–294. DOI: 10.1007/s10973-012-2465-5.
- [69] Kunio Ikemura, Kensuke Ichizawa, Mariko Yoshida, So Ito, and Takeshi Endo. “UV-VIS spectra and photoinitiation behaviors of acylphosphine oxide and bisacylphosphine oxide derivatives in unfilled, light-cured dental resins”. In: *Dent. Mater. J.* 27.6 (2008), pp. 765–774. DOI: 10.4012/dmj.27.765.

- [70] Carola Esposito Corcione, Giulio Malucelli, Mariaenrica Frigione, and Alfonso Maffezzoli. "UV-curable epoxy systems containing hyperbranched polymers: Kinetics investigation by photo-DSC and real-time FT-IR experiments". In: *Polym. Test.* 28.2 (2009), pp. 157–164. doi: 10.1016/j.polymertesting.2008.11.002.
- [71] C. Esposito Corcione, M. Frigione, A. Maffezzoli, and G. Malucelli. "Photo – DSC and real time – FT-IR kinetic study of a UV curable epoxy resin containing o-Boehmites". In: *Eur. Polym. J.* 44.7 (2008), pp. 2010–2023. doi: 10.1016/j.eurpolymj.2008.04.030.
- [72] C. Esposito Corcione, R. Striani, and M. Frigione. "UV-cured methacrylic-silica hybrids: Effect of oxygen inhibition on photo-curing kinetics". In: *Thermochim. Acta* 576 (2014), pp. 47–55. doi: 10.1016/j.tca.2013.11.028.
- [73] R. V. Ghorpade, S. M. Bhosle, S. Ponrathnam, C. R. Rajan, N. N. Chavan, and R. Harikrishna. "Photopolymerization kinetics of 2-phenylethyl (meth)acrylates studied by photo DSC". In: *J. Polym. Res.* 19.2 (2012). doi: 10.1007/s10965-011-9811-3.
- [74] Y. Irmouli, B. George, and A. Merlin. "Study of the polymerization of acrylic resins by photocalorimetry: interactions between UV initiators and absorbers". In: *J. Therm. Anal. Calorim.* 96.3 (2009), pp. 911–916. doi: 10.1007/s10973-009-0061-0.
- [75] Fengze Jiang and Dietmar Drummer. "Curing Kinetic Analysis of Acrylate Photopolymer for Additive Manufacturing by Photo-DSC". In: *Polymers* 12.5 (2020). doi: 10.3390/polym12051080.
- [76] C. A. Gracia-Fernández, P. Davies, S. Gómez-Barreiro, J. López Beceiro, J. Tarrío-Saavedra, and R. Artiaga. "A vitrification and curing study by simultaneous TMDSC-photocalorimetry". In: *J. Therm. Anal. Calorim.* 102.3 (2010), pp. 1057–1062. doi: 10.1007/s10973-010-0872-z.
- [77] Samuel Clark Ligon, Branislav Husár, Harald Wutzel, Richard Holman, and Robert Liska. "Strategies to reduce oxygen inhibition in photoinduced polymerization". In: *Chem. Rev.* 114.1 (2014), pp. 557–589. doi: 10.1021/cr3005197.
- [78] C. S. Bentivoglio Ruiz, L. D. B. Machado, J. E. Volponi, and E. Segura Pino. "Oxygen Inhibition and Coating Thickness Effects on Uv Radiation Curing of Weatherfast Clearcoats Studied by Photo-DSC". In: *J. Therm. Anal. Calorim.* 75.2 (2004), pp. 507–512. doi: 10.1023/B:JTAN.0000027140.27560.d1.
- [79] Shamini Bundell. "New 3D printer makes multi-material robots". In: *Nature* (2019). doi: 10.1038/d41586-019-03513-4.
- [80] James O. Hardin, Thomas J. Ober, Alexander D. Valentine, and Jennifer A. Lewis. "Microfluidic Printheads for Multimaterial 3D Printing of Viscoelastic Inks". In: *Adv. Mater.* 27.21 (2015), pp. 3279–3284. doi: 10.1002/adma.201500222.
- [81] Feng Li, Petr Smejkal, Niall P. Macdonald, Rosanne M. Guijt, and Michael C. Breadmore. "One-Step Fabrication of a Microfluidic Device with an Integrated Membrane and Embedded Reagents by Multimaterial 3D Printing". In: *Anal. Chem.* 89.8 (2017), pp. 4701–4707. doi: 10.1021/acs.analchem.7b00409.

- [82] Gabriel Loke, Rodger Yuan, Michael Rein, Tural Khudiyev, Yash Jain, John Joannopoulos, and Yoel Fink. "Structured multimaterial filaments for 3D printing of optoelectronics". In: *Nat. Commun.* 10.1 (2019), p. 4010. DOI: 10.1038/s41467-019-11986-0.
- [83] Johannes T. B. Overvelde. "How to print multi-material devices in one go". In: *Nature* 575.7782 (2019), pp. 289–290. DOI: 10.1038/d41586-019-03408-4.
- [84] Alexandra L. Rutz, Kelly E. Hyland, Adam E. Jakus, Wesley R. Burghardt, and Ramille N. Shah. "A multimaterial bioink method for 3D printing tunable, cell-compatible hydrogels". In: *Adv. Mater.* 27.9 (2015), pp. 1607–1614. DOI: 10.1002/adma.201405076.
- [85] Mark A. Skylar-Scott, Jochen Mueller, Claas W. Visser, and Jennifer A. Lewis. "Voxelated soft matter via multimaterial multinozzle 3D printing". In: *Nature* 575.7782 (2019), pp. 330–335. DOI: 10.1038/s41586-019-1736-8.
- [86] Lu-Yu Zhou, Qing Gao, Jian-Zhong Fu, Qian-Yong Chen, Jia-Pei Zhu, Yuan Sun, and Yong He. "Multimaterial 3D Printing of Highly Stretchable Silicone Elastomers". In: *ACS Appl. Mater. Interfaces* 11.26 (2019), pp. 23573–23583. DOI: 10.1021/acsami.9b04873.
- [87] Yuan-Fang Zhang, Ningbin Zhang, Hardik Hingorani, Ningyuan Ding, Dong Wang, Chao Yuan, Biao Zhang, Guoying Gu, and Qi Ge. "Fast-Response, Stiffness-Tunable Soft Actuator by Hybrid Multimaterial 3D Printing". In: *Adv. Funct. Mater.* 29.15 (2019), p. 1806698. DOI: 10.1002/adfm.201806698.
- [88] Laura Zorzetto, Luca Andena, Francesco Briatico-Vangosa, Lorenzo de Noni, Jean-Michel Thomassin, Christine Jérôme, Quentin Grossman, Anne Mertens, Richard Weinkamer, Marta Rink, and Davide Ruffoni. "Properties and role of interfaces in multimaterial 3D printed composites". In: *Sci. Rep.* 10.1 (2020), p. 22285. DOI: 10.1038/s41598-020-79230-0.
- [89] David G. Moore, Lorenzo Barbera, Kunal Masania, and André R. Studart. "Three-dimensional printing of multicomponent glasses using phase-separating resins". In: *Nat. Mater.* 19.2 (2020), pp. 212–217. DOI: 10.1038/s41563-019-0525-y.
- [90] Ela Sachyani Keneth, Rama Lieberman, Matthew Rednor, Giulia Scalet, Ferdinando Auricchio, and Shlomo Magdassi. "Multi-Material 3D Printed Shape Memory Polymer with Tunable Melting and Glass Transition Temperature Activated by Heat or Light". In: *Polymers* 12.3 (2020). DOI: 10.3390/polym12030710.
- [91] Carl J. Thrasher, Johanna J. Schwartz, and Andrew J. Boydston. "Modular Elastomer Photoresins for Digital Light Processing Additive Manufacturing". In: *ACS applied materials & interfaces* 9.45 (2017), pp. 39708–39716. DOI: 10.1021/acsami.7b13909.
- [92] Yong Tae Kim, Kurt Castro, Nirveek Bhattacharjee, and Albert Folch. "Digital Manufacturing of Selective Porous Barriers in Microchannels Using Multi-Material Stereolithography". In: *Micromachines* 9.3 (2018). ISSN: 2072-666X. DOI: 10.3390/mi9030125.

- [93] Karina Arcaute, Brenda K. Mann, and Ryan B. Wicker. "Fabrication of Off-the-Shelf Multilumen Poly(Ethylene Glycol) Nerve Guidance Conduits Using Stereolithography". In: *Tissue Eng. Part C Methods* 17.1 (2011), pp. 27–38. DOI: 10.1089/ten.TEC.2010.0011.
- [94] Céline A. Mandon, Loïc J. Blum, and Christophe A. Marquette. "Adding Biomolecular Recognition Capability to 3D Printed Objects". In: *Anal. Chem.* 88.21 (2016), pp. 10767–10772. DOI: 10.1021/acs.analchem.6b03426.
- [95] Yi Lu, Gazell Mapili, Gerry Suhali, Shaochen Chen, and Krishnendu Roy. "A digital micro-mirror device-based system for the microfabrication of complex, spatially patterned tissue engineering scaffolds". In: *J. Biomed. Mater. Res.* 77.2 (2006), pp. 396–405. DOI: 10.1002/jbm.a.30601.
- [96] Zheqin Dong, Haijun Cui, Haodong Zhang, Fei Wang, Xiang Zhan, Frederik Mayer, Britta Nestler, Martin Wegener, and Pavel A. Levkin. "3D printing of inherently nanoporous polymers via polymerization-induced phase separation". In: *Nat. Commun.* 12.1 (2021), p. 247. DOI: 10.1038/s41467-020-20498-1.
- [97] Michael Schmid, Simon Thiele, Alois Herkommer, and Harald Giessen. "Three-dimensional direct laser written achromatic axicons and multi-component microlenses". In: *Opt. Lett.* 43.23 (2018), pp. 5837–5840. DOI: 10.1364/OL.43.005837.
- [98] Michael Schmid, Florian Sterl, Simon Thiele, Alois Herkommer, and Harald Giessen. "3D printed hybrid refractive/diffractive achromat and apochromat for the visible wavelength range". In: *Opt. Lett.* 46.10 (2021), pp. 2485–2488. DOI: 10.1364/OL.423196.
- [99] Franziska Klein, Benjamin Richter, Thomas Striebel, Clemens M. Franz, Georg von Freymann, Martin Wegener, and Martin Bastmeyer. "Two-component polymer scaffolds for controlled three-dimensional cell culture". In: *Adv. Mater.* 23.11 (2011), pp. 1341–1345. DOI: 10.1002/adma.201004060.
- [100] Karina Arcaute, Brenda Mann, and Ryan Wicker. "Stereolithography of spatially controlled multi-material bioactive poly(ethylene glycol) scaffolds". In: *Acta Biomater.* 6.3 (2010), pp. 1047–1054. DOI: 10.1016/j.actbio.2009.08.017.
- [101] Markus M. Zieger, Patrick Mueller, Alexander S. Quick, Martin Wegener, and Christopher Barner-Kowollik. "Cleaving Direct-Laser-Written Microstructures on Demand". In: *Angew. Chem. Int.* 56.20 (2017), pp. 5625–5629. DOI: 10.1002/anie.201701593.
- [102] Vincent Chan, Pinar Zorlutuna, Jae Hyun Jeong, Hyunjoon Kong, and Rashid Bashir. "Three-dimensional photopatterning of hydrogels using stereolithography for long-term cell encapsulation". In: *Lab Chip* 10.16 (2010), pp. 2062–2070. DOI: 10.1039/C004285D.
- [103] Vincent Chan, Jae Hyun Jeong, Piyush Bajaj, Mitchell Collens, Taher Saif, Hyunjoon Kong, and Rashid Bashir. "Multi-material bio-fabrication of hydrogel cantilevers and actuators with stereolithography". In: *Lab Chip* 12.1 (2012), pp. 88–98. DOI: 10.1039/C1LC20688E.

- [104] Pamela Robles-Martinez, Xiaoyan Xu, Sarah J. Trenfield, Atheer Awad, Alvaro Goyanes, Richard Telford, Abdul W. Basit, and Simon Gaisford. "3D Printing of a Multi-Layered Polypill Containing Six Drugs Using a Novel Stereolithographic Method". In: *Pharmaceutics* 11.6 (2019). ISSN: 1999-4923. DOI: 10.3390/pharmaceutics11060274.
- [105] Daehoon Han, Zhaocheng Lu, Shawn A. Chester, and Howon Lee. "Micro 3D Printing of a Temperature-Responsive Hydrogel Using Projection Micro-Stereolithography". In: *Sci. Rep.* 8.1 (2018), p. 1963. DOI: 10.1038/s41598-018-20385-2.
- [106] Karina Arcaute, Brenda K. Mann, and Ryan B. Wicker. "Stereolithography of three-dimensional bioactive poly(ethylene glycol) constructs with encapsulated cells". In: *Ann. Biomed. Eng.* 34.9 (2006), pp. 1429–1441. DOI: 10.1007/s10439-006-9156-y.
- [107] Joseph Borrello, Philip Nasser, James Iatridis, and Kevin D. Costa. "3D Printing a Mechanically-Tunable Acrylate Resin on a Commercial DLP-SLA Printer". In: *Addit. Manuf.* 23 (2018), pp. 374–380. DOI: 10.1016/j.addma.2018.08.019.
- [108] Ashley R. Johnson, Cassie L. Caudill, John R. Tumbleston, Cameron J. Bloomquist, Katherine A. Moga, Alexander Ermoshkin, David Shirvanyants, Sue J. Mecham, J. Christopher Luft, and Joseph M. DeSimone. "Single-Step Fabrication of Computationally Designed Microneedles by Continuous Liquid Interface Production". In: *PloS one* 11.9 (2016), e0162518. DOI: 10.1371/journal.pone.0162518.
- [109] Anand K. Mishra, Thomas J. Wallin, Wenyang Pan, Patricia Xu, Kaiyang Wang, Emmanuel P. Giannelis, Barbara Mazzolai, and Robert F. Shepherd. "Autonomic perspiration in 3D-printed hydrogel actuators". In: *Sci. Robot.* 5.38 (2020). DOI: 10.1126/scirobotics.aaz3918.
- [110] Gazell Mapili, Yi Lu, Shaochen Chen, and Krishnendu Roy. "Laser-layered microfabrication of spatially patterned functionalized tissue-engineering scaffolds". In: *J. Biomed. Mater. Res.* 75.2 (2005), pp. 414–424. DOI: 10.1002/jbm.b.30325.
- [111] Da Chen and Xiaoyu Zheng. "Multi-material Additive Manufacturing of Metamaterials with Giant, Tailorable Negative Poisson's Ratios". In: *Sci. Rep.* 8.1 (2018), p. 9139. DOI: 10.1038/s41598-018-26980-7.
- [112] Yanfeng Lu, Satya Nymisha Mantha, Douglas C. Crowder, Sofia Chinchilla, Kush N. Shah, Yang H. Yun, Ryan B. Wicker, and Jae-Won Choi. "Microstereolithography and characterization of poly(propylene fumarate)-based drug-loaded microneedle arrays". In: *Biofabrication* 7.4 (2015), p. 045001. DOI: 10.1088/1758-5090/7/4/045001.
- [113] Alexander Thomas, Isabel Orellano, Tobias Lam, Benjamin Noichl, Michel-Andreas Geiger, Anna-Klara Amler, Anna-Elisabeth Kreuder, Christopher Palmer, Georg Duda, Roland Lauster, and Lutz Klok. "Vascular bioprinting with enzymatically degradable bioinks via multi-material projection-based stereolithography". In: *Acta Biomater.* 117 (2020), pp. 121–132. DOI: 10.1016/j.actbio.2020.09.033.

- [114] Qiming Wang, Julie A. Jackson, Qi Ge, Jonathan B. Hopkins, Christopher M. Spadaccini, and Nicholas X. Fang. "Lightweight Mechanical Metamaterials with Tunable Negative Thermal Expansion". In: *Phys. Rev. Lett.* 117.17 (2016), p. 175901. doi: 10.1103/PhysRevLett.117.175901.
- [115] Qi Ge, Zhe Chen, Jianxiang Cheng, Biao Zhang, Yuan-Fang Zhang, Honggeng Li, Xiangnan He, Chao Yuan, Ji Liu, Shlomo Magdassi, and Shaoxing Qu. "3D printing of highly stretchable hydrogel with diverse UV curable polymers". In: *Sci. Adv.* 7.2 (2021). doi: 10.1126/sciadv.aba4261.
- [116] Biao Zhang, Shiya Li, Hardik Hingorani, Ahmad Serjouei, Liraz Larush, Amol A. Pawar, Wei Huang Goh, Amir Hosein Sakhaei, Michinao Hashimoto, Kavin Kowsari, Shlomo Magdassi, and Qi Ge. "Highly stretchable hydrogels for UV curing based high-resolution multimaterial 3D printing". In: *J. Mater. Chem. B* 6.20 (2018), pp. 3246–3253. doi: 10.1039/C8TB00673C.
- [117] Ryan Hensleigh, Huachen Cui, Zhenpeng Xu, Jeffrey Massman, Desheng Yao, John Berrigan, and Xiaoyu Zheng. "Charge-programmed three-dimensional printing for multi-material electronic devices". In: *Nat. Electron.* 3.4 (2020), pp. 216–224. doi: 10.1038/s41928-020-0391-2.
- [118] Bagrat Grigoryan, Daniel W. Sazer, Amanda Avila, Jacob L. Albritton, Aparna Padhye, Anderson H. Ta, Paul T. Greenfield, Don L. Gibbons, and Jordan S. Miller. "Development, characterization, and applications of multi-material stereolithography bioprinting". In: *Sci. Rep.* 11.1 (2021), p. 3171. doi: 10.1038/s41598-021-82102-w.
- [119] Ebrahim Behroodi, Hamid Latifi, and Farhood Najafi. "A compact LED-based projection microstereolithography for producing 3D microstructures". In: *Sci. Rep.* 9.1 (2019), p. 19692. doi: 10.1038/s41598-019-56044-3.
- [120] Qi Ge, Amir Hosein Sakhaei, Howon Lee, Conner K. Dunn, Nicholas X. Fang, and Martin L. Dunn. "Multimaterial 4D Printing with Tailorable Shape Memory Polymers". In: *Sci. Rep.* 6 (2016). doi: 10.1038/srep31110.
- [121] Tobias Grix, Alicia Ruppelt, Alexander Thomas, Anna-Klara Amler, Benjamin P. Noichl, Roland Lauster, and Lutz Kloke. "Bioprinting Perfusion-Enabled Liver Equivalents for Advanced Organ-on-a-Chip Applications". In: *Genes* 9.4 (2018). issn: 2073-4425. doi: 10.3390/genes9040176.
- [122] Li-Hsin Han, Shalu Suri, Christine E. Schmidt, and Shaochen Chen. "Fabrication of three-dimensional scaffolds for heterogeneous tissue engineering". In: *Biomed. Microdevices* 12.4 (2010), pp. 721–725. doi: 10.1007/s10544-010-9425-2.
- [123] Asim Inamdar, Marco Magana, Frank Medina, Yinko Grajeda, and Ryan Wicker. *Development of an Automated Multiple Material Stereolithography Machine*. 2006. doi: 10.26153/TSW/7167.
- [124] Bilal Khatri, Marco Frey, Ahmed Raouf-Fahmy, Marc-Vincent Scharla, and Thomas Hanemann. "Development of a multi-material stereolithography 3D printing device". In: *Micromachines* 11.5 (2020). issn: 2072-666X. doi: 10.3390/mi11050532.

- [125] Neil D. Dolinski, Zachariah A. Page, E. Benjamin Callaway, Fabian Eisenreich, Ronnie V. Garcia, Roberto Chavez, David P. Bothman, Stefan Hecht, Frank W. Zok, and Craig J. Hawker. "Solution Mask Liquid Lithography (SMaLL) for One-Step, Multimaterial 3D Printing". In: *Adv. Mater.* 30.31 (2018), e1800364. DOI: 10.1002/adma.201800364.
- [126] Neil D. Dolinski, E. Benjamin Callaway, Caitlin S. Sample, Luke F. Gockowski, Roberto Chavez, Zachariah A. Page, Fabian Eisenreich, Stefan Hecht, Megan T. Valentine, Frank W. Zok, and Craig J. Hawker. "Tough Multimaterial Interfaces through Wavelength-Selective 3D Printing". In: *ACS Appl. Mater. Interfaces* (2021). DOI: 10.1021/acsaami.1c06062.
- [127] J. J. Schwartz and A. J. Boydston. "Multimaterial actinic spatial control 3D and 4D printing". In: *Nat. Commun.* 10.1 (2019), p. 791. DOI: 10.1038/s41467-019-08639-7.
- [128] Xiao Kuang, Jiangtao Wu, Kaijuan Chen, Zeang Zhao, Zhen Ding, Fengjingyang Hu, Daining Fang, and H. Jerry Qi. "Grayscale digital light processing 3D printing for highly functionally graded materials". In: *Sci. Adv.* 5.5 (2019), eaav5790. DOI: 10.1126/sciadv.aav5790.
- [129] Jérémy Odent, Sophie Vanderstappen, Antoniya Toncheva, Enzo Pichon, Thomas J. Wallin, Kaiyang Wang, Robert F. Shepherd, Philippe Dubois, and Jean-Marie Raquez. "Hierarchical chemomechanical encoding of multi-responsive hydrogel actuators via 3D printing". In: *J. Mater. Chem. A* 7.25 (2019), pp. 15395–15403. DOI: 10.1039/C9TA03547H.
- [130] Gregory I. Peterson, Johanna J. Schwartz, Di Zhang, Benjamin M. Weiss, Mark A. Ganter, Duane W. Storti, and Andrew J. Boydston. "Production of Materials with Spatially-Controlled Cross-Link Density via Vat Photopolymerization". In: *ACS Appl. Mater. Interfaces* 8.42 (2016), pp. 29037–29043. DOI: 10.1021/acsaami.6b09768.
- [131] Jiangtao Wu, Zeang Zhao, Xiao Kuang, Craig M. Hamel, Daining Fang, and H. Jerry Qi. "Reversible shape change structures by grayscale pattern 4D printing". In: *Multifunct. Mater.* 1.1 (2018), p. 015002. DOI: 10.1088/2399-7532/aac322.
- [132] Hang Yin, Yonghui Ding, Yao Zhai, Wei Tan, and Xiaobo Yin. "Orthogonal programming of heterogeneous micro-mechano-environments and geometries in three-dimensional bio-stereolithography". In: *Nat. Commun.* 9.1 (2018), p. 4096. DOI: 10.1038/s41467-018-06685-1.
- [133] Zhiheng Zhang, Nathaniel Corrigan, Ali Bagheri, Jianyong Jin, and Cyrille Boyer. "A Versatile 3D and 4D Printing System through Photocontrolled RAFT Polymerization". In: *Angew. Chem. Int.* 58.50 (2019), pp. 17954–17963. DOI: 10.1002/anie.201912608.
- [134] Sergey Vyazovkin, Alan K. Burnham, Loic Faveregeon, Nobuyoshi Koga, Elena Moukhina, Luis A. Pérez-Maqueda, and Nicolas Sbirrazzuoli. "ICTAC Kinetics Committee recommendations for analysis of multi-step kinetics". In: *Thermochim. Acta* 689 (2020), p. 178597. DOI: 10.1016/j.tca.2020.178597.

- [135] Austin C. Hayes, Jorge Osio-Norgaard, Shelly Miller, Gregory L. Whiting, and Marina E. Vance. "Air pollutant emissions from multi jet fusion, material-jetting, and digital light synthesis commercial 3D printers in a service bureau". In: *Build. Environ.* 202 (2021), p. 108008. DOI: 10.1016/j.buildenv.2021.108008.
- [136] Joel Bachmann. "Verfahren zur additiven Herstellung eines Formkörpers (3D-Druck von harten Gehäusen mit elastischem Kern.)" DE102020103257 (A1). 2021.
- [137] Joel Bachmann. "Verfahren zur additiven Herstellung eines Formkörpers (Druckluftbeaufschlagung bei Harz-Bad basierten 3D-Druck Verfahren)". DE102020103255 (A1). 2021.
- [138] Philip Obst, Joel Bachmann, and Lukas Knorr. "Verfahren zur additiven Herstellung eines Formkörpers (Herstellung von hart/weich-2K-Bauteilen mittels harzbasierter additiver Fertigung)". DE102020130690 (A1). 2022.
- [139] Philip Obst, Joel Bachmann, and Lukas Knorr. "Verfahren zur additiven Herstellung eines Formkörpers (Selbsteilende Materialien)". DE102020130690 (A1). 2022.